

CRANFIELD UNIVERSITY

JING SHI

A STUDY ON HIGH-VISCOSITY OIL-WATER TWO-PHASE FLOW IN
HORIZONTAL PIPES

SCHOOL OF ENERGY, ENVIRONMENT AND AGRIFOOD
Oil and Gas Engineering Centre

PhD

Academic Year: 2012 – 2015

Supervisor: Professor Hoi Yeung
September 2015

CRANFIELD UNIVERSITY

SCHOOL OF ENERGY, ENVIRONMENT AND AGRIFOOD
Oil and Gas Engineering Centre

PhD

Academic Year 2012- 2015

JING SHI

A STUDY ON HIGH-VISCOSITY OIL-WATER TWO-PHASE FLOW IN
HORIZONTAL PIPES

Supervisor: Professor Hoi Yeung
September 2015

This thesis is submitted in partial fulfilment of the requirements for the
degree of Doctor of Philosophy

© Cranfield University 2015. All rights reserved. No part of this
publication may be reproduced without the written permission of the
copyright owner.

ABSTRACT

A study on high-viscosity oil-water flow in horizontal pipes has been conducted applying experimental, mechanism analysis and empirical modelling, and CFD simulation approaches.

A horizontal 1 inch flow loop was modified by adding a designed sampling section to achieve water holdup measurement. Experiments on high-viscosity oil-water flow were conducted. Apart from the data obtained in the present experiments, raw data from previous experiments conducted in the same research group was collated. From the experimental investigation, it is found that that the relationship between the water holdup of water-lubricated flow and input water volume fraction is closely related to the oil core concentricity and oil fouling on the pipe wall. The water holdup is higher than the input water volume fraction only when the oil core is about concentric. The pressure gradient of water-lubricated flow can be one to two orders of magnitude higher than that of single water flow. This increased frictional loss is closely related to oil fouling on the pipe wall.

Mechanism analysis and empirical modelling of oil-water flow were conducted. The ratio of the gravitational force to viscous force was proposed to characterise liquid-liquid flows in horizontal pipes into gravitational force dominant, viscous force dominant and gravitational force and viscous force comparable flow featured with different basic flow regimes. For viscous force dominant flow, an empirical criterion on the formation of stable water-lubricated flow was proposed. Existing empirical and mechanistic models for the prediction of water holdup and/or pressure gradient were evaluated with the experimental data; the applicability of different models is demonstrated.

Three-dimensional CFD modelling of oil-water flow was performed using the commercial CFD code Fluent. The phase configurations calculated from the CFD model show a fair agreement with those from experiments and mechanism analysis. The velocity distribution of core annular flow is characterised with nearly constant velocity across the oil core when the oil viscosity is significantly

higher than the water viscosity, indicating that the high-viscosity oil core flows inside the water as a solid body. The velocity profile becomes similar to that of single phase flow as the oil viscosity becomes close to the water viscosity.

Key words:

Oil-water; high-viscosity oil; water holdup; oil fouling; pressure gradient; CFD

ACKNOWLEDGEMENTS

It is pleasant to express my sincere gratitude to all those who have contributed to the completion of the presented work. I am sincerely grateful to the following:

To Professor Hoi Yeung, my supervisor, for initiating the study and providing support and stimulating discussions throughout the duration of this work; without him, my study could not have been started and finished to a success.

To Dr Liyun Lao, for his advice on the design of the sampling section, training on the operation of a three-phase rig and useful comments on my manuscript of the experimental part.

To Stan Collins, our lab. manager, who offered valuable discussions and technical support on pressure measurement and data acquisition; to the lab technician Sheridan Cross who helped set up the experimental rig.

To Dr Mustapha Gourma, who was always ready to discuss with me on the CFD simulation and gave me useful comments on the CFD part of the manuscript; to Dr Yabin Zhao, who offered kind guide at the initial stage of my CFD simulation study; to Andy Gittings, the university research computing manager, who provided great support on high performance computing.

To Dr Hameed Al-Awadi, Dr Ezeddine Zorgani and Dr Solomon Alagbe, for providing raw experimental data to make the present large experimental data base; to my colleague Yahaya Baba who offered kind assist in my experiments; to Sasha Quills and Sam Skears for their administrative support.

To Dr Shiwei Fan who has been there to offer numerous discussions.

And to my family, my parents, brother, sister-in-law, and little niece for their love and support.

TABLE OF CONTENTS

ABSTRACT.....	i
ACKNOWLEDGEMENTS.....	iii
TABLE OF CONTENTS	v
LIST OF FIGURES.....	viii
LIST OF TABLES	xv
LIST OF ABBREVIATIONS.....	xvi
LIST OF SYMBOLS	xviii
1 INTRODUCTION.....	1
1.1 Background.....	1
1.1.1 Overview	1
1.1.2 Previous studies on high-viscosity oil-water flow at Cranfield University	2
1.2 Objectives	3
1.3 Thesis outline.....	3
2 LITERATURE REVIEW	5
2.1 Industrial background.....	6
2.1.1 An overview on heavy oil production and transportation	6
2.1.2 Industrial applications of water-lubricated heavy oil transport	10
2.2 Experimental studies on high-viscosity oil-water flow	13
2.2.1 Basic flow notations in oil-water flow	13
2.2.2 Previous experimental studies on high-viscosity oil-water pipeline flow.....	16
2.2.3 Summary.....	28
2.3 Modelling of multiphase flow in computational fluid dynamics	32
2.3.1 Fundamentals of computational fluid dynamics.....	32
2.3.2 Multiphase computational fluid dynamics	34
2.3.3 Numerical solution of transport equations	37
3 EXPERIMENTAL SETUP AND PROGRAMME	41
3.1 Introduction	41
3.2 Literature review on phase holdup measurement	41
3.3 Experimental setup	43
3.4 Experimental procedure and runs.....	50
3.4.1 Experimental procedure	50
3.4.2 Experimental runs	52
3.5 Assurance of experimental system	54
3.5.1 Pressure signals.....	54
3.5.2 Oil viscosity	56
3.5.3 Accuracy of the sampling measurement	58
3.5.4 Repeatability of the experiments	60

3.6 Summary	61
4 EXPERIMENTAL RESULTS	63
4.1 Introduction	63
4.2 Experimental data bank	63
4.3 Flow patterns	65
4.3.1 Flow patterns observed in experiments	65
4.3.2 Flow pattern maps	73
4.4 Inversion occurrence	86
4.5 Water holdup of water-lubricated flow	91
4.6 Pressure gradient of water-lubricated flow	96
4.7 Summary	104
5 MECHANISM ANALYSIS AND EMPIRICAL MODELLING	107
5.1 Introduction	107
5.2 Flow patterns of liquid-liquid flow	107
5.2.1 Literature review on flow patterns of liquid-liquid flows in horizontal pipes	107
5.2.2 Gravitation to viscous force ratio to characterise liquid-liquid flow systems	115
5.3 Inversion occurrence	129
5.4 Water holdup and pressure gradient of water-lubricated flow	132
5.4.1 Review on models of water-lubricated flow	133
5.4.2 Model development for water-lubricated flow	140
5.4.3 Evaluation of models	149
5.5 Summary	163
6 CFD SIMULATION SETUP AND PROGRAMME	167
6.1 Introduction	167
6.2 Mathematical models	168
6.2.1 VOF model	168
6.2.2 SST $k-\omega$ turbulence model	170
6.3 Physical models	171
6.4 Simulation setup	173
6.4.1 Boundary conditions	173
6.4.2 Solution setup	174
6.5 Simulation runs	175
6.6 Preliminary simulation results	180
6.6.1 Influence of mesh sizes	180
6.6.2 Influence of initialization methods	181
6.6.3 Influence of volume fraction interpolation schemes at phase interface	185
6.6.4 Influence of turbulence schemes	186
6.6.5 Influence of wall contact angles	189

6.7 Summary	194
7 SIMULATION RESULTS	195
7.1 Introduction	195
7.2 Flow patterns	195
7.2.1 Comparison with experimental flow patterns.....	195
7.2.2 Influence of parameters on flow pattern	200
7.2.3 Formation of water-lubricated flow	205
7.3 Water holdup of water-lubricated flow.....	206
7.4 Pressure gradient of water-lubricated flow.....	208
7.5 Cross-sectional flow characteristics of CAF	213
7.6 Summary	221
8 CONCLUSIONS AND RECOMMENDATIONS	223
8.1 Conclusions	223
8.2 Recommendations.....	229
REFERENCES.....	231
APPENDICES	241
Appendix A Tabulated experimental data	241
Appendix B Summary of data collected from the literature	253
Appendix C Calibration of pressure transducers.....	254
Appendix D Practical considerations on the experimental setup of the oil system	257
Appendix E Wall wettability and contact angle.....	261
Appendix F Preliminary experiments on restart of core annular flow	263
Appendix G Heavy oil production and transportation techniques.....	267

LIST OF FIGURES

Figure 1-1 Outline of the thesis structure.	4
Figure 2-1 Heavy oil production methods. EOR: enhanced oil recovery; CSS: cyclic steam stimulation; SAGD: steam-assisted gravity drainage; CHOPS: cold heavy oil production with sand; VAPEX: vapour-assisted petroleum extraction.	8
Figure 2-2 Heavy oil transportation methods.....	9
Figure 2-3 Sketches of flow patterns taken from Charles et al. (1961). (a) $U_{sw}=0.10$ ft/s; (b) $U_{sw}=0.682$ ft/s; (c) $U_{sw}=2.04$ ft/s.	17
Figure 2-4 Photographs of different flow patterns observed in up-flow and down-flow (Bai et al., 1992).	19
Figure 2-5 Pressure gradient versus input ratio for crude oil (a) and No.6 fuel oil (b), with the oil flow rate held constant (Arney et al., 1993).	21
Figure 2-6 Hypothetical water slugs with enveloped oil (McKibben et al. 2000).	23
Figure 2-7 Photographs of basic flow patterns of horizontal (a) and vertical (b) heavy oil-water flow (Bannwart et al. 2000).	24
Figure 2-8 Photographs of visualization section at the well head (a) and core annular flow developed (b) (Bannwart et al. 2012).	24
Figure 2-9 Sketch of flow patterns of heavy crude oil–water flow in a horizontal pipe (Wang et al. 2011).	27
Figure 2-10 Calculation steps in each iteration of different solvers.	38
Figure 3-1 PI&D of the experimental setup for high-viscosity oil-water tests.	44
Figure 3-2 Snapshot of the experimental setup.....	45
Figure 3-3 Pictures of the fluid sampling section.	49
Figure 3-4 A comparison between measured and calculated pressure gradients of single oil flow.	55
Figure 3-5 Oil viscosity with shear rate at various temperatures.	56
Figure 3-6 Oil viscosity versus temperature.	57
Figure 3-7 Collected samples during calibration of the whole sampling section volume. (a) $U_{sw}=0.6$ m/s; (b) $U_{sw}=0.8$ m/s; (c) $U_{sw}=1.0$ m/s.	58
Figure 3-8 Collected samples of two-phase flow. Flow condition: $\mu_o=5\ 000$ cP; $U_{so}=0.54$ m/s; $U_{sw}=0.40$ m/s, 0.59 m/s, 0.77 m/s, and 0.99 m/s from left to right.....	59

Figure 3-9 Sampling section with some oil remained after a sample collection.60

Figure 4-1 Photographs of flow patterns observed (CYL 680). The flow patterns are: a-OC; b1, b2-Inv; c1, c2-CAF; d-OPL; e1, e2-OLP. 67

Figure 4-2 Photographs of flow patterns observed (CYL 1000). The flow patterns are: a1, a2-OC; b1, b2-Inv; c-CAF; d-OPL..... 68

Figure 4-3 Sketches of flow patterns observed. The flow patterns are: a1, a2-OC; b1, b2-Inv; c1, c2, c3-CAF; d-OPL; e1, e2-OLP. 69

Figure 4-4 A typical average pressure gradient trend with input water volume fraction and the corresponding flow patterns (CYL 680, $U_{so}=0.1\text{m/s}$, $\mu_o=5000\text{ cP}$). 70

Figure 4-5 Flow regime maps (linear scale) of high-viscosity oil-water flow (CYL 680). (a) 3 300 cP; (b) 3 700 cP; (c) 5 000 cP; (d) 7 100 cP..... 75

Figure 4-6 Flow regime maps (logarithmic scale) of high-viscosity oil-water flow (CYL 680). (a) 3 300 cP; (b) 3 700 cP; (c) 5 000 cP; (d) 7 100 cP..... 77

Figure 4-7 Flow regime map of high-viscosity oil-water flow with U_{so} and U_{sw} as coordinates (CYL 1 000, $\mu_o=3800\text{ cP}$). 78

Figure 4-8 Flow regime map of high-viscosity oil-water flow with C_w and U_{so} as coordinates (CYL 1 000, $\mu_o=3800\text{ cP}$). 78

Figure 4-9 Comparison of flow pattern maps produced in the present study and Sotgia et al. (2008). Regimes defined in the present study are presented with markers. Regimes defined by Sotgia et al. (2008) are presented with boundary lines and regime descriptions: Wavy stratified; Wavy annular; CAF; Slug; Transition (between CAF/Slug and Dispersed); Dispersed. (a) U_{so} and U_{sw} as coordinates; (b) C_w and U_m as coordinates..... 82

Figure 4-10 Comparison of flow pattern maps produced in the present study and Grassi et al. (2008). Regimes defined in the present study are presented with markers. Regimes defined by Grassi et al. (2008) are presented with boundary lines and regime descriptions: Stratified; CAF; Plug/Slug; Dispersion of oil in wtaer. (a) U_{so} and U_{sw} as coordinates; (b) C_w and U_m as coordinates..... 83

Figure 4-11 Comparison of flow pattern maps produced in the present study and Trallero et al. (1997). Regimes defined by Trallero et al. (1997) are presented with boundary lines and regime descriptions: Stratified (ST); Stratified with mixing at the interface (ST & MI); Dispersion of oil in water and water (Do/w & w); Oil in water emulsion (o/w); Dispersion of water in oil and oil in water (Dw/o & Do/w); Water in oil emulsion (w/o). (a) U_{so} and U_{sw} as coordinates; (b) C_w and U_m as coordinates..... 85

Figure 4-12 Pressure gradient with input water volume fraction (CYL 1 000, $\mu_o=3800\text{ cP}$). (a) $U_{so}=0.06\text{ m/s}$; (b) $U_{so}=0.1\text{ m/s}$ 88

Figure 4-13 Pressure gradient with input water volume fraction at various superficial oil velocities (CYL 1 000, $\mu_o=3\ 800$ cP).	89
Figure 4-14 Pressure gradient with input water volume fraction at various nominal oil viscosities (CYL 1 000). (a) $U_{so}=0.1$ m/s; (b) $U_{so}=0.15$ m/s	90
Figure 4-15 Water holdup (H_w) versus input water volume fraction (C_w) at various U_{so} (CYL 680, $\mu_o=5\ 000$ cP). (a) $U_{so}=0.04$ m/s; (b) $U_{so}=0.11$ m/s; (c) $U_{so}=0.20$ m/s; (d) $U_{so}=0.39$ m/s; (e) $U_{so}=0.54$ m/s.	93
Figure 4-16 Water holdup (H_w) versus input water volume fraction (C_w) at various U_{so} (CYL 680, $\mu_o=3\ 300$ cP). (a) $U_{so}=0.06$ m/s; (b) $U_{so}=0.11$ m/s; (c) $U_{so}=0.21$ m/s; (d) $U_{so}=0.55$ m/s.	94
Figure 4-17 Oil-water slip ratio of CAF versus input water volume fraction (C_w) at various U_{so}	95
Figure 4-18 Pressure drop reduction factor with C_w at various U_{so} (CYL 1 000). (a) $\mu_o=3\ 800$ cP; (b) $\mu_o=13\ 200$ cP.	97
Figure 4-19 Ratio of water-lubricated two-phase flow pressure gradient to single water flow pressure gradient with C_w at various U_{so} (CYL 1 000). (a) $\mu_o=3\ 800$ cP; (b) $\mu_o=13\ 200$ cP.	98
Figure 4-20 Pressure gradient of water-lubricated flow versus the mixture velocity. (a) linear scale; (b) logarithmic scale.	100
Figure 4-21 Coefficient of resistance versus the Reynolds number of the water-lubricated two-phase flow and comparison with that of single water flow.	102
Figure 4-22 Pressure gradient of water-lubricated flow with input water volume fraction at various nominal oil viscosities (CYL 1 000). (a) $U_{so}=0.1$ m/s; (b) $U_{so}=0.15$ m/s.	103
Figure 5-1 Sketches of most frequently reported flow patterns of low-viscosity, unequal-density oil-water flow in horizontal pipes (adapted from Trallero et al. (1997) and Nädler and Mewes (1997)).	109
Figure 5-2 Sketches of flow patterns of low-viscosity, equal-density oil-water flow in horizontal pipes (adapted from Charles et al., 1961).	110
Figure 5-3 Sketches of major flow patterns of water-continuous high-viscosity oil-water flow in horizontal pipes (references: Joseph et al. (1997), Grassi et al. (2008), Sotgia et al. (2008), Sridhar et al. (2011), Al-Awadi (2011) and the present study).	113
Figure 5-4 Liquid-liquid flows characterised with different basic flow patterns and the corresponding gravitation to viscous force ratio (G/V).	123
Figure 5-5 Basic flow patterns developed with gravitation to viscous force ratio (G/V) and C_w in gravitational force dominant two-phase oil-water flow (S_G).	124

Figure 5-6 Specific dispersed flow patterns with gravitation to viscous force ratio (G/V) and C_w	124
Figure 5-7 Basic flow patterns formed with gravitation to viscous force ratio (G/V) and C_w in gravitational force and viscous force comparable two-phase oil-water flow (S_{GV}).	126
Figure 5-8 Basic flow patterns formed with gravitation to viscous force ratio (G/V) and C_w in mainly viscous force dominant two-phase oil-water flow (S_V and S_{GV}).	127
Figure 5-9 Basic flow patterns formed with gravitation to viscous force ratio (G/V) and C_w in two-phase oil-water flow, S_G , S_V , and S_{GV} . Source data: Nädler and Mewes (1997), Trallero et al. (1997), Angeli and Hewitt (2000), Lovick and Angeli (2004), Wegmann and Rudolf von Rohr (2006), Vielma et al. (2008), Grassi et al. (2008), Sotgia et al. (2008) and the present study. The dash lines represents approximate transitions between S_V , S_{GV} and S_G .	128
Figure 5-10 Froude number versus input water volume fraction for high-viscosity oil-water flows. All the data points except the one denoted as intermittent were continous water-assisted flow (CWA) (adapted from McKibben et al., 2000b).	129
Figure 5-11 Input water volume fraction versus Fr for high-viscosity oil-water flow.	131
Figure 5-12 Schematic description of CAF configuration (Brauner, 1998).	137
Figure 5-13 Schematic graph on the force balance of core annular flow.....	140
Figure 5-14 Estimated effective wall roughness versus input water volume fraction for various U_{so} . (a) CYL 1000, $\mu_o=3\ 800$ cP; (b) CYL 1000, $\mu_o=13\ 200$ cP; (c) CYL 680, $\mu_o=3\ 700$ cP; (d) CYL 680, $\mu_o=7\ 100$ cP.....	144
Figure 5-15 Estimated effective wall roughness versus C_k for various U_{so} . (a) CYL 1000, $\mu_o=3\ 800$ cP; (b) CYL 1000, $\mu_o=13\ 200$ cP; (c) CYL 680, $\mu_o=3\ 700$ cP; (d) CYL 680, $\mu_o=7\ 100$ cP.....	145
Figure 5-16 Estimated effective wall roughness versus C_k for various oil viscosities (a) CYL 1000; (b) CYL 680.....	146
Figure 5-17 Estimated effective wall roughness versus $1-C_k$. (a) logarithmic scale; (b) linear scale.....	148
Figure 5-18 Overall comparison between measured water holdups (data from the present study, $\mu_o=3\ 300$ cP and $5\ 600$ cP) and predicted counterparts. (a) Arney et al. (1993); (b) Brauner (1998); (c) Present study.	150
Figure 5-19 Water holdup (H_w) versus input water volume fraction (C_w) at different superficial oil velocities (data from the present study, $\mu_o=3\ 300$ cP	

and 5 600 cP). (a) $U_{so}=0.06$ m/s; (b) $U_{so}=0.1$ m/s; (c) $U_{so}=0.2$ m/s; (d) $U_{so}=0.5$ m/s.....	151
Figure 5-20 Water holdup (H_w) versus input water volume fraction (C_w) (data from Charles et al. (1961), $\rho_o = \rho_w$, $\mu_o=16.8$ cP).....	153
Figure 5-21 Overall comparison between measured pressure gradients (data from the present study, μ_o ranges from 3 300 cP to 16 000 cP) and predicted counterparts. (a) Arney et al. (1993); (b) Brauner (1998).....	154
Figure 5-22 Ratio of two-phase flow pressure gradient to single water flow pressure gradient (RTW) versus input water volume fraction (data from the present study, μ_o ranges from 3 300 cP to 16 000 cP) (a) RTW calculated from predicted pressure gradients; (b) RTW calculated from measured pressure gradients.....	155
Figure 5-23 Comparison between measured pressure gradients (data from Charles et al., 1961; $\rho_o = \rho_w$, $\mu_o=16.8$ cP) and predicted counterparts.	157
Figure 5-24 Comparison of predicted pressure gradients using various sets of b and n for the model of Bannwart (2001) with the present experimental data. The the bisector is aslo shown (the dash line).....	158
Figure 5-25 Comparison between measured and predicted pressure gradients from the model of McKibben et al. (2000b).....	160
Figure 5-26 Comparison between measured and predicted pressure gradients from the model of McKibben et al. (2013).....	161
Figure 5-27 Comparison between measured and predicted pressure gradient from the model propped in the present study.....	161
Figure 6-1 (a) Schematic of horizontal pipe with Tee junction inlets (Geometry A); (b) Mesh of the water inlet part.	172
Figure 6-2 Snapshots of flow patterns calculated using different meshes (the red represents oil and the blue represents water). (a) Mesh A; (b) Mesh B; (c) Mesh C; (d) Mesh D.	181
Figure 6-3 Pressure gradients calculated using different meshes.....	181
Figure 6-4 Monitored pressure and water holdup of cross-sections with simulation time (Run H-7, water initialization). (a) Face area-weighted average pressure; (b) Face area-weighted average water volume fraction.	182
Figure 6-5 Monitored pressure and water holdup of cross-sections with simulation time (Run H-7-2, oil initialization). (a) Face area-weighted average pressure; (b) Face area-weighted average water volume fraction.	183

Figure 6-6 Comparison of histograms of normalised pressure drop from measurement (a) and simulation (b).....	184
Figure 6-7 Development of phase configuration with simulation time. (a) Water initialization (Run H-7); (b) Oil initialization (Run H-7-2).	185
Figure 6-8 Predicted flow patterns from simulations using different volume fraction interpolation schemes at the interface and the corresponding experimental flow pattern. (a) Geo-Reconstruct scheme (Run H-3); (b) CICSAM scheme (Run H-3-2); (c) snapshot form recorded experimental flow.	186
Figure 6-9 Cross-sectional turbulence characteristics from runs using different turbulence schemes. (a) standard $k-\epsilon$ (Run L-9-2); (b) RNG $k-\epsilon$ (Run L-9-3); (c) SST $k-\omega$ without turbulence damping (Run L-9-4); (d) SST $k-\omega$ with turbulence damping (Run L-9).....	189
Figure 6-10 Wall contact angles.	190
Figure 6-11 Illustration of the wall contact angle (θ_w).	191
Figure 6-12 Calculated flow patterns (the red represents oil and the blue represents water) with different wall contact angles and the corresponding experimental flow pattern (oil core inside annular water) for a low-viscosity oil-water case. (a) 175°; (b) 60°; (c) a flow pattern drawing based on experiments (Charles et al., 1961).....	192
Figure 6-13 Calculated flow patterns (the red represents oil and the blue represents water) with different wall contact angles and the corresponding experimental flow pattern (oil core inside annular water) for a high-viscosity oil-water case. (a) 175°; (b) 120°; (c) 60°; (b) 5°; (e) snapshot form recorded experimental flow.....	193
Figure 7-1 Adapted flow pattern map after Charles et al. (1961). Simulation runs performed are marked out.	196
Figure 7-2 Caculated phase configurations at various cross-sections (the red represents oil and the blue represents water). (a) Run H-7; (b) Run H-9; (c) Run H-19; (d) Run H-21.....	199
Figure 7-3 Change of phase configuration with change of oil viscosity at $U_{so}=0.4$ m/s, and $U_{sw}=0.2$ m/s (the red represents oil and the blue represents water). (a) 5 000 cP ($GV=0.16$; Run H-9); (b) 1 000 cP ($GV=0.96$; Run H-12); (c) 500 cP ($GV=1.92$; Run H-13); (d)100 cP ($GV=9.68$; Run H-14).....	202
Figure 7-4 Change of phase configuration with change of pipe diameter at $U_{so}=0.4$ m/s, and $U_{sw}=0.2$ m/s (the red represents oil and the blue represents water). (a) 26 mm ($GV=0.16$; Run H-9); (b) 76 mm ($GV=1.68$; Run H-20).....	203

Figure 7-5 Phase configuration in a 76 mm I.D horizontal pipe at $U_{so}=2.0$ m/s, and $U_{sw}=0.5$ m/s ($G/V=0.4$, Run H-21; the red represents oil and the blue represents water).....	203
Figure 7-6 Change of phase configuration with change of superficial oil velocities. (the red represents oil and the blue represents water). (a) $U_{so}=0.12$ m/s ($Fr=0.8$; Run H-4); (b) $U_{so}=0.4$ m/s ($Fr=2.67$; Run H-9). (c) $U_{so}=0.8$ m/s ($Fr=5.34$; Run H-19).....	204
Figure 7-7 Change of phase configuration with change of oil densities. (the red represents oil and the blue represents water). (a) 910kg/m^3 ($Fr=2.67$; Run H-9); (b) 960kg/m^3 ($Fr=4.06$; Run H-10); (c) 1100kg/m^3 ($Fr=2.48$; Run H-11).	204
Figure 7-8 Comparison of predicted flow regimes with the proposed inversion criterion for the formation of stable water-lubricated flow.....	205
Figure 7-9 Comparison of predicted water holdups with experimental counterparts from Charles et al. (1961).	206
Figure 7-10 Water holdup versus input water volume fraction from measurements (Charles et al, 1961) and CFD model.	207
Figure 7-11 Pressure (a) and pressure gradient (b) along the horizontal pipe.	211
Figure 7-12 Pressure drop reduction factor (PDRF) from simulations and measurements versus input water volume fraction (C_w) at different superficial oil velocities. (a) $U_{so}=0.1$ m/s; (b) $U_{so}=0.4$ m/s.....	212
Figure 7-13 Dimensionless phase distribution and velocity profiles of low-viscosity equal-density CAF at different distances downstream the junction; left hand side for phase distribution and right hand side for velocity distribution.	214
Figure 7-14 Turbulent kinetic energy and intensity of developed low-viscosity equal-density CAF.	216
Figure 7-15 Dimensionless phase distribution and velocity profiles of high-viscosity oil CAF at different distances downstream the junction; left hand side for phase distribution and right hand side for velocity distribution. ...	217
Figure 7-16 Turbulent kinetic energy and intensity of developed high-viscosity oil CAF.....	220

LIST OF TABLES

Table 2-1 Summary of experimental studies on high-viscosity oil-water flow in horizontal pipes.	30
Table 3-1 Summary of experimental runs.	53
Table 3-2 A comparison of pressure gradients obtained from the two gauge pressure transducers and the differential pressure transducer.....	54
Table 3-3 A comparison of pressure gradients of two-phase flow with similar flow conditions.	61
Table 4-1 Collated experimental data on high-viscosity oil-water flow in 1 inch horizontal pipe.	64
Table 4-2 Photographs and histograms of pressure drop signals of different flow patterns (CYL 680, $U_{so}=0.1\text{ m/s}$, $\mu_o=5\ 000\ \text{cP}$).....	72
Table 4-3 Summary of the data sets used for flow map comparison.....	80
Table 5-1 Summary of experimental studies on liquid-liquid flows in horizontal pipes.....	120
Table 5-2 Core holdup and pressure reduction factor for CAF with a laminar core ^{a)}	139
Table 6-1 Summary of simulation runs.....	177
Table 6-2 Meshes used for mesh independence study.	180
Table 6-3 Predicted flow patterns and pressure gradients with different turbulence schemes and comparison with experiments.	187
Table 7-1 Comparison of predicted flow patterns with experimental counterparts from Charles et al. (1961).	197
Table 7-2 Comparison of typical flow patterns from simulations and the corresponding experimental counterparts from the present experimental study.....	198
Table 7-3 Measured and predicted water holdups for water-lubricated high-viscosity oil-water flow.	208
Table 7-4 Comparison of predicted pressure gradients with experimental counterparts from Charles et al. (1961).	209
Table 7-5 Comparison of predicted pressure gradients with experimental counterparts from the present study.	210

LIST OF ABBREVIATIONS

This section includes the most commonly used abbreviations used in this thesis. The abbreviations are defined the first time when they are used in the thesis.

API	American petroleum institute
AVCHD	advanced video coding high definition
BV	ball valve
bbbl	oil barrel
CAF	core annular flow
CWA	continuous water-assited flow
CFD	computational fluid dynamics
DAQ	data acquisition
DN	nominal diameter
DP	differential pressure transducer
DV	diaphragm valve
Do/w	dispersed oil in water
Dw/o	dispersed water in oil
Do/w & w	dispersion of oil in water & water
FAD	free air delivery
I	intermittent flow
I-D	transition from intermittent flow to disperased flow
I.D.	internal diameter
Inv	inversion
LES	large eddy simulation
MI	mixing at the interface
NI	national instruments
NS	Navier-Stokes
OBL	oil bubbles in water
OC	oil-continuous
OLP	oil lumps in water
OPL	oil plugs in water
PCP	progressive cavity pump

PDRF	pressure drop reduction factor
PRESTO!	pressure staggering option
PT	pressure transducer
PVC	polyvinyl chloride
RANS	Reynolds-averaged Navier-Stokes
RTW	ratio of two-phase flow to single water flow
S_G	gravitational force dominant flow
S_V	viscous force dominant flow
S_{GV}	gravitational force and viscous force comparable flow
SIMPLE	semi implicit method for pressure linked equations
SST	shear stress transport
ST	stratified flow
TP	two phase
TT	temperature transducer
3-D	three-dimensional
VOF	volume of fluid

LIST OF SYMBOLS

This section includes the most commonly used notation in this thesis. In order to avoid departing from conventions normally used in the literature, a few symbols denote more than one quantity.

A	pipe cross-sectional area, m^2
A_o	cross-sectional area occupied by oil, m^2
A_w	cross-sectional area occupied by water, m^2
C_H	water holdup coefficient
C_k	effective wall roughness coefficient
C_o	input oil volume fraction
C_w	input water volume fraction
D	internal pipe diameter, m
F	force per unit mass, m/s^2
F	force per unit volume, $kg/(m^2s^2)$
f	Fanning friction factor
g	gravitational acceleration, m/s^2
H_o	oil holdup
H_w	water holdup
h	holdup ratio ($h = \frac{H_w/H_o}{C_w/C_o}$)
k	kinetic energy of turbulence, m^2/s^2
k	effective relative wall roughness
p	pressure, N/m^2
Q	total flow rate, m^3/s
Q_o	oil flow rate, m^3/s
Q_w	water flow rate, m^3/s
t	time, s
U_m	mixture velocity, m/s
U_{so}	superficial oil velocity, m/s
U_{sw}	superficial water velocity, m/s
U_w	average water velocity, m/s
u	velocity, m/s

Greek letters

α_o	volume fraction of the oil phase
α_w	volume fraction of the water phase
ε	oil holdup
ε	turbulence dissipation rate, m^2/s^3
θ_w	wall contact angle, $^\circ$
λ	friction factor
μ	molecular viscosity, $\text{kg}/(\text{m}\cdot\text{s})$
μ_t	turbulent viscosity, $\text{kg}/(\text{m}\cdot\text{s})$
ρ	density, kg/m^3
ρ_o	density of oil, kg/m^3
ρ_w	density of water, kg/m^3
σ	interfacial tension, N/m
τ_w	wall shear stress, N/m^2
ω	specific turbulence dissipation rate, $1/\text{m}$

Subscripts

α	annulus
c	core
i	interface
k	kinetic energy
k	phase indicator
k	effective wall roughness
m	mixture
o	oil
p	particle
t	turbulence
w	water
w	wall
ω	specific dissipation rate

Dimensionless numbers

Ca	Capillary number ($Ca = \frac{\mu U}{\sigma}$)
Eo	Eötvös number ($Eo = \frac{\Delta \rho g D^2}{\sigma}$)
Fr	Froude number ($Fr = \frac{U_{so}}{\sqrt{g D \frac{\Delta \rho}{\rho_w}}}$)
G/V	Gravitation to viscous force ratio ($G/V = \frac{\Delta \rho g D^2}{\mu U}$)
Re	Reynolds number ($Re = \frac{\rho U D}{\mu}$)
We	Weber number ($We = \frac{\rho U^2 D}{\sigma}$)
y^+	non-dimensional wall distance ($y^+ = \frac{\rho u_\tau y}{\mu}$)

1 INTRODUCTION

1.1 Background

1.1.1 Overview

With the depletion of conventional light crude oil, the large resources of heavy and extra heavy crude oil are becoming increasingly important in the oil industry. At ambient temperature, heavy crude oil does not flow easily in the reservoir and pipeline due to high viscosity. Technologies to enhance the mobility of heavy crude oil are required in both heavy oil production and transportation.

The traditional method for heavy crude oil transport is to reduce the viscosity of heavy oil. This can be accomplished by heating, diluent addition or a combination of both. Water-lubricated flow technology provides an alternative to oil viscosity reduction technologies. In this method, high-viscosity oil is transported inside continuous water which lubricates the pipe. The most ideal flow regime is core annular flow (CAF) in which heavy oil is transported with a small amount of water. Compared with single phase oil flow transport, the pressure gradient of water-lubricated high-viscosity oil-water flow is dramatically reduced. This method is very attractive due to its low initial investment and operating cost.

A good understanding of the flow behaviours from experimental and analytical studies can provide risk reduction for the industrial application of water-lubricated heavy oil transport. Over the years, a number of studies on water-lubricated flow have been carried out, e.g., Charles et al. (1961), Ooms et al (1984), Arney et al. (1993), Joseph et al. (1999), McKibben et al. (2000a, 2000b), Al-Awadi (2011), and Bannwart et al. (2012). Some pilot tests show promise of safe operation of water-lubricated flow (see Joseph et al., 1999; McKibben et al. (2000b) and Bannwart et al., 2012). It is established now that the input water volume fraction needs to be sufficient and the flow rate needs to be high enough to maintain stable water-lubricated flow. However, specific criteria on safe and economically viable operation conditions are not well

established yet. Accurate prediction of oil-water flow characteristics, such as flow regime, water holdup, and pressure gradient is important for engineering design and operation. Most of the existing models do not account for the influence of oil fouling on the pipe wall which might underestimate the pressure gradient of water-lubricated flow.

Apart from the industrial background, high-viscosity oil-water flow is a branch of liquid-liquid two-phase flow. Previous studies have demonstrated that the flow characteristics of high-viscosity oil-water flow differ from those of low-viscosity oil-water flow. The physics underlying the liquid-liquid two-phase flow characteristics need further investigation.

1.1.2 Previous studies on high-viscosity oil-water flow at Cranfield University

High-viscosity oil related multiphase flows have been studied in the Oil and Gas Engineering Centre (called 'Process Systems Engineering Group' before 2014), Cranfield University since 2010. Concerning high-viscosity oil-water flow, experiments in a horizontal 1 inch pipe were carried out by Al-Awadi (2011), Zorgani (2012) and Alagbe (2013). Two different oils were used. In the experiments of Al-Awadi (2011), oil CYL 1 000 was used and the oil viscosity investigated varied between 3 800 and 16 000 cP. In the experiments of Zorgani (2012), oil CYL 680 was used and an oil viscosity of around 5 000 cP was investigated. In the experiments of Alagbe (2013), oil CYL 680 was used and the oil viscosity investigated varied between 3 700 and 7 100 cP. In these experiments, flow regimes were visually observed and recorded, and pressure gradients were measured.

A large amount of experimental data was produced from the above studies, especially from Al-Awadi (2011) and Alagbe (2013). The above authors not only experimentally investigated oil-water flow, but also other multiphase flows such as oil-gas, oil-sand, oil-water-gas or oil-water-sand. The experimental data produced in earlier studies were not compared to or made use of in later studies'

analysis. A collation of the raw data from previous studies can be useful to make a large data base for analysis.

1.2 Objectives

The general objective of the present study is to investigate horizontal high-viscosity oil-water flow to have an improved understanding of the flow characteristics. To that end, the experimental approach, mechanism analysis and empirical modelling, and computational fluid dynamics (CFD) approach were used. The specific objectives are presented as below:

1. Determine an appropriate measurement technique for water holdup measurement; design modification of the experimental rig to facilitate water holdup measurement; carry out experiments on high-viscosity oil-water flow to obtain new data, especially water holdup.
2. Collate raw data from previous experimental studies and the present experimental study to make a large data base for analysis.
3. Analyse experimental results and compare with the literature data. Develop an improved understanding of the flow characteristics.
4. Evaluate existing empirical or mechanistic models with the experimental data to shed some light on their applicability ranges.
5. Perform 3-D CFD modelling of oil-water flow using the commercial CFD package ANSYS Fluent. Investigate the ability of the multiphase computational fluid dynamics models incorporated in Fluent. Obtain cross-sectional flow information and get improved knowledge of flow characteristics.

1.3 Thesis outline

The structure of the thesis is illustrated in Figure 1-1 as well as relation between the contents and the objectives introduced in Section 1.2.

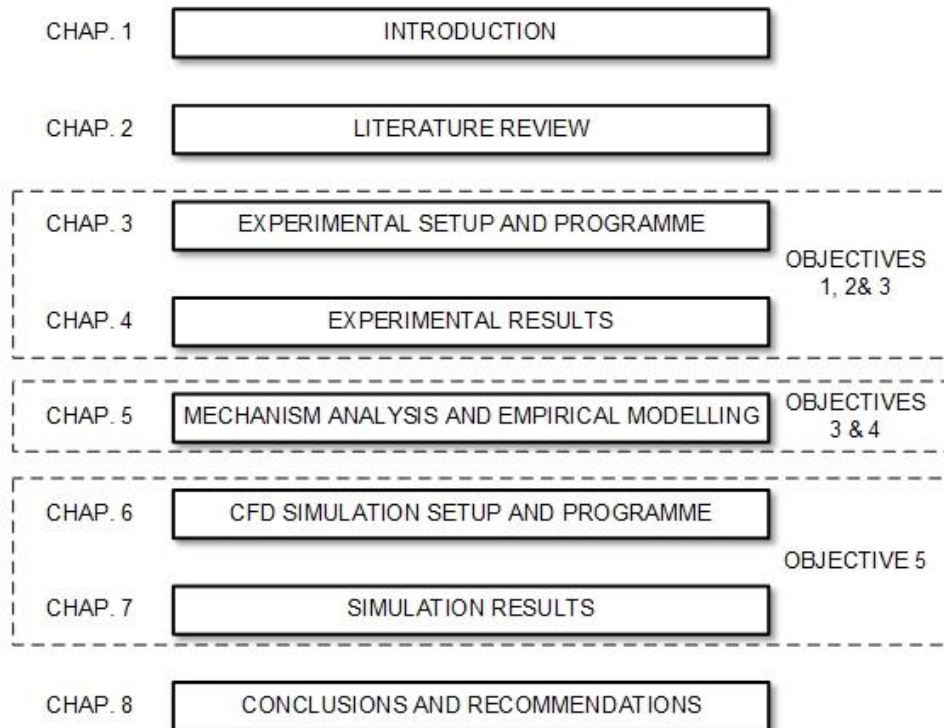


Figure 1-1 Outline of the thesis structure.

Chapter 2 gives a brief literature review on the industrial background of the present study, previous experimental studies, and basic theories and methodologies on multiphase flow modelling in computational flow dynamics.

Chapter 3 introduces the experimental setup and programme. Chapter 4 discusses the experimental results.

Chapter 5 focuses on mechanism analysis and empirical modelling. Mechanisms governing the flow characteristics are discussed. The existing empirical and mechanistic models are evaluated with the experimental data.

Chapter 6 introduces CFD simulation setup and programme.

Chapter 7 discusses the simulation results.

Chapter 8 gives conclusions from the present study and suggestions for future work.

2 LITERATURE REVIEW

Oil-water two-phase flow is a particular example of multiphase flow. The term multiphase flow is used to refer to any fluid flow consisting of more than one phase or component. One could classify multiphase flow according to the state of the different phases, e.g., gas-liquid flow, liquid-liquid flow, and gas-solids flow. Alternatively, multiphase flow can be classified according to the components of the different phases, e.g., water-gas flow, oil-gas flow, oil-water flow and oil-water-gas flow.

Two-phase oil-water flow is frequently encountered in the petroleum industry. Accurate prediction of oil-water flow characteristics, such as flow regime, water holdup, and pressure gradient is important for engineering design and operation. A lot of studies on oil-water pipeline flow can be found in the literature. A good review on oil-water flow covering different flow regimes can be found in Brauner et al. (1998). Reviews on oil-water core annular flow can be found in Oliemans and Ooms (1986), Joseph et al. (1997), and Ghosh et al. (2009). Existing experimental and theoretical investigations indicate that the mechanisms of high-viscosity oil-water flow are not the same as that of low-viscosity oil-water flow. Most of the existing mechanistic models have been developed on the basis of low-viscosity oil-water experimental data and cannot predict flow characteristics accurately for high viscous flow (Zhang et al., 2012). Further experimental and theoretical investigations on two-phase oil-water flow are needed.

Three ways for the model exploration could be classified (Brennen, 2005): (1) experimentally, investigating flow behaviours in laboratory tests and developing empirical models; (2) theoretically, developing models from the view of fluid dynamics and physical analysis; and (3) computationally, using the state-of-the-art technique of computational fluid dynamics (CFD) to numerically model flow behaviours. Experimental studies are essential; they provide not only the phenomenal knowledge about flow behaviours, but also the data base for the validation of theoretical models and computational models. Besides, empirical

models developed from experimental data could sometimes give satisfactory prediction for some particular scales. A reliable theoretical or computational model is of great importance for the understanding of physical phenomena and the full scale flow behaviour prediction.

In this chapter, an introduction on the industrial background of the present study on high-viscosity oil-water flow is first presented in Section 2.1. In Section 2.2, a review on previous experimental studies on high-viscosity oil-water pipeline flow in the literature is presented based on chronological order and research groups. Theoretical models for the prediction of water holdup and pressure gradient are not introduced here; they will be reviewed in Chapter 5 where various models are discussed and evaluated. In Section 2.3, basic theories and methodologies on modelling of multiphase flow in computational flow dynamics, especially in the CFD code FLUENT which is used in the present study is reviewed. This background knowledge is essential for the following CFD study of high-viscosity oil-water flow, both in the aspects of simulation setup and understanding of simulation results.

2.1 Industrial background

2.1.1 An overview on heavy oil production and transportation

Heavy crude oil or extra heavy crude oil is any type of crude oil which does not flow easily. It is referred to as 'heavy' because its density is higher than that of light crude oil. The American Petroleum Institute gravity, or API gravity, is a measure of how heavy or light a petroleum liquid is compared to water. It is calculated as

$$API\ Gravity = \frac{141.5}{SG\ at\ 60^{\circ}F\ (15.56\ ^{\circ}C)} - 131.5 \quad (2-1)$$

where SG is the specific gravity of the fluid, $SG = \rho_o / \rho_w$. Lower API gravity ratings reflect heavier types of crude oil. Heavy crude oil is defined as having 22.3° API or less (Alboudwarej et al., 2006).

Though the term 'heavy oil' is a reference to the high density of those oils, it is the viscosity that we care most about since that is the essential property that governs the well productivity and pipeline mobility. There is no standard relationship between viscosity and gravity in general. However, 'heavy' and 'viscous' tend to be used interchangeably to describe heavy oils because heavy oils tend to be more viscous than conventional oils. The definition of the threshold viscosity between light oil and heavy oil varies slightly by different authors. Alboudwarej et al. (2006) stated that the conventional oil viscosity may range from 1 to 10 cP, and heavy oil and extra heavy oil may range from less than 20 to more than 1 000 000 cP. The U.S. Geological Survey (USGS) defines that the upper limit of light oil as 100 cP; heavy oil has a viscosity more than 100 cP (Veil and Quinn, 2008).

It is estimated that the world's total oil resources amount to 9~13 trillion barrels, of which around 70% is made up of heavy oil, extra-heavy oil and bitumen. Canada and Venezuela have very large known heavy crude accumulations (Alboudwarej et al., 2006). With the depletion of conventional light crude oil, the large resources of heavy and extra heavy crude oil are becoming increasingly important in the oil industry.

Heavy oil production technologies could be classified as mining and in situ well production. Different well production methods could be further divided into cold processes and thermal processes. Figure 2-1 shows the classification of heavy oil production technologies. A detailed introduction on different production methods can be found in Appendix E.

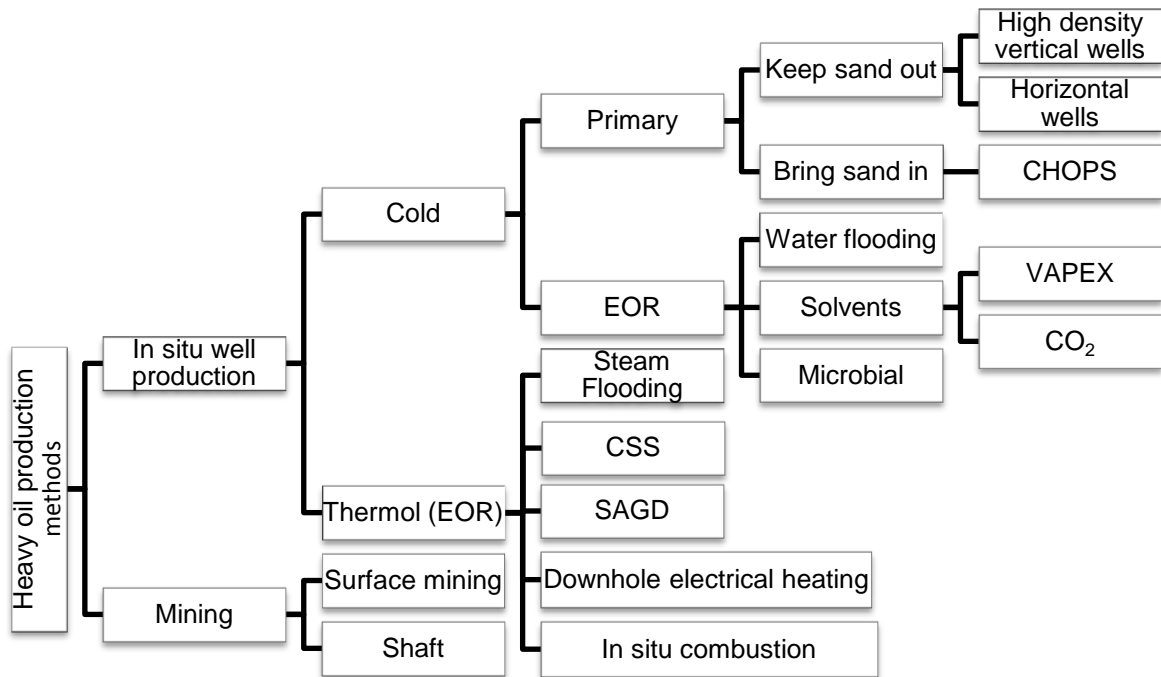


Figure 2-1 Heavy oil production methods. EOR: enhanced oil recovery; CSS: cyclic steam stimulation; SAGD: steam-assisted gravity drainage; CHOPS: cold heavy oil production with sand; VAPEX: vapour-assisted petroleum extraction.

Compared to the traditional light crude production, heavy crude oil production is more difficult due to its high viscosity. Enhanced oil recovery (EOR) technologies are usually used in heavy oil production. For a particular heavy oil field, its geology and reservoir conditions dictate its best production method among those available. Many factors such as fluid properties, formation continuity, rock mechanics, drilling technology, completion options, surface facilities, and environmental influence are considered to select a production method. One thing to be noted is that water or water steam is injected into the reservoir in various processes, e.g., water flooding, steam flooding, CSS (cyclic steam stimulation) and SAGD (steam-assisted gravity drainage). For the process of in situ combustion, water would be produced in the reservoir. Compared to traditional light crude oil production, more water is produced together with heavy crude oil. In heavy oil production, oil-water two-phase flow in the production well and pipeline from the well to the processing plant is common.

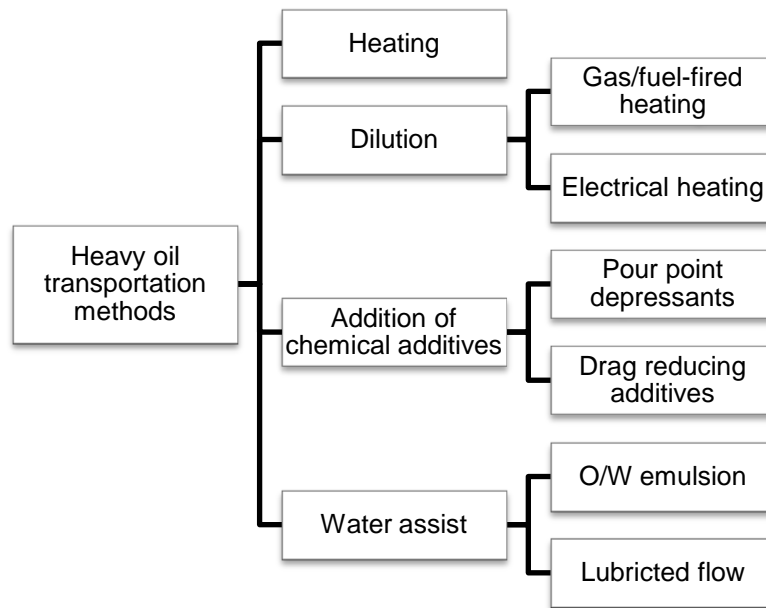


Figure 2-2 Heavy oil transportation methods.

The transportation of heavy oil has become a complex and highly technical operation too due to its high viscosity. Heavy oil transportation technologies could be generally divided into four approaches – heating, use of diluents, use of chemical additives, and water assist (see Figure 2-2). The philosophy behind these methods is to reduce oil's viscosity and/or the friction between the pipeline and the heavy oil. A detailed introduction on transportation methods can be found in Appendix E.

Among the transportation methods, the traditional gas/fuel-fired heating is a widely proven method. It can be very energy consuming as a large amount of feedstock is needed to heat the heavy oil reaching a desired low viscosity. It is feasible in warm parts of the world like Nigeria, Venezuela and California as low power requirement and low pipe insulation requirement may lower the initial investment and operating cost. The electrical heating was proposed originally and mainly applied for subsea pipelines. The dilution method is widely used where condensate or lighter crude oil is available. High additional investment is needed if the diluents are to be recycled. Addition of pour point depressants or drag reducing additives is usually applied with heating, dilution or heavy oil

multiphase flow together. Those chemical agents could be very effective, but certain chemical additives may be only effective for certain oils. The formula of an additive usually goes through a lot of trial and error experiments. Reducing the viscosity of heavy oil via formation of o/w emulsion with the help of surfactant agents is an effective method. Some crude oils are suitable to form very stable emulsions at low surfactant concentrations. It is not easy to produce stable o/w emulsions with heavy oils. In some cases, especially with extra-heavy oils, the formation of an o/w emulsion does not occur (Martínez-Palou et al., 2011). Water-lubricated transport of heavy crude oil reduces the friction between high-viscosity oil and pipe wall via phase distributions of two-phase oil-water flow in which oil flows inside annular-continuous water. The most ideal phase configuration of water-lubricated flow is the so-called 'core annular flow' in which the oil flows as a core surrounded with annular water. The water-lubricated flow to transport heavy oil has the lowest initial investment as well as operating cost. The stability of water-lubricated heavy oil flow, oil fouling and corrosion of the pipe wall and the difficulties of restarting the flow in case of shutdown are obstacles for its implementation. A survey on applications of water-lubricated heavy oil transport is presented in the following section.

2.1.2 Industrial applications of water-lubricated heavy oil transport

Isaacs and Speed (1904) were the first to discuss water lubrication of oils in a US Patent (No. 759 374). The density of the lubricating fluid needs to be greater than oil in the above authors' invention. They noted that concentric flow can be established if a helical motion is imparted to the flowing liquids by rifling the pipe. In this idea, the centripetal force caused in helical motion can separate the fluids into concentric oil surrounded by annular water and stabilise the flow.

The patent application (No. 2 533 878) by Clark and Shapiro (1950) of the Socony Vacuum Oil Company is the first that appears to address the problem of core-annular flows of heavy petroleum (Joseph and Renardy, 1993). Clark and Shapiro (1950) proposed to use additives and surface active agents to control the emulsification of water into oil. Pilot tests were reported by the above

authors in a 3 mile (4.8 km) length of 6 inch (152.4 mm) pipe which rose approximately 300 feet (91.4 m) in its first 3000 feet (914m). The crude oil used had a gravity of about 13.7° API (975 kg/m³); the viscosity was not given. They “found that the flow of viscous petroleum in pipe lines can be greatly facilitated by the use of water containing minute proportions of a water-soluble anionic surface-active agent and of an alkali-metal phosphate and having its PH adjusted to within the range pH 5.7 to pH 7.0, preferably pH 6.5”. It is also reported that “we prefer to use the treated water in proportions of 8% to 15% of the total liquid carried by the pipe line. However, the water is capable of facilitating the flow of viscous petroleum when employed in greater proportions. The upper limit is critical only in the sense that the use of additional water does not further facilitate flow sufficiently to compensate for the additional load which it imposes upon the capacity of pipe and pumps”.

The emulsification of water into oil is an undesirable condition as the water lubrication effect would be lost. Joseph and Renardy (1993) commented on this issue that the emulsification occurs readily in oils with viscosities less than 500 cP. Lubricated pipelining is a viable proposition for heavy oils with viscosities higher than 500 cP.

The emulsification or dispersion of water into oil is most likely to occur when the flow is run through a pump. Clifton and Handley (1958) of Shell Development Company proposed in a US Patent (No. 2,821,205) to reduce the emulsification by extracting the water before the pumping station and re-injecting it afterwards. Broussard et al. (1976) of Shell Oil Company in a US Patent (No. 3,977,469) proposed to subject the emulsion formed after a pump to sufficiently higher shear rate in conduit flow for a sufficiently long time to break the emulsion and create a water rich zone near the conduit wall and reform the core annular flow.

Probably the most important commercial line to date was the 6 inch (152 mm) diameter, 34 mile (38.6 km) long Shell line from the North Midway Sunset Reservoir near Bakersfield, California, to central facilities at Ten Section (Joseph and Renardy, 1993; Joseph et al., 1997). The line was run for 12 years

from 1970 until the Ten Section facility was closed. The oil was produced by secondary recovery using steam injection, gathered in a heated pipeline system and stored in a 30 000 bbl (4770 m³) tank before shipment. The oil had a viscosity around 50 000 cP at 37.8°C. Purchased water and water used for steam injection were used for water lubrication. The liquids were injected into the line with the aid of specially designed nozzle; the oil flowed through the centre of the nozzle while water was injected through a jacket surrounding the oil. When lubricated by water at a volume flow rate of 30% of the total, the pressure drop varied between 900 psi (6205 kPa) and 1 100 psi (7584 kPa) at a flow rate of 24 000 barrels per day (~1.8 m/s). When larger pressure at a threshold of unacceptability occurred, clearing the oil off the pipe wall was carried out. In the sixth year of operation, the fresh water was replaced with water produced at the well site which contained various natural chemicals leached from the reservoir. After that the pressure drop never varied much from the acceptable 900 psi; the core annular flow remained stable as long as the flow rate in the pipeline maintained a minimum around 1 m/s.

Núñez et al. (1998) reported an application of water-lubricated transport of heavy oil in Venezuela. “On the bottom of Lake Maracaibo is a tributary system of 24 inch (61cm) pipelines used to collect Bachaquero Pesado crude oil from pumping stations for oil production from nearby wells. Typically at a pumping station, the Bachaquero crude contains 16% produced water. As much as 24% more water is added to keep the pressure drops low. Whenever oil fouling causes a pressure build-up, it is washed away by adding more water. The system has been running this way for more than 30 years”. “The superficial velocities in the tributaries are low, ranging from 0.006 to 0.023 m/s”. “It is unknown if the efficiency of Maracaibo lubricated pipelines can be improved by reducing the amount of lubricating water or by increasing the volume flow rate of oil”.

A recent industrial application of water lubricated flow is for the transport of bitumen in Canada. The first bitumen upgrading facilities in northern Alberta were built near the oil sand mine sites. The bitumen was upgraded to a relatively low viscosity synthetic crude oil before further transportation. However, with depletion of the original ore supplies, the oil sand companies have begun to open new mines located at increasing distances from the upgrading facilities. The extraction plant at Syncrude's new Aurora Mine produces a bitumen-rich stream due to a hot-water extraction process. The bitumen-rich stream is transported around 35 km to the Mildred Lake upgrader using the self-lubricated froth flow technology (Sanders et al., 2004).

Compared to other transport techniques such as heating, lubrication, oil-in-water emulsion, the uncertainties that associated with the formation of water-in-oil emulsion, oil fouling, pumping difficulties after a shutdown limit the implementation of water-lubricated heavy oil transport. Núñez et al. (1998) concluded that the greater risk associated with an unproven technology was the reason for selecting traditional methods over the more attractive and economic water-lubricated flow technology. Though industrial applications of water-lubricated heavy oil transport are limited, promise of its successful application is shown. An improved understanding on high-viscosity oil-water can help reduce the technological uncertainty.

2.2 Experimental studies on high-viscosity oil-water flow

2.2.1 Basic flow notations in oil-water flow

(1) Flow regime

One of the most important aspects of two-phase flow is the physical distribution of the two phases under various flowing conditions; this physical distribution is often termed as flow regime or flow pattern.

Flow regimes depend on a number of parameters, such as operating conditions, fluid properties, flow rates and the orientation and geometry of the pipe etc. (Crowe, 2006). The transition between different flow regimes may be a gradual

process. Experimentally, direct visual observation using a length of transparent pipe is the primal way to study flow regimes; this way is still indispensable and widely used today. Modern measurement techniques are also developed to get information of phase volume fractions and phase distribution, e.g., local sampling, electrical resistance tomography (ERT), electrical capacitance tomography (ECT), radiation absorption methods, and ultrasonic techniques.

Because of the observation method, descriptions of flow regimes depend to a large extent on observers and their interpretations, and some slightly different terms defined by different researchers for actually one flow pattern are seen in the literature. Most of the flow patterns' names are easy to understand. The widely used terms for the description of liquid-liquid flow regimes include, for example, stratified flow, dispersed flow, core annular flow, and slugs/plugs or bubbles of one phase in another, etc. A detailed review on flow regimes of liquid-liquid flow is presented in Chapter 5 where the mechanisms underlying the flow regimes are investigated.

(2) Superficial velocity

The term 'superficial velocity' is widely used to describe flow conditions of multiphase flow. Take oil-water two phase flow for example, the superficial oil velocity (U_{so}) is the oil velocity as if the oil was flowing alone in the pipe, i.e. the total oil throughput (Q_o in m^3/s at the operating temperature and pressure) divided by the total area (A) of the cross section of the pipe; for the superficial water velocity (U_{sw}), the same can be derived. The sum of U_{so} and U_{sw} is the multiphase mixture velocity (U_m). Expressions are given as follows:

$$U_{so} = \frac{Q_o}{A} \quad (2-2)$$

$$U_{sw} = \frac{Q_w}{A} \quad (2-3)$$

$$U_m = U_{so} + U_{sw} \quad (2-4)$$

(3) Hold-up

When two fluids flow simultaneously in a pipeline, the in situ volume ratio can be different from the input volume ratio. Differences in density and/or viscosity give rise to an important feature of two-phase flow - the occurrence of the 'slip' of one phase past the other, or the 'hold-up' of one phase relative to the other (one phase accumulating in the pipe) (Oliemans, 1986). The definitions of phase holdup and holdup ratio are as follows (Oliemans, 1986):

- Phase holdup (or in situ volume fraction)

$$H_w = \frac{A_w}{A} \quad (2-5)$$

$$H_o = \frac{A_o}{A} = 1 - H_w \quad (2-6)$$

- Phase input volume fraction

$$C_w = \frac{Q_w}{Q_w + Q_o} \quad (2-7)$$

$$C_o = \frac{Q_o}{Q_w + Q_o} = 1 - C_w \quad (2-8)$$

- Holdup ratio

$$h = \frac{H_w/H_o}{C_w/C_o} \quad (2-9)$$

where H_w is the water holdup, H_o the oil holdup; A is the pipe cross-sectional area, A_w and A_o are the cross-sectional areas occupied by water and oil, respectively; C_w is the input water volume fraction, C_o the input oil volume fraction; Q_w and Q_o are volumetric flow rates of water and oil, respectively; h represents the ratio of the phase holdup ratio, H_w/H_o , to the phase input volume fraction ratio, C_w/C_o .

The water holdup is associated with local phase velocities. The water phase is an accumulating one when its holdup is larger than its input volume fraction. In other words, when the holdup ratio, h , is greater than unity, water is the accumulating phase; when it is less than unity, oil is the accumulating phase.

2.2.2 Previous experimental studies on high-viscosity oil-water pipeline flow

(1) Research Council of Alberta, University of Alberta (Canada)

Charles et al. (1961) experimentally investigated equal density oil-water flow in a horizontal 1 inch (I.D.=26 mm) pipe with a transparent plastic test section of 7.3 m length. Oil and water flows were combined concentrically via a nozzle in which the oil was introduced inside the water. Three different oils with viscosities of 6.29, 16.8, and 65.0 cP were used in their experiments. Carbon tetrachloride was added to the oils to give the oils the same density as the water. The oils used are relatively lowly viscous compared to the more viscous oil that we aim to study in this thesis. Also, as the densities of the phases are matched, the forces acting on the phases are inertial force, viscous force, and interfacial stress. For most of the studies on liquid-liquid flow in the literature, as the densities of the phases are not matched, the gravitational force is another force affecting the flow behaviours in addition to forces mentioned above. However, core annular flow was among the flow patterns observed and the water lubrication effect in reducing the pressure gradient was demonstrated. The work of Charles et al. (1961) is the first systematic laboratory experimental study on liquid-liquid pipeline flow in which core annular flow was observed. Arney et al. (1993) remarked that the paper of Charles et al. (1961) is a landmark in the study of liquid-liquid two-phase flow.

In the experiments of Charles et al. (1961), similar series of flow patterns were observed for three oils. Figure 2-3 shows sketches of flow patterns for the 16.8 cP oil taken from Charles et al. (1961). For a fixed water velocity, the flow pattern of water drops in oil was observed at high oil velocities. With decrease of the oil velocity, flow patterns of oil in water concentric (i.e., core annular flow), oil slugs in water, oil bubbles in water, and oil drops in water were observed. The core annular flow became disturbed and some water was entrained into the oil with increase of the water velocity.

Charles et al. (1961) obtained phase holdups by applying two quick-action valves to trap fluids and a pig to drain liquids into volume measuring equipment. In general, the water holdup was found to be greater than the input water volume fraction when water was the continuous phase in contact with the pipe wall, indicating that water was held back. The pressure gradient change with increase of input water-oil ratio was drawn in Charles et al. (1961). It was shown that the pressure gradient was reduced most markedly in the flow patterns of core annular flow and oil slugs in water flow with increase of the input water-oil ratio.

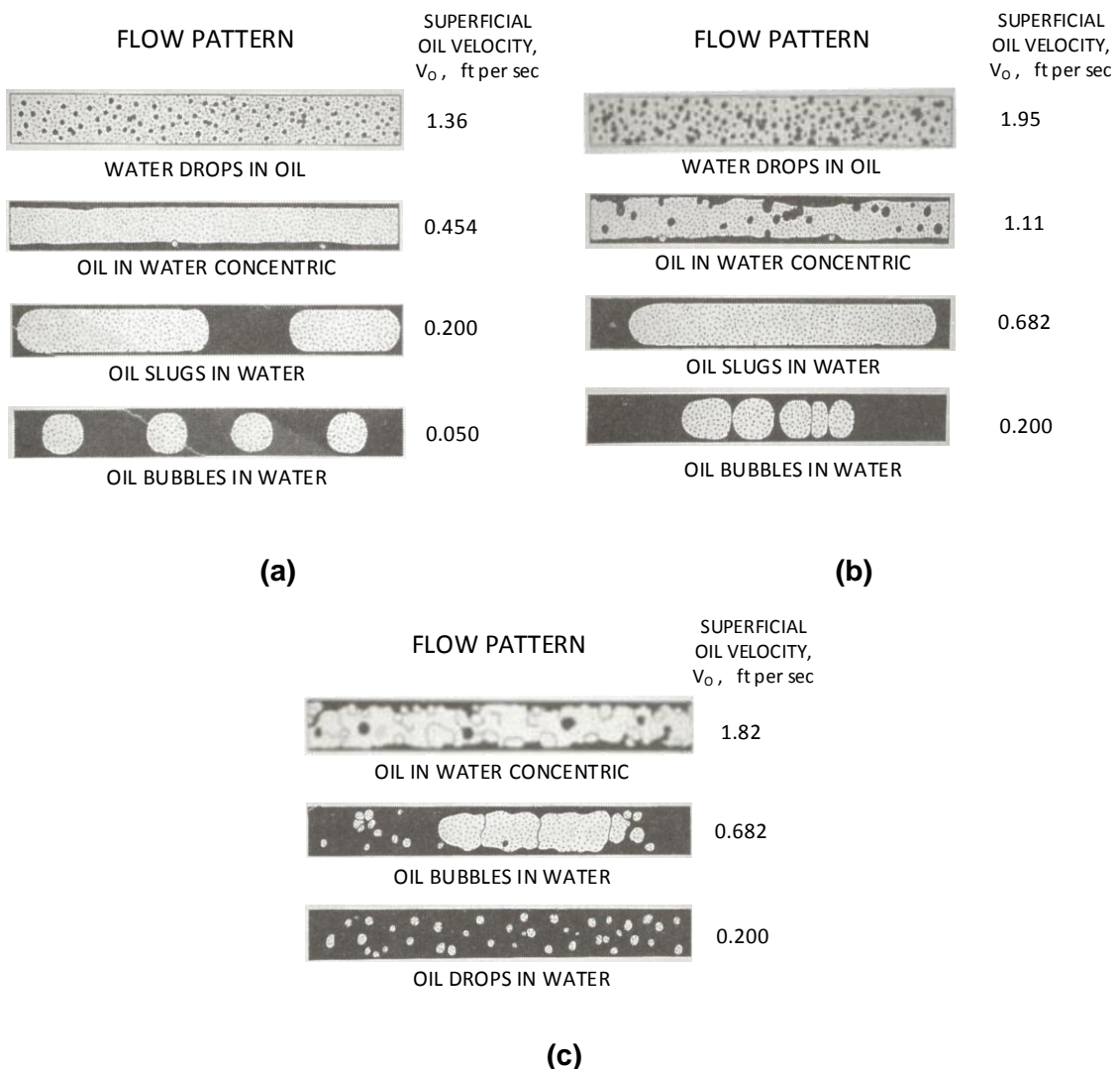


Figure 2-3 Sketches of flow patterns taken from Charles et al. (1961). (a) $U_{sw}=0.10$ ft/s; (b) $U_{sw}=0.682$ ft/s; (c) $U_{sw}=2.04$ ft/s.

(2) Delft University of Technology, Koninklijke/Shell Laboratorium (The Netherlands)

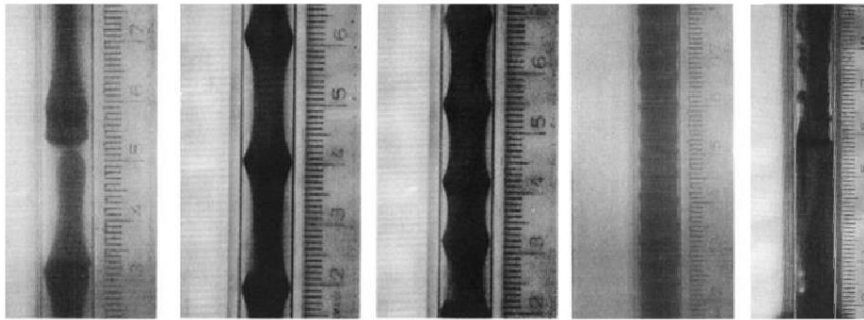
Ooms et al (1984) carried out experiments in a 50m length of 2 inch and a 888m length of 8 inch horizontal rig. Their study focused on core annular flow thus only this particular flow regime was discussed. In the 2 inch pipe tests, the oil used had a density of about 970 kg/m^3 , viscosity varied from 2 300 to 3 300 cP. The oil and water were introduced concentrically via an inlet device. It was reported that although the oil core was introduced concentrically, it adjusted itself eccentrically due to the density difference. Core annular flow was developed as long as the superficial oil velocity was above a critical value of around 0.1 m/s. During some of the experimental tests, a rectangular roughness element was placed against the pipe wall at a certain location inside the pipe to study the reaction of the flow to such a disturbance. The core-annular flow passed this disturbance without difficulty and became steady again a few diameters downstream. In the 8 inch pipe tests, the oil used had a density of about 955 kg/m^3 , viscosity varied from 1 200 to 2 200 cP. The superficial oil velocity was fixed at 1.0 m/s. The 8 inch pipe consisted of 22 bends. It is reported that the bends did not pose problems for the stable core annular flow. In a following study reported in Oliemans et al. (1987) from the same group, water holdups of core annular flow were determined from photographs. The water holdup was found to be higher than the input water volume fraction, indicating that the average oil velocity is higher than the average water velocity.

(3) University of Minnesota (USA)

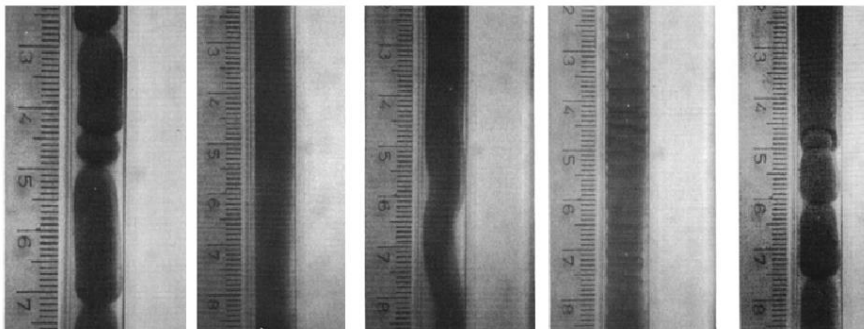
Bai et al. (1992) investigated water-lubricated high-viscosity oil-water flow through a vertical pipe. This is the earliest experimental study on vertical high-viscosity oil-water pipeline flow found in the literature. The test section was an inverted-U loop glass pipe with a total height of 180 inch (0.46 m); the pipe I.D. was 3/8 inch (9.5 mm). The oil (viscosity 601 cP, density 905 kg/m^3) and water were injected into the pipeline concentrically via an inlet device. High resolution

video recordings were made. The water hold-ups were obtained by trapping fluids with quick-action valves.

The observed flow patterns can be generally classified into CAF, oil plugs in water, oil bubbles in water, and dispersed oil in water. Bai et al. (1992) further classified CAF with different characteristics into bamboo waves, disturbed bamboo waves, disturbed CAF (including nearly perfect CAF and corkscrew CAF), and oil sticks to the wall. Photographs of typical flow patterns taken from Bai et al. (1992) are shown in Figure 2-4. The minimum pressure gradient of water-lubricated flow was found in the flow pattern of bamboo waves in up-flow and disturbed core-annular flow in down-flow.



(a) Flow patterns in up-flow (from the left to the right: oil plugs, thin bamboo waves, thick bamboo waves, disturbed bamboo waves, and oil sticks to the wall).



(b) Flow patterns in down-flow (from left to the right: oil plugs, nearly perfect CAF, corkscrew CAF, disturbed bamboo waves, and oil sticks to the wall).

Figure 2-4 Photographs of different flow patterns observed in up-flow and down-flow (Bai et al., 1992).

Arney et al. (1993) conducted experiments on two-phase high-viscosity oil-water flow in a horizontal pipe using waxy crude oil (stable water-in-oil emulsion, viscosity between 200 000 and 900 000 cP after yielding) and No. 6 fuel oil (viscosity 2 700 cP, density 989 kg/m³). The test section was a glass pipe of 6.35 m length and 15.9 mm I.D. It was reported that originally a transparent PVC pipe (15.7 mm I.D.) was used. The pipeline was cleaned regularly with detergent and water. This method worked well with the waxy crude oil, but not for the No. 6 fuel oil. The No. 6 fuel oil tended to adhere to the wall of the PVC pipe and the oil clots formed could not be cleaned from the pipe wall with detergent and water. The PVC pipe section was changed to the glass pipe as the glass was preferentially wetted by water. Oil fouling on the wall of the glass pipe could be removed by running clean water through the pipe.

In the experiments, pressure drops were obtained. Video recordings were made by high-speed video system. Water hold-ups were measured using a removable section with two pairs of ball valves installed on the ends. Unstable core annular flow with oil fouling clots on the pipe wall, termed as 'oil sticks to the wall' by Arney et al. (1993), was observed at low water flow rates. With increase of water flow rates, perfect core annular flow (PCAF), wavy core annular flow (WCAF), and oil slugs in water were observed. For the two different oils, the change of the pressure gradient with change in input water-oil ratio was similar as shown in Figure 2-5. For a fixed oil flow rate, the pressure gradient was reduced most with addition of water in the region of unstable CAF (i.e., oil sticks to the wall) or PCAF. The water holdup was found to be higher than the input water volume fraction in general. Modelling of core annular flow was also conducted by Arney et al. (1993); this aspect is introduced in Chapter 6.

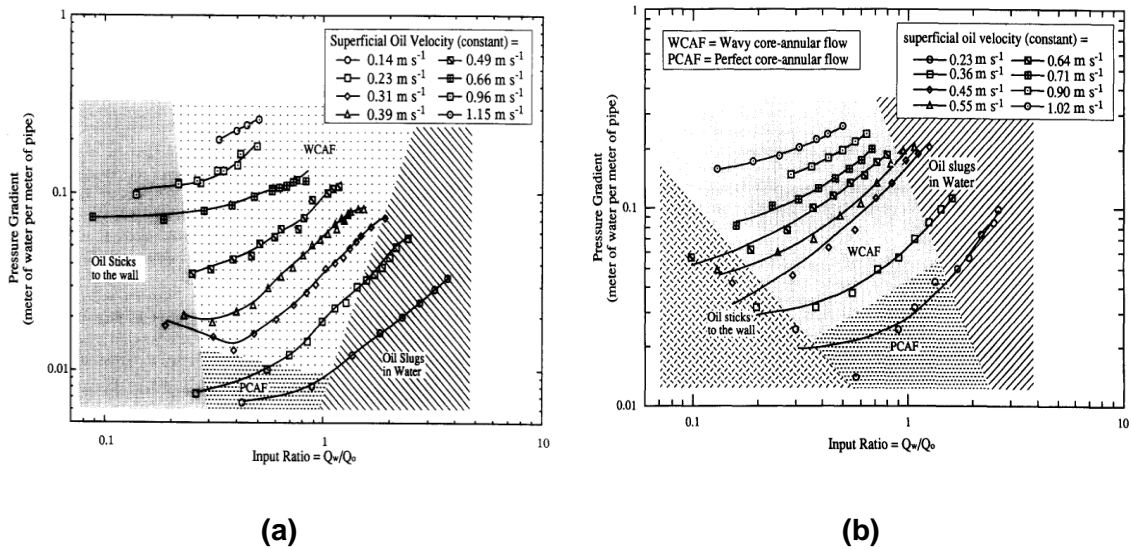


Figure 2-5 Pressure gradient versus input ratio for crude oil (a) and No.6 fuel oil (b), with the oil flow rate held constant (Arney et al., 1993).

Joseph et al. (1999) investigated self-lubricated transport of bitumen froth. The background of this study is the industrial bitumen production and transportation. Bitumen froth is produced from the oil sands using the hot water extraction process. When transported in a pipeline, water present in the froth is released in regions of high shear, i.e., near the pipe wall, forming a lubricating layer of water that allows bitumen froth pumping at greatly reduced pressure. Slightly different from water-lubricated flow, the water is not added as a lubricant particularly but released from the flow itself. This transportation of bitumen froth was termed as self-lubrication by Joseph et al. (1999). Experiments establishing the features of the self-lubrication were carried out in a 25 mm diameter, 6 m long return loop in a laboratory at the University of Minnesota and in a 0.6 m diameter, 1 000 m long pilot pipeline at Syncrude, Canada. The released water in the froth was a colloidal dispersion of small clay particles. It was found that the pressure gradient of the self-lubricated bitumen froth was about 10 to 20 times higher than that for water alone. Self-lubrication was lost when the flow velocity was reduced below 0.5-0.7 m/s. The longest test in the laboratory pipe was for 96 hours; no build-up of fouling was observed even though the test started in a pipeline fouled from previous tests. The above authors thought that

the clay particles in the released water layer may protect oil core from attaching the pipe wall.

(4) Saskatchewan Research Council (Canada)

McKibben et al. (2000a) conducted experiments in laboratory pipelines establishing the features of concurrent flow of heavy oil and water in horizontal wells (flow at low bulk velocity, typically below 0.1 m/s). Their first series of experiments were carried out in a steel pipe (I.D.=53 mm) with three short glass sections for visual observation. A lube oil with a density around 885 kg/m³, viscosity ranging from 620 to 960 cP was used. Methanol was added to water to reduce its density; the water used had a density ranging from 906 to 930 kg/m³, and viscosity 1.1 to 2.0 cP. Different water injection methods were examined, including continuously or alternately through a tee junction, or through thin longitudinal slots in the pipe wall. It was found that some distance was required for the flow to become fully developed but the injection method did not affect the ultimate flow regime or pressure gradient as long as the water and oil were injected continuously. At a mixture flow velocity of 0.045 m/s, two flow regimes, namely water slugs in oil and stratified flow, were observed visually; the transition from water slugs in oil to stratified flow occurred when the water-oil ratio reached about 20%. The ratio of the pressure gradient of the two-phase flow to that of single oil flow was close to 1. Similar experiments were conducted with crude oil (density 985 kg/m³; viscosity around 10 000 cP) and brine (density 1 010 kg/m³; viscosity 1 cP). For these tests, the pipeline was coated with oil thus recognition of flow regimes through visual observation section was not achieved. The pressure gradient ratios were less than 1. More experiments using the crude oil and brine were conducted at flow velocities ranging from 0.03 to 0.12 m/s. It was found that at low flow rates, the pressure gradient fluctuated between high (consistent with the pressure gradient of single oil flow) and very low values, indicating intermittent flow. At higher flow velocities (typically above 0.1 m/s), the pressure gradient was steady and very low. For the intermittent flow at low flow velocities which characterize wellbore

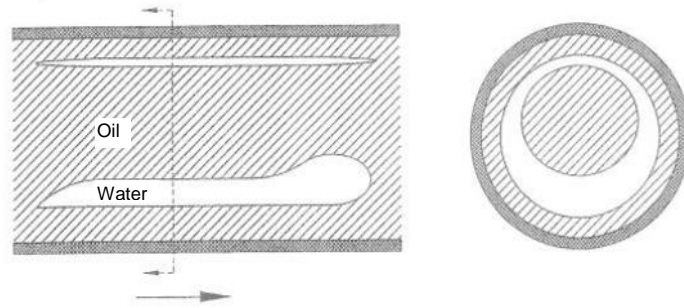


Figure 2-6 Hypothetical water slugs with enveloped oil (McKibben et al. 2000).

flows, the time-averaged pressure gradient was lower than the pressure gradient of single oil flow although the total flow rate increased. The authors proposed a tentative phase configuration for the intermittent flow as shown in Figure 2-6. The flow at higher flow rates having steady and very low pressure gradients were described as ‘continuous water-assisted flow (CWA)’ and was further discussed in McKibben et al. (2000b).

McKibben et al. (2000b) investigated concurrent flow of heavy oil and water at velocities typical of oil-field gathering systems. Laboratory experiments were conducted in two pipelines with I.D. 53 mm and 105 mm. The temperature of the oil was controlled to obtain different oil viscosities. For tests in the 53 mm pipeline, the oil viscosity varied between 5 800 and 91 600 cP, oil density between 958 and 987 kg/m³, mixture flow velocity between 0.5 to 1.2 m/s, and water fraction between 0.10 and 0.36. For tests in the 105 mm pipeline, the oil viscosity was 7 100 cP, oil density was between 958 and 987 kg/m³, the mixture flow velocities tested were 0.3 and 0.77 m/s, and the water fraction was 0.10. Apart from the laboratory experiments, field tests were also conducted in a filed pipeline (I.D. 80.4 mm; length 1 336 m). Core annular flow with an oil layer on the pipe wall, or continuous water-assisted flow as termed by McKibben et al. (2000b) was found to be achieved in steel pipelines provided the water fraction and the mixture velocity were high enough. The experimental data collected was used to obtain an empirical correlation for the prediction of pressure gradient of water-assisted flow. Introduction on the correlation can be found in

Chapter 5. The correlation has not been evaluated with dependent experimental data. Evaluation of this model with more experimental data is necessary.

(5) University of Campinas (Brazil)

Bannwart et al. (2004) reported flow patterns of heavy oil-water flow in experiments carried out in a flow loop comprising both vertical and horizontal test sections (glass pipe, I.D. 28.4 mm). The oil (viscosity 488 cP, density 925.5 kg/m³) and water were introduced concentrically via an injection nozzle. Basic flow patterns observed were shown in Figure 2-7. Dispersed oil in water, oil bubbles, and core annular flow were observed in both vertical and horizontal pipe; stratified flow was only developed in the horizontal pipe.

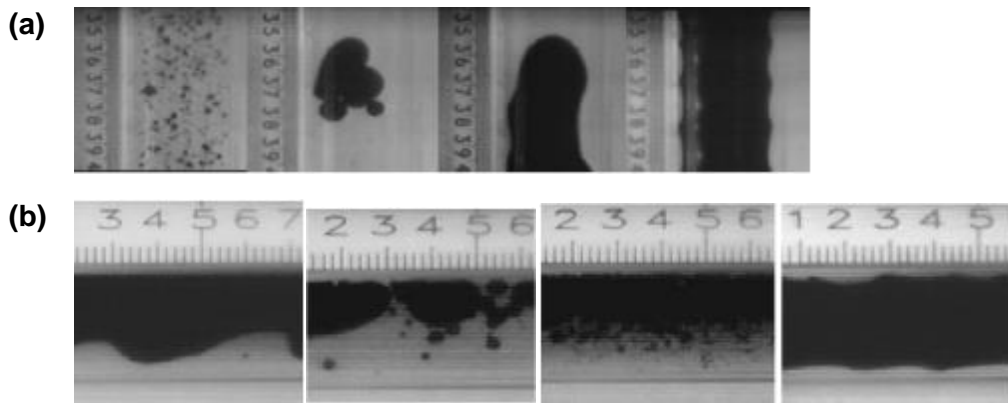


Figure 2-7 Photographs of basic flow patterns of horizontal (a) and vertical (b) heavy oil-water flow (Bannwart et al. 2000).

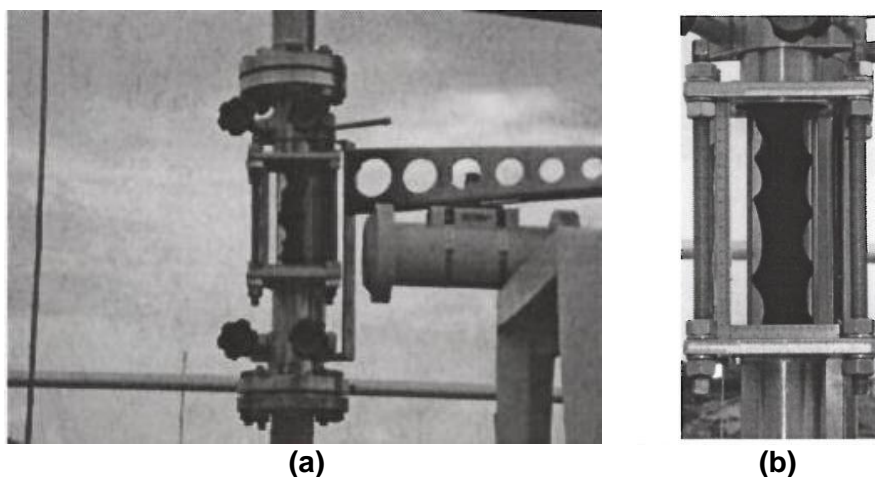


Figure 2-8 Photographs of visualization section at the well head (a) and core annular flow developed (b) (Bannwart et al. 2012).

Bannwart et al. (2012) carried out experiments on water-lubricated heavy oil flow in a pilot vertical well (production casing diameter 9 inch; production tubing diameter 62 mm; 300 m deep). The water and oil (dead crude oil, viscosity around 2 000 cP, density 950 kg/m³) were pumped from individual tanks to the test well, and then the mixture in the well flowed upward to a separator tank, from which the water and oil were pumped back to their respective tanks after separation. An injection nozzle was installed at bottom hole to initiate the formation of core annular flow. A visualization section was installed at the head of the test well (see Figure 2-8). Oil and water flow rates under which core annular flow was supposed to form according to some previous laboratory experimental studies were tested. They compared bottom-hole pressure of core annular flow to that of single oil flow and found that there was a decrease of about 25%. They also pointed out that given the safety limitation of the flow loop, it was possible for core annular flow to reach an oil flow rate up to 2.5 times as high as the maximum single oil flow rate.

(6) University of Brescia, University of Modena and Reggio Emilia (Italy)

Grassi et al. (2008) investigated high-viscosity oil-water flow in horizontal and slightly inclined pipes. The test pipe consisted of six transparent polycarbonate tubes of I.D. 21 mm, having a total length of 9m. The test pipe was sustained by a steel beam which was hinged to a vertical support; the beam rotation around the hinge allowed the system inclination up to $\pm 15^\circ$. Paraffin oil (viscosity around 800 cP, density around 886 kg/m³) and tap water were used. The oil and water were introduced concentrically via an inlet device. The water was introduced in the pipe at highest possible flow rate to flush the pipe before injection of oil. No significant differences in flow regimes were observed in their experiments carried out in the same system with 0°, +10°, -10°, and +15° inclination. Flow regime maps were produced; core annular flow and dispersed oil in water were obtained in a wide range of input flow rates. Oil fouling on the pipe wall was only observed at low oil and water flow rates. The measured pressure gradients of core annular flow were compared with predications from a

two-fluid model proposed in Brauner (1998) (this model is reviewed in Chapter 5) and a good agreement was shown.

Sotgia et al. (2008) experimentally studied water continuous high-viscosity oil-water flow in horizontal pipes with diameters ranging from 21 to 40 mm. The high viscosity oil is an emulsion composed of a small amount of water in mineral oil (Milpar 220, viscosity 919 cP and 889 kg/m^3 at $20 \text{ }^\circ\text{C}$). The oil and water were introduced concentrically via an inlet device. The water was introduced in the pipe at very high flow rate to flush the pipe before the injection of oil. Flow patterns observed include wavy stratified flow, oil slugs in water, core annular flow, and dispersed oil in water. Flow pattern maps were produced. The lowest pressure gradient was found to be near the transition between the core annular flow and stratified flow. The measured pressure gradients of core annular flow were compared with core annular flow models proposed by Arney et al. (1993) and Brauner (1998). The measured pressure gradients were higher than predictions from the two models for the majority of the data.

(7) The University of Tulsa (USA)

Sridhar et al. (2011) conducted an experimental study on high-viscosity oil-water flow in horizontal and slightly inclined pipes. The pipe I.D. is 50.8 mm and pipe inclination angles are -2° , 0° , $+5^\circ$, and $+10^\circ$. A mineral oil was used with viscosity varied from 200 to 1 100 cP. The water holdup was obtained by measuring trapped fluids in a removable spool piece. Stratified flow and core annular flow were observed; oil film on the pipe wall was observed. No significant variation of flow patterns was observed with change in inclination angles.

(8) China University of Petroleum (China)

Wang et al. (2011) conducted an experimental study on the concurrent flow of heavy crude and water in a horizontal stainless steel pipe. The test section I.D. was 25.4 mm and overall length was 50 m. The crude oil (viscosity around 628 cP at $60 \text{ }^\circ\text{C}$) and water were collected from an oil field. The oil and water were

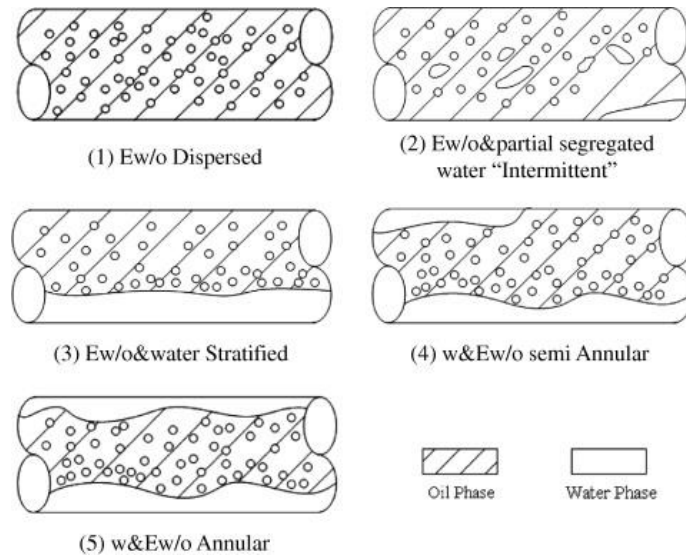


Figure 2-9 Sketch of flow patterns of heavy crude oil–water flow in a horizontal pipe (Wang et al. 2011).

first mixed in a stirred vessel, then the mixture was transported through the pipeline. A local sampling device was used to get samples at different locations along the pipe diameter. It was found that at low mixture velocities and water fractions, a water-in-oil emulsion occupied the whole pipe cross section. Segregated water appeared as the velocity or the water volume fraction increased. At high water fractions and mixture velocities, core annular flow with the water-in-oil emulsion in the core surrounded by a water layer appeared. Sketches of the flow patterns taken from Wang et al. (2011) are shown in Figure 2-9. The formation of core annular flow can be linked to the self-lubricated bitumen froth reported in Joseph et al. (1999). In both studies, the formation of core annular flow requires high flow rates. It is suggested that the water migrates into the region of high shear at the wall of the pipe provided the flow velocity is sufficient.

(9) Cranfield University (UK)

Al-Awadi (2011) experimentally investigated general characteristics of high-viscosity-oil-related multiphase flow including oil-gas, oil-water, oil-water-gas, and oil-water-sand in a horizontal perplex pipe (I.D. 26 mm). The oil used was Total CYL 1 000. In the high-viscosity oil-water tests, the oil viscosity varied

between 3 800 and 16 000 cP, density varied between 920 and 938 kg/m³. The water and oil were injected through a Tee junction. Different methods of water injection (horizontally or vertically through the Tee junction) were tested initially and no considerable differences were observed in established flow patterns and measured pressure gradients. The oil was introduced into the pipe before the injection of water; the water flow rate was increased from the lowest possible velocity to higher velocities to observe the inversion from oil-continuous flow to water-continuous flow. An unstable transitional flow pattern characterised with spiral motion of water and oil was observed before stable core annular flow was formed. Oil fouling film on the pipe wall was observed for different regimes of water-lubricated flow, including core annular flow, oil lumps in water, and dispersed oil in water. The pressure gradient was significantly reduced from that of single oil flow when water-lubricated flow was formed.

Alagbe (2013) conducted more experiments on water-sand, oil-water, and oil-water-sand in the same flow loop with a different oil Total CYL 680. Concerning the high-viscosity oil-water flow tests, the oil viscosity varied between 3 700 and 7 100 cP, density varied between 905 and 920 kg/m³. More experimental data on higher water flow rates were collected.

2.2.3 Summary

A summary of previous experimental studies on high-viscosity oil-water flow in horizontal pipes is listed in Table 2-1. Based upon the previous work, current understanding on high-viscosity oil-water flow in horizontal pipes and questions that need further investigation were summarised as below:

- With addition of water into high-viscosity oil pipeline flow, water-lubricated flow, including core annular flow, oil slugs/plugs in water, dispersed oil lumps in water can develop. Stratified flow is observed in some experiments, while not in some other experiments.

As a lot of studies focus on core annular flow, flow maps of high-viscosity oil-water flow covering a wide range of phase flow rates are limited. Discrepancy is shown among those limited flow maps.

- Core annular flow is the most favourable flow regime for effective transport of high-viscosity oil-water flow. For this flow regime, an oil-rich zone develops in the central portion of the pipe, and water-rich sleeve forms near the pipe wall. Depending on the oil and water properties and flow rates, entrainment or emulsification of water into the oil might occur.
- Oil fouling film on the inner wall of the pipe was observed in some experiments while not in some other experiments; this might be associated with the experimental procedure (e.g., whether use special injection device to favour the formation of CAF at the injection point; whether use water/detergent regularly to wash the pipe; the sequence of the phase injection), wall wettability, and experimental run time. For industrial operations of water-lubricated heavy oil transport, oil fouling on the pipe wall is inevitable. With the oil coating film on the pipe wall, the pressure gradient of water-lubricated flow is still very low. The pilot experiments show that the water-lubricated flow can be operated for a long time without accumulation of oil on the pipe wall if properly controlled. The general perception to maintain stable water-lubricated flow is that the input water volume fraction needs to be sufficient and the flow rate needs to be high enough; specific criteria are not well established.
- Most of the existing empirical or mechanistic models of CAF have been developed without consideration of the oil fouling on the pipe wall. To accurately predict the pressure gradient of water-lubricated heavy oil flow in industrial operations, the influence of oil fouling film on the pressure gradient has yet to be investigated.
- There are very limited water holdup data in the literature. The available data show that the water holdup of core annular flow is higher than the input water volume fraction, suggesting that the oil core flows faster than the annular water.

Table 2-1 Summary of experimental studies on high-viscosity oil-water flow in horizontal pipes.

Authors	Pipe I.D. (mm)	μ_o (cP)	ρ_o (kg/m ³)	ρ_w (kg/m ³) ^a	σ (N/m)	Velocity range (m/s)	Reported flow patterns ^b	Additional Measurements
Charles et al. (1961)	26	6.29,16.8, 65.0	998	998	0.045	U_{so} : 0.02-0.9; U_{sw} :0.03-1.07	CAF, I, D	-dp/dz, H_w
Ooms et al. (1984)	50; 203	2 300-3 300; 1 200-2 200	~970; ~955	998	-	U_{so} : ~1; U_{sw} : 0.01-0.25	CAF	-dp/dz
Oliemans et al. (1987)	50	3 000	978	998	-	U_{so} : 0.50-2.5; U_{sw} : 0.03-0.6	CAF	dP/dl, H_w , interfacial wave information
Arney et al. (1993)	16	200 000-900 000; 2 700	985; 989	998	-; 0.26;	U_{so} :0.14-1.16; U_{sw} :0.06-0.65	CAF, I	-dp/dz, H_w
Joseph et al. (1999)	25; 600	-	-	1050	-	U_m : 0.25-2.5; U_m : 0.9-1.14	CAF ^c	-dp/dz
McKibben et al. (2000a)	53	620~960; 5 300-11 200	885; 971-985	906-930; 1010	-	U_m :0.045; U_m :0.03~0.12	ST, I; I	-dp/dz
McKibben et al. (2000b)	53; 105	5 800-91 600; 7 100	958-987; 958-984	998	-	U_m :0.5-1.2; U_m :0.3~0.77	CWA ^d	-dp/dz

Table 2-1 Continued.

Authors	Pipe I.D. (mm)	μ_o (cP)	ρ_o (kg/m ³)	ρ_w (kg/m ³) ^{a)}	σ (N/m)	Velocity range (m/s)	Observed flow patterns ^{b)}	Additional Measurements
Bannwart et al. (2004)	28	488	926	998	-	U_{so} : 0.007-2.5; U_{sw} :0.04-0.5	ST, CAF, I, D	-dp/dz
Grassi et al. (2008)	21	800	886	998	0.05	U_{so} : 0.03-0.7; U_{sw} :0.2-2.5	ST, CAF, I, D	-dp/dz
Sotgia et al. (2008)	21-40	919	889	998	0.02	U_{so} : 0.1-1.0; U_{sw} : 0.1-2.51	ST, CAF, I, D	-dp/dz
Sridhar et al. (2011)	52	220, 1 070	884	998	0.03	U_{so} :0.1-1.0; U_{sw} :0.1-0.5	ST, CAF	-dp/dz
Wang et al. (2011)	25	628	953	-	0.01	U_m :0.045; C_w : 0.1-0.7	ST, CAF, D ^{e)}	-dp/dz
Al-Awadi(2011)	26	3 800-16 000	920-938	998	-	U_{so} :0.06-0.57; U_{sw} :0.01-1.0	CAF, I	-dp/dz
Alagbe (2013)	26	3 700-7 100	905-920	998	0.02	U_{so} :0.06-0.4; U_{sw} :0.2-1.0	CAF, I	-dp/dz

^{b)} The water densities and viscosities are not reported in most of the studies in the literature; when they are not reported, the water density is regarded as 998 kg/m³ here unless brine water or field water was used. The water viscosity is not listed here as in all the studies, the water viscosity is about 1 cP.

^{b)} Different nomenclatures are used by different authors. Here only the basic flow patterns are listed, including ST (stratified flow), CAF (core annular flow), I (intermittent flow, including slugs/plugs/bubbles of one phase in another phase), and D (dispersed flow).

^{c)} For bitumen froth, the CAF has oil-rich core and water-rich annulus. ^{d)} the term of continuous water-assisted (CWA) flow is used by the authors to describe the flow. Specific flow regimes of CAF and I are possible phase configurations. ^{e)} For emulsion, the ST and CAF have oil-rich phase and water-rich phase.

2.3 Modelling of multiphase flow in computational fluid dynamics

2.3.1 Fundamentals of computational fluid dynamics

Computational fluid dynamics (CFD) is an important tool in the study of complex flows. It relies on the numerical solution of the partial differential equations that govern the motion of the fluids. The governing equations of fluid flow represent mathematical statements of the conservation laws of physics: (1) mass is conserved; (2) momentum is conserved; (3) energy is conserved. By enforcing these conservation laws over discrete spatial volumes in a fluid domain, it is possible to achieve a systematic account of the changes in mass, momentum and energy as the flow crosses the volume boundaries. The resulting equations can be written as:

- Continuity equation:

$$\frac{\partial \rho}{\partial t} + \nabla \cdot (\rho \mathbf{u}) = 0 \quad (2-10)$$

- Momentum equation:

$$\frac{\partial}{\partial t} (\rho \mathbf{u}) + \nabla \cdot (\rho \mathbf{u} \cdot \mathbf{u}) = -\nabla p + \nabla \cdot [\mu (\nabla \mathbf{u} + \nabla \mathbf{u}^T)] + \mathbf{S}_M \quad (2-11)$$

- Energy equation:

$$\frac{\partial}{\partial t} (\rho i) + \nabla \cdot (\rho \mathbf{u} \cdot i) = -p \nabla \cdot \mathbf{u} + \nabla \cdot (k \nabla T) + \Phi + S_i \quad (2-12)$$

Where ρ is density, \mathbf{u} is instantaneous velocity, \mathbf{S}_M is body force, i is internal thermal energy, T is temperature, Φ represents a viscous dissipation term, and S_i represents energy source term. The first two equations are applied when energy transfer in the fluid system is not concerned; they are usually referred to as Navier-Stokes (NS) equations. Detailed introduction on the transport equations can be found in Anderson et al. (1995) and Versteeg and Malalasekera (2007).

Solving the governing equations without any modelling is called direct numerical simulation (DNS). Most flows encountered in engineering practice are turbulent. Turbulent flow exhibits scales of significantly different magnitudes. DNS resolves the Navier-Stokes equations on spatial grids that are sufficiently fine, resolving all the scales of motion. DNS is highly costly in terms of computing resources, and is not feasible for industrial flow computations now.

Modelling is often employed to account for the turbulent effects. The Reynolds-averaged Navier-Stokes (RANS) approach is the traditional approach. The RANS approach focuses on the mean flow and the effects of turbulence on mean flow properties. The Navier-Stokes equations are time-averaged (or called Reynolds-averaged) and extra terms appear in the Reynolds-averaged Navier-Stokes equations due to the interactions between various turbulent fluctuations. These extra terms are modelled with different classic turbulence models, e.g., $k-\varepsilon$ models, $k-\omega$ models, and Reynolds Stress Model. The modelling results could be reasonably accurate and the computational resources are modest, so this approach has been the mainstay of engineering flow calculations. Another approach for turbulence modelling is large eddy simulation (LES). The LES lies between traditional techniques and DNS. This method involves space filtering of the unsteady Navier-Stokes equations prior to the computation, which passes the larger eddies and rejects the smaller eddies. The large scale motions are resolved exactly, while smaller scale motions are modelled. The demands on computing resources are large. Increasingly, research is directed towards extending the range of applications of LES. Detailed introduction on different turbulence models can be found in Ferziger and Peric (2012), Versteeg and Malalasekera (2007), and Fluent theory guide (2012).

Multiphase flow requires even further modelling due to the complex behaviour of interaction between the phases. Approaches for multiphase flow modelling in computational fluid dynamics are introduced in the following section.

2.3.2 Multiphase computational fluid dynamics

Multiphase computational fluid dynamics deals with the formulation and solutions of fluid flow equations where the flow under investigation has more than one component. There are three main approaches for modelling multiphase flows: Euler-Lagrange approach, Euler-Euler approach and volume of fluid (VOF) approach.

(1) *The Euler-Lagrange approach*

In the Euler-Lagrange approach, the fluid phase is treated as a continuum by solving the Navier-Stokes equations. These equations contain special source terms that represent the influence of the dispersed phase such as the drag force that a particle exerts. The dispersed phase is tracked by solving the equation of motion for each particle

$$\frac{d\mathbf{u}_p}{dt} = \sum \mathbf{F}_i \quad (2-13)$$

where \mathbf{u}_p is the particle velocity, \mathbf{F}_i represents forces acting on the particle. The drag force is generally included and other forces that can be of importance are, for example, lift force, virtual mass force and history force. Formulations of different forces can be found in Ranade (2002) and Fluent theory guide (2012). When performing numerical modelling it is up to the modeller to judge which forces that are of importance to include on the right hand side of equation 2-13. Adding more forces to a model increases accuracy but also increases complexity.

As this modelling approach resolves information on the level of a single particle, it is quite computationally expensive. To decrease the computational cost one can choose to track clusters of particles instead. However, this approach is still computationally expensive. Therefore, the Euler-Lagrange modelling is suitable for dilute dispersed flow, meaning flows with a low volume fraction of the dispersed phase.

(2) The Euler-Euler Approach

In the Euler-Euler approach, the different phases are treated mathematically as interpenetrating continua. Since the volume of a phase cannot be occupied by the other phases, the concept of phasic volume fraction is introduced. These volume fractions are assumed to be continuous functions of space and time and their sum is equal to one. One set of conservation equations are solved for each phase. Coupling between the phases is achieved through a shared pressure and interphase exchange coefficients. The interphase exchange coefficients need to be modelled. A number of models, suitable for different flow types, have been developed and a detailed introduction of interphase exchange modelling can be found in Fluent theory guide (2012).

A simplified version of an Euler-Euler model is the mixture model. As in the Euler-Euler models both phases are treated as interpenetrating continua. The mixture model solves the Navier-Stokes equations for the mixture fluid based on mixture properties, such as mixture velocity, mixture viscosity etc. To track the different phases, a transport equation for the volume fraction is also solved. The phases are allowed to move with different velocities by using the concept of slip velocity, which in turn includes further modelling.

Euler-Euler models are appropriate for separated flows where both phases can be described as a continuum. Besides, the Euler-Euler approach can also be used to model dispersed flows when the overall motion of particles is of interest rather than tracking individual particles. To be able to describe a dispersed phase as a continuum, the volume fraction should be high. Therefore, this approach is suitable for dense flows. The mixture model is a good substitute for the full Euler-Euler models in several cases. A full Euler-Euler model may not be feasible when there is a wide distribution of the particulate phase or when the interphase laws are unknown or their reliability can be questioned. A simpler model like the mixture model can perform as well as a full multiphase model while solving a smaller number of variables than the full multiphase model (Fluent theory guide, 2012).

(3) The VOF Model

The VOF model belongs to the Euler-Euler framework where all phases are treated as continuous, but contrary to the previous presented models the VOF model does not allow the phases to be interpenetrating. It is designed for two or more immiscible fluids where the position of the interface between the fluids is of interest. In the VOF model, a single set of momentum equations is shared by the fluids. The tracking of interface is accomplished by the solution of a continuity equation for the volume fraction of one (or more) of the phases:

$$\frac{\partial(\rho_k \alpha_k)}{\partial t} + \nabla \cdot (\rho_k \alpha_k \mathbf{u}) = 0 \quad (2-14)$$

where α_k is the volume fraction of a secondary phase. The phase volume fraction has a value of 1 when a cell is entirely filled with the k^{th} fluid, a value of 0 when a cell is empty of the k^{th} fluid, and a value between 0 and 1 if an interface is present in the control volume. It is noted that the phase volume fraction does not uniquely identify the interface. Several different interface configurations may correspond to the same value of phase volume fraction. Several specialised techniques have been proposed to track the interface accurately, e.g., the geometric reconstruction (piecewise-linear) scheme, the donor-acceptor scheme, and the compressive interface capturing scheme for arbitrary meshes (CICSAM).

The VOF model is used to model immiscible fluids with clearly defined interface. Accuracy of the VOF model decreases with interface length scale getting closer to the computational grid scale. Therefore, this model is popular for modelling separated flow in which interface length scale is large. It is seldom applied to dispersed multiphase flows containing a large number of dispersed phase particles as that would be computationally very demanding (Ranade, 2002). For the present study on high-viscosity oil-water flow, core annular flow is the flow pattern of most interest. The interface of oil core and annular flow is in a magnitude close to or higher than the pipe diameter, therefore the VOF model is suitable for the modelling of CAF in a pipeline.

2.3.3 Numerical solution of transport equations

(1) Review on numerical solution methods

The mathematical models are non-linear, coupled partial differential equations. These can be solved analytically only for very simple cases. For real life flows one must use numerical methods, i.e., discretization methods, to transform the equations into algebraic approximations equations in terms of the variables at some discrete locations in space and time. The most popular discretization methods are finite difference (FD), finite volume (FV) and finite element (FE) methods. All methods yield the same solution if the grid (number of discrete locations used to represent the differential equations) is adequately fine. However, some methods are more suitable to particular classes of problems than others and the preference is often determined by ease of application, required computational resources and familiarity of the user (Ranade, 2002). As the CFD code ANSYS Fluent is used for the simulation of liquid-liquid flow in the present study, methods applied in Fluent are introduced as follows.

ANSYS Fluent solvers are based on finite volume method. The integral form of the conservation equations is used as its starting point to ensure global conservation. The solution domain is divided into a number of computational cells. The differential equation is integrated over the volume of each computational cell to obtain the algebraic equations. Variable values are stored at the cell centres and interpolation is used to express variable values at cell faces in terms of the cell centre values.

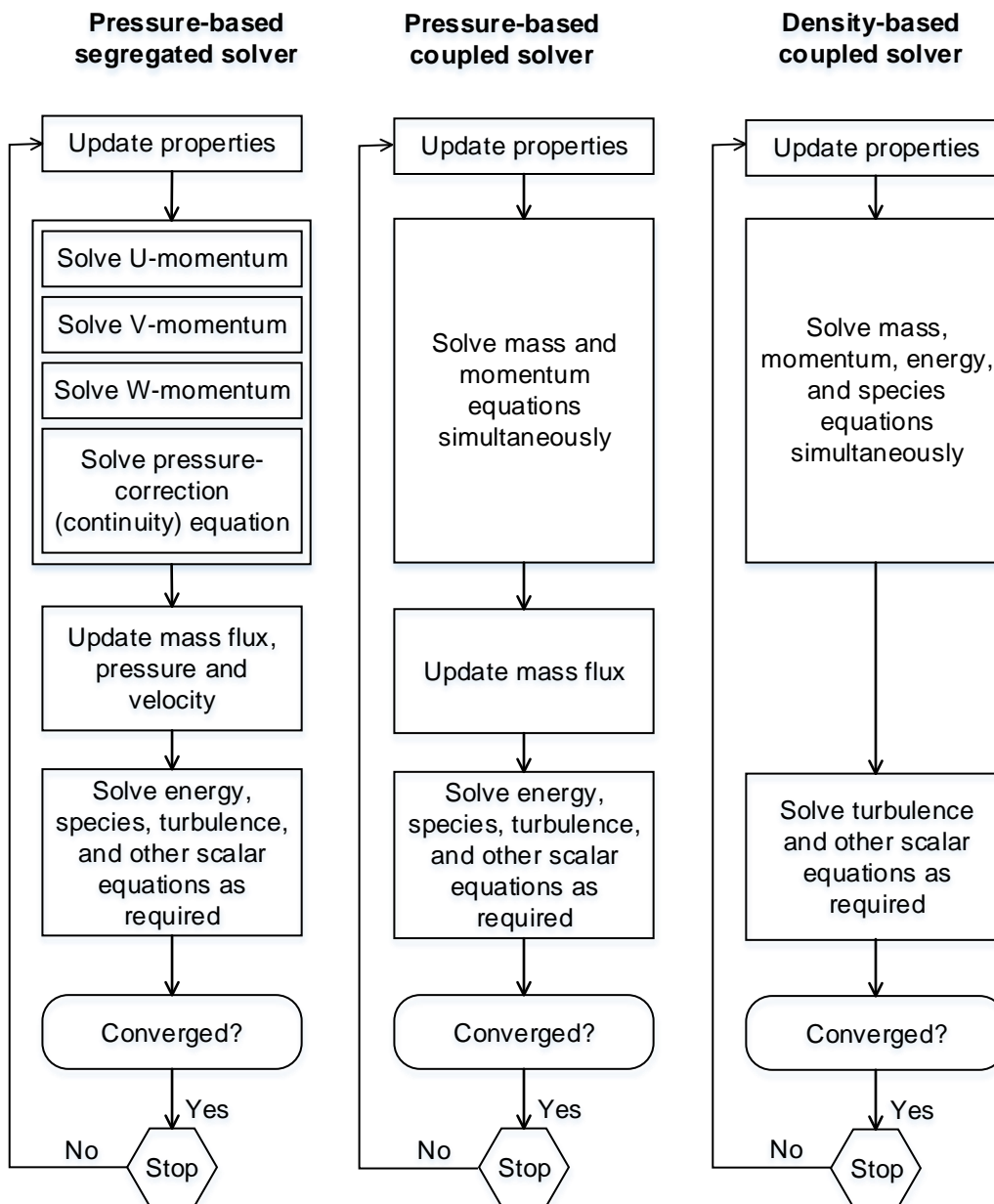


Figure 2-10 Calculation steps in each iteration of different solvers.

There are two kinds of solvers available in Fluent, namely pressure-based solver (further divided into segregated solver, and coupled solver), and density-based coupled solver. The pressure-based approach was developed for low-speed incompressible flows, while the density-based approach was mainly used for high-speed compressible flows. Both methods have been extended and reformulated to solve for a wide range of flow conditions beyond their traditional

or original intent. Figure 2-11 outlines the calculation steps in each iteration of different solution methods.

The VOF multiphase flow model implemented in Fluent is limited to the pressure-based solver. A pressure-based segregated solver makes use of a pressure correction equation. Firstly, the momentum equations are solved using a guessed pressure. If the resulting velocities do not satisfy the continuity equation a pressure correction equation is solved to update the pressure field. With the updated pressure the velocity fields are also updated and this process is repeated until the obtained velocity fields satisfy both the momentum equations and the continuity equation. One of the most widely used pressure correction schemes is the SIMPLE (Semi Implicit Method for Pressure Linked Equations) scheme but a number of versions exist. As the equations are solved in a subsequent manner, only one discrete equation needs to be stored at a time which results in lower memory requirements. Due to the iterative nature of the solution algorithm the convergence rate is often slower.

In a pressure-based coupled solver, the momentum and continuity equations are solved simultaneously. As the discrete system of all equations needs to be stored at the same time, the memory requirement is larger for a coupled solver (requiring 1.5–2 times more memory than the segregated solver) and it takes more time to complete one iteration loop. However, in return the total number of iterations to achieve convergence is usually lowered when using a coupled solver (Fluent Theory Guide, 2012).

(2) Errors in CFD simulation

Errors in CFD simulations arise mainly from two sources: inherent errors in representing reality by the set of transport equations (physically deficient representation); and errors arising from inexact solution methods (numerically deficient representation). Having established adequate control of numerical errors, the simulated results may be compared with experimental data to evaluate errors in physical modelling.

Numerical errors mainly come from the representation of the governing flow equations and other physical models as algebraic expressions in a discrete domain of space and time. The discrete spatial domain is known as the grid or mesh. The temporal discreteness is manifested through the time step taken. A consistent numerical method will approach the continuum representation of the equations and zero discretization error as the number of grid points increases and the size of the grid spacing tends to zero. As the mesh is refined, the solution should become less sensitive to the grid spacing and approach the continuum solution. A grid dependence study is a useful procedure for determining the level of discretization error existing in a CFD solution.

3 EXPERIMENTAL SETUP AND PROGRAMME

3.1 Introduction

Experiments on high-viscosity-oil-related multiphase flow have been conducted in the Process Systems Engineering (PSE) laboratory, Cranfield University. Concerning high-viscosity oil-water flow, Al-Awadi (2011), Zorgani (2012) and Alagbe (2013) have performed experiments on high-viscosity oil-water flow in a horizontal 1 inch pipe (I.D.=26 mm). All the previous experiments collected pressure signals and flow pattern information.

Another important parameter in oil-water two-phase flow is phase holdup as there may be slip between the phases. Experimental information of phase holdup is of importance in understanding flow characteristics as well as validating models. In the present study, a modification on the 1 inch three-phase rig was made aiming at measuring water holdup using a sampling method. Experiments on high-viscosity oil-water flow were performed in the upgraded 1 inch flow loop. The newly collected data, especially the water holdup data, contributes to the data bank of high-viscosity oil-water flow.

This chapter first presents a literature review (Section 3.2) on phase holdup measurement in high-viscosity oil-water flow. Upon review of different available measurement methods, a water holdup measurement section was designed considering measurement accuracy, feasibility and construction expenses. The whole experimental setup is introduced in Section 3.3, followed by the experimental procedure and runs (Section 3.4). Check of the experimental system with some preliminary experimental results is presented in Section 3.5.

3.2 Literature review on phase holdup measurement

A basic method to achieve phase holdup measurement is sampling method. The theory of this method is straightforward - to get samples which can represent the in situ phase contents and obtain phase holdups after phase separation. Usually two quick-action valves are used to trap fluids, and then the trapped fluids are measured with volume measurement instrumentations.

Though the principle of this method is simple, the application of this method might not be easy due to its essence of offline measurement. Charles et al. (1961) applied this method in their pioneering work on oil-water two-phase flow with relatively low viscosity oils (6.29, 16.8 and 65 cP). After fluids were trapped with two quick-action valves, a pig was used to drain liquids out to get the samples. Applying the sampling method, Arney et al. (1993) measured water holdups of oil-water flow for viscous oils. A removable section with a pair of ball valves was used to trap fluids. Sridhar et al. (2011) also reported water holdup measurements by sampling method. Two quick-action valves were used to trap fluids in a removable spool piece section.

Photographs taken during experimental runs can also be made use of to extract information of water holdups of core annular flow. The water holdup information is determined upon the assumption that the shape of the oil core is perfect circular with this method. Oliemans et al. (1987) applied this method to obtain the water holdup information.

Intrusive methods such as conductivity probes, wire mesh, are unfeasible due to oil adhesion. A non-intrusive method based on a capacitance probe was investigated recently by Strazza et al. (2011). A capacitance probe with two concave electrodes was developed specifically for core annular flow. Oil holdup was obtained assuming a perfect oil core. Further validation is needed for the application of this method. The radiation methods such as Gamma densitometers and X-ray are expensive and the required health and safety conditions must be ensured. Also, for high viscosity heavy oil, the oil density is normally higher than traditional crude light oil and is close to the water density. The small density difference between heavy oil and water leads to similar absorption coefficients, which makes the radiative methods less attractive for the measurement of high-viscosity oil-water flow.

Considering measurement accuracy, feasibility and construction expenses, the sampling method was used in the present study.

3.3 Experimental setup

The whole experimental setup is illustrated in Figure 3-1. The flow loop was designed for 'once-through' experiments. Briefly, single oil and water flow meet at a Tee junction, then flows forward together through a horizontal multiphase flow test line. After the test line, the fluids are collected into a gravity separator. On separation of the phases, oil and water are pumped back to their tanks separately. Figure 3-2 shows a picture of the experimental setup. A detailed introduction on the experimental setup is as follows.

(1) Oil system

Oil is stored in a tank with a capacity of 0.15 m³. The tank was made from plastic material and insulated with fibres on the periphery. The oil is pumped by a variable speed progressive cavity pump (PCP). The pump has a maximum capacity of 0.72 m³/h with a safety switch to turn off the pump at maximum discharge pressure of 10 bar gauge pressure.

Single oil flow is metered using a Coriolis flow meter (Endress+Hausser's Promass 83I DN 50); the flow meter has three outputs - mass flow rate, density and viscosity with measurement accuracy of 0.1%, 0.5 kg/m³ and 0.5% respectively. A further discussion on the performance of the oil pump and some practical considerations on the setup of the oil system are presented in Appendix D.

Upstream the horizontal multiphase flow test section, a T-port three way ball valve is used to control the single phase oil flow direction. By controlling the valve, the oil flows into either the horizontal multiphase flow test line or a bypass line back to the oil tank to achieve single oil flow circulation.

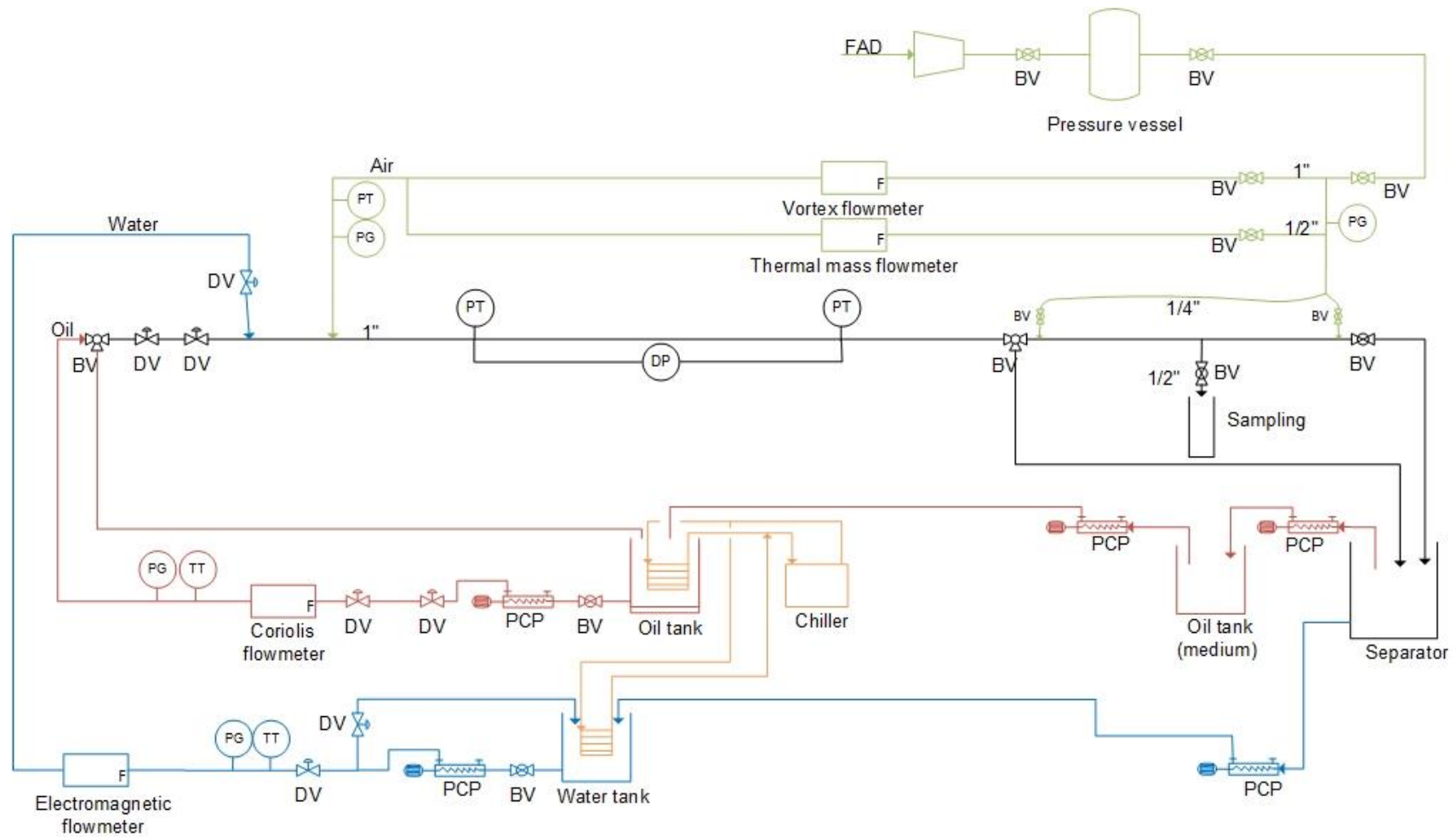


Figure 3-1 PI&D of the experimental setup for high-viscosity oil-water tests.

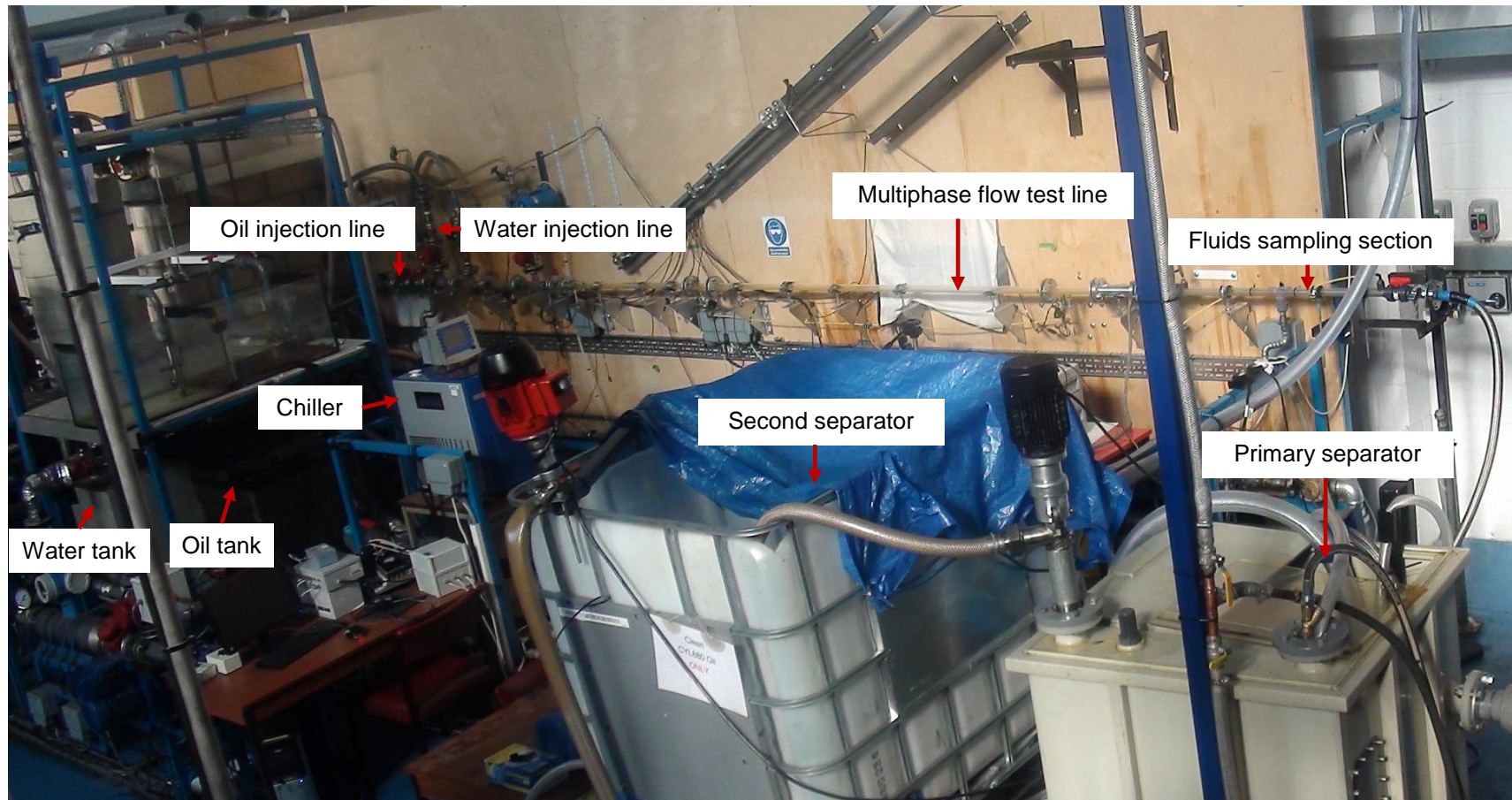


Figure 3-2 Snapshot of the experimental setup.

(2) Water system

The water system in general is similar to the oil system. Water is stored in a water tank (0.15 m³ capacity, made from plastic material and insulated with fibres on the periphery) and pumped by a variable speed PCP. The water pump has a maximum capacity of 2.18 m³/h with a safety switch to turn off the pump at the maximum discharge pressure of 10 bar gauge pressure.

Downstream the PCP, there is a water bypass line which is deigned to divert part of fluid back to the water tank when lower water flow rate in the multiphase flow test line is desired. Single water flow flowing into the multiphase flow test line is metered using an electromagnetic meter (Endress+Hauser's Promag 50P DN 50).

(3) Liquid cooling and heating system

A bath circulator with external coils for heat exchange (HAAKE Phoenix II circulator, manufactured by Thermo Fisher Scientific) is installed to control the temperature of oil and water. The coils are placed inside the oil and water tanks and connected with the bath unit through insulated hoses. A mixture of deionized water and ethylene glycol (4:1) was used as the bath liquid for the present study. The bath liquid temperature can range from -5 to +150 °C.

By running cold or hot bath liquid in the coils, the temperature of oil and/or water can be controlled. Single liquid flow can be circulated through the bypass line to help reach thermal equilibrium. A hand-held thermocouple thermometer with a liquid crystal display (LCD) was used to monitor oil/water temperature. Besides, the temperatures can be monitored by in-line temperature transducers during circulation of single oil and/or water through the bypass lines.

(4) Separation system

Bulk flow of multiphase fluids are collected into a separator of 0.5 m³ capacity. The separator is a rectangular shaped tank with viewing windows to allow monitoring liquid levels and separation process. A residence time of around

12~20 hours was given for complete separation of oil and water after a series of experimental runs.

On separation of the phases in the separator, water is pumped back to the water tank. Oil is pumped to a medium storage tank first. This tank is used for further separation of oil and water as well as for temporary storage of oil before further pumping it back to the oil tank. Care was taken when pumping water and oil back to the respective tanks. Proper amounts of oil and water were always left in the separator to avoid pumping water into the oil tank or oil into the water tank.

(5) Multiphase flow test line

The multiphase flow test line is made up of Perspex and clear PVC pipes with 26-mm internal diameter. The level of the multiphase flow line was checked and adjusted to horizontal by an automatic level (GEO-FENNEL No. 10 32x, level accuracy: $\pm 0.5''$). The whole flow test line can be divided into three major sections – the flow development section after the junction, the visual observation and pressure drop measurement section, and the fluids sampling section.

(1) The visual observation and pressure drop measurement section

Downstream the fluids mixing point, two gauge pressure transducers and one differential pressure transducer are installed in the multiphase flow test line fabricated from a Perspex pipe. The two gauge pressure transducers are positioned at 2.04 m and 3.77 m from the water injection junction. The two gauge pressure transducers used are WIKA pressure transmitter model S-11, with gauge pressure range 0~6 bar, over pressure limit 35 bar, accuracy $\leq \pm 0.25\%$ of span, and time response ≤ 10 ms. The differential pressure transducer used is GE Sensing DRUCK PMP 4170, with pressure range -200 to +200 mbar and accuracy $\pm 0.08\%$ of full scale. The high port and low port of the differential pressure transducer are connected to the pressure-tapping points where the two gauge pressure transducers are connected to. To prevent

overload on one side of the differential pressure transducer, a connection between the high port and low port is fitted with an isolating bypass.

Both the gauge pressure transducers and the differential pressure transducer were used in our experimental runs associated with relatively small pressure drops, which includes our major tests when water is the continuous phase. Only the gauge pressure transducers were used in experimental runs associated with high pressure drop such as single oil flow tests at higher oil flow rates.

During tests, the flow was recorded via observation section upstream the second pressure transducer using a digital HD video camera recorder (Sony HDR-CX550V). The FX mode of the high definition image quality (HD) was selected and movies were recorded with AVCHD 1920×1080i format and frame rate of 60 f/s. In the present study, the videos were used to qualitatively identify flow regimes. An optical matching box was not used. However, a transparent box filled with water to reduce optical distortion caused by refraction is recommended.

(2) Fluids sampling section

A section for the measurement of water holdup is located downstream the pressure drop measurement and flow pattern observation section in the multiphase flow test line. This section (see Figure 3-3) was newly designed in the present study. It contains two ball valves placed 1.04 m (40d) apart. The upstream one, BV1, is a three way T-port ball valve which can divert the flow to the bypass line when shutting off the flow in the main flow line. The downstream one, BV2, is a two way straight ball valve. A sampling port line with a ball valve, BV3, through which the sampling fluid flows into volume measurement equipment, is connected to the middle of the horizontal section. Two air hoses connecting air supply are placed near the two valves to flush liquids out. The liquids are collected into a graduated cylinder (capacity: 1 000 ml, precision: ± 10 ml) for each experimental run.

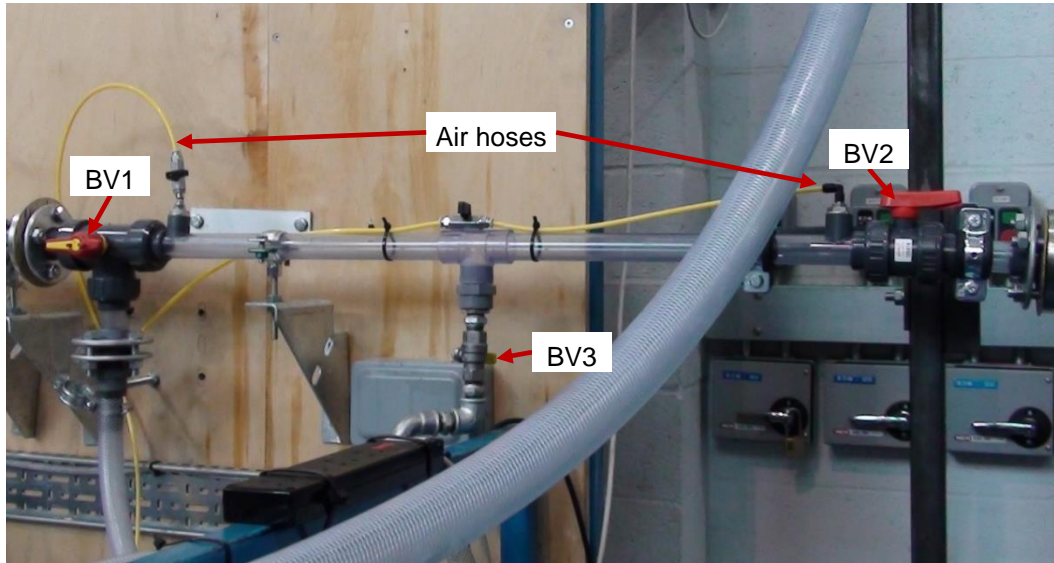


Figure 3-3 Pictures of the fluid sampling section.

The whole volume of fluid that would be trapped in the sampling section, $V1$, was calibrated with water. It is noted that the collected volume of trapped water includes a small section of volume in the sampling port line above the valve BV3. This volume, $V2$, was calibrated with water before the branches were connected together. Thus, the volume of the horizontal sampling section, $V3$, is

$$V3 = V1 - V2 \quad (3-1)$$

For water-assisted heavy oil flow, as water is always the continuous phase, the small section in the vertical port line above the valve BV3 is occupied by water. Denoting $V4$ as the collected water volume of two-phase liquids, the volume of water in the horizontal sampling section, $V5$, can be expressed as

$$V5 = V4 - V2 \quad (3-2)$$

Thus the water holdup, H_w , can be calculated as

$$H_w = \frac{V4 - V2}{V1 - V2} \quad (3-3)$$

The oil holdup can be obtained following

$$H_o = 1 - H_w \quad (3-4)$$

(6) Data acquisition system

Raw data acquired from online instrumentations, including the flowmeters, pressure transducers, differential pressure transducer, and temperature sensors are saved to a desktop computer using a National Instruments (NI) LabView data acquisition system at a sampling frequency of 250 Hz. The NI Compact DAQ chassis 9172 is used to control the timing, synchronization, and data transfer between NI C Series I/O modules and the external computer. The NI C Series modules used are NI 9205 for analogue input signals from flow meters and pressure transducers, NI 9211 for thermocouple input, and NI 9401 for digital output (5 V/TTL) to achieve arming or disarming the Emergency Stop circuit.

The fluid samples are measured offline. For each sample, the volume of water was read and taken note at intervals of several hours until the reading became constant with time. Usually, the reading became constant after around 48 hours after complete separation of oil and water.

3.4 Experimental procedure and runs

3.4.1 Experimental procedure

The objective of experiments is to study the flow characteristics of high-viscosity oil-water two-phase flow. The three major aspects of the study, data for which were obtained in each experimental run, were flow pattern, pressure gradient, and water holdup.

The preparation before a series of tests started with pumping oil and water back to respective tanks from the separator after complete separation. The liquid cooling and heating system was used to cool or heat the liquids if the desired temperatures of liquids were not the same as room temperature. The valves along the flow loop were checked.

After the preparation, a series of experimental runs were conducted following a procedure introduced as below:

- 1) Start the data acquisition system. Check if the desired oil temperature/viscosity is achieved; if achieved, go to the next step; if not, allow more time for the chilling or heating process of oil (use the bypass line to circulate oil to achieve homogeneous oil temperature).
- 2) Inject oil into the multiphase flow test line. The desired oil flow rate, U_{so} , is adjusted by controlling the speed of the PCP pump. Then inject water into the multiphase flow test line. The desired water flow rate, U_{sw} is adjusted by controlling the speed of the PCP pump; the valves on the water bypass line are adjusted together when low water flow rate is desired. This sequence of injection was applied until the inversion from oil-continuous flow regime to annular-water-continuous flow regime was observed. Once the inversion was achieved, the opposite sequence of injection (i.e., inject water first followed by oil injection) was applied in the experiments for the practical purpose of saving oil.
- 3) Collect data from online instrumentations for a duration of 30 seconds when the real-time liquid flow rates and differential pressure displayed on the Labview are stable (depending on the flow rates, the time for flow to reach stable varied. The slower the flow, the longer was the time required to obtain stable conditions. Normally, the two-phase flow reach stable after a duration in which the whole test line fluid is displaced by the mixed fluid, varying between 5- 30s). At the same time, record flow behaviours at the visual observation section with the high-speed camcorder.
- 4) Start collecting a sample of fluids for this experimental run once the data collection in 4) is finished. The procedure to collect a sample is as follows.
 - i. Close the straight port/open the L port of the three way ball valve upstream the sampling section, and at the same time close the two way ball valve downstream the sampling section. The flow is

then trapped between the two valves. Switch off the oil and water pumps.

- ii. Collect the sample into a graduated cylinder by opening the valve on the sampling port line. After most of the water flows into the cylinder by gravity, using the air from compressor to flush the remaining fluids into the cylinder. Collect as much fluids as possible. The collection can be finished when no water is visually seen and the drainage of the remained thin oil film becomes tedious.
 - iii. Close the valve on the sampling port line. Then open the straight port/close the L port of the three way ball valve upstream the sampling section, and open the two way ball valve downstream the sampling section to prepare for the next sample collection.
- 5) Repeat from Step 2) to change to another flow condition (change water flow rate at a fixed oil flow rate first to cover different water flow rates, then change oil flow rate to cover different oil flow rates).

It is noted that for the water-continuous-flow, the injection sequence showed little effect on the developed flow patterns or the measured pressure drop. However, it is an open question that whether the injection sequence would affect the inversion occurrence. This study investigated only the injection sequence of adding water into the oil flow which is the most likely scenario of producing water-lubricated heavy oil flow in industrial applications. The influence of injection sequence on the inversion from oil-continuous to annular-water-continuous is worth checking in any future study.

3.4.2 Experimental runs

Two different oil viscosities were investigated in the present study. At least four different oil flow rates were tested for each oil viscosity. The water flow rate or the input water volume fraction was varied under a constant oil flow rate. Five to ten different water flow rates in the range of 0.04 to 1.2 m/s, apart from a water

flow rate of zero, were tested for a constant oil flow rate. An outline of experimental runs is given in Table 3-1.

Table 3-1 Summary of experimental runs.

Oil temperature (°C)	Oil viscosity (cP)	Oil density (kg/m ³)	U_{so} (m/s)	U_{sw} (m/s)
~11.5	5 600 cP	910	0.04	0, 0.07-1.18
			0.11	0, 0.07-1.18
			0.20	0, 0.07-1.18
			0.39	0.1-1.18
			0.54	0.2-1.18
~20.5	3 300 cP	905	0.06	0, 0.04-1.18
			0.11	0, 0.04-1.18
			0.21	0, 0.05-1.18
			0.54	0.2-1.18

3.5 Assurance of experimental system

3.5.1 Pressure signals

It is of importance to evaluate the pressure transducers as the pressure gradient is one of the important parameters for analysis. The pressure transducers were calibrated before experimental runs (see Appendix C). The performance of pressure transducers was further checked with single oil flow data.

A comparison of pressure gradients of single oil flow obtained from the two gauge pressure transducers and the differential pressure transducer is shown in Table 3-2. The pressure gradients obtained agree well. The difference varies from 0 to 0.4 kPa/m, corresponding to 0 to 7 mbar over the distance of the pressure transducers, which is within the accuracy range of the pressure transducers.

Table 3-2 A comparison of pressure gradients obtained from the two gauge pressure transducers and the differential pressure transducer.

μ_o (cP)	U_{so} (m/s)	Pressure gradient ^{a)} (kPa/m)	Pressure gradient ^{b)} (kPa/m)
3 090	0.060	9.147	9.221
	0.081	12.158	12.251
	0.101	14.912	15.029
	0.122	17.720	17.875
	0.148	20.944	21.082
3 300	0.051	10.571	10.556
	0.097	15.783	15.945
	0.205	31.214	31.301

^{a)} From the two gauge pressure transducers;

^{b)} From the differential pressure transducer;

The single oil flow in our experiments is always laminar flow as the oil viscosity is very high ranging from 3 000 cP to 5 600 cP with corresponding Reynolds number in the range of 0.2 to 5. The experimental results from the two gauge pressure transducers were compared to theoretical pressure drops calculated from the Darcy–Weisbach equation for laminar flow as shown in Figure 3-4. A good agreement is shown between the measurements and the calculated theoretical counterparts for the lower oil viscosity investigated. For higher oil viscosity, slight variance can be observed. The measured pressure gradient is higher than the calculated value at low oil flow rate, close to its counterpart at medium oil flow rate, and lower than its counterpart at higher oil flow rate. However, there is no evidence to doubt the accuracy of the pressure sensors. The oil temperature varied slightly for a fixed experimental temperature during experiments, hence the oil viscosity. Also, another possible source for this kind of deviation is that the local heating caused by friction at higher flow rate can reduce the oil viscosity slightly.

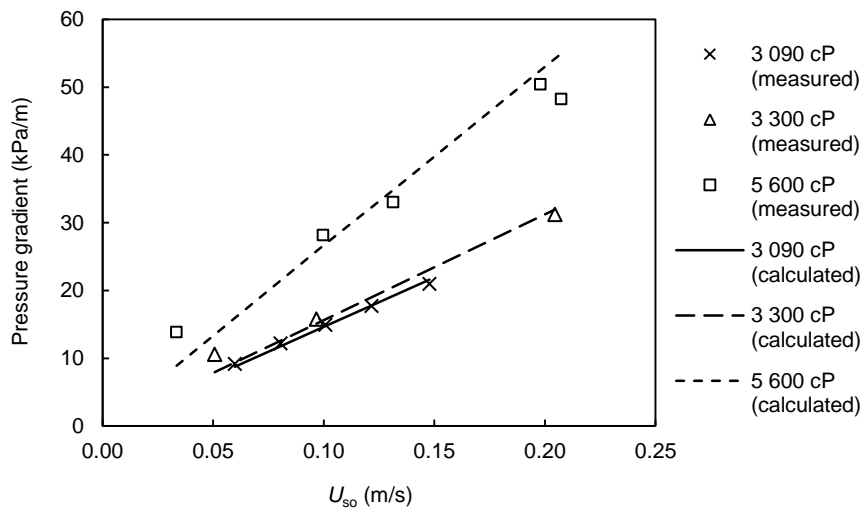


Figure 3-4 A comparison between measured and calculated pressure gradients of single oil flow.

3.5.2 Oil viscosity

The oil used in the present study is mineral oil CYL 680. The oil has a wide range of viscosity depending on temperature. During experiments, the Coriolis flow meter gives real-time measurements of oil viscosity. Besides readings from the Coriolis flow meter, oil viscosity was double checked on the bench with a rheometer system (Malvern Kinexus pro+).

The rheometer system consists of a rheometer, a temperature control unit and its instrument software. The main part is a rheometer, including the base unit and the measuring geometry. It applies controlled shear deformation to a sample under test to enable measurement of viscosity. The measuring geometry used in the present study is a cup and bob, i.e., concentric cylinders. The viscosity of the oil at different temperatures was measured. At each temperature, an increasing shear rate from 1 to 500 s^{-1} was applied to obtain the oil's viscosity profile at different shear rates. Figure 3-5 shows measured oil viscosity profiles with shear rate at various temperatures. It is observed that at 30 and 40 $^{\circ}\text{C}$, the oil viscosity is nearly constant for the wide range of shear rate investigated. Below 30 $^{\circ}\text{C}$, the oil viscosity shows little change with increase of shear rate from 1 s^{-1} to 200 s^{-1} , while noticeable drop above a shear rate of 200 s^{-1} . This might be caused by the local heating effect caused by friction at high shear rate (see Schramm, 1994).

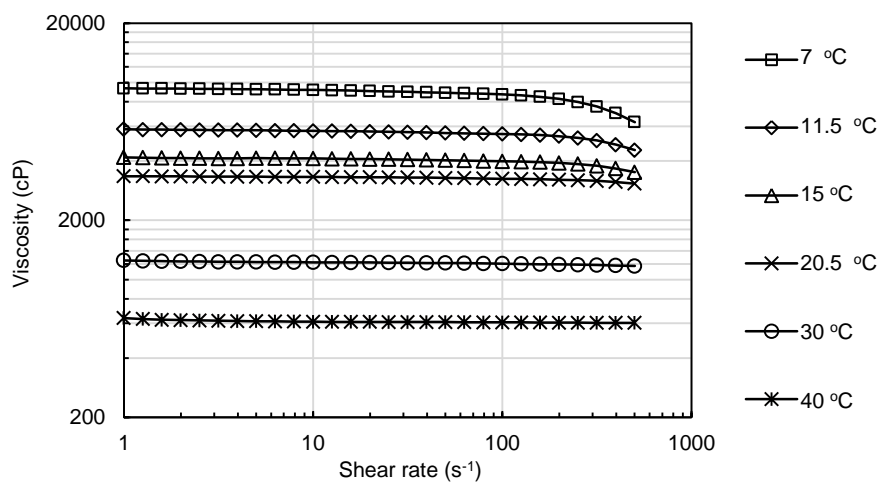


Figure 3-5 Oil viscosity with shear rate at various temperatures.

The shear rate at the inner wall of pipe can be described with

$$\dot{\gamma} = \frac{32Q}{\pi D^3} = \frac{8V}{D} \quad (3-5)$$

The present experiments were conducted in two average oil temperatures of 11.5 and 20.5 °C. The oil velocity investigated ranged from 0.04 to 0.54 m/s. Correspondingly, the shear rate ranged from 12 to 170 s⁻¹. Referring to Figure 3-5, the oil viscosity change between 12 and 170 s⁻¹ is small comparing to the average viscosity (< 5% of the average viscosity).

Figure 3-6 shows the oil viscosity versus the temperature. The oil temperature was controlled by the heating and cooling system as introduced in the experimental setup (see Section 3.3). Due to heat transfer with the ambient and the local heating from friction, the oil temperature varied slightly for a set temperature in the experiments (normally within ±1°C). Therefore, the oil viscosity also varied. When the oil viscosity is mentioned in the thesis, it always means the nominal oil viscosity.

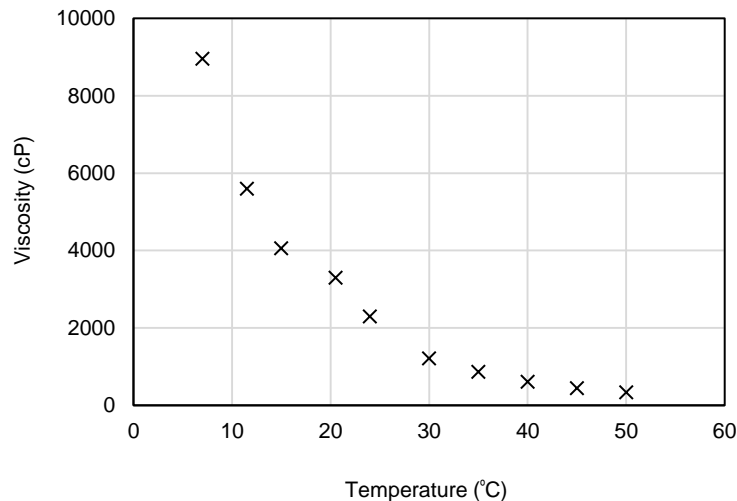


Figure 3-6 Oil viscosity versus temperature.

3.5.3 Accuracy of the sampling measurement

The whole volume of fluid that would be trapped in the sampling section, V_1 , was calibrated with water by running single water flow in the flow loop. The volumes of samples obtained for three different water flow rates varied within 10 ml as shown in Figure 3-7. As the whole volume obtained included a small section of volume, V_2 , in the sampling port line, that volume was calibrated too with water to obtain the volume in the horizontal sampling section. The calibrated V_1 and V_2 were around 538 ml and 28 ml respectively. Thus a volume of 510 ml was used as the whole volume of the horizontal sampling section for the calculation of water holdup as introduced in Section 3.3.

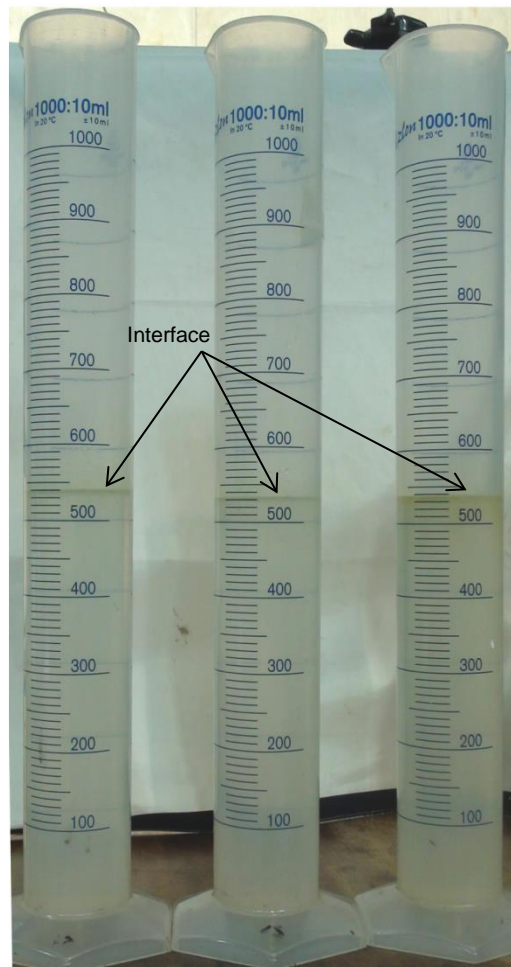


Figure 3-7 Collected samples during calibration of the whole sampling section volume. (a) $U_{sw} = 0.6$ m/s; (b) $U_{sw} = 0.8$ m/s; (c) $U_{sw} = 1.0$ m/s.

Figure 3-8 shows a picture of fluids samples obtained during oil-water two-phase flow runs. When the two-phase flow was trapped in the sampling section, the flow became stratified quickly with water at the bottom and oil at the top. By opening the valve in the sampling port line, most of the water ran out under gravitational force. Then air was used to flush the remaining liquids out. As the oil is very viscous, it was found to be difficult to drain the oil out of the sampling section completely in moderate sampling time. When most of the oil was flushed out, the drainage of the remained thin oil film in the pipe becomes tedious. The sampling process was stopped when no/little water was observed in the sampling section and the oil remained was in the form of thin film (see Figure 3-9). This can explain why the whole volume collected for two-phase flow was always lower than the calibrated whole volume. Clearly the volume of the collected oil was not accurate. However, the volume of the collected water can reasonably represent the in situ water volume of the sampling section.

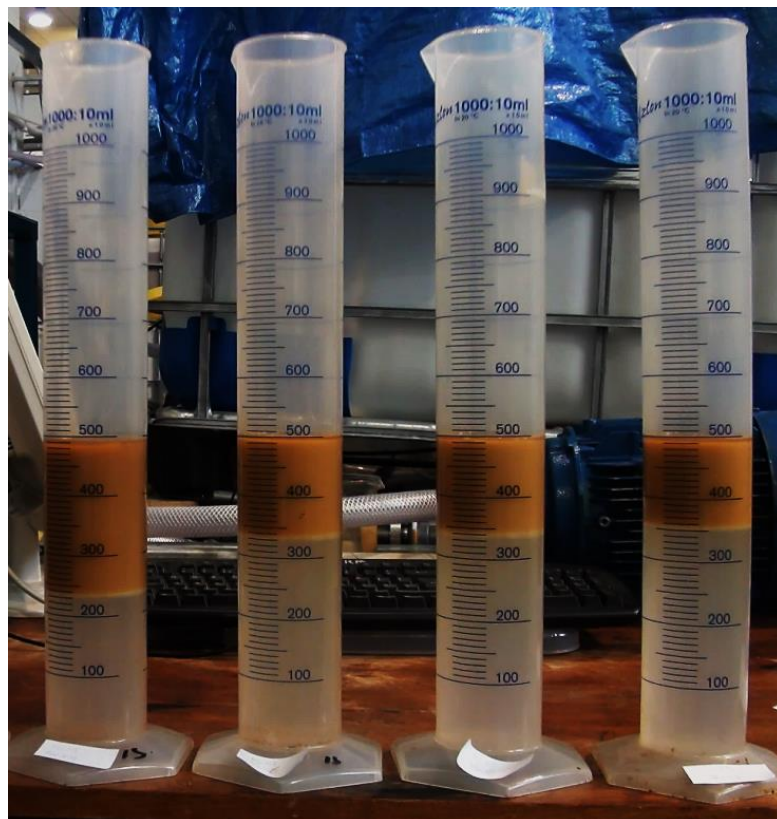


Figure 3-8 Collected samples of two-phase flow. Flow condition: $\mu_o=5\ 000$ cP; $U_{so}=0.54$ m/s; $U_{sw} = 0.40$ m/s, 0.59 m/s, 0.77 m/s, and 0.99 m/s from left to right.



Figure 3-9 Sampling section with some oil remained after a sample collection.

The samples were collected into graduated cylinders. The precision of the graduated cylinders used is ± 10 ml. In order to read the volume accurately, the observation was taken at an eye level and read at the bottom of a meniscus of the water level. The volume of water for each sample was taken note at intervals of several hours since its collection until the reading became constant on complete separation of oil and water (usually waited for 48 to 52 hours). Uncertainties in the total volume of the trapped fluids and the collected water volume can also affect the accuracy of results. The total volume of the trapped fluids varied within 10ml in three runs of the calibration. The sampling process was stopped when no/little water was observed in the sampling section to reduce the uncertainty in the collected water volume. Assuming a total error of ± 30 ml in the measured water volume, the relative error of this sampling method is estimated approximately within $\pm 6\%$ (± 30 ml/510 ml).

3.5.4 Repeatability of the experiments

To check the repeatability of the present experiments, some experimental runs with similar flow conditions were conducted twice. Table 3-2 lists the measured pressure gradients of comparable experimental runs. It is noted that it is difficult to have exactly same flow conditions as the flow rates were controlled manually

Table 3-3 A comparison of pressure gradients of two-phase flow with similar flow conditions.

Run	U_m (m/s)	U_{so} (m/s)	U_{sw} (m/s)	Oil temperature (°C)	Pressure gradient (kPa/m)
1-a	0.587	0.403	0.184	12.45	1.841
1-b	0.582	0.387	0.196	11.05	1.944
2-a	1.091	0.096	0.994	12.05	2.876
2-b	1.055	0.105	0.950	10.98	2.659

and the oil average temperature varied due to heat transfer with the ambient and local heating from friction. Nevertheless, a reasonable repeatability of the pressure gradient measurement is demonstrated.

3.6 Summary

The experimental setup is introduced in this chapter. Check of the experimental system with preliminary experimental results is presented. The experimental procedure and runs are introduced. Discussions of experimental results are presented in the following Chapter 4.

4 EXPERIMENTAL RESULTS

4.1 Introduction

Raw data, including pressure signals and recorded videos of flow regimes, from previous experiments (Al-Awadi, 2011; Zorgani, 2012; Alagbe, 2013) were collated. These data and data from the present experiments (including pressure signals, recorded videos of flow regimes, and water holdup) constitute the data base for our analysis.

Experimental results are discussed in this chapter. The discussions are divided into four aspects: (1) flow patterns; (2) inversion occurrence; (3) water holdup of water-lubricated flow; and (4) pressure gradient of water-lubricated flow.

4.2 Experimental data bank

Al-Awadi (2011), Zorgani (2012) and Alagbe (2013) performed experiments on high-viscosity oil-water flow in a 1 inch flow pipeline. Pressure gradients and flow patterns were obtained from the above studies. The present study carried out experiments in the upgraded 1 inch flow pipeline. Pressure gradients, flow patterns, and water holdups were obtained from the present study. All the experimental data were collated for analysis. An outline of the collated data is shown in Table 4-1. Detailed data can be found in Appendix A.

Table 4-1 Collated experimental data on high-viscosity oil-water flow in 1 inch horizontal pipe.

Data set ^{a)}	Oil	Nominal oil viscosity (cP)	Oil density (kg/m ³)	U_{so} (m/s)	U_{sw} (m/s)	Measurements
A	CYL1000	3 800	920	0.06, 0.1, 0.15, 0.2, 0.57	0, 0.01~1.0	Pressure drop; flow patterns
		8 300	931	0.3	0, 0.01~1.0	
		13 200	935	0.06, 0.1, 0.14	0, 0.01~0.3	
		16 000	938	0.1	0, 0.02~0.3	
B	CYL 680	5 000	910	0.1	0, 0.02~0.1	Pressure drop; flow patterns
C	CYL 680	3 700	906	0.1, 0.15, 0.35	0, 0.2~1.0	Pressure drop; flow patterns
		5 000	910	0.06, 0.1, 0.2, 0.4	0, 0.2~1.0	
		7 100	916	0.06, 0.1, 0.2, 0.4	0, 0.2~1.0	
D	CYL 680	3 300	905	0.06, 0.11, 0.21, 0.54	0, 0.07-1.18	Pressure drop; flow patterns; water holdup
		5 000	910	0.04, 0.11, 0.20, 0.39, 0.54	0, 0.04-1.18	

^{a)} Experimental data from Al-Awadi (2011); B- experimental data from Zorgani (2012); C- experimental data from Alagbe (2013); D-experimental data from the present study.

4.3 Flow patterns

4.3.1 Flow patterns observed in experiments

The identification of flow patterns is mainly based on visual observation during experiments and recorded videos. Pressure gradient values are used as reference. The main flow patterns are classified as follows and the photographs of typical flow patterns observed are shown in Figure 4-1 and 4-2.

Oil-Continuous (OC) OC is when oil is the dominant continuous phase in the pipe. It can be further divided into two specific regimes: a) no water is visually seen; water might distribute inside the oil in the form of bubbles or drops (see Figure 4-1 (a) and Figure 4-2 (a1)); and b) small streams of water could be seen at irregular intervals (see Figure 4-2 (a2)).

Inversion (Inv) Inv is a transitional flow pattern from oil-continuous to annular-water-continuous; continuous water stream, but not in the form of strictly annular-continuous, begins to form at this stage. The most frequently observed phase configurations are shown in Figure 4-1 (b1, b2) and Figure 4-2 (b1, b2). Continuous water stream and oil stream moves forward spirally; dual continuous water and oil alternating with just oil stream could be seen sometimes, which is an unstable transition pattern.

Core Annular Flow (CAF) CAF is a most frequently observed flow pattern in experiments. A continuous oil core flows within annular continuous water. The interface of the two phases is normally wavy, with different wave lengths in different flow conditions (see Figure 4-1 (c1), (c2) and Figure 4-2 (c)). Different degree of oil fouling ripples adjacent to the internal wall of the pipe can be clearly observed.

Oil Plugs in Water (OPL) OPL is like a flow pattern when the CAF is cut into pieces with moderate lengths. Oil plugs flow forward within the water with some intervals one by one (see Figure 4-1 (d) and Figure 4-2 (d)). It is a flow pattern following the CAF with increase of the water flow rate, or a flow pattern after the

inversion under low oil flow rates. Similar to CAF, oil fouling film on the pipe wall can be observed.

Dispersed Oil Lumps in Water (OLP) OLP is characterised with indefinite and irregular oil lumps inside the continuous water (see Figure 4-1 (e1), (e2)). With increasing water flow rate, larger oil lumps are broken further into relatively smaller oil lumps. The term of dispersed flow which is widely used in low-viscosity oil-water flow is adopted in some studies to describe this kind of phase configuration (see Sotgia et al, 2008; Grassi et al., 2008). It is noted that the dispersed phase is normally in the form of drops in low-viscosity oil-water flow while the dispersed oil is rarely in the form of drops in the present study due to the high-viscosity of the oil phase. The term of dispersed oil lumps is used in the present study for the purpose of distinguishing the dispersed oil in water of high-viscosity oils from that of low-viscosity oils.

Figure 4-3 shows sketches of the different flow patterns described above. As mentioned above that oil fouling ripples adjacent to the internal wall of the pipe can be clearly observed in the experiments, the oil fouling on the pipe wall is depicted in the sketches to emphasize this phenomenon in high-viscosity oil-water flow.

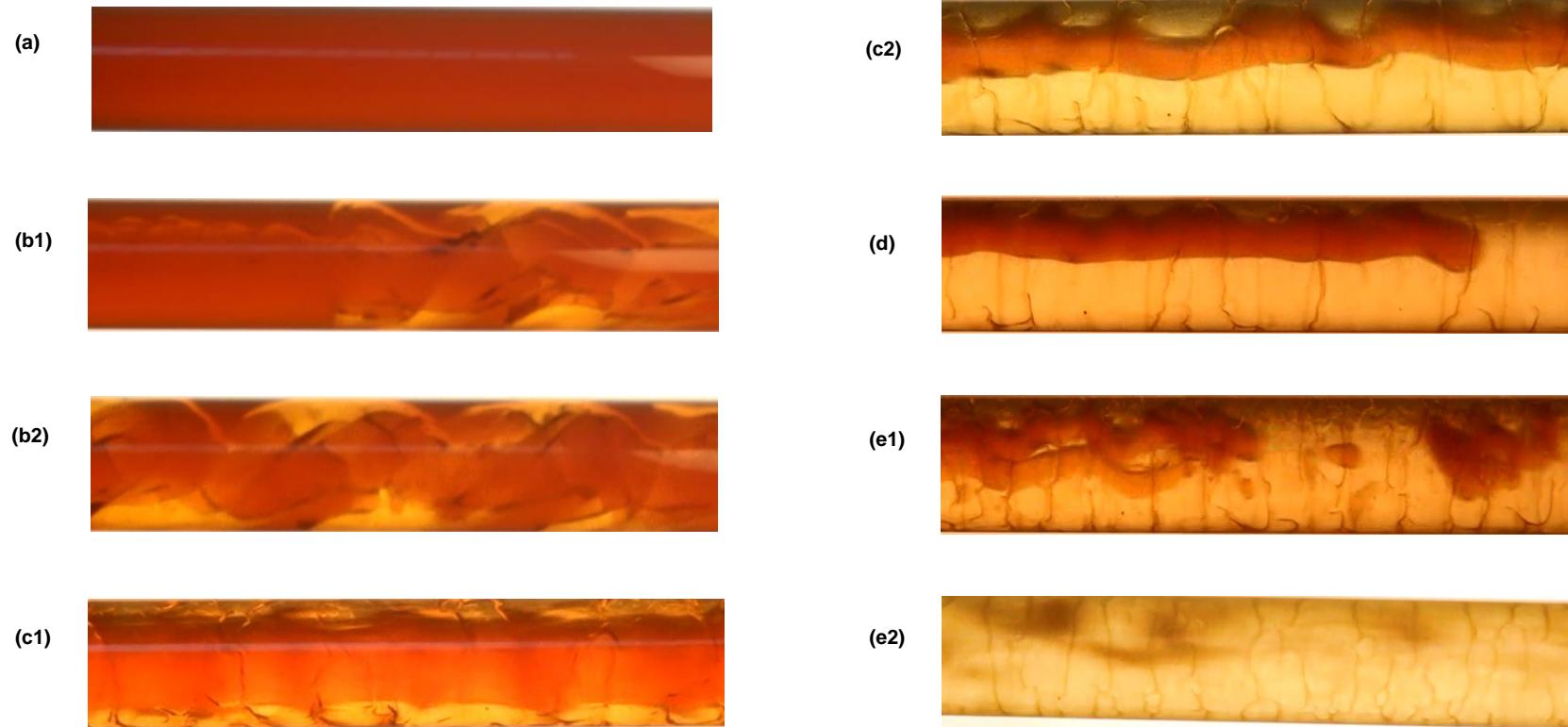


Figure 4-1 Photographs of flow patterns observed (CYL 680). The flow patterns are: a-OC; b1, b2-Inv; c1, c2-CAF; d-OPL; e1, e2-OLP.

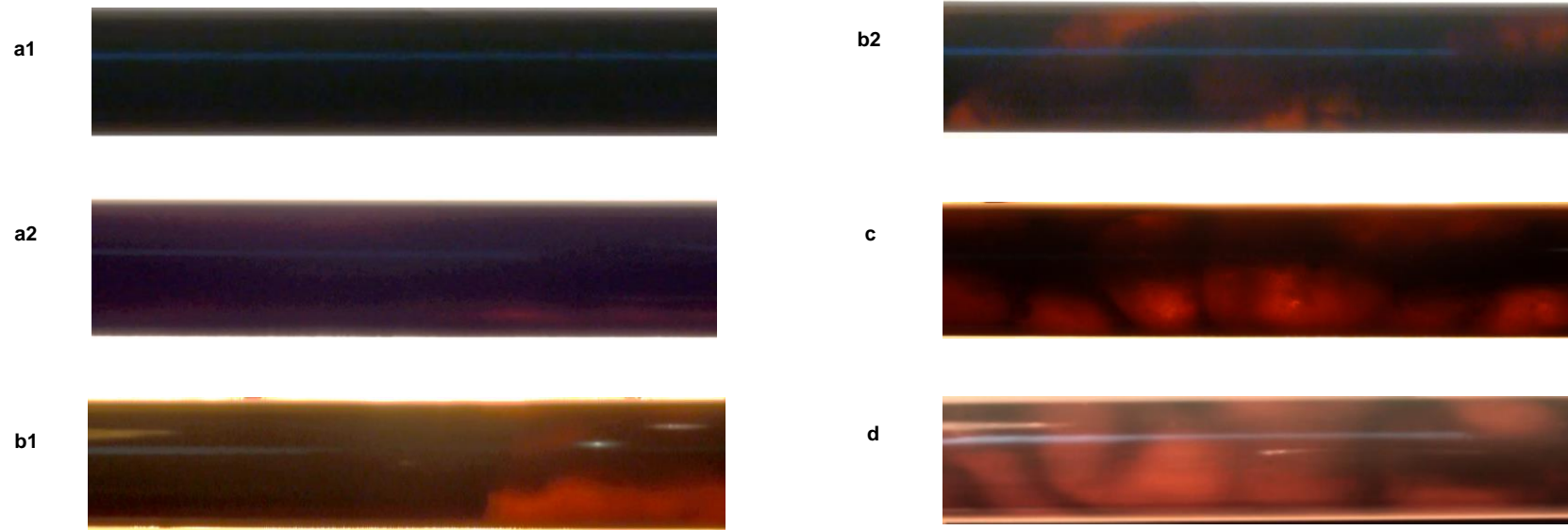


Figure 4-2 Photographs of flow patterns observed (CYL 1000). The flow patterns are: a1, a2-OC; b1, b2-Inv; c-CAF; d-OPL.

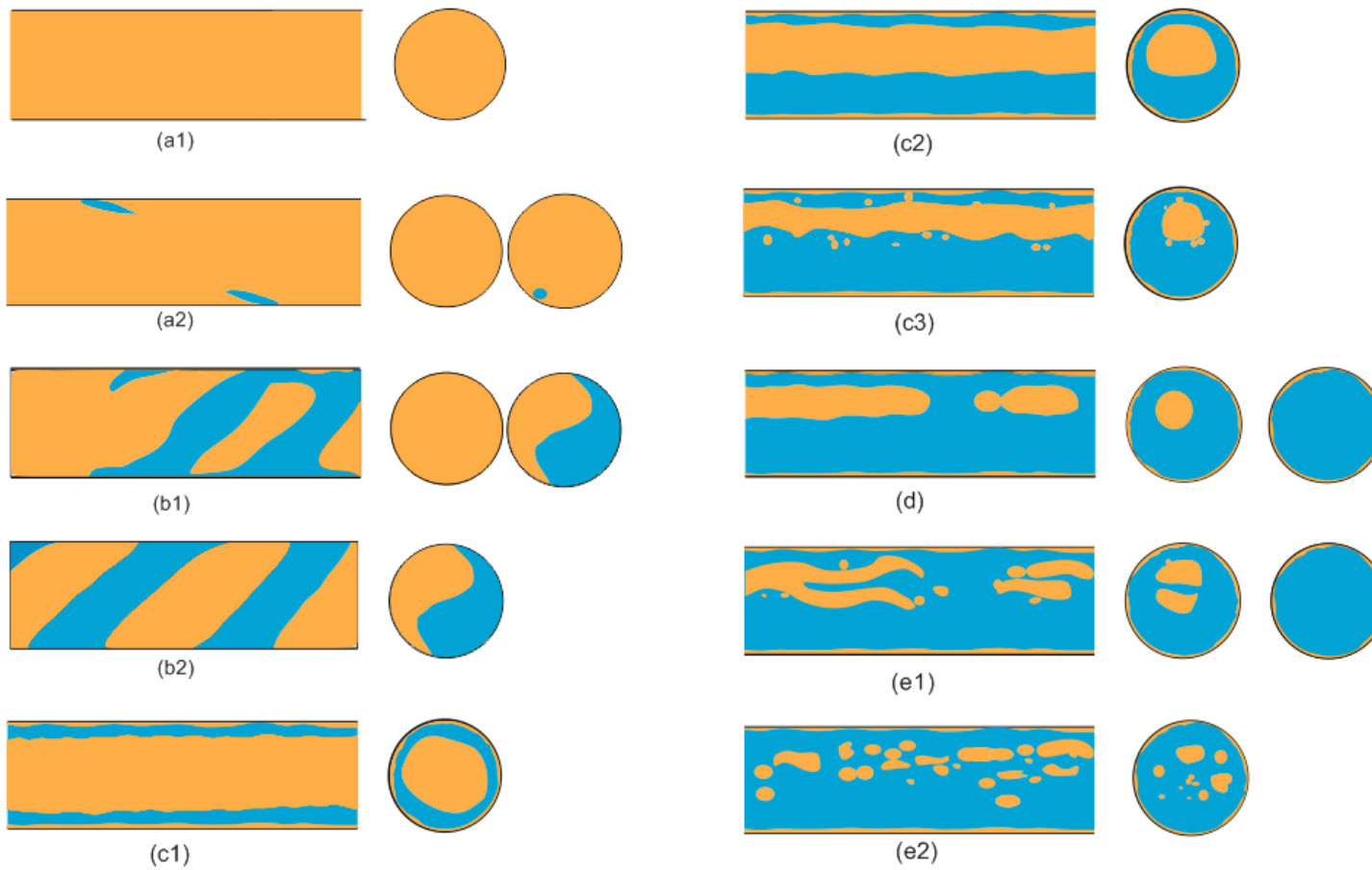


Figure 4-3 Sketches of flow patterns observed. The flow patterns are: a1, a2-OC; b1, b2-Inv; c1, c2, c3-CAF; d-OPL; e1, e2-OLP.

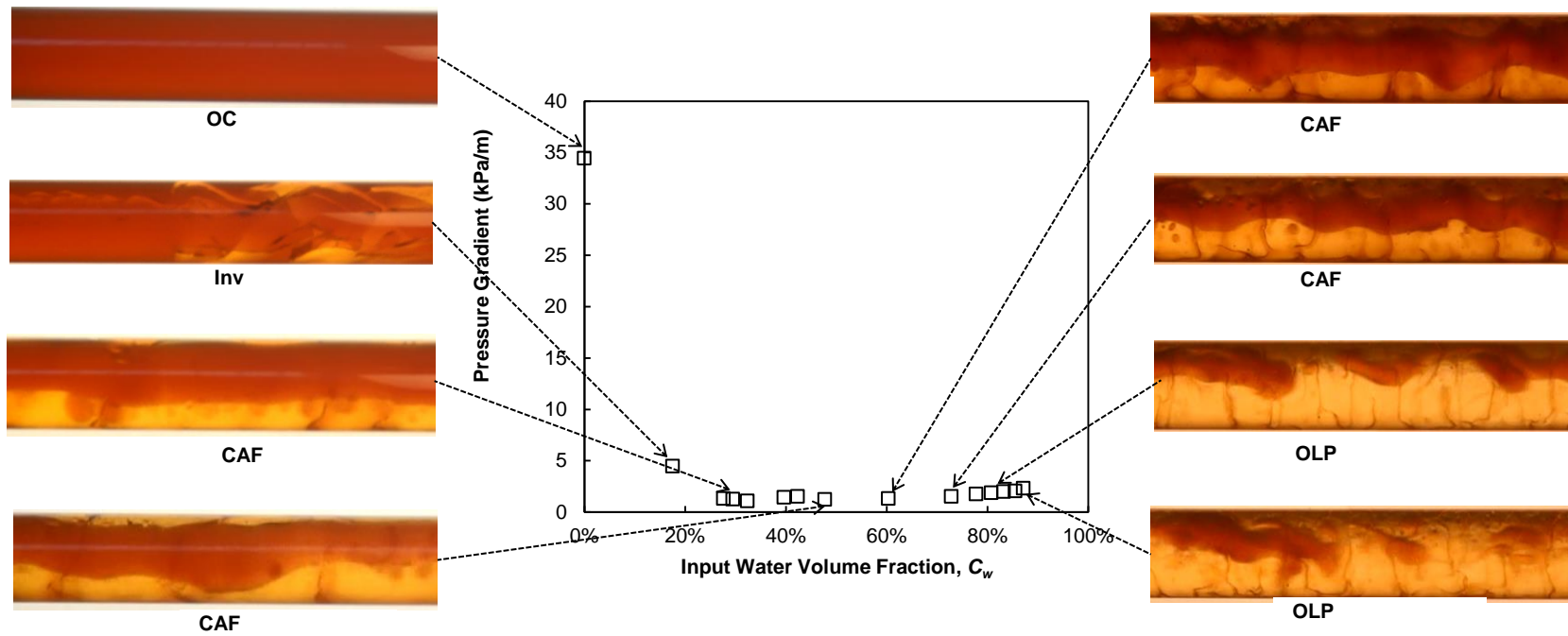

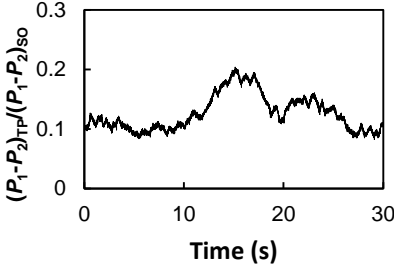
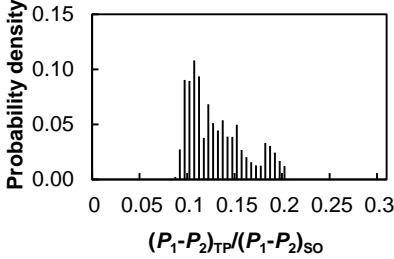

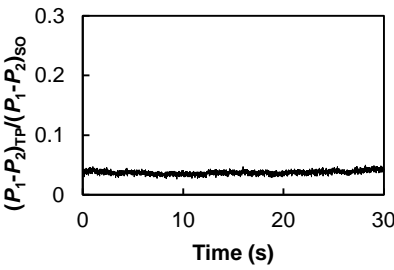
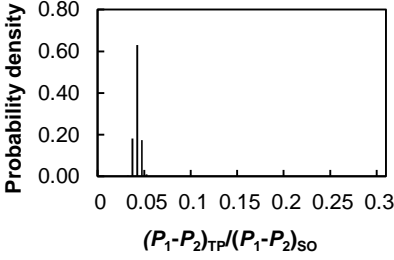

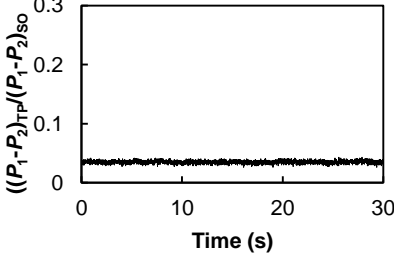
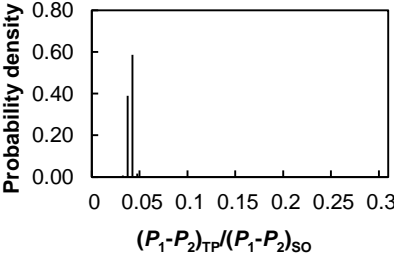

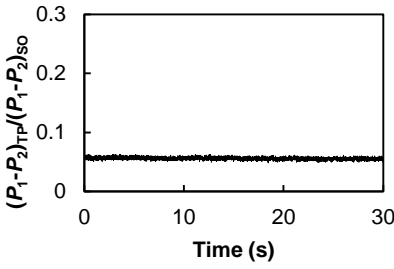
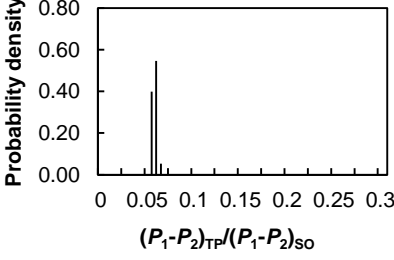


Figure 4-4 A typical average pressure gradient trend with input water volume fraction and the corresponding flow patterns (CYL 680, $U_{so}=0.1\text{m/s}$, $\mu_o=5\ 000\ \text{cP}$).

A typical average pressure gradient trend with increase of input water volume fraction and the corresponding flow patterns are shown in Figure 4-4. The average pressure gradient is obtained from 30 seconds of logged pressure signals sampled at 250 Hz. For a constant oil flow rate, with increase of the input water volume fraction, inversion from oil-continuous to core annular flow occurs at a certain amount of water with a sharp pressure gradient decrease. With further increase in water flow rate, the flow pattern develops from core annular flow to dispersed oil lumps in water; the pressure gradient in general shows slight increase.

Table 4-2 shows the photographs and histograms of pressure drop signals of different flow patterns. The pressure drop signals of two-phase flow are normalised with respect to that of single oil flow $((P_1-P_2)_{TP}/(P_1-P_2)_{SO})$ for a comparative study. To obtain a histogram, the normalised pressure drops in 30 seconds are binned in the range between 0 and 0.3 with an interval of 0.005. Then the values fall into each interval are counted. A rectangle is erected over the bin with height proportional to the probability density, i.e., the number of cases in each bin divided by the total samples, i.e., 7500. The pressure drop of the inversion flow regime demonstrates relatively higher variation than the other flow patterns. This is associated with the transient characteristic of the inversion flow regime. A peak probability density at the normalised pressure drop around 0.05 is exhibited for flow patterns beyond the inversion. This indicates that the pressure drop for flow patterns beyond the inversion has no high variations. The histograms of pressure drops for the core annular flow and dispersed oil lumps in water are similar. It is demonstrated that the pressure signals can be used to distinguish the inversion from oil-continuous flow to water-continuous flow. However, it is not viable to distinguish different flow patterns in water-continuous region beyond the inversion from the pressure signals.

Table 4-2 Photographs and histograms of pressure drop signals of different flow patterns (CYL 680, $U_{so}=0.1\text{m/s}$, $\mu_o=5\ 000\ \text{cP}$).

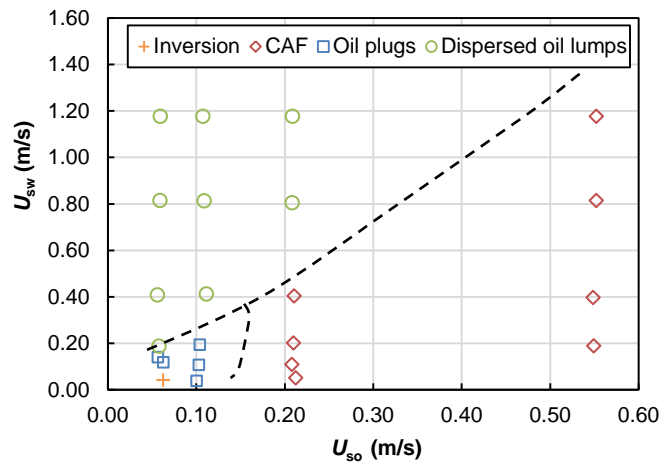
Flow patterns	Dimensionless pressure gradient	Histogram of dimensionless pressure drop
 <p>Inv ($U_{sw}=0.023\text{m/s}$)</p>	 <p>$(P_1-P_2)_{TP}/(P_1-P_2)_{SO}$</p> <p>Time (s)</p>	 <p>Probability density</p> <p>$(P_1-P_2)_{TP}/(P_1-P_2)_{SO}$</p>
 <p>CAF ($U_{sw}=0.04\text{m/s}$)</p>	 <p>$(P_1-P_2)_{TP}/(P_1-P_2)_{SO}$</p> <p>Time (s)</p>	 <p>Probability density</p> <p>$(P_1-P_2)_{TP}/(P_1-P_2)_{SO}$</p>
 <p>CAF&OF ($U_{sw}=0.1\text{m/s}$)</p>	 <p>$(P_1-P_2)_{TP}/(P_1-P_2)_{SO}$</p> <p>Time (s)</p>	 <p>Probability density</p> <p>$(P_1-P_2)_{TP}/(P_1-P_2)_{SO}$</p>
 <p>OLP&OF ($U_{sw}=0.6\text{m/s}$)</p>	 <p>$(P_1-P_2)_{TP}/(P_1-P_2)_{SO}$</p> <p>Time (s)</p>	 <p>Probability density</p> <p>$(P_1-P_2)_{TP}/(P_1-P_2)_{SO}$</p>

4.3.2 Flow pattern maps

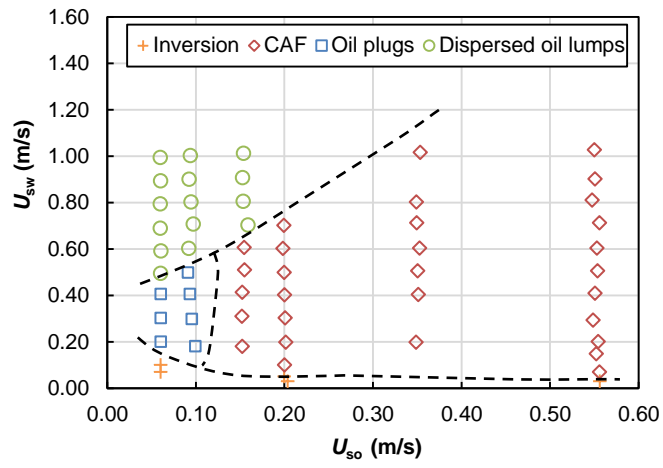
(1) Flow pattern maps of the present study

Flow pattern maps produced for the experiments with the oil CYL 680 in four different nominal oil viscosities are shown in Figure 4-5. The major flow patterns observed are consistent, featuring inversion, core annular flow (CAF), oil plugs and dispersed oil lumps. The transition trend between different flow patterns is also consistent in each flow map. Due to limitation of the experimental rig on achievable minimum water flow rate (around 0.05 m/s), the inversion flow regime was only observed in limited flow conditions when low water flow rates were achieved. With increase of the water flow rate, oil plugs in water is developed for low oil flow rate; CAF is developed when oil flow rate is high. Further increasing the water flow rate, transitions from oil plugs or CAF to oil lumps in water occur.

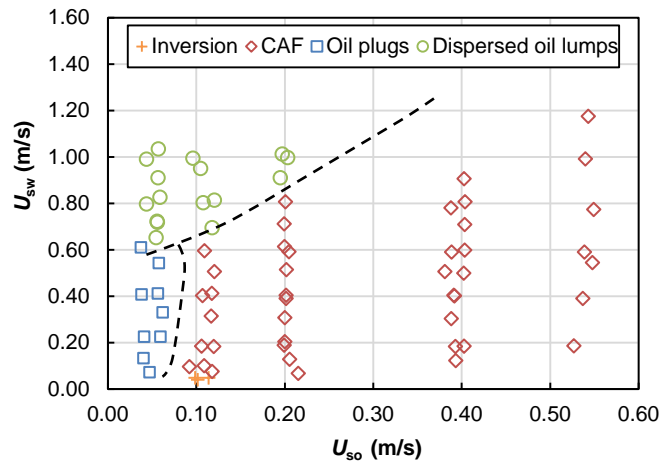
All the flow maps show that CAF develops in a wide range of oil and water flow rates. It is the dominate flow pattern for higher oil flow rates (higher than 0.1 m/s). The region of CAF expands with increasing oil viscosity. It can be seen that CAF is not formed at U_{so} around 0.1 m/s in Figure 4-5 (a) and (b) for oil nominal viscosity of 3 300 and 3 700 cP respectively. While in Figure 4-5 (c) and (d) for oil nominal viscosity of 5 000 and 7 100 cP, CAF is developed at U_{so} around 0.1 m/s.



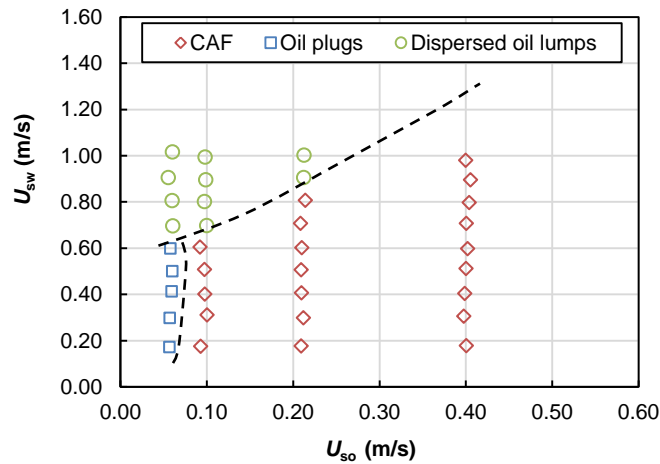
(a)



(b)



(c)

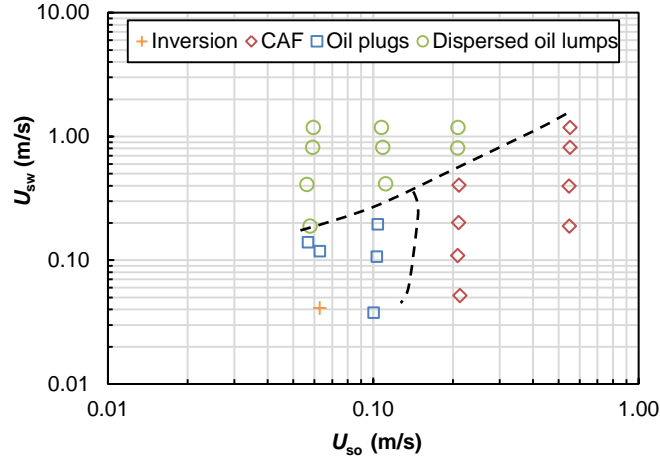


(d)

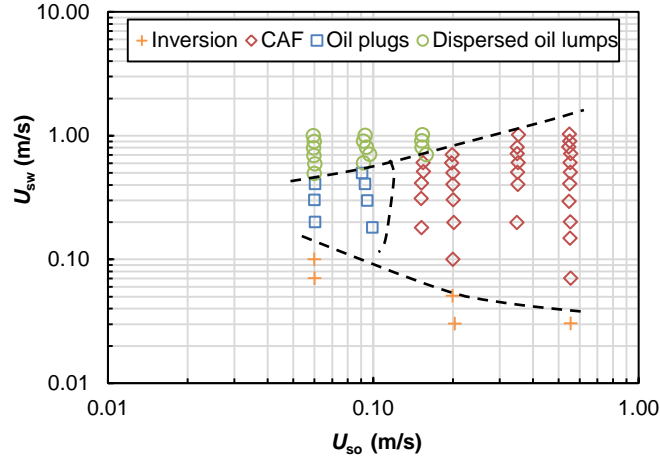
Figure 4-5 Flow regime maps (linear scale) of high-viscosity oil-water flow (CYL 680). (a) 3 300 cP; (b) 3 700 cP; (c) 5 000 cP; (d) 7 100 cP.

To have a clear view on the inversion region on the flow pattern map, the flow regime maps shown in Figure 4-5 are re-presented in logarithmic scale as shown in Figure 4-6. Though the inversion was observed in limited flow conditions, it can be observed from Figure 4-6 (b) that the inversion from oil-continuous to water-continuous tends to occur at a lower water input volume fraction with increase of oil flow rate. This trend is also indicated in Figure 4-6 (a) where the inversion flow regime is formed at U_{sw} around 0.04 m/s for U_{so} around

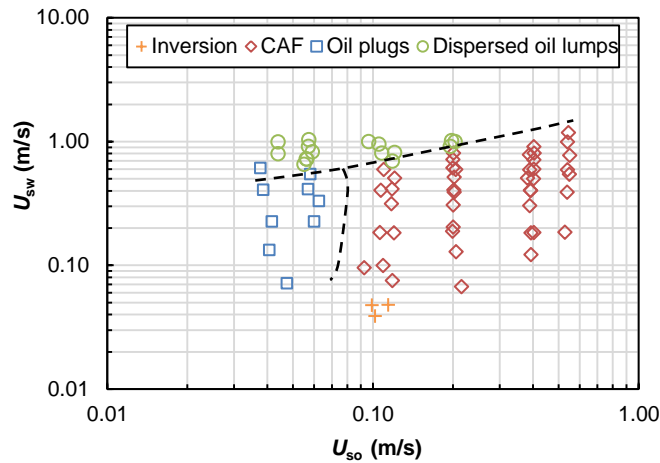
0.06 m/s, while oil plugs in water is formed at similar U_{sw} for U_{so} around 0.1 m/s, suggesting the inversion occurs at a U_{sw} lower than 0.04 m/s. This shows that it is more economical to transport heavy oil at a high U_{so} as a small U_{sw} is required to form water-lubricated flow.



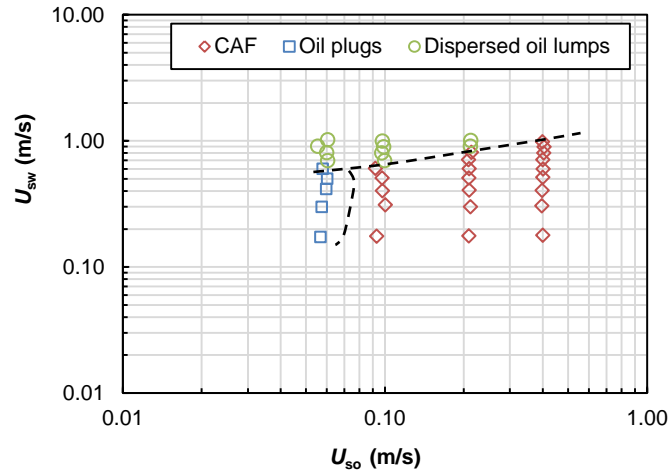
(a)



(b)



(c)



(d)

Figure 4-6 Flow regime maps (logarithmic scale) of high-viscosity oil-water flow (CYL 680). (a) 3 300 cP; (b) 3 700 cP; (c) 5 000 cP; (d) 7 100 cP.

The inversion flow regime at very low water flow rates was observed more often in experiments conducted by Al-Awadi (2011). With focus on the inversion from oil-continuous to water-continuous, high water flow rates were less covered in the experiments conducted by the above author. A flow regime map for oil-water flow with the oil CYL 1 000 of nominal viscosity around 3 800 cP is shown in Figure 4-7. The flow map in general is similar to the above flow maps shown in Figure 4-6, but it has more coverage at low water flow rates. The inversion

occurs at U_{sw} ranging from 0.02 m/s to 0.07 m/s with corresponding input water volume fraction varying from 0.05 to 0.5. Similar to the observation from Figure 4-6, the inversion from oil-continuous to water-continuous occurs at a lower input water volume fraction with increase of the superficial oil velocity. This can be more clearly demonstrated in a flow regime map represented with coordinates of C_w and U_{so} (see Figure 4-8). More discussion on the the occurrence of inversion can be found in Chapter 5.

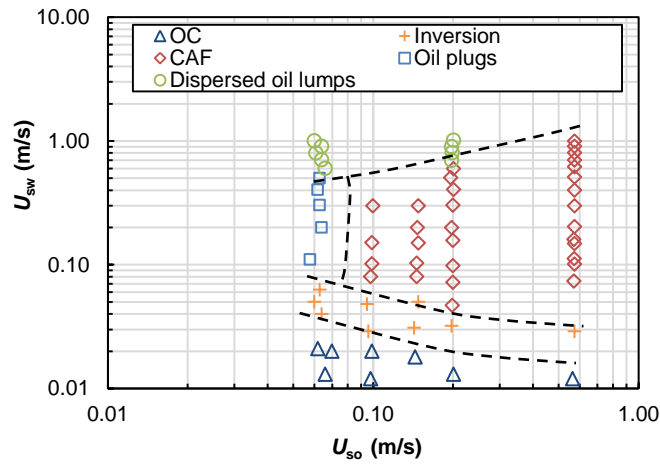


Figure 4-7 Flow regime map of high-viscosity oil-water flow with U_{so} and U_{sw} as coordinates (CYL 1 000, $\mu_o=3\ 800$ cP).

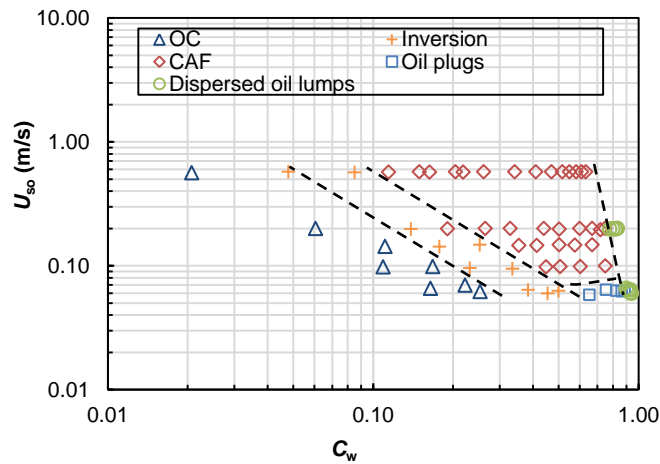


Figure 4-8 Flow regime map of high-viscosity oil-water flow with C_w and U_{so} as coordinates (CYL 1 000, $\mu_o=3\ 800$ cP).

(2) Comparisons of flow pattern maps with literature data

Most of the flow pattern maps for liquid-liquid flow in the literature are presented either with superficial phase velocities (U_{so} and U_{sw}) or the input water volume fraction and mixture velocity (C_w and U_m) as coordinates; this kind of flow pattern maps can be easily perceived, giving information of flow patterns under commonly used flow conditions. However, flow pattern maps produced from different studies show considerable discrepancies. Angeli and Hewitt (2000) summarised that in addition to phase velocities, pipe diameter, density ratio, viscosity ratio and wetting properties of the pipe wall can also influence flow patterns. All these factors contribute to variations of flow pattern maps produced from different studies.

Comparisons of flow pattern maps with selected literature data are presented in this section. Ooms et al. (1984), Oliemans et al. (1987), and McKibben et al. (2000a and 2000b) studied high-viscosity oil-water flow with overlapped oil viscosity with the present study. However, no flow regime maps were produced in the above studies. Grassi et al. (2008) and Sotgia et al. (2008) reported flow pattern maps of oil-water flow with oil viscosity around 800 cP and 919 cP respectively. Core annular flow and dispersed flow (the counterpart of dispersed oil lumps defined in the present study) are two major flow patterns in their flow pattern map, which is comparable to some extent with the present study. The flow pattern maps produced in Grassi et al. (2008) and Sotgia et al. (2008) were used to compare with a flow pattern map produced in the present study. Another comparison was made with the flow pattern map of Trallero et al. (1997) of which the oil viscosity is much lower than the present study. A summary of the data sets used for flow map comparison is shown in Table 4-3. Due to small or large differences of the flow systems, variations of the flow pattern maps are expected. The purpose of the comparison is to perceive the degree of variations of flow regime maps of different flow systems, hence the similarity of different liquid-liquid flows.

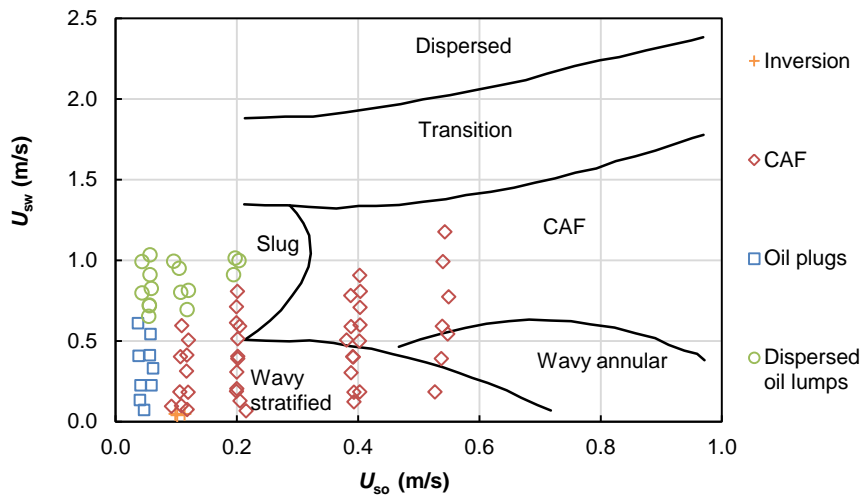
Table 4-3 Summary of the data sets used for flow map comparison.

Data sources	Pipe I.D. (mm)	μ_o (cP)	ρ_o (kg/m ³)	σ (N/m)	Flow rates (m/s)
Trallero et al. (1997)	50	28.8	884	0.036	U_{so} :0.01~1.6; U_{sw} :0.02~1.6;
Grassi et al. (2008)	21	800	886	0.05	U_{so} :0.03~0.7; U_{sw} :0.2~2.5;
Sotgia et al. (2008)	26	919	889	0.02	U_{so} :0.1~1.0; U_{sw} :0.1~2.5;
Present study	26	5 000	910	0.02	U_{so} :0.04~0.54; U_{sw} :0.02~1.1;

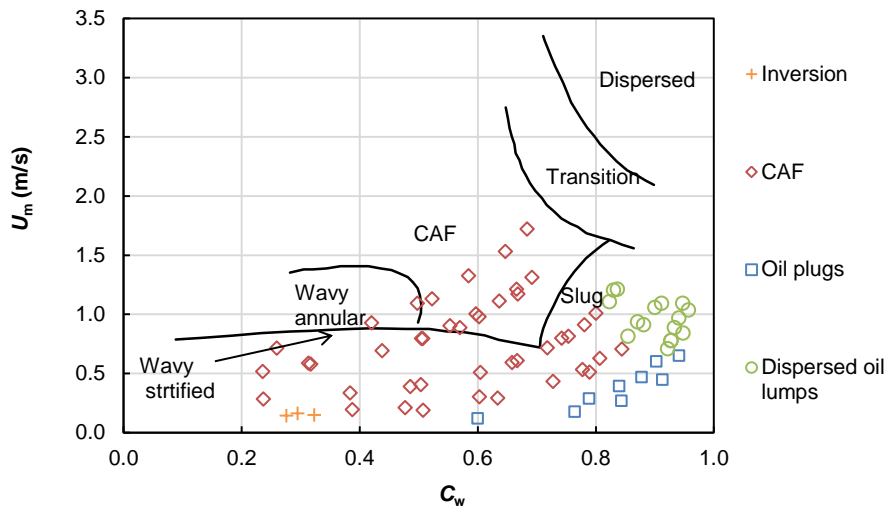
Figure 4-9 (a) and 4-9 (b) show a comparison of flow pattern maps produced in the present study with that produced by Sotgia et al. (2008), presented in U_{so} and U_{sw} , and C_w and U_m , respectively. The core annular flow (CAF) defined in the present study corresponds to the CAF and wavy annular defined by Sotgia et al. (2008); the oil plugs correspond to the slug flow; the dispersed oil lumps can be linked to both the Transition and Dispersed flow. For the same region of interest, it can be observed that there is an overlapped area of CAF. For the whole region of each study, similar trends of transitions among flow regimes of oil plugs/slugs, CAF, and dispersed oil lumps are shown. The transition from oil plugs/slugs to annular flow occurs predominantly with increase of U_{so} ; the transition from annular flow and oil plugs/slugs to dispersed oil lumps occurs predominantly with increase of U_{sw} .

The major difference between the two maps is that wavy stratified flow covers the low mixture flow rate and low to medium water volume fraction region (U_m : 0.7 ~ 0.9 m/s, C_w : 0.1~0.7) in Sotgia et al. (2008), while stratified flow was rarely observed in the present study. Instead, the inversion flow regime characterised with spiral motion of oil and water was observed at very low mixture flow rate and low water volume fraction (U_m around 0.3 m/s, and C_w around 0.3) in the present study. As the pipe diameter and the interfacial tension are similar between the two studies, the oil viscosity and density are possible factors resulting in the difference. The gravitational force due to the density difference between oil and water which makes the phases stratified is less significant in the present study than in Sotgia et al. (2008). Also the higher oil viscosity in the present study favours the formation of CAF. Another factor which might cause

the difference is the fluids injection sequence. In the present study, the oil was injected into the pipe followed by water from low to high flow rate to observe the inversion from oil-continuous flow to annular-water-continuous flow. In the study of Sotgia et al. (2008), the opposite injection sequence was applied. By reducing the water flow rate at a constant oil flow rate, wavy stratified flow was observed. The inversion flow regime observed in the present study is an unstable transitional flow regime. It is unknown that whether stratified flow can be finally developed further downstream the mixing point in a longer pipe. The flow development length is not established for multiphase flow as it is different for different flow regimes and initial conditions. Whether this unstable inversion flow regime would stay the same transitional characteristic, become stable or even develop into stratified flow in a longer pipe is not investigated in the present study due to experimental limitation. It is noted that the other flow patterns are regarded as developed in the present study with regard to the stable pressure drop. Despite the uncertainty in the flow regime of inversion, it is well demonstrated in Figure 4-9 that the region of core annular flow extends as the oil viscosity increases. The stratified flow rarely develops or if it develops, its region is quite small comparing to core annular flow and dispersed oil lumps in water flow. According to Joseph et al. (1997), there is a strong tendency for two immiscible fluids with significant viscosity difference to arrange themselves so that the low-viscosity constituent is in the region of higher shear. When the oil viscosity is very high, the gravitational force which tends to stratify two immiscible fluids must be competing with another force which tends to form water-lubricated flow. Therefore, the interface of stratified flow has a higher curvature if stratified flow develops at limited conditions for high-viscosity oil-water flow. The wavy stratified flow with high interface curvature can be regarded as a transitional regime to the core annular flow. Further investigation on the flow patterns of liquid-liquid flows is presented in Chapter 5.

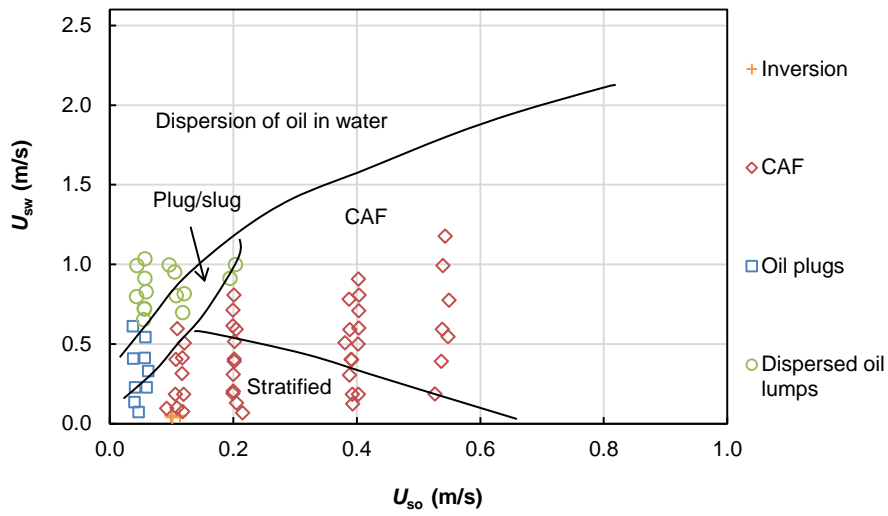


(a)

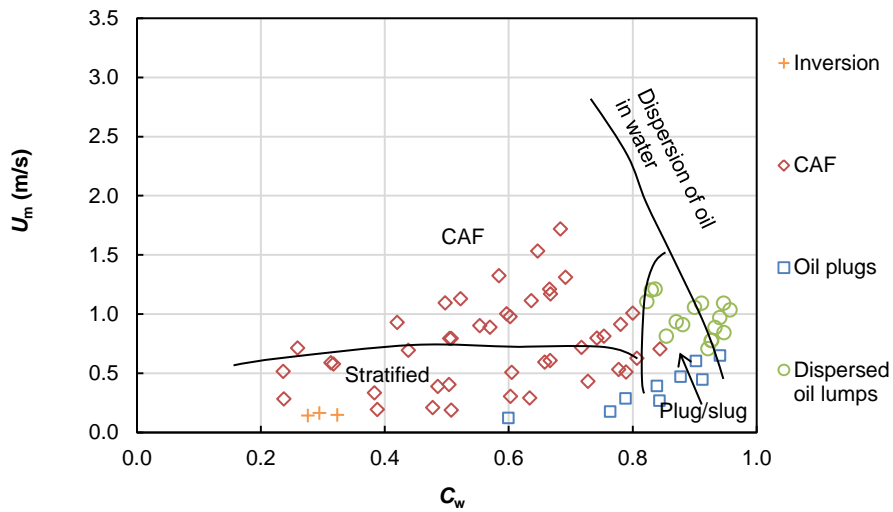


(b)

Figure 4-9 Comparison of flow pattern maps produced in the present study and Sotgia et al. (2008). Regimes defined in the present study are presented with markers. Regimes defined by Sotgia et al. (2008) are presented with boundary lines and regime descriptions: Wavy stratified; Wavy annular; CAF; Slug; Transition (between CAF/Slug and Dispersed); Dispersed. (a) U_{so} and U_{sw} as coordinates; (b) C_w and U_m as coordinates.



(a)

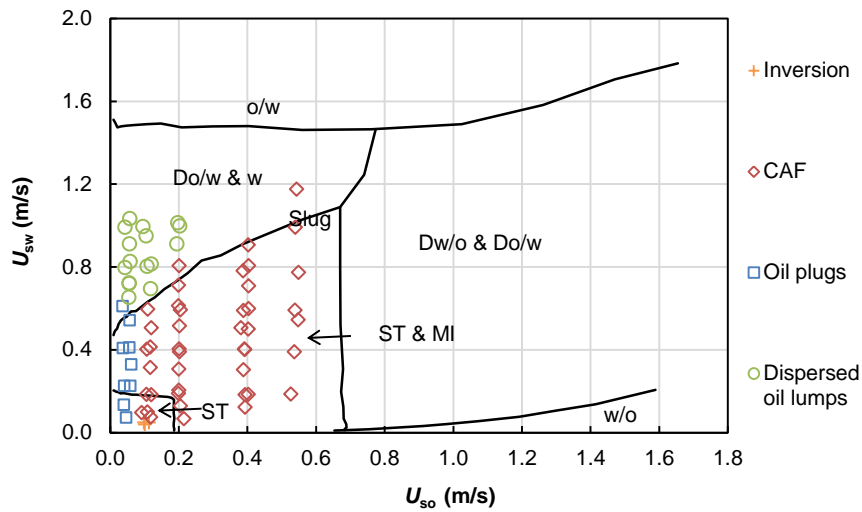


(b)

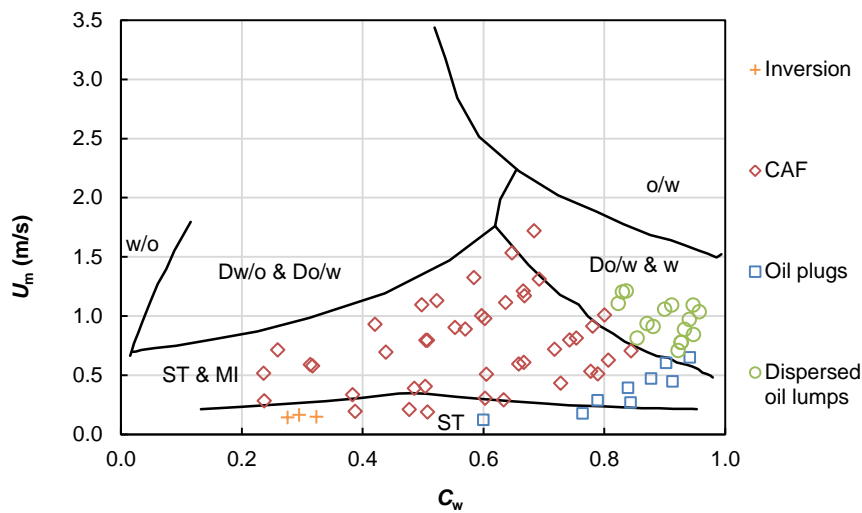
Figure 4-10 Comparison of flow pattern maps produced in the present study and Grassi et al. (2008). Regimes defined in the present study are presented with markers. Regimes defined by Grassi et al. (2008) are presented with boundary lines and regime descriptions: Stratified; CAF; Plug/Slug; Dispersion of oil in water. (a) U_{so} and U_{sw} as coordinates; (b) C_w and U_m as coordinates.

Figure 4-10 (a) and 4-10 (b) show a comparison of flow pattern maps of the present study and Grassi et al. (2008). As demonstrated in Figure 4-9, there is an overlapped area of CAF. Comparing Figure 4-10 with Figure 4-9, the flow pattern maps produced in Grassi et al. (2008) and Sotgia et al. (2008) demonstrate more similarity. This can be explained by the fact that the properties of oils between the above two studies are similar as well as the investigated ranges of phase flow rates. It is noted that the region of CAF in the flow map of Grassi et al. (2008) is larger than that of Sotgia et al. (2008). This is thought to be associated with the differences in pipe diameter and interfacial tension. A smaller pipe diameter and a higher interfacial tension contribute to the larger region of CAF in Grassi et al. (2008).

A comparison between the flow maps produced in the present study and Trallero et al. (1997) is shown in Figure 4-11. The flow maps are less comparable as the observed flow regimes are dramatically different. The only link is the occurrence of dispersed oil lumps in the present study and the dispersion of oil in water and water (Do/w & w) in Trallero et al. (1997) at higher water volume fractions. The breakup of the oil phase occurs when the turbulent kinetic energy in the water is sufficiently high. For low viscosity oil, the oil phase is readily dispersed into droplets, while the oil is dispersed into lumps for very viscous oil. The striking difference in the flow patterns is thought to come primarily from the large difference in oil viscosity. Most experimental studies on low-viscosity oil-water flow in the literature report flow regimes similar with those of Trallero et al. (1997), while high-viscosity oil-water flow sees a major flow pattern of CAF. Further discussion on the physics behind can be found in Chapter 5.



(a)



(b)

Figure 4-11 Comparison of flow pattern maps produced in the present study and Trallero et al. (1997). Regimes defined by Trallero et al. (1997) are presented with boundary lines and regime descriptions: Stratified (ST); Stratified with mixing at the interface (ST & MI); Dispersion of oil in water and water (Do/w & w); Oil in water emulsion (o/w); Dispersion of water in oil and oil in water (Dw/o & Do/w); Water in oil emulsion (w/o). (a) U_{so} and U_{sw} as coordinates; (b) C_w and U_m as coordinates.

4.4 Inversion occurrence

As water-lubricated flow is the favourable flow in heavy oil transport, the conditions under which the inversion from oil-continuous to annular-water-continuous occurs are of importance. A parametric investigation on the occurrence of the inversion is conducted making use of the pressure gradient trend with input water volume fraction. This is the basis of the further mechanism investigation presented in Chapter 5.

The input water volume fraction is a primary condition of interest on the issue of the inversion occurrence. The typical trends of pressure gradient with input water volume fraction (C_w) from experimental data are shown in Figure 4-12. With recorded flow patterns as reference, the categories of flow regimes with change of C_w are also marked.

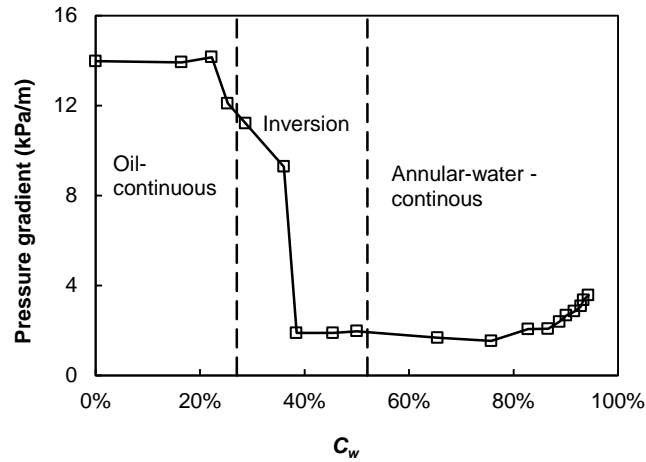
In general, the oil-water two-phase flow appears as oil-continuous at very low C_w . The magnitude of the pressure gradient of oil-continuous two-phase flow is close to that of single phase oil flow. With increase in C_w , the inversion from oil-continuous to annular-water-continuous occurs. The inversion is not completed abruptly at a particular input water volume fraction but within a certain range of the input water volume fraction. The inversion region can be distinguished with a sharp drop in the pressure gradient soon after the initiation of the inversion. The inversion is completed with the flow exhibiting a low pressure gradient similar to that of water-lubricated flow just after the inversion. The conditions under which the inversion is completed, i.e., the water-lubricated flow is initiated, is of interest as stable water-lubricated flow is the favourable flow in heavy oil transport.

In the oil-continuous region, the pressure gradient is observed to first increase slightly from the single oil flow pressure gradient then decrease moderately with increase of C_w for a limited experimental runs (in low oil flow rates for relatively low oil viscosity below 5 000 cP) as shown in Figure 4-12 (a). The slight increase of the pressure gradient is due to the increase of the mixture velocity, while the decrease is associated with partial water lubrication effect. As

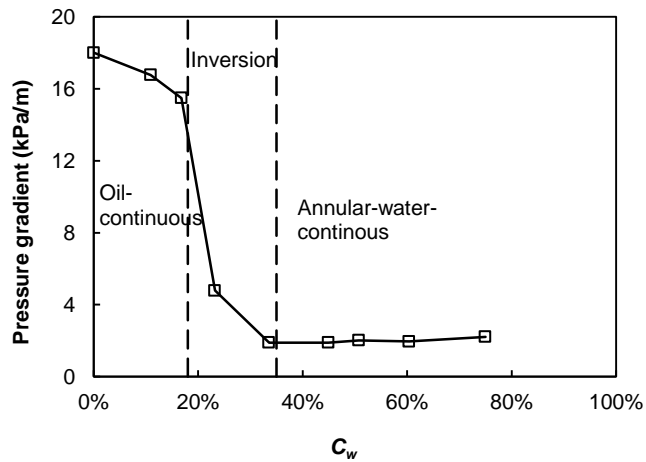
introduced in the description of the oil-continuous regime, the oil-continuous flow can be further distinguished into two specific phase configurations: a) no water is visually seen; and b) little streams of water could be seen at irregular intervals. The slight increase part in the pressure gradient corresponds to the phase configuration in which no water is visually observed, while the decrease part corresponds to the flow pattern where little streams of water can be observed at intervals. When no water is visually observed, it is probable that the water is dispersed inside the oil phase in the form of bubbles or drops. This phase configuration has little water lubrication effect and the pressure gradient can be increased just due to increase in the mixture velocity with increase in the water content. Besides, water-in-oil emulsion has been reported to have increased effective mixture viscosity with increase of water content, which can result in higher pressure gradient with increase in water content too (see Wang et al., 2011). When discontinuous water streams can be observed, the streams of water partially lubricated the pipe and contribute to a reduced average pressure gradient since that water streams are not inside the dominant continuous oil but adjacent to the pipe. Partial water lubrication effect on reducing the pressure gradient is also reported in McKibben et al. (2000a).

Figure 4-12 (b) shows a typical pressure trend for the majority of experimental runs. Different from the pressure trend in the oil-continuous region as shown in Figure 4-12 (a), the pressure gradient decreases gradually from the single oil flow pressure gradient without the initial increase. However, there is probably a slight increase stage before the decrease of the pressure gradient if lower input water volume fractions can be realised in the experiments. It appears that the partial water lubrication due to the discontinuous water streams occurs at a very small amount of water for high viscosity and/or high velocity oil. When the oil is more viscous or the oil inertia is higher, the flowing oil phase is more like a rigid body thus the small amount of water exists as discontinuous streams adjacent to the pipe rather than dispersed drops inside the oil phase. The partial water lubrication effect due to the discontinuous water streams on reducing the pressure gradient is not significant as the continuous oil phase is still dominant.

It should be noted that in Figure 4-12 lines connecting the experimental points are used for the purpose of clearly indicating the possible trend; the exact pressure gradient line may vary slightly. The following sections adopt lines connecting the experimental points for the same purpose.



(a)



(b)

Figure 4-12 Pressure gradient with input water volume fraction (CYL 1 000, $\mu_o=3\ 800$ cP). (a) $U_{so}=0.06$ m/s; (b) $U_{so}=0.1$ m/s.

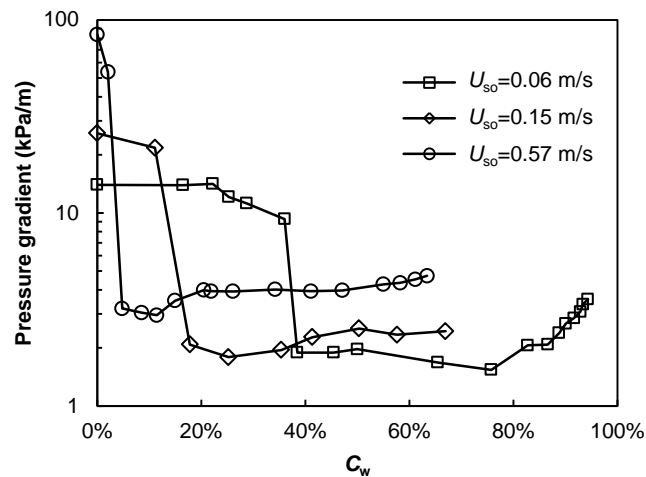
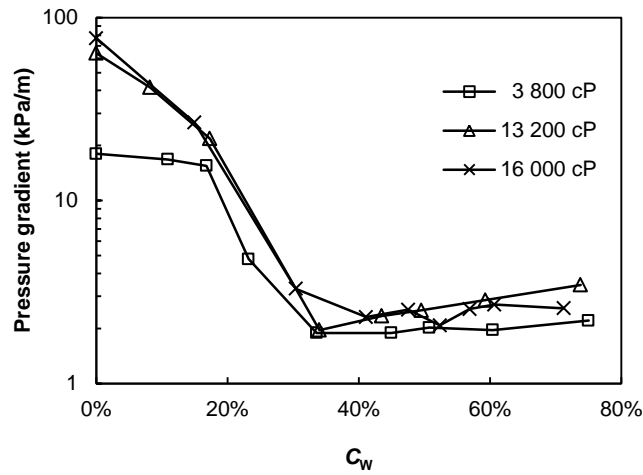


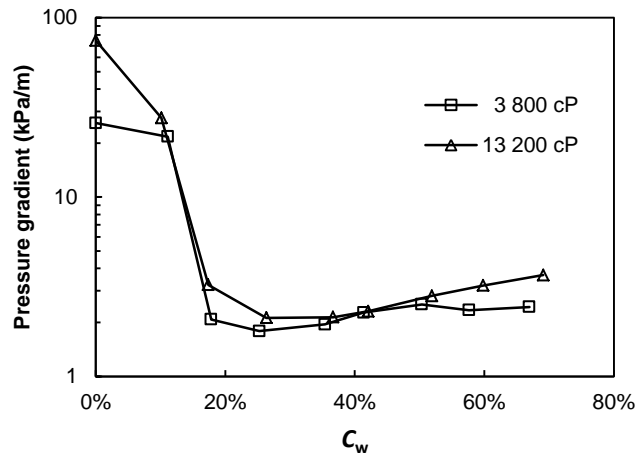
Figure 4-13 Pressure gradient with input water volume fraction at various superficial oil velocities (CYL 1 000, $\mu_o=3\ 800$ cP).

The pressure gradient with input water volume fraction at various superficial oil velocities is shown in Figure 4-13. As the sharp drop in the pressure gradient reflects the inversion region, it is indicated that the stable water-lubricated flow develops at a lower C_w with increase of U_{so} . This trend has been demonstrated in the flow pattern maps (see Section 4.3.2) and is emphasised here again.

The pressure gradient with input water volume fraction at various oil viscosities is shown in Figure 4-14. It is demonstrated that for a specific U_{so} , the stabilized low pressure gradient hence stable water-lubricated flow develops around a similar C_w for oils with different viscosities. As discussed above, in the oil-continuous region, the partial water lubrication due to the sporadic water streams occurs at a lower input water volume fraction for higher viscosity oil. Reflected in Figure 4-14, the pressure gradient starts to decrease gradually at very low input water volume fractions for the higher oil viscosities of 13 200 cP and 16 000 cP, while not for the lower oil viscosity of 3 800 cP.



(a)



(b)

Figure 4-14 Pressure gradient with input water volume fraction at various nominal oil viscosities (CYL 1 000). (a) $U_{so}=0.1$ m/s; (b) $U_{so} =0.15$ m/s

To conclude, the inversion from oil-continuous to water-lubricated flow is not completed abruptly but within a certain range of water content. For the oil viscosity range investigated in the present study, i.e., between 3 300 and 16 000 cP, the completion of the inversion, or the transition to stable water-lubricated flow, is closely related to the input water volume fraction and the superficial oil velocity. The mechanism behind is further discussed in Chapter 5.

4.5 Water holdup of water-lubricated flow

The relation between the measured water holdups (H_w) and the input water volume fractions (C_w) under different superficial oil velocities is shown in Figure 4-15. The error bars show a $\pm 6\%$ error range (see Section 3.5.3 in Chapter 3).

The interesting trend demonstrated by Figure 4-15 is that at lower superficial oil velocities (see Figure 4-15 (a) and (b)), H_w is lower than C_w , indicating that the water phase is flowing faster, and oil is accumulating. Referring to the recorded flow patterns under these flow conditions, the common feature of the flow patterns is that the oil core, continuously or discontinuously flows eccentrically in the upper part of the pipe. When the eccentricity of the oil is higher with a thin water layer between the top of the oil and the upper wall of the pipe, the shear between the top side of the oil core and the thin water layer would be higher than that of less eccentric oil core. In general, the flow with higher oil flow rate is less eccentric than flow with lower oil flow rate, leading to less accumulation of the oil phase. This can explain that H_w is closer to C_w in Figure 4-15 (b) than in Figure 4-15 (a). For a certain oil flow rate, the difference between H_w and C_w is thought to be associated with the degree of oil fouling which occupy part of the fluid passage and contributes oil accumulation. It is observed that at lower C_w just after the inversion, the oil fouling is lighter due to lower water flow rate hence lower turbulent kinetic energy which causes random contact of the oil core with the pipe wall. The oil fouling first gets heavier with increase in C_w with increase of the turbulent kinetic energy in the annular phase, then become lightened at very high C_w when the water flush effect on removing the oil fouling outweighs the effect of oil-wall contact on thickening the oil fouling. This can explain why H_w is closer to C_w at very low and very high C_w in both Figure 15 (a) and Figure (b).

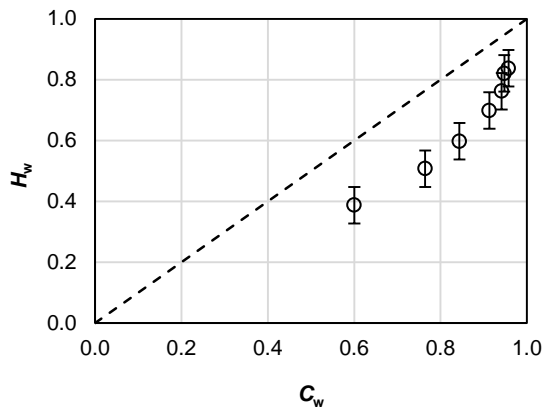
When the superficial oil velocity is very high, the oil core is nearly concentric at a wide range of water contents due to high oil inertia. As shown in Figure 4-15 (e) for $U_{so}=0.54$ m/s, the measured water holdup is always higher than the input

water volume fraction, indicating that the oil core is flowing faster than the annular water phase.

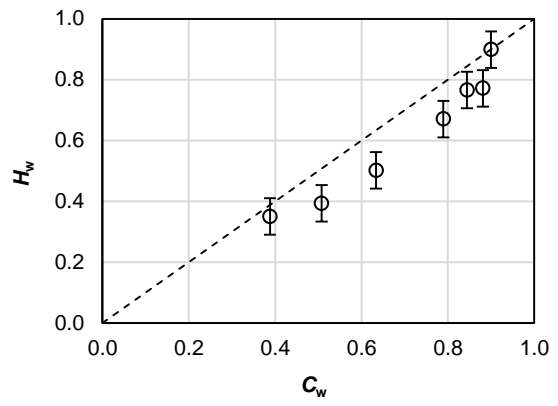
At medium superficial oil velocities as shown in Figure 4-15 (c) and (d), the trends of H_w with C_w are like transitions between that of low oil flow rate when the eccentricity of oil phase is high and that of high oil flow rate when the oil core is virtually concentric. Again, this trend can be explained by the degree of oil core eccentricity and oil fouling on the pipe inner wall.

Similar trends at different superficial oil velocities can be observed for another series of tests with oil nominal viscosity of 3 300 cP as shown in Figure 4-16. The influence of oil viscosity on water holdup is insignificant comparing Figure 4-16 to Figure 4-15.

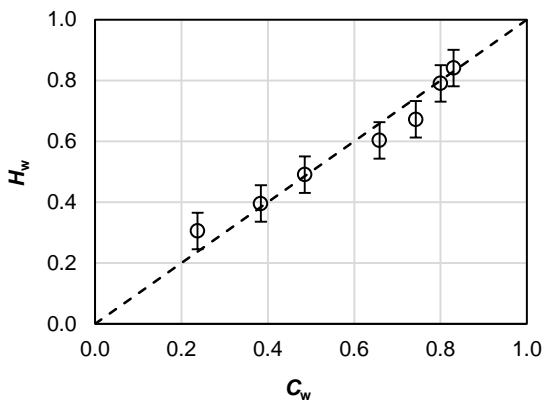
From the above analysis, it is shown the water holdup of water-lubricated flow is not only related to the input water volume fraction, but also with the oil flow rate which is thought to be closely related to the degree of oil eccentricity inside the continuous water.



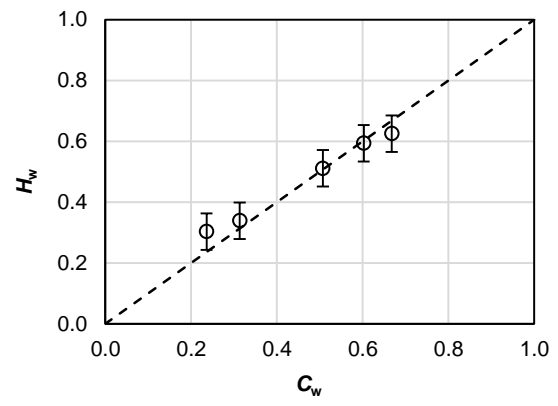
(a)



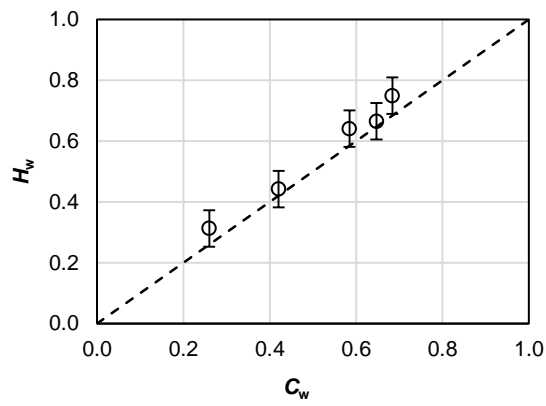
(b)



(c)



(d)



(e)

Figure 4-15 Water holdup (H_w) versus input water volume fraction (C_w) at various U_{so} (CYL 680, $\mu_o=5\ 000$ cP). (a) $U_{so}=0.04$ m/s; (b) $U_{so}=0.11$ m/s; (c) $U_{so}=0.20$ m/s; (d) $U_{so}=0.39$ m/s; (e) $U_{so}=0.54$ m/s.

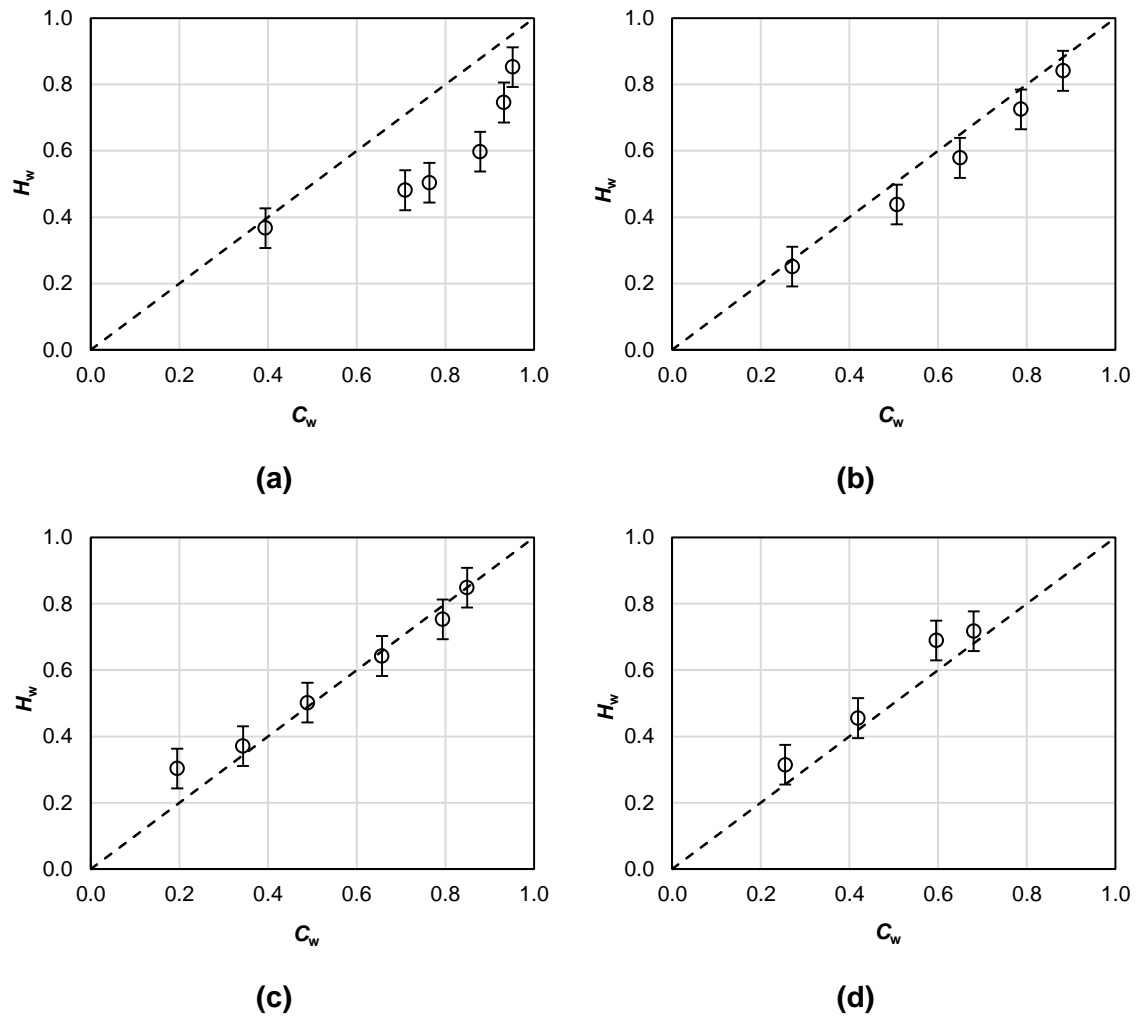


Figure 4-16 Water holdup (H_w) versus input water volume fraction (C_w) at various U_{so} (CYL 680, $\mu_o=3\ 300$ cP). (a) $U_{so}=0.06$ m/s; (b) $U_{so}=0.11$ m/s; (c) $U_{so}=0.21$ m/s; (d) $U_{so}=0.55$ m/s.

From the measured water holdup, the oil-water slip ratio (s) of core annular flow can be obtained based on the mass balance ($s = U_o/U_w$; $U_o = U_{so}/(1 - H_w)$; $U_w = U_{sw}/H_w$). Figure 4-17 shows the oil-water slip ratio of CAF versus the input water volume fraction. The slip ratio of 1 is marked with a dash line. The oil-water slip ratio of CAF varies from 0.5 to 1.4 for the present experimental conditions. At the lower U_{so} of 0.11 m/s, the oil-water slip ratio is lower than 1, indicating the average velocity of the oil core is lower than that of the annular water. At the higher U_{so} of 0.54 m/s, the oil-water slip ratio is higher than 1, suggesting the oil core is flowing faster than the annular water. At the medium

U_{so} around 0.2 and 0.4 m/s, the slip ratio varies from around 1. The change of the oil-water slip ratio with input water volume fraction at various U_{so} corresponds to the change of water holdup with input water volume fraction at various U_{so} . It demonstrates that the oil core is flowing faster than the annular water when the oil core is virtually concentric, while slower than the annular water when the oil core has a high degree of eccentricity. This is also demonstrated in our CFD simulation results which are presented in Chapter 7.

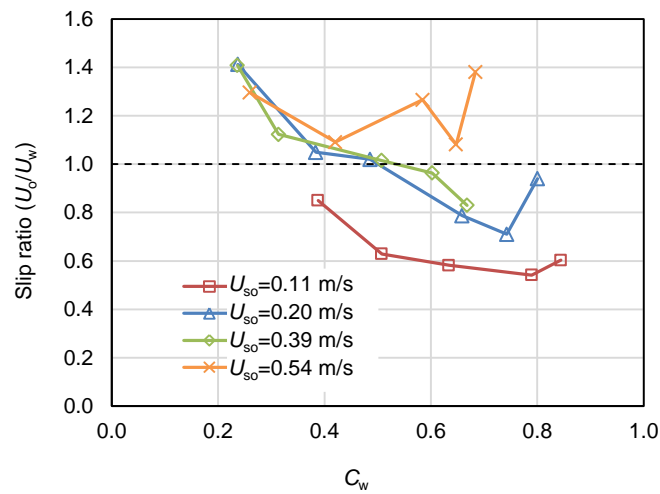


Figure 4-17 Oil-water slip ratio of CAF versus input water volume fraction (C_w) at various U_{so} .

4.6 Pressure gradient of water-lubricated flow

The pressure gradient of water-lubricated flow was compared to its counterpart of single oil and water flow. Two ratios were adopted to gauge the relative magnitude of pressure gradient of water-lubricated flow.

PDRF (Pressure Drop Reduction Factor) is defined as the pressure gradient of oil-water flow to single oil flow at the same oil flow rate (Arney et al., 1903). It reflects the water lubrication effect on reducing pressure drop.

$$\text{PDRF} = \frac{\left(-\frac{dp}{dz}\right)_{oil-water\ flow\ at\ Q}}{\left(-\frac{dp}{dz}\right)_{single\ oil\ flow\ at\ Q_o}} \quad (4-1)$$

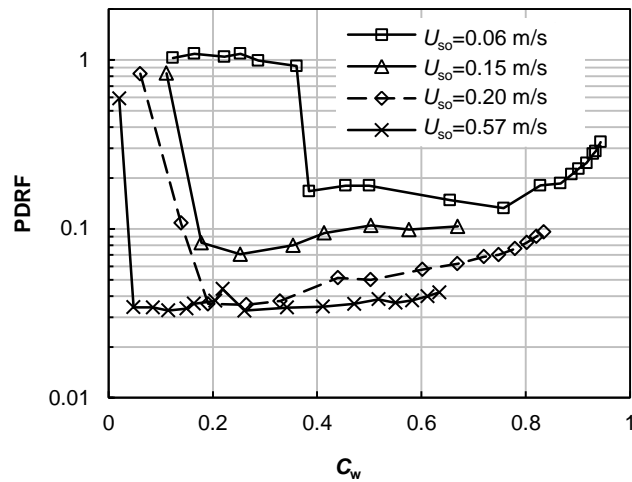
$$Q_o = (1 - C_w)Q \quad (4-2)$$

where Q represents the total flow rate, Q_o the oil flow rate, and C_w the input water volume fraction.

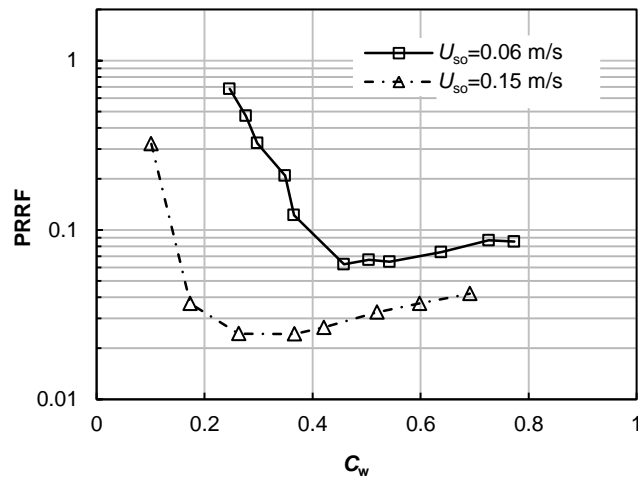
RTW is defined as the ratio of the pressure gradient of two-phase flow to the pressure gradient of single water flow at same mixture flow rate (Rodriguez et al., 2009). It reflects the relative magnitude of the pressure gradient of water-lubricated two-phase oil-water flow to that of single water flow.

$$\text{RTW} = \frac{\left(-\frac{dp}{dz}\right)_{oil-water\ flow\ at\ Q}}{\left(-\frac{dp}{dz}\right)_{single\ water\ flow\ at\ Q}} \quad (4-3)$$

The change of PDRF with increase of input water volume fraction is shown in Figure 4-18. Similar to the pressure gradient change with input water volume fraction, the sharp drop in PDRF indicates the inversion zone. It is demonstrated that the pressure gradient of water-lubricated flow is reduced to 2% to 20% of the pressure gradient of single oil flow. This reduction in pressure gradient is significant for high viscous oil. Comparing Figure 4-18 (a) and (b), it also shows that the pressure drop reduction effect is more pronounced for oils with higher viscosities.



(a)

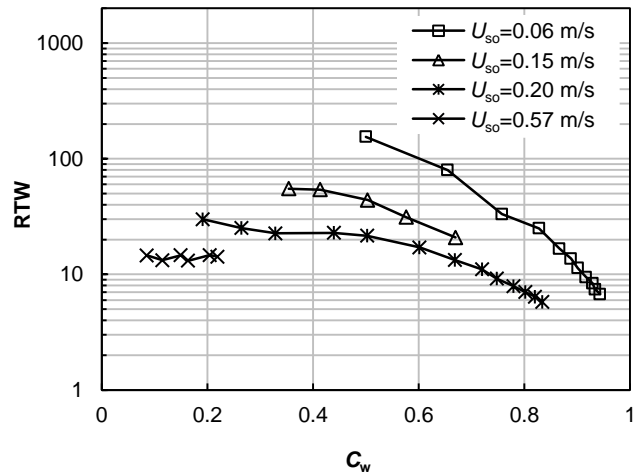


(b)

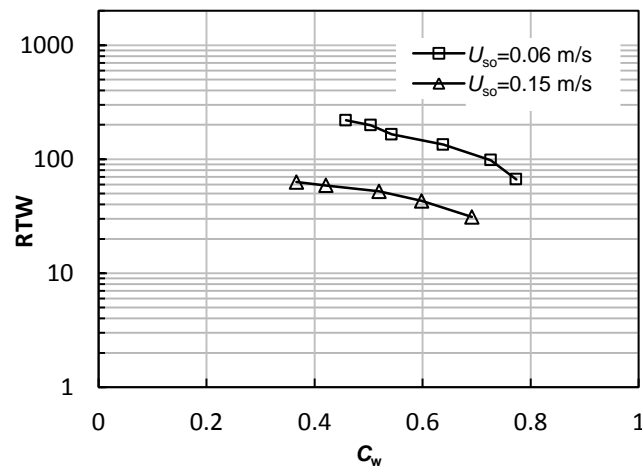
Figure 4-18 Pressure drop reduction factor with C_w at various U_{so} (CYL 1 000). (a) $\mu_o = 3\ 800$ cP; (b) $\mu_o = 13\ 200$ cP.

The change of RTW with increase of input water volume fraction for water-lubricated flow is shown in Figure 4-19. Ideally, the pressure gradient of water-lubricated flow would be reduced to have an order of magnitude of single water flow pressure gradient. The RTW in Figure 4-19 ranges from 5 to 200. This increased frictional loss is thought to be mainly associated with the oil fouling on the pipe wall. The RTW decreases with increase in either C_w or U_{so} . From recorded videos, it can be observed that the oil fouling lightens at high U_{sw} or C_w .

Also, the oil phase is more concentric under a high U_{so} thus less contact with the pipe wall. For practical applications, it is most desirable to have a higher U_{so} rather than a higher C_w to transport oil with a small amount of water. Therefore, the oil flow rate should not be too low to maintain a stable water-lubricated flow with less oil fouling.



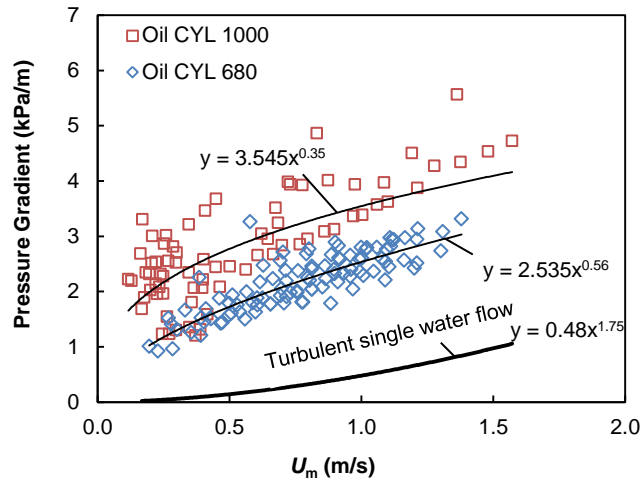
(a)



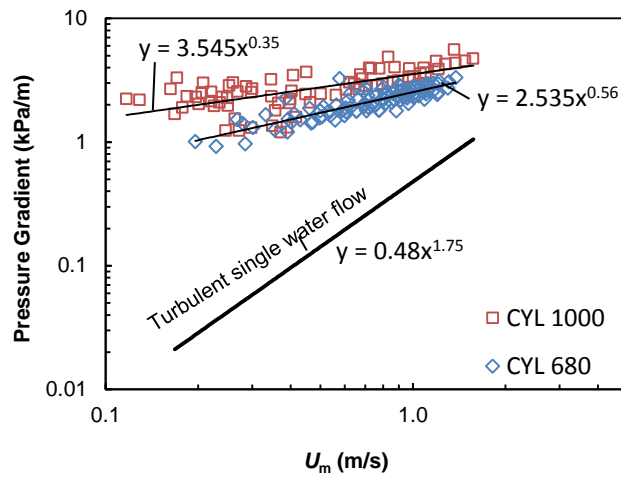
(b)

Figure 4-19 Ratio of water-lubricated two-phase flow pressure gradient to single water flow pressure gradient with C_w at various U_{so} (CYL 1 000). (a) $\mu_o = 3\ 800$ cP; (b) $\mu_o = 13\ 200$ cP.

The measured pressure gradient of water-lubricated flow against the mixture velocity is depicted in Figure 4-20. Different from single phase flow, the pressure gradient of water-lubricated flow at a particular mixture velocity varies slightly for various water contents. This is demonstrated by the scattered experimental data points. Also, for the two different oils, similar trends of pressure gradient with the mixture velocity are shown; the pressure gradient with the oil CYL 1000 is generally higher than that with the oil CYL 680. This is probably related to the different wettability of the pipe wall to the different oils. It was observed during experiments that the oil fouling on the pipe wall was heavier in general with the oil CYL 1000 than the oil CYL 680. Trend lines based on experimental data and calculated pressure gradients using the Blasius friction factor for the single water flow at the mixture velocity are also drawn for a comparative study. It is shown in Figure 4-20 that the pressure gradient of water-lubricated heavy oil flow is one to two orders of magnitude higher than that of single water flow, as have been demonstrated by RTW in Figure 4-19. Oil fouling is thought to be a major source for the increased pressure drop. The pressure gradient of two-phase flow shows a slower increase rate with increase of U_m . This can be explained by the fact that the oil fouling reduces at higher mixture velocity resulting in reduced frictional loss due to oil fouling, which counterbalances some pressure gradient increase due to velocity increase. A higher U_m can be resulted from a higher U_{so} or a higher U_{sw} . Once the water-lubricated flow is developed, the oil phase is more concentric at a higher U_{so} or higher oil inertia, resulting in less oil contact of the oil with the pipe wall. At the same U_{so} , a higher U_{sw} can flush away the oil fouling film on the pipe wall more effectively.



(a)



(b)

Figure 4-20 Pressure gradient of water-lubricated flow versus the mixture velocity. (a) linear scale; (b) logarithmic scale.

Figure 4-21 shows the coefficient of resistance, λ ($\lambda = \frac{-dp/dz}{(\rho_m/2D)U_m^2}$), versus the Reynolds number of the water-lubricated two-phase flow which is defined as $Re = \frac{\rho_m U_m D}{\mu_w}$. For comparison, the frictional resistance of single water flow in a pipe is shown as well. For single water flow through a pipe, the frictional resistance is calculated as follows (White, 2003).

For laminar flow ($Re < 2300$), the friction factor varies linearly with the inverse of Reynolds number. It can be calculated using the Hagen-Poiseuille equation:

$$\lambda = \frac{64}{Re} \quad (4-4)$$

For turbulent flow through hydraulic smooth pipes, the friction factor can be approximated by the empirical Blasius formula for the range $4000 < Re < 10\,000$:

$$\lambda = \frac{0.3164}{Re^{0.25}} \quad (4-5)$$

For turbulent flow through rough pipes, both Reynolds number and the pipe wall roughness influence the friction factor. At high Reynolds number, the friction factor of rough pipes becomes constant, dependent only on the pipe roughness.

The Colebrook–White equation (Colebrook, 1939) can be used to approximate the friction factor for both hydraulic smooth pipes and rough pipes. It is expressed as

$$\frac{1}{\sqrt{\lambda}} = -2 \log\left(\frac{\varepsilon}{3.7D} + \frac{2.51}{Re\sqrt{\lambda}}\right) \quad (4-6)$$

where ε represents the roughness height.

Figure 4-21 is a dimensionless representation of Figure 4-20. It demonstrates that the resistance friction factor for the water-lubricated flow in the present study is between 0.1 and 10 in the mixture Reynolds number range between 2 500 and 40 000. For the same Reynolds number range, the friction factor for single water flow is around 0.02. The friction factor of water-lubricated heavy oil flow is one to two orders of magnitude higher than that of single water flow. With increase of the Reynolds number hence the mixture velocity, the friction factor of the water-lubricated flow shows a quicker decreases. This can be explained by the reduced oil fouling on the pipe wall with increase of the mixture velocity as explained above.

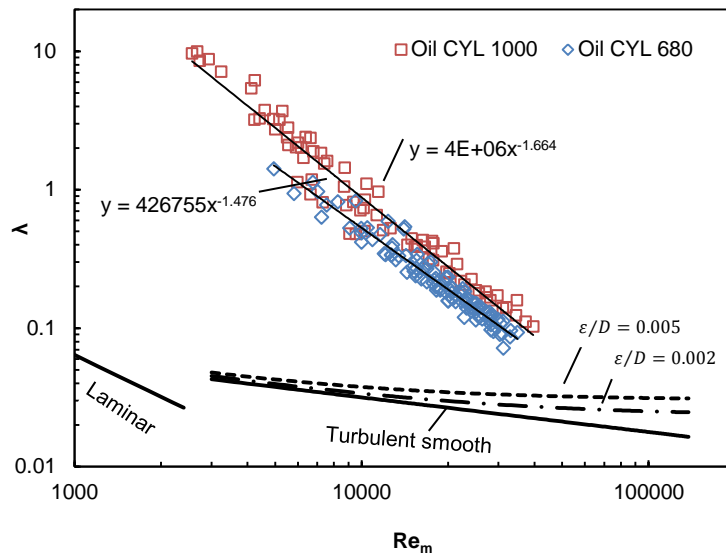
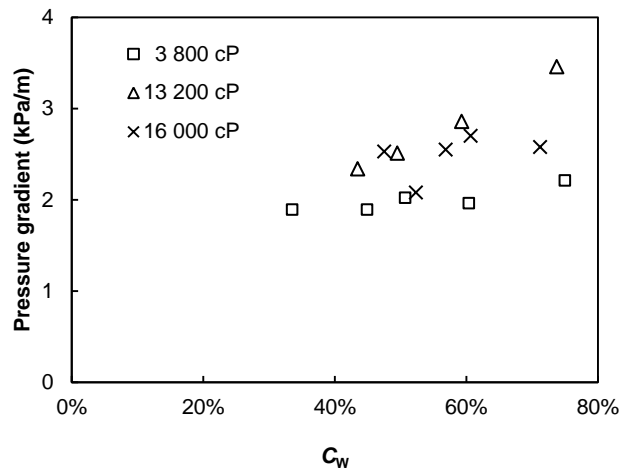
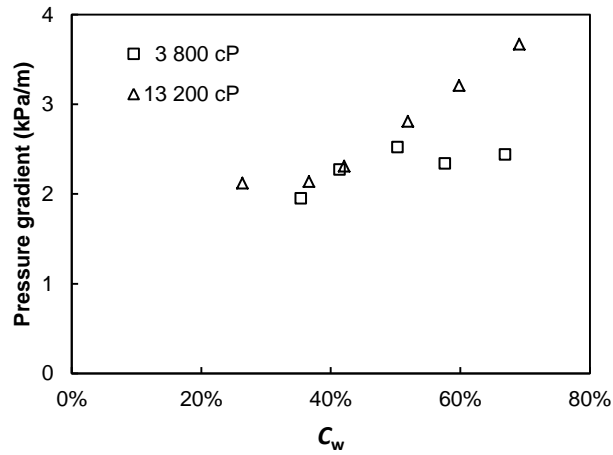


Figure 4-21 Coefficient of resistance versus the Reynolds number of the water-lubricated two-phase flow and comparison with that of single water flow.

Figure 4-22 shows the pressure gradient of water-lubricated flow with C_w at various nominal oil viscosities. The pressure gradients have a same order of magnitude (between 1 and 4 kPa/m) for different oil viscosities investigated. The influence of oil viscosity on the pressure gradient of water-lubricated heavy oil flow is not straightforward. At a same C_w , the pressure gradient of water-assisted flow with a lower oil viscosity can be lower, equal or higher than that of flow with a higher oil viscosity. This can be explained from two possible opposite influences of oil viscosity on the pressure gradient. Oil-water flow with a higher oil viscosity tends to have higher frictional resistance due to oil fouling on the internal wall of the pipe, which contributes to a higher pressure gradient than flow with a lower oil viscosity. However, the more viscous the oil is, the more turbulence damping effect of the oil core on the annular water, which contributes to less energy dissipation hence a lower pressure gradient than flow with a lower oil viscosity.



(a)



(b)

Figure 4-22 Pressure gradient of water-lubricated flow with input water volume fraction at various nominal oil viscosities (CYL 1 000). (a) $U_{so}=0.1$ m/s; (b) $U_{so}=0.15$ m/s.

4.7 Summary

Experimental results on high-viscosity oil-water flow were discussed in flow patterns, the inversion occurrence, water holdup of water-lubricated flow, and pressure gradient of water-lubricated flow.

The major flow patterns observed in high-viscosity oil-water flow through a 1 inch horizontal pipe are oil-continuous flow, inversion, core annular flow (CAF), oil plugs, and dispersed oil lumps. Flow pattern maps were produced based on experimental results. The CAF is the dominant flow regime covering a wide range of oil and water flow rates. The region of CAF expands with increase of oil viscosity. Comparisons of flow regime maps with literature data were presented. Different degree of variations on the flow regime maps is shown and the affecting factors are discussed. Oil viscosity, oil density, and pipe diameter are demonstrated to be some major parameters affecting the flow patterns and flow pattern maps apart from phase flow rates.

The inversion from oil-continuous to water-lubricated flow is not completed abruptly but gradually in a certain range of water content. The inversion region can be distinguished with a sharp drop in the pressure gradient soon after the initiation of the inversion at particular water content. The average pressure gradient of oil-continuous two-phase flow can be reduced before the inversion due to partial lubrication from discontinuous water streams. The stable water-lubricated flow develops at a lower input water volume fraction with increase of the superficial oil velocity. For the oil viscosity range investigated in the present study (3 300 to 16 000 cP), the oil viscosity shows minor effect on the critical input water volume fraction where stable water-lubricated flow develops.

The relationship between the water holdup (H_w) and input water volume fraction (C_w) is presented. It is found that the water holdup of water-lubricated flow is not only related to the input water volume fraction, but also with the oil flow rate which is observed to associated with oil concentricity and oil fouling on the pipe wall. Generally speaking, for the present flow conditions, H_w is found to be lower than C_w at low oil flow rates when the oil phase is more eccentric. H_w gets close

to C_w at medium oil flow rates, and becomes higher than C_w when the oil phase is more concentric. Correspondingly, the oil-water slip ratio of core annular flow is lower than 1 when the oil core is more eccentric, and higher than 1 for virtually concentric CAF.

The pressure gradient of water-lubricated flow is reduced to 2% to 20% of the pressure gradient of single oil flow for the flow conditions investigated. This shows the great energy-saving benefit of water-lubricated heavy oil transport. The pressure gradient of water-lubricated flow can be one to two orders of magnitude higher than that of single water flow. This increased frictional loss is thought to be mainly associated with the oil fouling on the pipe inner wall. The influence of oil fouling on the pressure gradient should be accounted for to improve the present models which rarely consider oil fouling influence.

5 MECHANISM ANALYSIS AND EMPIRICAL MODELLING

5.1 Introduction

Flow characteristics of high-viscosity oil-water flow have been discussed based on experimental results in Chapter 4. To have a better understanding of the flow behaviours, mechanisms behind these are investigated and discussed. Evaluation of existing empirical and mechanistic models is presented as well as attempts on model development.

Similar to the experimental results discussion presented in Chapter 4, the investigation on flow mechanisms and modelling of high-viscosity oil-water flow includes the aspects of 1) flow patterns of liquid-liquid flow; 2) inversion occurrence; and 3) prediction of water holdup and pressure gradient of water lubricated flow.

5.2 Flow patterns of liquid-liquid flow

It has been demonstrated in Chapter 4 that the flow regime maps produced from different studies can differ slightly or significantly. Some flow maps are comparable with same basic flow patterns and similar transition trends, while some flow maps are not comparable with different basic flow regimes (see Section 4.3.2 in Chapter 4). The physics behind the flow regimes was investigated. The investigation started from a survey of flow patterns in liquid-liquid flows in horizontal pipelines. The gravitation to viscous force ratio was proposed and validated to characterise different liquid-liquid flows with different basic flow regimes.

5.2.1 Literature review on flow patterns of liquid-liquid flows in horizontal pipes

Diverse flow patterns in liquid-liquid flows have been reported in the literature. The identification of flow patterns is commonly based on visual observation and photograph/video techniques when visual observation is possible. Some recent studies applied conductivity probes (e.g., Vielma et al, 2008; Liu et al., 2008),

high frequency impedance probes (e.g., Angeli and Hewitt, 2000) or hot-film anemometer probes (e.g., Farar and Bruun, 1996; McKibben et al., 2000a) to obtain local phase configuration information. Non-invasive measurement techniques such as Gamma densitometers, X-ray, or particle image velocimetry (PIV) are also applied (e.g., Kumara et al, 2010; Yang, 2014). A review on liquid-liquid flow patterns in horizontal pipeline flow is presented as follows.

5.2.1.1 Low-viscosity oil-water flow

(1) Most studies - stratified and dispersed flow

Trallero et al. (1997) reviewed flow patterns of low-viscosity ($1.3 \leq \mu_o/\mu_w \leq 167$), unequal-density ($0.75 \leq \rho_o/\rho_w \leq 0.9$) oil-water flow in horizontal pipes with internal diameters ranging from 24 to 59 mm. He proposed six flow patterns in two basic categories - segregated flow (ST, ST & MI) and dispersed flow (Do/w & w, Do/w, Dw/o & Do/w, Dw/o). Two more specific flow patterns – Dw/o & w and Dw/o & Do/w & w, which can be categorised into the dispersed flow, were reported by Nädler and Mewes (1997). Figure 5-1 shows sketches of these flow patterns. Nädler and Mewes (1997) also observed that there is little effect of viscosity on the flow characteristics from measurements conducted for oil viscosities of 22, 27 and 35 cP. Angeli and Hewitt (2000) studied flow structures in 1 inch stainless steel and acrylic resin pipes respectively. Though different nomenclatures were used by the authors, flow patterns observed are consistent with the flow patterns depicted in Figure 5-1. A flow regime of Three Layer (3L) was proposed to describe flow in which a mixed layer is present between the water and oil layers at the bottom and top of the pipe respectively. This flow regime corresponds to ST & MI when the mixing at the interface is intense leading to a thick mixing layer. They also found that flow patterns in the steel pipe were in general more disturbed (i.e., having a wider fully dispersed region) than those in the acrylic pipe and attributed this to the higher roughness of the steel pipe. Lovick and Angeli (2004) used the term of dual continuous flow (both

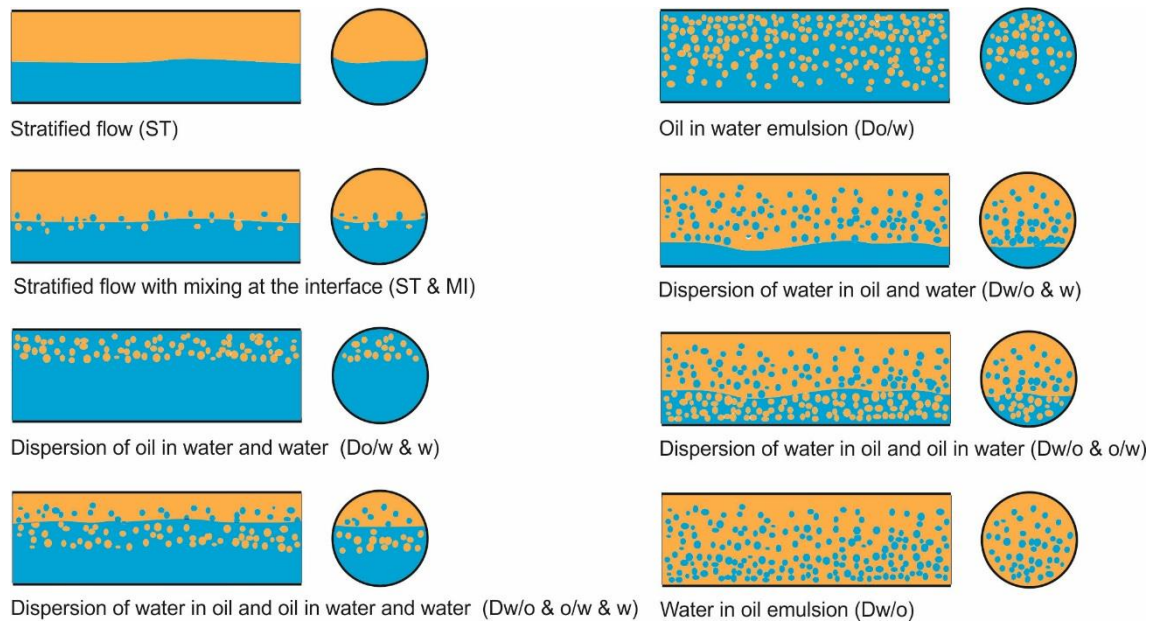


Figure 5-1 Sketches of most frequently reported flow patterns of low-viscosity, unequal-density oil-water flow in horizontal pipes (adapted from Trallero et al. (1997) and Nädler and Mewes (1997)).

phases retain their continuity at the top and bottom of the pipe while there is interspersed) to describe transition between stratified flow and dispersions of one phase in another phase. Following this classification, dual continuous flow includes ST & MI and Dw/o & Do/w defined by Trallero et al. (1997), Dw/o & w and Dw/o & Do/w & w by Nädler and Mewes (1997) and 3L by Angeli and Hewitt (2000).

Most experimental studies on low-viscosity oil-water flow in the literature show consistence in flow structures. Stratified flow and dispersed flow are two basic phase configurations; transition between the basic flow regimes leads to more specific flow structures. However, there are a few low-viscosity oil-water studies in which different flow patterns were observed as presented in the following two sections.

(2) Density-matched oil-water flow – annular, intermittent, and dispersed flow

Different flow characteristics are shown for density-matched oil-water flow. Charles et al. (1961) investigated equal-density oil-water flow in a horizontal 1

inch pipe. Oils with viscosities of 6.29, 16.8 and 65.0 cP were used in the experiments. Five flow patterns, namely dispersed oil drops in water (Do/w), core annular flow (CAF), oil slugs in water (OSL), oil bubbles in water (OBL), and dispersed water drops in oil (Dw/o), were observed. OSL and OBL can be grouped into intermittent flow. These phase configurations are shown in Figure 5-2. Compared to the flow patterns of low-viscosity unequal-density oil-water flow introduced above, the common flow patterns are Do/w and Dw/o. The annular and intermittent flow regimes were newly observed flow patterns while stratified flow was not observed. It is apparent that this significant difference in flow structures comes from the equal-density of the two phases. Without the difference of gravitational forces, the two phases do not become stratified. The Weber number ($We = \frac{\rho U^2 D}{\sigma}$) which represents the relative effect of the inertial force versus interfacial tension can be used to describe the flow characteristics. When the flow kinetic energy of the two immiscible liquids is not sufficient to cause the formation of dispersed flow, the flow exists in forms of one phase flowing forward, continuously (e.g., CAF) or discontinuously (e.g., OPL and OBL), inside the other phase. Normally the phase with a higher viscosity would flow inside the phase with a lower viscosity (see reviews on core annular flow by Oliemans and Ooms (1986) and Joseph et al., (1997)).

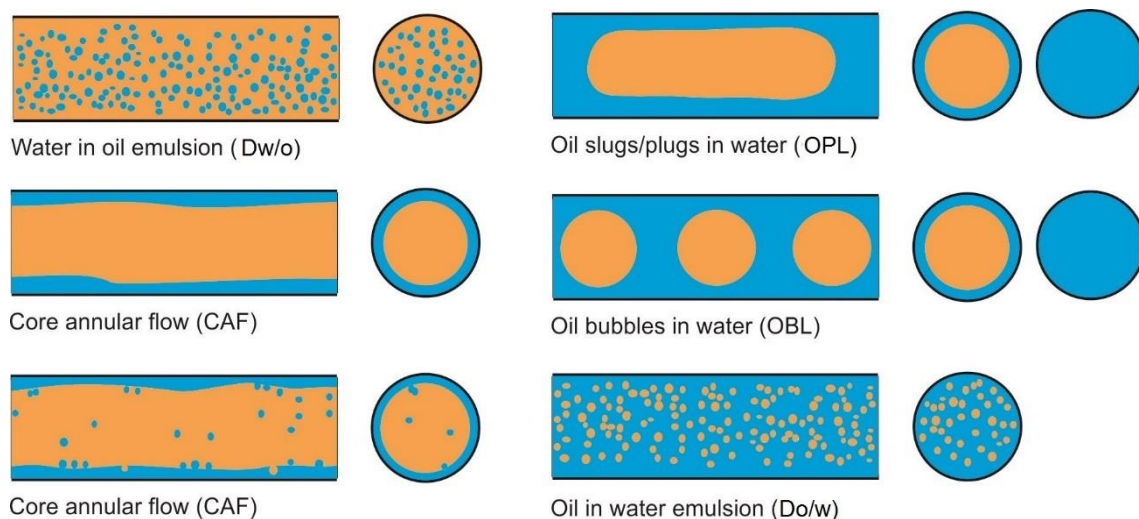


Figure 5-2 Sketches of flow patterns of low-viscosity, equal-density oil-water flow in horizontal pipes (adapted from Charles et al., 1961).

(3) Flow in small diameter pipes – stratified, annular, Intermittent, and dispersed flow

The flow patterns of oil-water flow in small diameter pipes also show difference from those observed in most studies on low-viscosity oil-water flow. It is difficult to define a size range for the so-called small diameter pipes. Normally the pipe I.D. is smaller than 1 inch and larger than 2 mm when the term of small diameter is used (e.g., see Barnea et al, 1983; Beretta et al., 1997).

Russell et al. (1959) conducted experiments on horizontal oil-water flow in a 20.5 mm I.D pipe. The viscosity of the oil used in their experiments is 16.8 cP. Stratified, intermittent (oil slugs/plugs, oil bubbles in water), and dispersed flow were observed. Though this study was among the studies surveyed by Trallero et al. (1997) in their review on low-viscosity oil-water flow patterns, the intermittent flow did not draw the above authors' attention since all the other studies in their survey reported exclusively stratified and dispersed flow.

Wegmann and Rudolf von Rohr (2006) conducted experiments on horizontal oil-water flow in pipes with internal diameters of 5.6 and 7mm. The viscosity of the paraffin oil used in their experiments varied from 4.3 cP to 5.2 cP. They observed stratified, intermittent (oil slugs/plugs in water), annular, and dispersed flow. Dispersions of water in the oil core of annular flow were observed. A comparison was made between the flow pattern map produced from their experiments to that produced by Angeli and Hewitt (2000). As one can expect, a large difference between the flow pattern maps was shown since the types of flow patterns observed in the two studies are not consistent (only stratified and dispersed flow were encountered in Angeli and Hewitt (2000)).

In general, expect for stratified flow and dispersed flow, intermittent flow and/or annular flow are encountered for low-viscosity unequal-density oil-water flow in small diameter pipes.

5.2.1.2 High-viscosity oil-water flow

Since the experiment of Charles et al. (1961), experiments on high-viscosity oil-water flow have been carried out due to the great potential of core annular flow in transporting heavy crude oil. Ooms et al. (1984) conducted experiments on high-viscosity oil-water flow in horizontal pipes. Oil viscosities investigated by the above authors vary from 2 300 to 3 300 cP in a 2 inch pipe and 1 200 to 2 200 cP in an 8 inch pipe. It was reported that CAF would form as long as the oil was supplied at velocity above a certain critical value (~ 0.1 m/s). With a focus on CAF, only CAF was reported without information of other flow structures formed in their experiments. Studies focused on CAF can also be found in Oliemans et al. (1987) and Bannwart (1998). McKibben et al. (2000a and 2000b) investigated heavy oil-water flows in horizontal pipelines. Experiments were conducted in pipelines with internal diameters of 53 and 105 mm using high-viscosity lube oil and crude oil. They found that at low mixture velocities and/or low water fractions there exists an intermittent phase where water intermittently reduces the pressure gradient of heavy oil flow and associated this phase with water slugs which envelop some oils. They also observed continuous water-assisted flow with oil fouling on the internal pipe wall at high velocities and/or water fractions. Grassi et al. (2008) conducted experiments on oil-water flow in both horizontal and slightly inclined (up to $\pm 15^\circ$) pipes (I.D.=21 mm) using oil with a viscosity around 800 cP. Core annular flow and dispersed oil in water were found to be the dominant flow regimes; oil slugs/plugs in water and stratified flow were also observed under a few limited flow conditions. No substantial differences were found with change in inclination angles. It should be noted that the specific phase configuration of dispersed oil in water for high-viscosity oil-water flow is different from that for low-viscosity oil-water flow in the degree of dispersion. Emulsion or fine dispersed drops of one phase in the other phase is developed in low-viscosity oil-water flow, while the dispersed oil in water defined by Grassi et al. (2008) shows the characteristic that the oil is dispersed into lumps with varying sizes. Sotgia et al. (2008) reported their experimental investigation on oil-water flow in horizontal pipes (I.D. varies from

21 to 40 mm) using oil with a viscosity around 900 cP. Flow patterns observed are similar to those reported by Grassi et al (2008). Sridhar et al. (2011) conducted experiments on high-viscosity oil-water flow in horizontal and slightly inclined pipes. The oil used has a viscosity range from 200 to 1 100 cP. The basic two flow structures observed are stratified flow and core annular flow. More specific flow nomenclatures were used by the authors depending on whether there were dispersed oil drops at the interface and whether oil fouling film on the pipe wall was observed. The present study investigated flow characteristics of high-viscosity oil-water flow in a horizontal 1 inch pipe with oil viscosity varying from 3 300 cP to 16 000 cP. A transition between oil-continuous and water-continuous flow characterised with spiral motion of water and oil was observed. Specific flow structures in water-continuous flow were further classified into core annular flow, oil plugs in water and dispersed oil lumps in water.

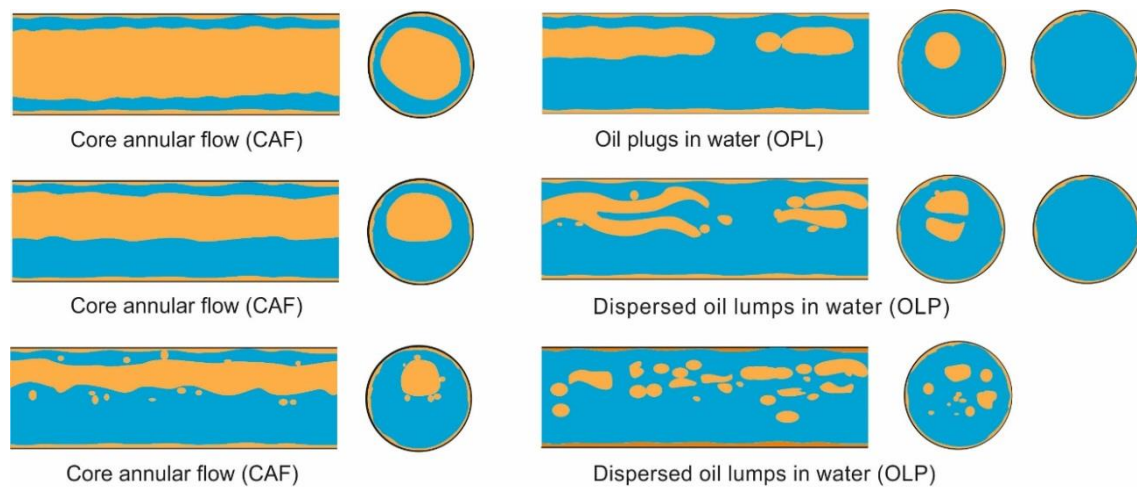


Figure 5-3 Sketches of major flow patterns of water-continuous high-viscosity oil-water flow in horizontal pipes (references: Joseph et al. (1997), Grassi et al. (2008), Sotgia et al. (2008), Sridhar et al. (2011), Al-Awadi (2011) and the present study).

In general, CAF is a dominant flow pattern developed in a wide range of phase flow rates in high-viscosity oil-water flows. Intermittent (oil slug/plugs in water) and dispersed oil in water are usually encountered. Oil dispersion in water is different from Do/w emulsions in views of irregularity and variety in the shape and size of the dispersed phase, and the instability of the mixture. Stratified flow is reported for limited flow conditions. Specific flow structures in oil-continuous flow are less reported due to reduced region of oil-continuous flow, difficulty in visual observation for oil-continuous flow as well as more interest on water-continuous flow. Figure 5-3 shows sketches of most frequently reported water-continuous flow patterns in horizontal high-viscosity oil-water pipeline flow. The characteristics of core annular flow vary depending on flow conditions. More concentric CAF is reported for oils with higher densities and/or higher flow rates. Eccentric CAF is normally observed for oils with relatively smaller densities and/or under higher water content. Besides, droplets may form at the interface of the phases. It is also noted that oil fouling on the pipe wall is depicted out in Figure 5-3. Oil fouling on the pipe wall in high-viscosity oil-water flow is mentioned or emphasised in various published works such as Grassi et al. (2008), McKibben et al. (2000a and 2000b), Sridhar et al. (2011), Al-Awadi (2011), Alagbe (2013), and the present study. It is an important phenomenon for high-viscosity oil-water flow.

5.2.1.3 Summary

In general, the diverse flow patterns in horizontal oil-water pipeline flow can be grouped into four basic categories: 1) stratified flow with either smooth or wavy interface (ST); 2) dispersed flow (D); 3) intermittent flow, including slugs/plugs and elongated bubbles of one phase in another phase (I); and 4) core annular flow, (CAF). Other phase configurations can be regarded as transitional flow regimes between two of the above basic flow regimes.

Oil viscosity plays an essential role in flow structures of oil-water flow, though the influence of oil viscosity may not be evident for certain ranges. Low-viscosity oil-water flow and high-viscosity oil-water flow are characterised with different

flow patterns. For low-viscosity oil-water flow, different flow characteristics are shown for density-matched oil-water flow, or for flow in small diameter pipes. This suggests that the density difference and pipe diameter also affect phase configurations. It is suspected that the quantitative change of flow system parameters, such as liquid viscosity, density and pipe diameter, leads to qualitative change of flow structures at critical conditions.

5.2.2 Gravitation to viscous force ratio to characterise liquid-liquid flow systems

Brauner (1998) proposed that a pipe flow system could be characterized by a dimensionless Eötvös number (Eo'). The Eo' is expressed as

$$Eo' = \frac{\Delta\rho g D^2}{8\sigma} \quad (5-1)$$

where $\Delta\rho$ is the density differential, kg/m^3 ; g is the gravitational acceleration, m/s^2 ; D is the pipe internal diameter, m ; and σ is the interfacial tension, N/m . The factor '8' was introduced by the above author when the Young-Laplace equation for predicting the interface shape in stratified flow was solved, as this dimensionless group was evolved in the analysis (see Brauner et al., 1998). More widely, the Eötvös number (Eo) is defined as

$$Eo = \frac{\Delta\rho g D^2}{\sigma} \quad (5-2)$$

In this thesis, the notations of Eo' and Eo are used for specific context and general context separately.

The Eötvös number is the ratio of gravitational force to surface or interfacial tension. For liquid-liquid flows with a small Eötvös number, the interfacial tension plays a dominant role and core annular flow is a natural configuration which complies with the interfacial tension. For liquid-liquid flows with a large Eötvös number, the gravitational force has more influence on the flow characteristics thus the flow tends to stratify. Brauner (2002) suggested that it is beneficial to preliminarily classify the liquid-liquid flow system according to

whether $Eo' \gg 1$ or $Eo' < 1$. This is a first attempt to characterize liquid-liquid flows in a big picture. Mechanisms for the formation of different flow patterns were discussed by the above author for liquid-liquid flows of $Eo' \gg 1$ and $Eo' < 1$ separately. However, as the effect of viscosity ratio is not included in Eo' , highly viscous oil-water flow systems were further dealt with separately. Also, there is ambiguity concerning the amplitude of the lower threshold of Eo' for gravity dominant flows ($Eo' \gg 1$). A criterion for the existence of core annular flow was proposed by Bannwart (2001) making use of Eo' . The criterion is that CAF is likely to form when $Eo' < \frac{4}{\pi\varepsilon}$ (ε is the volume fraction of the core, $Eo' < 2.55$ with $\varepsilon = 0.5$).

A survey on the Eo' of different liquid-liquid flows was conducted as included in Table 5-1. We can observe that CAF tends to form in liquid-liquid flows with low Eo' , while CAF can also develop in liquid-liquid flows with higher Eo' , e.g, experiments of Sridhar et al. (2001), McKibben et al. (2000b) and Ooms et al. (1984). For liquid-liquid flows with higher Eo' , CAF is formed only for oils with high viscosity.

The Eötvös number incorporates the parameters of phase densities, pipe diameter, and surface tension which can affect flow structures of oil-water flow. However, the oil viscosity is not included in this dimensionless number. From the above review on flow patterns of liquid-liquid flows in horizontal pipes, it is demonstrated that the oil viscosity plays an essential role in phase configuration of oil-water flows. Also, the influence of interfacial tension on phase configuration is not clearly reflected in Table 5-1. The interfacial tension between oil and water varies from 0.017 to 0.062 N/m and CAF can be formed under either a large or small interfacial tension.

To include the role that oil viscosity plays in the phase configuration of liquid-liquid flows, it is proposed to use the ratio of the gravitational force to viscous force to characterise liquid-liquid flows featured with different basic flow regimes. The gravitation to viscous force ratio can be expressed as

$$G/V = \frac{\Delta\rho g D^2}{\mu U} \quad (5-3)$$

The gravitation to viscous force ratio reflects the competitive role of gravitational force and viscous force on phase configuration of oil-water flows. The viscous force is expressed as the product of the characteristic viscosity and velocity; the viscosity and velocity of the more viscous phase, normally the oil phase, i.e., μ_o and U_o , are used as the characteristic viscosity and velocity. When the local oil phase velocity is not known, the mixture velocity, U_m , can be used as the characteristic velocity. For liquid-liquid flows with a high G/V , the gravitational force dominates, or the viscous force is relatively small hence the fluid is easy to be broken up when the flow kinetic energy is high, stratified flow (ST) or fine dispersions of one fluid in another (D) are two basic flow structures developed. For liquid-liquid flows with a low G/V , the effect of the gravitational force is relatively small hence stratified flow is less likely to form. The flow configures itself in forms of oil core flowing inside annular water, continuously to form annular (CAF) or discontinuously to form intermittent (I), in which the shear stress can be minimised. Also when the flow turbulence kinetic energy is high, the higher viscosity phase is too viscous to be broken into fine drops but lumps of irregular sizes and shapes. This kind of flow structure can be regarded as a transition from intermittent to the ultimate dispersed flow. For liquid-liquid flows with a medium G/V , the gravitational force and the viscous force together affect flow structures and all the four basic phase configurations, i.e., ST, CAF, I, D, can be developed.

It is noted that the gravitation to viscous force ratio can be expressed as the ratio of the Eötvös number (E_o) to the Capillary number (Ca), or the ratio of the Reynolds number to the Froude number, i.e., $G/V = E_o/Ca = Re/Fr$. The Eötvös number represents the relative effect of the gravitational force versus interfacial tension as introduced in Equation (5-2). The capillary number represents the relative effect of the viscous forces versus interfacial tension between two immiscible liquids (see Equation 5-4). The Reynolds number represents the

relative effect of the inertial force versus viscous force, and the Froude number the relative effect of the inertial force versus gravitational force (see Equation 5-5 and 5-6).

$$Ca = \frac{\mu U}{\sigma} \quad (5-4)$$

$$Re = \frac{\rho U D}{\mu} \quad (5-5)$$

$$Fr = \frac{U}{\sqrt{g D \frac{\Delta \rho}{\rho}}} = \frac{U^2}{g D \frac{\Delta \rho}{\rho}} \quad (5-6)$$

For the gravitation to viscous force ratio, the interfacial tension and inertial force are not included. The interfacial tension and inertial force are also important in the phase configuration of liquid-liquid flow. However, when looking at the liquid-liquid flow characterised with different basic flow regimes instead of specific flow regimes, it is thought that the gravitational force and viscous force are two most influential forces.

A summary of liquid-liquid flows in horizontal pipes with attention on the basic flow patterns developed and the corresponding G/V are presented in Table 5-1. As the oil phase average velocity is usually not known, the mixture flow velocity is used as the characteristic velocity to estimate the gravitation to viscous force ratio. It can be observed that the magnitude of this dimensionless number corresponds to certain flow patterns as analysed above. For liquid-liquid flows with high gravitation to viscous force ratio, only ST and D are formed (e.g., Angeli and Hewitt, 2000; Lui et al., 2008; Lovick and Angeli, 2004; Trallero et al., 1997; Vielma et al., 2008; Nädler and Mewes, 1997). For liquid-liquid flows with low gravitation to viscous force ratio, CAF and I are the basic flow regimes (e.g., McKibben et al., 2000b; Al-Awadi, 2011; Alagbe, 2013; and the present study). One exception is the study of Charles et al. (1961) of which the gravitational force or buoyancy force to stratify the fluids is not affecting the phase configuration. This study is excluded in this context in our analysis due to the

essential difference for density-matched liquid-liquid flow. Some studies have a gravitation to viscous force ratio range overlapping both the high and the medium categories, e.g., Russell et al. (1959), and Sridhar et al. (2011), thus the reported flow patterns are among the possible flow patterns in both gravitational force dominant flow and gravitational force and viscous force comparable flow. Also, some studies have low to medium gravitation to viscous force ratios, e.g., Grassi et al. (2008) and Sotgia et al. (2008), thus the reported flow patterns are among the possible flow patterns in both viscous force dominant flow and gravitational force and viscous force comparable flow.

Table 5-1 Summary of experimental studies on liquid-liquid flows in horizontal pipes.

	Pipe I.D. (mm)	μ_o (cP)	ρ_o (kg/m ³)	σ (N/m)	Velocity range (m/s)	Eo' $(\frac{\Delta\rho g D^2}{8\sigma})$	G/V $(\frac{\Delta\rho g D^2}{\mu U})$	Basic flow patterns observed ^{a)}
Angeli and Hewitt (2000)	24	1.6	801	0.017	U_m :0.3-3.9	8.2	150-3 700	ST,D
Liu et al. (2008)	26.1	3.47	838	0.028	U_{so} : 0.05-0.96; U_{sw} :0.05-0.96	4.8	160-3 080	ST,D
Lovick and Angeli (2004)	38	6	828	0.0396	U_m : 0.8-3	7.6	100-600	ST,D
Trallero et al. (1997)	50	28.8	884	0.036	U_{so} : 0.01-1.6; U_{sw} :0.02-1.6	9.7	30-3 800	ST, D
Vielma et al. (2008)	50	18.8	859	0.029	U_{so} : 0.03-1.75; U_{sw} : 0.03-1.75	14.7	50-3 500	ST, D
Nädler and Mewes (1997)	59	22, 27, 35	845	0.04 ^b	U_m :0.1-1.6	16.3	100-2 400	ST, D
Russell et al. (1959)	20.5	18	832	0.04 ^b	U_{so} : 0.02-0.9; U_{sw} :0.04-1.08	2.1	18 -700	ST, I, D
Wegmann and Rudolf von Rohr (2006)	5.6, 7	4.3-5.2	818-821	0.062	U_{so} :0.01-2.5; U_{sw} :0.01-2	0.11- 0.17	2.4-80	ST, CAF, I, D

Table 5-1 Continued.

	Pipe I.D. (mm)	μ_o (cP)	ρ_o (kg/m ³)	σ (N/m)	Velocity range (m/s)	Eo' $(\frac{\Delta\rho g D^2}{8\sigma})$	G/V $(\frac{\Delta\rho g D^2}{\mu U})$	Basic flow patterns observed ^{a)}
Grassi et al. (2008)	21	800	886	0.05	U_{so} : 0.03-0.7; U_{sw} :0.2-2.5	1.2	0.2-4	ST, CAF, I, D
Sotgia et al. (2008)	21-40	919	889	0.02	U_{so} : 0.1-1.0; U_{sw} : 0.1-2.51	1.8-6.5	0.4-50	ST, CAF, I, D
Charles et al. (1961)	26	6.29, 16.8, 65	998	0.045	U_{so} : 0.02-0.9; U_{sw} :0.03-1.07	0	0	CAF, I, D
Sridhar et al. (2011)	52.5	220, 1 070	884	0.0304	U_{so} : 0.1-1.0; U_{sw} :0.1-0.5	12.8	2.4-140	ST, CAF
McKibben et al. (2000a)	53	620-920	884-885	0.04 ^{b)}	U_m :0.045	9.7 ^{c)}	72-112	ST
		5 300-11 000	971-976	0.04 ^{b)}	U_m :0.03-0.12	1.9-2.3 ^{c)}	0.4-4.8	CAF, I
McKibben et al. (2000b)	53	5 800-91 600	958-987	0.04 ^{b)}	U_m :0.5-1.2	0.9-3.4 ^{c)}	0.002-0.4	CAF, I
		105	7 100	958-984	0.04 ^{b)}	U_m :0.3-0.77	4.7-13.5 ^{c)}	0.07-2
Al-Awadi (2011)	26	3 840-16 000	906-938	0.04 ^{b)}	U_{so} :0.06-0.57; U_{sw} :0.01-1.0	1.2-2.0 ^{c)}	0.01-1.6	CAF, I
Alagbe (2013)	26	3 700-7 100	905-920	0.02	U_{so} :0.06-0.4; U_{sw} :0.2-1.0	3.2-3.8	0.04-0.8	CAF, I

Table 5-1 Continued.

	Pipe I.D. (mm)	μ_o (cP)	ρ_o (kg/m ³)	σ (N/m)	Velocity range (m/s)	Eo' $(\frac{\Delta\rho g D^2}{8\sigma})$	G/V $(\frac{\Delta\rho g D^2}{\mu U})$	Basic flow patterns observed ^{a)}
The present study	26	3 300-16 000	905-938	0.02	U_{so} :0.04-0.57; U_{sw} :0.01-1.18	1.2-3.8	0.01-1.6	CAF, I
Ooms et al. (1984)	50, 203.2	1 200-3 300	953-968	0.04 ^{b)}	U_{so} : 1.0; U_{sw} :0.01-0.25	2.3-55 ^{c)}	0.1-3.2	CAF ^{d)}
Oliemans et al. (1987)	50	3 000	978	0.04 ^{b)}	U_{so} : 0.5-1.0; U_{sw} : 0.03-0.25	1.5 ^{c)}	0.08-0.4	CAF ^{d)}
Bannwart (1998)	22.5	270	989	0.04 ^{b)}	U_{so} : 0.30-0.63; U_{sw} : 0.03-0.28	0.14 ^{c)}	0.1-0.5	CAF ^{d)}
Rodriguez and Baldani (2012)	26	280	828	0.034	U_{so} : 0.03-0.15; U_{sw} :0.1-0.15	4	12-32	ST ^{e)}

^{a)} Different nomenclatures are used by different authors. Only the basic flow patterns are listed.

^{b)} The interfacial tension is not reported; a medium value of 0.04 is used here as an estimate to calculate the corresponding Eo' .

^{c)} The Eo' is obtained with an estimated interfacial tension of 0.04.

^{d)} This experiment specifically focuses on core annular flow thus no other flow patterns are reported.

^{e)} This experiment specifically focuses on stratified flow thus no other flow patterns are reported.

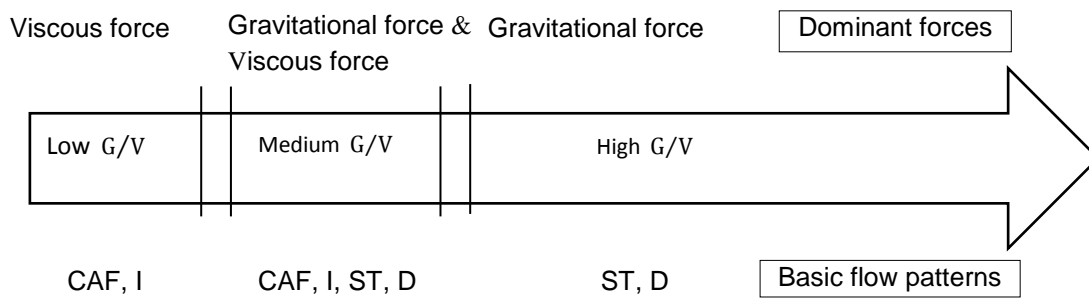


Figure 5-4 Liquid-liquid flows characterised with different basic flow patterns and the corresponding gravitation to viscous force ratio (G/V).

The change of basic flow patterns of liquid-liquid flows with the gravitation to viscous force ratio, $G/V = \frac{\Delta\rho g D^2}{\mu U}$, is illustrated by the diagram shown in Figure 5-4. An oil-water flow system can be gravitational force dominant flow (S_G), viscous force dominant flow (S_V), or gravitational force and viscous force comparable flow (S_{GV}). One can expect that the interface of stratified flow in S_{GV} has a higher curvature under effects of both the gravitational force and viscous force, which is different from the relatively flatter phase interface of stratified flow in S_G . Also, the dispersed flow in S_{GV} is different from the dispersed flow in S_G in terms of drop sizes and/or shapes.

The different flow maps produced from different experiments would be more comparable when the liquid-liquid flow systems are dominated by same force(s). Figures 5-5 to 5-8 demonstrate comparisons of flow maps with coordinates of the gravitation to viscous force ratio (G/V) and input water volume fraction (C_w). They are re-presentations of reported flow maps in the literature with either the superficial phase velocities (U_{so} and U_{sw}) or the input water volume fraction and the mixture velocity (C_w and U_{mix}) as coordinates.

Figure 5-5 shows a flow map for the gravitational force dominant oil-water flows (S_G). It is adapted from five different flow maps produced by Nädler and Mewes (1997), Trallero et al. (1997), Angeli and Hewitt (2000), Lovick and Angeli (2004) and Vielma et al. (2008). The five flow systems have diameters ranging from 24

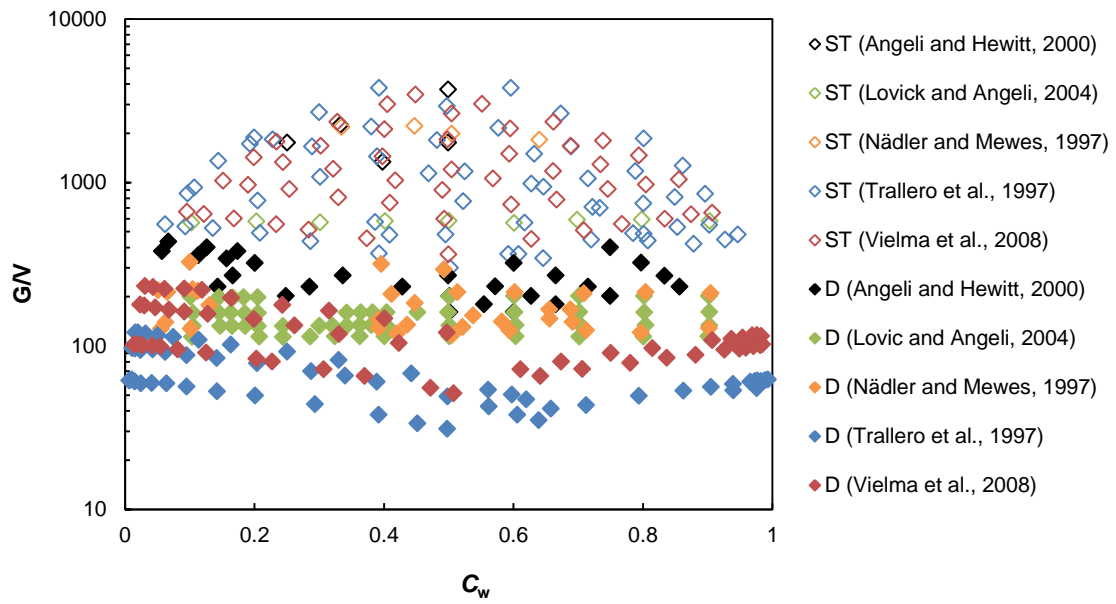


Figure 5-5 Basic flow patterns developed with gravitation to viscous force ratio (G/V) and C_w in gravitational force dominant two-phase oil-water flow (S_G).

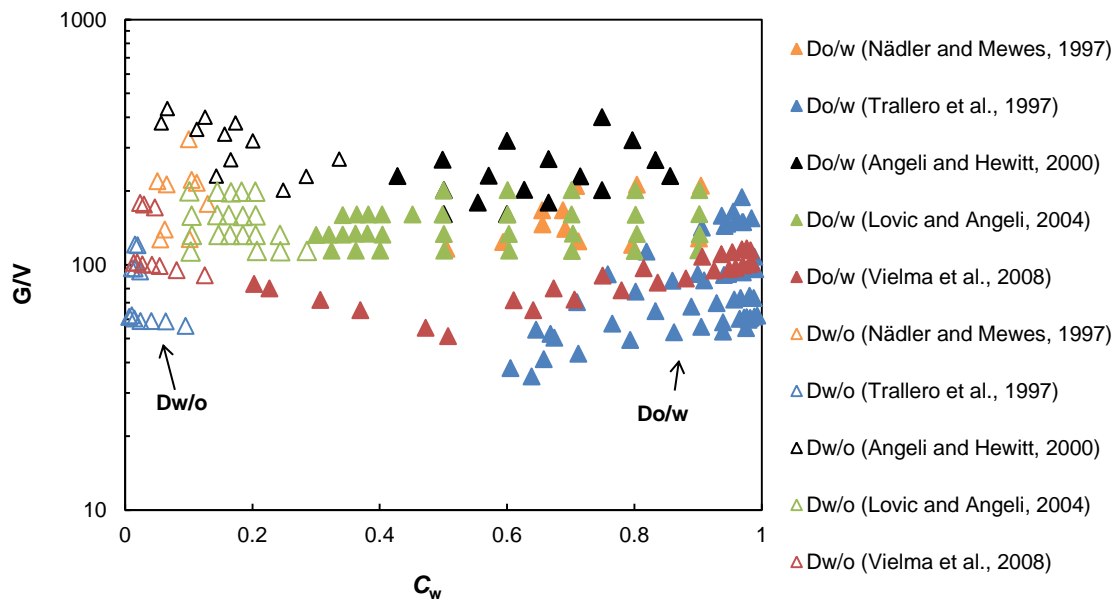


Figure 5-6 Specific dispersed flow patterns with gravitation to viscous force ratio (G/V) and C_w .

to 59 mm, oil densities from 801 to 884 kg/m³, and oil viscosity from 1.6 to 28.8 cP. The basic flow patterns reported for these flow systems are ST and D. These oil-water flows locate in a range of G/V from 40 to 4 000 approximately. It is interesting to observe that the stratified flow covers the range of G/V from 400 to 4 000 approximately, and the dispersed flow covers the range of G/V from 40 to 400 approximately.

Specific flow regimes for the dispersed flow are shown in Figure 5-6. It demonstrates that the dispersed water in oil (Dw/o) develops at low C_w , and the dispersed oil in water (Do/w) develops at high C_w . The dual-continuous flow such as Dw/o & W and Dw/o & Do/w develops at medium C_w around 0.4; this is a transitional buffer zone from oil-continuous to water-continuous flow. The transition from oil-continuous flow to dual-continuous occurs at a lower C_w with decrease of G/V . The decrease of G/V is mainly caused by increase of the oil viscosity or mixture velocity. To maintain a stable Dw/o, the turbulence level in the continuous oil phase needs to be sufficiently high to disperse the water phase into stable small droplets (Brauner, 2002). The turbulent kinetic energy of the oil phase decreases with increase of viscosity. Though the turbulent kinetic energy of the oil phase increases with increase of the mixture velocity, the turbulent kinetic energy of the water phase increases at the same time and can increase more quickly with increase of the mixture velocity due to a lower viscosity. When the turbulence level in the water phase is sufficiently high, the water phase can disperse the oil phase into drops initiating the transition from oil-continuous to dual-continuous flow. The transition from dual-continuous flow to water-continuous or the completion of the inversion occurs at a higher C_w for a lower G/V caused by the increase of the oil viscosity when comparing different experimental studies. This can be explained similarly from the degree of the phase turbulent kinetic energy. To maintain a stable Do/w, the turbulence level in the continuous water phase needs to be sufficiently high to disperse the oil phase into stable small droplets. When the oil is more viscous, the water phase needs higher turbulent kinetic energy to disperse the oil phase thus the critical water volume fraction to form stable Do/w increases. It is worth remarking that

apart from the influences of oil viscosity and mixture velocity, other parameters such as the interfacial tension, phase volume fraction increase method (continuously or discontinuously) and transition direction (from oil-continuous to water-continuous or the opposite) can also affect the transition from Dw/o to Do/w (see Brauner, 2002; Ioannou et al, 2005; Piela et al., 2006; Piela et al., 2008; Piela et al., 2009). It is hardly possible to include all the influences of different parameters on the inversion in one map.

Figure 5-7 shows a flow map for gravitational force and viscous force comparable flow (S_{GV}). This flow map is adapted from the two flow maps produced by Wegmann and Rudolf von Rohr (2006). The above authors conducted oil-water experiments in two small diameter pipes (5.6 and 7 mm) with a low-viscosity oil (4.3-5.2 cP). All the four basic flow patterns, i.e., ST, CAF, I, and D, are reported for these flow systems. The flow systems cover the range of G/V between 2 and 40. The stratified flow mainly covers the region of low to medium C_w and G/V between 10 and 40. The core annular flow mainly covers the region of low to medium C_w and G/V between 2 and 10. The intermittent flow develops at medium to high C_w and G/V between 2 and 40. The dispersed flow develops at low to medium C_w and G/V between 2 and 10.

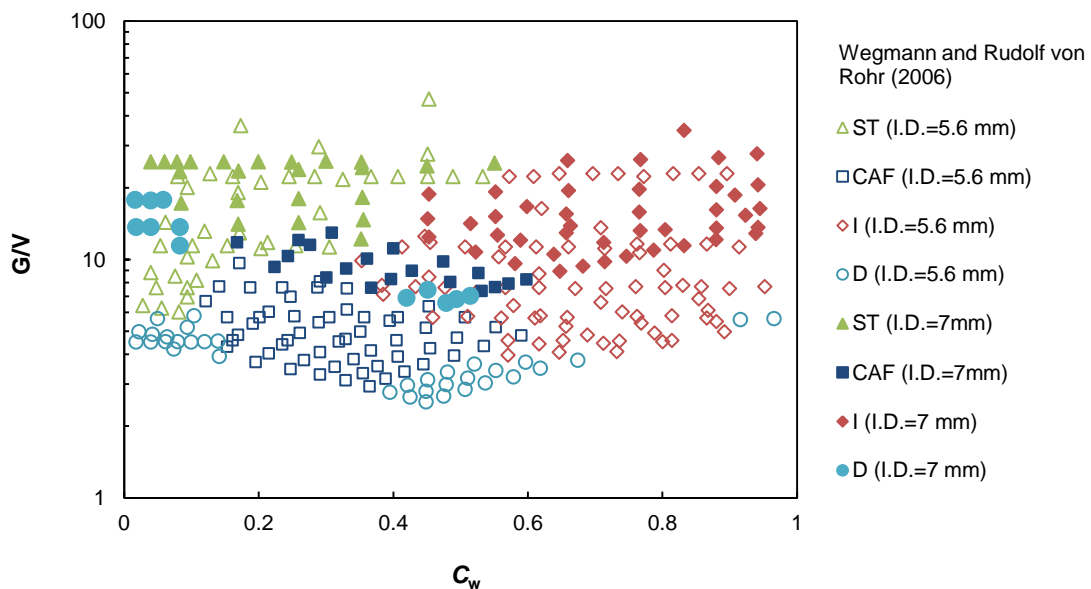


Figure 5-7 Basic flow patterns formed with gravitation to viscous force ratio (G/V) and C_w in gravitational force and viscous force comparable two-phase oil-water flow (S_{GV}).

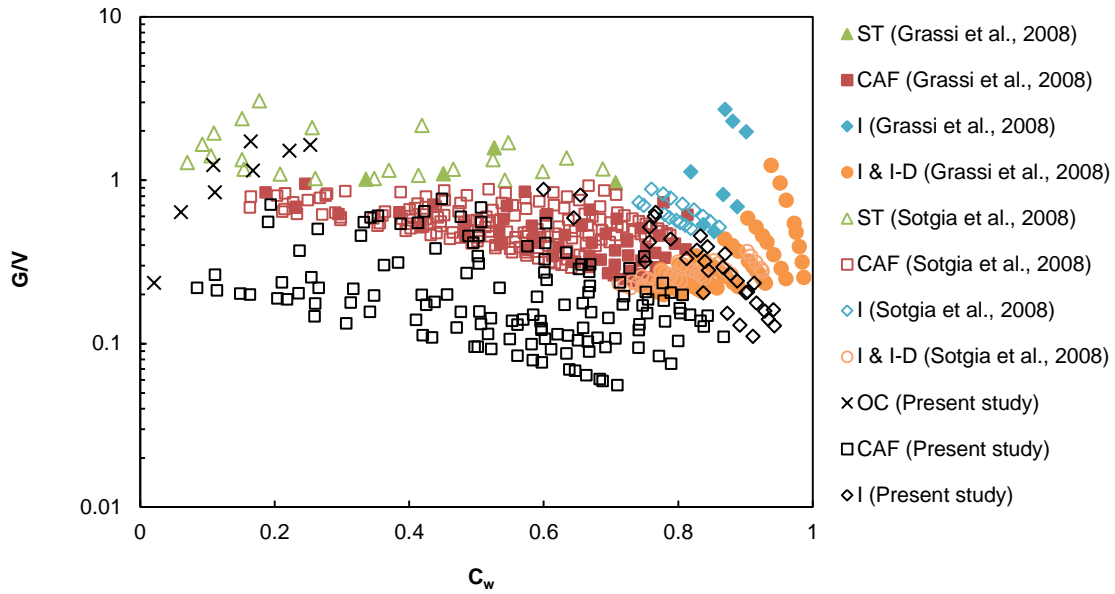


Figure 5-8 Basic flow patterns formed with gravitation to viscous force ratio (G/V) and C_w in mainly viscous force dominant two-phase oil-water flow (S_v and S_{GV}).

Figure 5-8 shows comparisons of flow maps produced by Grassi et al. (2008), Sotgia et al. (2008) and the present study. The liquid-liquid flow in the present study is mainly viscous force dominant flow having G/V lower than 1. The liquid-liquid flows investigated by Grassi et al. (2008) and Sotgia et al. (2008) cover low to medium G/V . It shows that the transition from gravitational force and viscous force comparable flow to viscous force dominant flow is around $G/V = 1$. Below 1, ST is rarely formed. CAF and I are the two basic flow patterns. The CAF covers a wide range of C_w . At very low C_w , the flow is oil-continuous flow, and at very high C_w , the flow is intermittent flow or transition from intermittent flow to dispersed flow (I-D). It is noted that the term of dispersed flow was used by Grassi et al. (2008) and Sotgia et al. (2008) to describe dispersed oil lumps in water. In this context, the dispersed flow defined by the above authors is grouped into I & I-D.

Combing all the experimental test points from Figures 5-5 to 5-8, a flow map is shown in Figure 5-9 with S_G , S_{GV} , and S_v covering different areas. The capability of the proposed gravitation to viscous force ratio to categorise different liquid-liquid flows is demonstrated. At very low G/V , the liquid-liquid flow is viscous

force dominant flow. The liquid-liquid flow becomes gravitational force and viscous force comparable flow when G/V increases to above a critical value around 1. The gravitational force and viscous force comparable flow becomes gravitational force dominant flow when G/V further increases to above a critical value around 40. These transitions of liquid-liquid two-phase flows can be analogical to the laminar-to-turbulent transition in single phase flow.

With respect to core annular flow, Figure 5-9 shows that CAF is the dominant flow regime in a viscous force dominant oil-water flow having G/V below 1. The transition from oil-continuous flow to CAF in a viscous force dominant oil-water flow is further investigated in the following section.

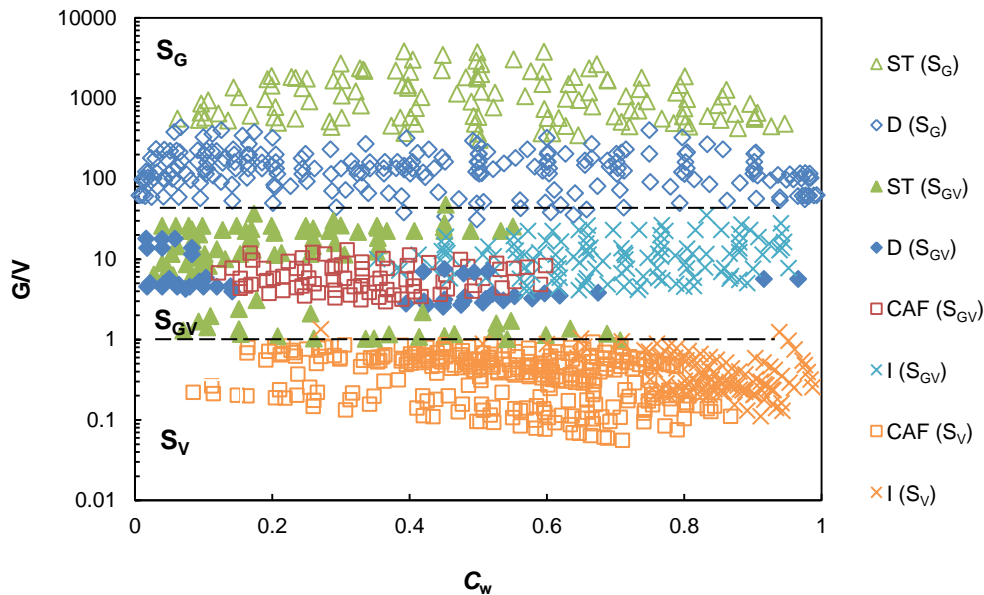


Figure 5-9 Basic flow patterns formed with gravitation to viscous force ratio (G/V) and C_w in two-phase oil-water flow, S_G , S_V , and S_{GV} . Source data: Nädler and Mewes (1997), Trallero et al. (1997), Angeli and Hewitt (2000), Lovick and Angeli (2004), Wegmann and Rudolf von Rohr (2006), Vielma et al. (2008), Grassi et al. (2008), Sotgia et al. (2008) and the present study. The dash lines represents approximate transitions between S_V , S_{GV} and S_G .

5.3 Inversion occurrence

For high-viscosity oil-water flow, the transition of most interest is the inversion from oil-continuous to annular-water-continuous. With increase in water content, the pressure gradient is reduced most near the completion of the inversion. The water content at which the inversion is completed is the lowest water content to form stable annular-water-continuous flow. Inversion occurrence prediction is of importance to guide the operation of water-lubricated heavy oil transport.

McKibben et al. (2000a and 2000b) suggested that the Froude number ($Fr = \frac{U_m}{\sqrt{gD \frac{(\rho_w - \rho_o)}{\rho_w}}}$) which reflects the ratio of the inertial force to gravitational force can be considered to describe the inversion. The mixture velocity, U_m , was used as the characteristic velocity for the calculation of Fr in McKibben et al. (2000b). Though no criteria was given by the above authors, an empirical inversion line in the flow map presented with the Froude number and input water volume fraction was drawn depicting the inversion (see Figure 5-10). In our experimental results, it is demonstrated that the superficial oil velocity affects the inversion occurrence (see Section 4.4 in Chapter 4). Following this direction, the inversion occurrence was investigated.

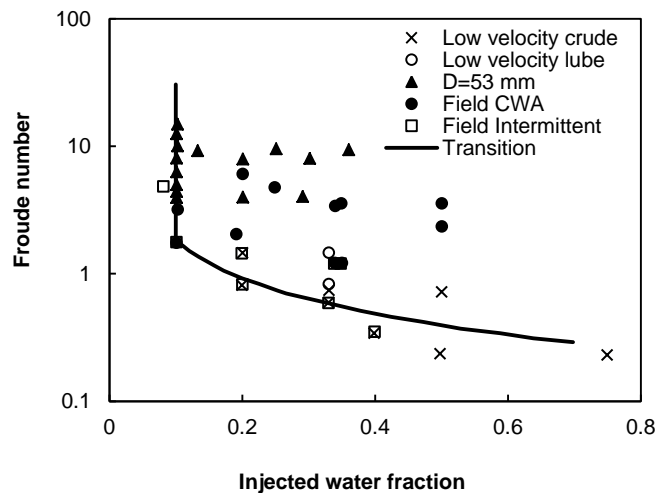


Figure 5-10 Froude number versus input water volume fraction for high-viscosity oil-water flows. All the data points except the one denoted as intermittent were continuous water-assisted flow (CWA) (adapted from McKibben et al., 2000b).

The use of Fr and input water volume fraction to describe the inversion from oil-continuous to annular-water-continuous can be linked to the use of Fr and water holdup to describe the transition from stratified flow to slug and/or annular flow in gas-liquid flow. In gas-liquid flow, the mechanism for the transition from stratified to slug and/or annular is usually explained from the Kelvin-Helmholtz theory (see Taitel and Dukler, 1976). According to the Kelvin-Helmholtz theory, the transition to slug and/or annular occurs when the gas flow velocity is sufficiently higher than the liquid wave propagation velocity. Similarly, the oil flow velocity is thought to be the critical parameter for the transition to annular flow in liquid-liquid flow. The inversion probably occurs when the oil flow velocity is sufficient higher than the water wave propagation velocity. Also, it is demonstrated in our experimental results that the oil flow rate affects the inversion occurrence significantly. Therefore, the Froude number with U_{so} as the characteristic velocity instead of U_m is adopted in our investigation of the inversion occurrence. In the following text, the Froude number has the definition

of $Fr = \frac{U_{so}}{\sqrt{gD \frac{(\rho_w - \rho_o)}{\rho_w}}}$ unless otherwise specified.

Figure 5-11 presents the flow regime map in views of the Fr and C_w for the oil viscosities (3 300 to 16 000 cP) investigated in the present study. Also, the inversion line given in McKibben et al. (2000b) as shown in Figure 5-10 is redrawn in Figure 5-11 for a comparison. As the Froude number used in McKibben et al. (2000b) was calculated with U_m as the characteristic velocity, a conversion was performed following

$$Fr = Fr_m (1 - C_w) \quad (5-7)$$

Where Fr_m is the Froude number with U_m as the characteristic velocity, and Fr is the Froude number with U_{so} as the characteristic velocity.

As the transition from oil-continuous to water-lubricated flow is a buffer zone, a regression to fit the experimental data points of the completion of the inversion is shown in Figure 5-11. The completion of inversion is of our concern as stable

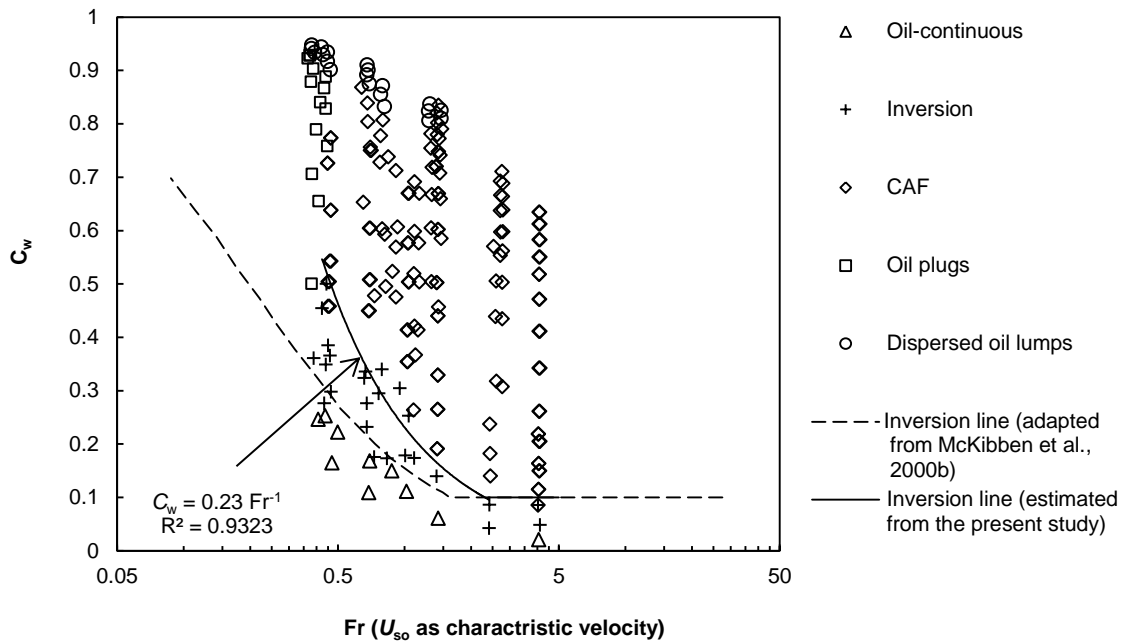


Figure 5-11 Input water volume fraction versus Fr for high-viscosity oil-water flow.

core annular flow starts to be formed after the inversion completion. The empirical inversion line given in McKibben et al. (2000b) appears to be the initiation of the inversion where the pressure gradient starts to be reduced. It is noted that the transition line estimated by McKibben et al. (2000b) is obtained from their experimental data with different pipe diameters of 53 and 105 mm. The transition line fits well between the oil-continuous flow and the inversion buffer zone of the present study, which shows the feasibility of Fr to describe the inversion for high-viscosity oil-water flow in different pipe diameters.

Figure 5-11 demonstrates that the input water volume fraction required to form stable core annular flow decreases with increase in Froude number until to a critical Froude number above which the inversion occurs as long as the water content is above a minimum of around 10%. The Froude number range for the present experimental data is from 0.4 to 4; the Froude number range for the experimental study of McKibben et al. (2000b) is from around 0.1 to 30. An empirical criterion for the formation of stable CAF is obtained as

$$Fr > Fr_c,$$

$$C_w \geq 0.1 \quad (5-8)$$

$$0.4 < Fr < Fr_c,$$

$$C_w \geq 0.23Fr^{-1} \quad (5-9)$$

$$Fr = \frac{U_{so}}{\sqrt{gD \frac{(\rho_w - \rho_o)}{\rho_w}}} \quad (5-10)$$

where the Fr_c is around 2.5. Equation (5-9) is tentative when it is applied for Fr lower than 0.4 and the feasibility must be checked.

The minimum input water volume fraction to form stable water-lubricated flow can be estimated through the above empirical criterion. It provides quantitative estimations of safe and economically viable operation conditions of water-lubricated high-viscosity oil-water flow for viscous force dominant oil-water flow.

5.4 Water holdup and pressure gradient of water-lubricated flow

Accurate prediction of the water holdup and pressure gradient of water-lubricated flow can provide guide to the design and operation of engineering practice. Simple empirical/phenomenological and mechanistic models take little account of the details across the flow direction, but they can be quite successful for predicting design parameters such as the pressure gradient and water holdup. Compared to three dimensional CFD modelling, they are computationally cheap and can provide useful solutions for industrial applications.

The empirical/phenomenological models associated with water-lubricated flow in the literature treat the oil-water flow as one mixture fluid and propose empirical correlations for the mixture fluid properties and the friction factor. The mechanistic models treat the immiscible fluids separately with their own sets of governing equations; they are called two-fluid models as well. The mechanistic models normally require closure relationships developed from experimental

data to get solutions thus the mechanistic models are actually semi-empirical. A review on existing models in the literature is presented first, followed by an attempt on development of an empirical model. Finally, evaluation of models with experimental data is presented.

5.4.1 Review on models of water-lubricated flow

(1) Arney et al. (1993)

Arney et al. (1993) deduced a counterpart (\Re) similar to the Reynolds number by applying the Navier-Stokes equation to the perfect liquid-liquid laminar core annular flow. The deduced Reynolds number, \Re , is defined as

$$\Re = \frac{\rho_m U_m D}{\mu_w} [1 + \eta^4 (m - 1)] \quad (5-11)$$

$$\eta = \frac{d_o}{D} = \sqrt{1 - H_w} \quad (5-12)$$

$$m = \frac{\mu_w}{\mu_o} \quad (5-13)$$

where ρ_m is the mixture density, $\rho_m = (1 - H_w)\rho_o + H_w\rho_w$; U_m the mixture velocity, $U_m = U_{so} + U_{sw}$; d_o the oil core diameter; H_w the water holdup. A reliable estimate of d_o (or H_w) is needed for the calculation of \Re , hence the pressure gradient. An empirical correlation between water holdup, H_w , and input water volume fraction, C_w , was given as

$$H_w = C_w [1 + 0.35(1 - C_w)] \quad (5-14)$$

The friction factor for the perfect laminar CAF, λ , is expressed as

$$\lambda = \frac{64}{\Re} \quad (5-15)$$

For turbulent flow, the Blasius formula was adopted, thus

$$\lambda = \frac{0.316}{\Re^{0.25}} \quad (5-16)$$

Knowing the friction factors, the pressure gradient of core annular flow can be estimated following the Darcy-Weisbach equation

$$-\frac{dp}{dz} = \frac{\lambda}{D} \frac{\rho_m U_m^2}{2} \quad (5-17)$$

As the λ in the model of Arney et al. (1993) is deduced theoretically for perfect laminar CAF, oil fouling on the pipe inner wall is not considered in the model. It is likely that this model would under predict the pressure gradient of high-viscosity oil CAF in which oil fouling is normally observed.

(2) Bannwart (2001)

Bannwart (2001) proposed to use the traditional expressions of the pressure gradient with a modified mixture viscosity and modified friction factor coefficients.

For laminar-laminar perfect core annular flow, the pressure gradient can be expressed as

$$-\frac{dp}{dz} = 64 \left(\frac{\rho_m U_m D}{\mu_m} \right)^{-1} \frac{\rho_m U_m^2}{2D} = \frac{32\mu_m U_m}{D^2} \quad (5-18)$$

where ρ_m is the mixture density, $\rho_m = \varepsilon\rho_o + (1 - \varepsilon)\rho_w$; U_m is the mixture velocity, $U_m = U_{so} + U_{sw}$; μ_m is the mixture viscosity, and it is defined as

$$\frac{1}{\mu_m} = \frac{\varepsilon^2}{\mu_o} + \frac{1 - \varepsilon^2}{\mu_w} \cong \frac{1 - \varepsilon^2}{\mu_w} \quad (5-19)$$

where ε is the oil holdup. In Bannwart (2001), the oil holdup follows

$$\varepsilon = \frac{1}{1 + s_{i,o} \frac{U_{sw}}{U_{so}}} \quad (5-20)$$

where $s_{i,o}$ is the slip ratio of the two fluids. It is noted that this parameter is usually unknown as well. Bannwart (2001) reported different values of $s_{i,o}$ for different flow systems based on wave speed measurement; $s_{i,o}=1$ was adopted for simplicity when it is unknown.

For laminar-turbulent core annular flow (when the annulus Reynolds number $Re_{sw} = \frac{\rho_w U_w D}{\mu_w} > 2000$), the pressure gradient can be expressed as

$$-\frac{dp}{dz} = b \left(\frac{\rho_m U_m D}{\mu_m} \right)^{-n} \frac{\rho_m U_m^2}{2D} \quad (5-21)$$

A modified expression for the mixture viscosity was proposed by Bannwart (2001) for turbulent annular flow, which is expressed as

$$\frac{1}{\mu_m} = \frac{\varepsilon}{\mu_o} + \frac{1 - \varepsilon}{\mu_w} \cong \frac{1 - \varepsilon}{\mu_w} \quad (5-22)$$

Instead of the normally used coefficients of b and n in single phase flow, e.g., $b = 0.316$ and $n = 0.25$, the coefficients were determined from regression of experimental data in Bannwart (2001). According to the author, the coefficients account for the wall conditions (fouling and roughness) in the two-phase flow. Using this method to fit two groups of experiments of high-viscosity oil-water flow in steel and cemented pipes respectively, the parameters obtained by Bannwart (2001) are $b = 0.305$, $n = 0.159$ for cemented pipe and $b = 0.066$, $n = 0.047$ for oil fouled steel pipe with $s_{i,o} = 1$.

The model of Bannwart (2001) requires three unknowns, namely the slip ratio of two fluids and two friction factor coefficients, which are supposed to be determined from experiments. A slip ratio of 1 is recommended when it is unknown, while b and n are not specified. The general applicability of this model is limited.

(3) McKibben et al. (2000b and 2013)

McKibben et al (2000b) proposed a correlation from their experimental data to predict the pressure gradient of water-lubricated heavy oil flow. This model is also based on the traditional expression of the pressure gradient. A modified Fanning friction factor, f_m , was adopted to roughly account for the water lubrication effect empirically.

$$-\frac{dp}{dz} = \frac{2f_m}{D} \rho_w U_m^2 \quad (5-23)$$

$$f_m = \frac{1410}{\text{Re}_w} \quad (5-24)$$

$$\text{Re}_w = \frac{DU_m\rho_w}{\mu_w} \quad (5-25)$$

A new empirical correlation for the Fanning friction factor was proposed by McKibben et al (2013) accounting for more parameters' influences. The new model follows:

$$-\frac{dp}{dz} = \frac{2f_m}{D} \rho_m U_m^2 \quad (5-26)$$

$$f_m = 15\text{Fr}_m^{-0.5} f_w^{1.3} f_o^{0.32} C_w^{-1.2} \quad (5-27)$$

$$\text{Fr}_m = \frac{U_m}{\sqrt{gD}} \quad (5-28)$$

where ρ_m is the mixture density, $\rho_m = (1 - C_w)\rho_o + C_w\rho_w$; U_m the mixture velocity, $U_m = U_{so} + U_{sw}$; Fr_m is a Froude number that accounts for the difficulty in establishing stable water-lubricated flows for heavy oils at low velocities, $\text{Fr}_m > 0.35$; f_w is the Fanning friction factor for the aqueous phase; f_o is the Fanning friction factor for oil; and C_w is the total volume fraction of the aqueous phase.

Essentially, the empirical models proposed by McKibben et al. (2000b and 2013) are similar to that of Bannwart (2001). Both models adopted the traditional expressions of the pressure gradient for single phase flow with modifications/correlations of the friction factors and/or mixture properties. The model of Bannwart (2001) has coefficients which are not specified but to be determined from experimental data. The models given in McKibben et al. (2000b and 2013) have no unknown coefficients. The coefficients were determined from experimental data with a wide coverage of oils (viscous lube oil, heavy crude oil and bitumen, viscosity ranging from 620 to 91 600 cP) and

normal pipe diameters (50, 100 and 260 mm). Due to this fact, it is likely that the empirical models of McKibben et al. (2000b and 2013) can give some reasonable predictions for particular scales such as when flow conditions are within their experimental coverage. The models of Bannwart (2001) and McKibben et al. (2000b and 2013) have not been evaluated in the literature. These models need validation with independent experimental data sets.

(4) Brauner (1998)

Brauner (1998) applied the two-fluid approach to model concentric core annular flow. The model development is presented as follows.

Considering developed annular flow as illustrated in Figure 5-12, the integral forms of the momentum equations for the annulus (a) and the core (c) are:

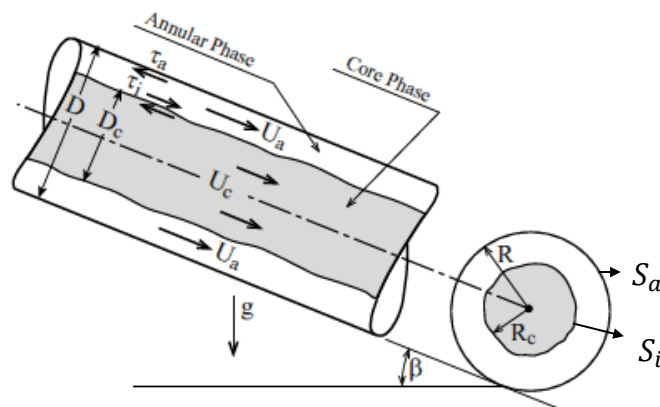


Figure 5-12 Schematic description of CAF configuration (Brauner, 1998).

$$-A_a \left(\frac{dp}{dz} \right) - \tau_a S_a + \tau_i S_i + \rho_a A_a g \sin \beta = 0 \quad (5-29)$$

$$-A_c \left(\frac{dp}{dz} \right) - \tau_i S_i + \rho_c A_c g \sin \beta = 0 \quad (5-30)$$

Eliminating the pressure drop yields:

$$\frac{4}{D(1 - \tilde{D}_c^2)} \left(-\tau_a + \frac{\tau_i}{\tilde{D}_c} \right) + (\rho_a - \rho_c) g \sin \beta = 0 \quad (5-31)$$

where $\tilde{D}_c = D_c/D$. As conventionally used in two-fluid models, τ_a and τ_i are expressed as:

$$\tau_a = \frac{1}{2} f_a \rho_a U_a^2, \quad f_a = C_a \left[\frac{\rho_a D (1 - \tilde{D}_c^2) U_a}{\mu_a} \right]^{-n_a} \quad (5-32)$$

$$\tau_i = \frac{1}{2} f_i \rho_c (U_c - c_i U_a) U_c, \quad f_i = F_i C_c \left[\frac{\rho_c D_c U_c}{\mu_c} \right]^{-n_c} \quad (5-33)$$

where $C_{a,c}$, $n_{a,c}$ are constants depending on the flow regime of each phase; $C=16$, $n=1$ for laminar flow and $C=0.046$, $n=0.2$ for turbulent flow. $c_i = u_i/U_a$ and u_i is the interfacial velocity. The coefficient F_i denotes possible augmentation of the interfacial shear due to interfacial waviness. For core annular flow, the augmentation of the interfacial shear factor due to waviness can be ignored (i.e., $F_i = 1$).

The mass balances on the annular and core phases relate U_a and U_c to the core diameter and superficial phase velocities:

$$\tilde{U}_c = \frac{U_c}{U_{cs}} = \frac{1}{\tilde{D}_c^2}, \quad \tilde{U}_a = \frac{U_a}{U_{as}} = \frac{1}{1 - \tilde{D}_c^2} \quad (5-34)$$

Combining Equations (5-30) to (5-33), the core diameter can be determined by the following non-dimensional equation:

$$(1 - \tilde{D}_c^2) \tilde{D}_c^{n_c - 5} [1 - \tilde{D}_c^2 (1 + c_i \tilde{Q})] - X^2 + Y (1 - \tilde{D}_c^2)^3 = 0 \quad (5-35)$$

where $\tilde{Q} = Q_a/Q_c$, $X^2 = \frac{C_a Re_{as}^{-n_a} \rho_c \tilde{Q}^2}{C_c Re_{cs}^{-n_c} \rho_a} = \frac{(dP/dz)_{as}}{(dP/dz)_{cs}}$, $Y = \frac{1}{2} \frac{(\rho_a - \rho_c) D g \sin \beta}{\rho_c U_{cs}^2} \frac{1}{C_c Re_{cs}^{-n_c}}$.

Re_{as} , Re_{cs} are the superficial Reynolds numbers of the annular and core liquids respectively. The physical solution for \tilde{D}_c is between 0 and 1 and the corresponding core holdup is \tilde{D}_c^2 . After solving the solution (5-34) for \tilde{D}_c , the pressure gradient can be obtained according to Equation (5-28) and/or (5-29). The dimensionless pressure gradient, i.e., pressure drop reduction factor, is expressed as:

$$\frac{d\tilde{P}_c}{dZ} = \frac{(-dP/dz)}{(-dP/dz)_{cs}} = \frac{X^2}{(1 - \tilde{D}_c^2)^2} - \frac{\rho_m}{\Delta \rho} Y \quad (5-36)$$

The above mechanistic model can be solved numerically. For horizontal two-phase flow ($Y=0$) with laminar core and either laminar or turbulent annulus, simple explicit solutions for the core phase holdup \tilde{D}_c^2 and the pressure gradient can be derived and were given by Brauner (1998) as summarized in Table 5-2.

Table 5-2 Core holdup and pressure reduction factor for CAF with a laminar core ^{a)}.

	Laminar core – laminar annulus (L-L)	Laminar core – turbulent annulus (L-T)
X^2	$\tilde{\mu} \tilde{Q}$	$\frac{0.046}{16} \tilde{\mu} \tilde{Q} Re_{as}^{0.8}$ or $\frac{0.046}{16} \tilde{\mu}^{0.2} \left(\frac{\rho_a}{\rho_c}\right)^{0.8} \tilde{Q} Re_{as}^{0.8} \tilde{Q}^{1.8}$
c_i	2	1.15~1.2
\tilde{D}_c^2	$\frac{1 + \tilde{Q} - \left(1 + \frac{\tilde{\mu}}{\tilde{Q}}\right)^{0.5} \tilde{Q}}{1 + 2\tilde{Q} - \tilde{\mu} \tilde{Q}}$	$\frac{1 + \frac{\tilde{Q} c_i}{2} \left[1 - \left(1 + \frac{4X^2}{\tilde{Q}^2 c_i^2}\right)^{0.5}\right]}{1 + \tilde{Q} c_i - X^2}$
ϕ	$\frac{\tilde{\mu}}{\tilde{Q}} \left[\frac{1 + 2\tilde{Q} - \tilde{\mu} \tilde{Q}}{1 - \tilde{\mu} + \left(1 + \frac{\tilde{\mu}}{\tilde{Q}}\right)^{0.5}} \right]^2$	$X^2 \left[\frac{1 + \tilde{Q} c_i - X^2}{\frac{\tilde{Q} c_i}{2} - X^2 + \left(\frac{\tilde{Q}^2 c_i^2}{4} + X^2\right)^{0.5}} \right]^2$

^{a)} $\tilde{Q} = Q_a/Q_c$ and $\tilde{\mu} = \mu_a/\mu_c$

The model of Brauner (1998) applied the two-fluid approach to concentric core annular flow. As mentioned by the author herself, the predicted pressure gradient via this model may underestimate measured values in CAF operation due to the increase of wall friction associated with oil fouling and eccentricity of the oil core.

5.4.2 Model development for water-lubricated flow

In this study, an attempt has been made to incorporate the influence of oil fouling and eccentricity of oil core via a modified closure law for the wall shear stress. An empirical model was developed. The model gives a clue on the modelling of the influence of oil fouling and eccentricity of the oil core on the pressure gradient. However, it must be noted that the developed model should be re-evaluated as more data become available. The development of the empirical model is presented as follows.

To obtain a closure law for the wall shear stress, τ_w , the measured pressure gradients were used to obtain the overall average wall shear stress. For water-lubricated high-viscosity oil-water flow with oil fouling on the pipe wall, treating the oil fouling as a static part of the pipe, the force balance as shown in Figure 5-13 over a length of pipe is:

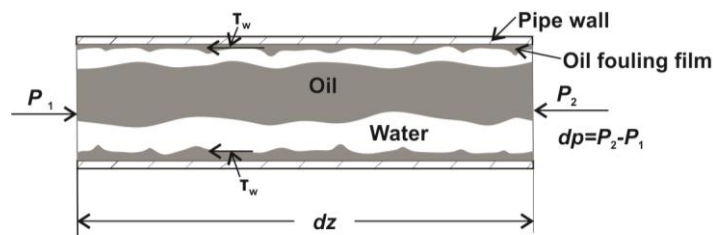


Figure 5-13 Schematic graph on the force balance of core annular flow.

$$\tau_w \pi D dz = -dp \frac{\pi D^2}{4} \quad (5-37)$$

Hence

$$\tau_w = \frac{(-dP/dz)D}{4} \quad (5-38)$$

The wall friction factor then can be obtained through

$$f_w = \frac{2\tau_w}{\rho_w U_w^2} \quad (5-39)$$

$$U_w = \frac{U_{sw}}{H_w} \quad (5-40)$$

A reliable estimate of water holdup, H_w , is needed for the calculation of f_w . In the present study, measurements of H_w were conducted. A modified correlation of that proposed by Arney et al. (1993) for prediction of the water holdup was developed based on our experimental data. The modified correlation is expressed as

$$H_w = C_w [1 + 0.31(1 - C_w)] C_H \quad (5-41)$$

$$C_H = e^{-0.31 \left(\frac{1}{Fr}\right)^{1.067} (1 - C_w)^{0.67}} \quad (5-42)$$

$$\frac{1}{Fr} = \frac{\sqrt{gD \frac{(\rho_w - \rho_o)}{\rho_w}}}{U_{so}} \quad (5-43)$$

where C_H is a coefficient associated with the oil core concentricity and oil fouling. It is defined as a function of $\frac{1}{Fr}$, and the input oil volume fraction, $1 - C_w$. It is noted that $\frac{1}{Fr}$ is treated as a new dimensionless number which is the ratio of the gravitational force to the inertial force instead of the reciprocal of the Froude number to include the case of $\frac{1}{Fr}=0$ when $\rho_w = \rho_o$. $C_H=1$ when the oil core is

fully concentric; the oil core is fully concentric when the immiscible fluids are density-matched (i.e., $\frac{1}{Fr}=0$). $C_H < 1$ means that the oil core is eccentric.

Equation 5-41 was proposed on the basis that the empirical correlation of Arney et al. (1993) (see Equation 5-14) works well for virtually concentric CAF as discussed in the following section. The basic form of the correlation of Arney et al. (1993) was adopted from which the predicted water holdup is always higher than the input water volume fraction. As discussed in our experimental results (see Section 4.5 in Chapter 4), H_w is higher than C_w at high oil flow rates when the oil phase is virtually concentric. H_w gets close to C_w at medium oil flow rates, and becomes lower than C_w when the oil phase is far off concentric. Therefore, a coefficient, C_H , was used to account for the influence of oil core concentricity and oil fouling on water holdup. The coefficient should have a value of 1 when the oil core is almost concentric and a value between 0 and 1 when it is eccentric. The Froude number and the input water volume fraction were used to correlate the degree of oil core concentricity and fouling and their influences on water holdup. Equations 5-41 and 5-42 were obtained from experimental data. Comparison on the performance of the correlation with that of Arney et al. (1993) can be found in the next section.

Brauner (1998) adopted the wall friction factor which is usually used in single phase flow through a hydraulic smooth pipe. In a hydraulic smooth pipe, the wall friction factor is the function of the flow Reynolds number alone. Most pipes used in engineering structures cannot be regarded as being hydraulically smooth. The resistance to the flow through a rough wall is larger than that through a smooth pipe. As oil fouling film is not treated separately with its own transport equations in the mechanistic model, the pipe wall with oil fouling film is effectively much rougher than the pipe itself. In the present study, the wall friction factor used in single phase flow through a rough pipe was adopted. An explicit form of the Colebrook equation (Zigrang and Sylvester, 1985) was used for estimation of the effective wall roughness.

$$\frac{1}{\sqrt{4f_w}} = -2 \log \left(\frac{k}{3.7} - \frac{4.518}{\text{Re}_w} \log \left(\frac{6.9}{\text{Re}_w} + \left(\frac{k}{3.7} \right)^{1.11} \right) \right) \quad (5-44)$$

$$\text{Re}_w = \frac{\rho_w U_w D_{we}}{\mu_w} \quad (5-45)$$

$$D_{we} = \frac{4A_w}{\pi D} = H_w D \quad (5-46)$$

where D_{we} is the hydraulic diameter of the water phase, A_w is the cross-sectional area of the water phase. k is the effective relative wall roughness. In the original definition, k is defined as the ratio of the roughness of the inner surface to the pipe internal diameter, $k = \varepsilon/D$. In our context, k is a dimensionless effective wall roughness indicator; it is used to account for the influence of oil fouling and oil phase eccentricity on the wall shear stress. Both oil fouling film and oil core eccentricity can increase the effective wall roughness.

Our final objective is to obtain a correlation for the effective wall roughness (i.e., k) of water-lubricated high-viscosity oil-water flow to account for the influence of oil fouling and oil phase eccentricity. From previous experimental analysis, it is demonstrated that the oil flow rate and water volume fraction are two major parameters affecting the degree of oil phase concentricity and oil fouling. Figure 5-14 shows the estimated k versus input water volume fraction for various superficial oil velocities. It is shown that the effective wall roughness decreases with increase of the input water volume fraction for a constant superficial oil velocity. This is related to the reduced oil fouling and oil eccentricity with increase of the input water volume fraction. For different superficial oil velocities, the effective wall roughness is lower when the superficial oil velocity is higher. The superficial oil velocity mainly affects the concentricity of oil core which indirectly affects the frequency of oil core contact with the pipe wall. Apart from the superficial oil velocity, the eccentricity of the oil core can also be affected by the density difference of the two fluids.

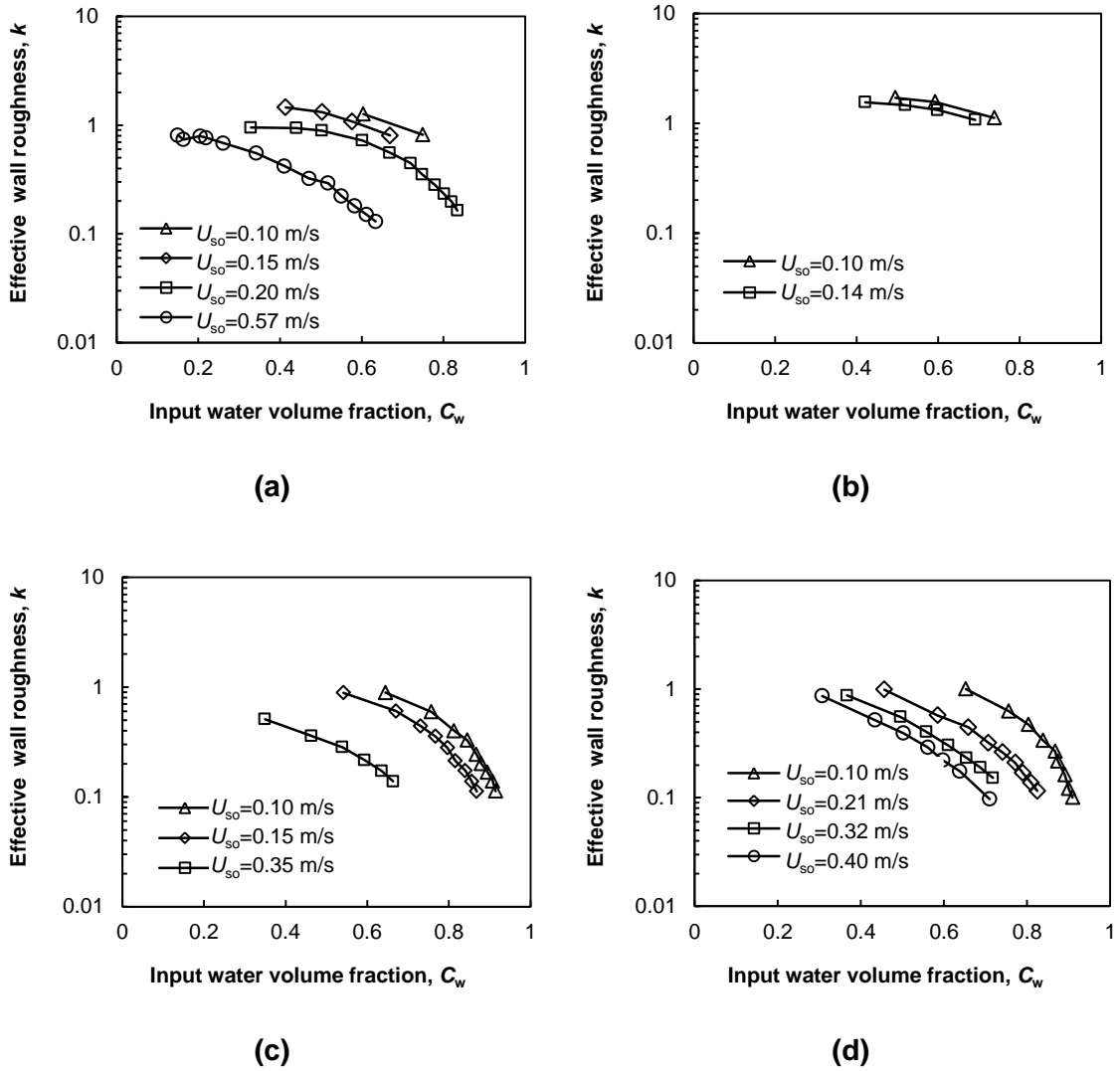


Figure 5-14 Estimated effective wall roughness versus input water volume fraction for various U_{so} . (a) CYL 1000, $\mu_o=3\ 800$ cP; (b) CYL 1000, $\mu_o=13\ 200$ cP; (b) CYL 680, $\mu_o=3\ 700$ cP; (b) CYL 680, $\mu_o=7\ 100$ cP.

A parameter which can represent the influence of water content and oil flow rate on the effective wall roughness was sought. It was found that the effective wall roughness gets almost unified at various U_{so} with change of a parameter, C_k , which is defined in a form similar to that of C_H .

$$C_k = e^{-\left(\frac{1}{Fr}\right)^{0.8}(1-C_w)} = e^{-\left(\sqrt{\frac{gD(\rho_w-\rho_o)}{\rho_w}}/U_{so}\right)^{0.8}(1-C_w)} \quad (5-47)$$

where $\frac{1}{Fr}$ is the ratio of gravitational force to inertial force as defined in Equation (5-43). $C_k=1$ when the oil core is fully concentric. When C_k is close to 1, it means that the oil core is virtually concentric due to a high U_{so} , or the oil fouling on the pipe inner wall is light due to a high C_w .

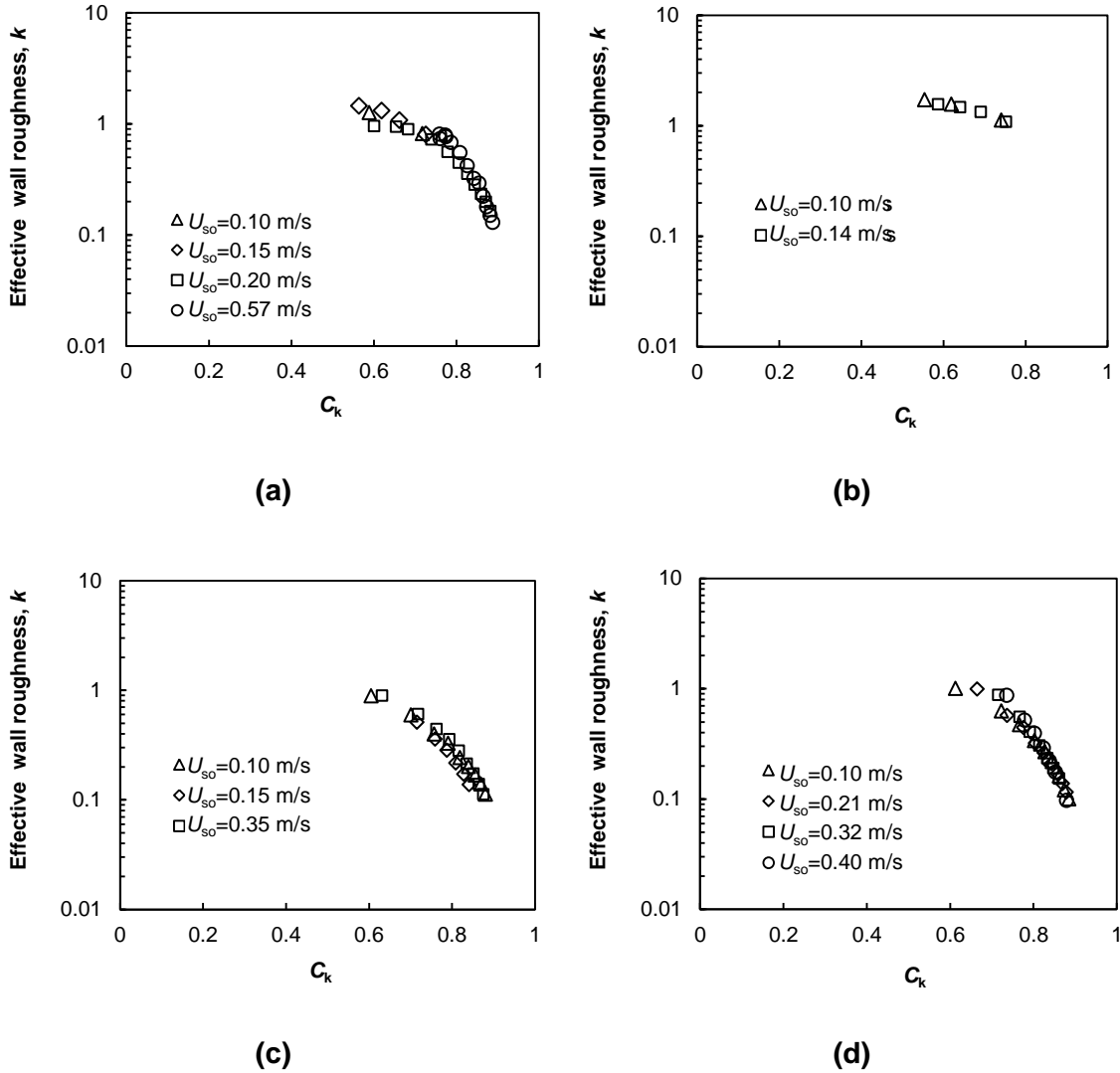


Figure 5-15 Estimated effective wall roughness versus C_k for various U_{so} . (a) CYL 1000, $\mu_o=3\ 800$ cP; (b) CYL 1000, $\mu_o=13\ 200$ cP; (c) CYL 680, $\mu_o=3\ 700$ cP; (d) CYL 680, $\mu_o=7\ 100$ cP.

Figure 5-15 shows the estimated effective wall roughness versus C_k for various superficial oil velocities, which is a representation of Figure 5-14. It demonstrates that the effective wall roughness has minor variation at a specific C_k for various U_{so} . The effective wall roughness decreases with increase of C_k , i.e., when the oil core gets more concentric or the oil fouling on the inner pipe wall gets lightened.

Figure 5-16 shows the influence of oil viscosity on the estimated effective wall roughness. It is shown that when C_k is close to 1, the effective wall roughness is very close for different oil viscosities. At lower C_k when the oil fouling is heavier, the effective wall roughness gets scattered; the effective wall roughness does not monotonically increase with increase of oil viscosity. As has been discussed in the experimental analysis (see Section 4.6 in Chapter 4), the oil viscosity affects the pressure gradient in two counterbalanced ways – frictional resistance and turbulence damping. It is difficult to accurately account for the complicated influences of oil viscosity in a simple empirical model. As the scatter of the effective wall roughness with change of oil viscosity is not significant, the influence of oil viscosity on effective wall roughness is not considered in the present study.

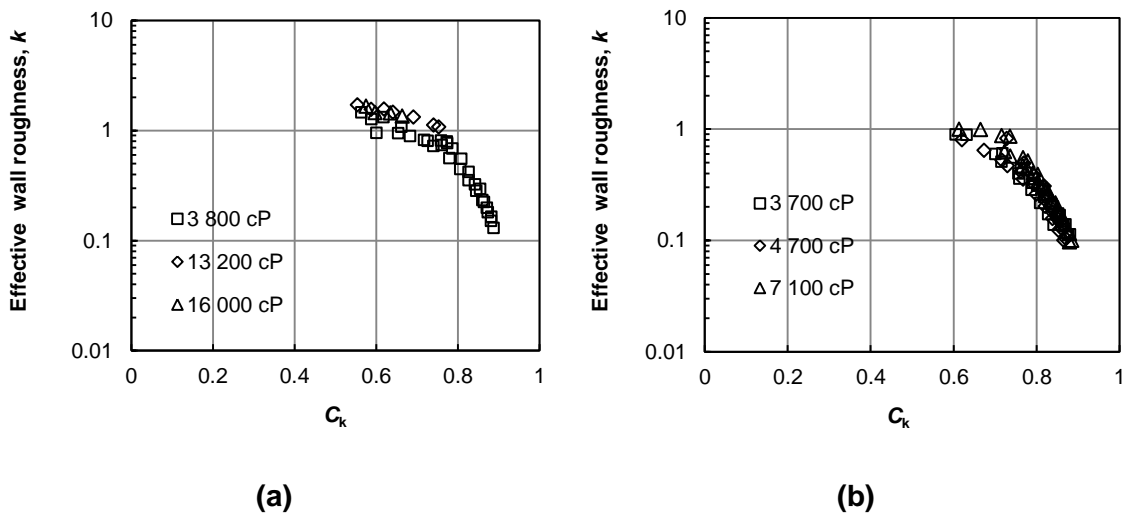


Figure 5-16 Estimated effective wall roughness versus C_k for various oil viscosities (a) CYL 1000; (b) CYL 680.

It is noted that the effective wall roughness is reduced more quickly in Figure 5-16 (b) than that in Figure 5-16 (a). As Figure 5-16 (a) and (b) represent the effective wall roughness change against C_k for two different oils, it is suspected that the difference is due to the different wettability of the pipe wall by the two oils. The wettability of the Perpex pipe with the two oils were not measured in the present study due to limitation in measurement instrumentation, but it was observed that the oil fouling on the pipe wall was generally heavier during experiments conducted with CYL 1000. It is possible that the pipe wall has a smaller contact angle with CYL 1000, i.e., the pipe would get fouled more heavily with CYL 1000 than with CYL 680. Considering this aspect, it would be more accurate to obtain different closure laws for the different oils, or incorporate the influence of the wettability of the pipe wall by the oil. However, as no quantitative information of the wettability is available in the present study, the possible influence of wall wettability is ignored here. A discussion on possible measurement methods of wall wettability is presented in Appendix E.

The combined data for the two different oils is shown in Figure 5-17. An attempt was made to obtain a correlation from the whole data shown in Figure 5-17. The power law was tested and found to be able to fit the experimental data reasonably. The distributions of a wide variety of physical phenomena approximately follow a power law over a wide range of magnitudes. The power laws have a good attribute of scale invariance. The final correlation for the effective wall roughness obtained from the present experimental data is expressed as

$$k = a(1 - C_k)^n \quad (5-48)$$

Where a and n are constant coefficients, $a = 7.2$, and $n = 1.88$. C_k is a dimensionless number defined as Equation (5-47) to reflect the influence of oil phase concentricity and oil fouling on the effective wall roughness. The effective wall roughness due to oil phase concentric and oil fouling, i.e., k becomes zero when $C_k = 1$. It is worth remarking that the coefficients a and n are determined from the present experimental data base covering two different oils (CYL 680

and CYL 1 000) through a Perspex pipe, it is possible that these coefficients obtained from the present experiments do not suit for flow systems with great difference in wettability of the pipe by the oil, e.g., a different pipe material and/or oil. Like all empirical correlations, this closure law needs validation with more experimental data.

Equations (5-44), (5-47), and (5-48) together constitute of our developed closure laws for the wall shear stress of water-lubricated flow. Together with Equation (5-41) for estimation of the water holdup, the pressure gradient of water-lubricated flow can be obtained.

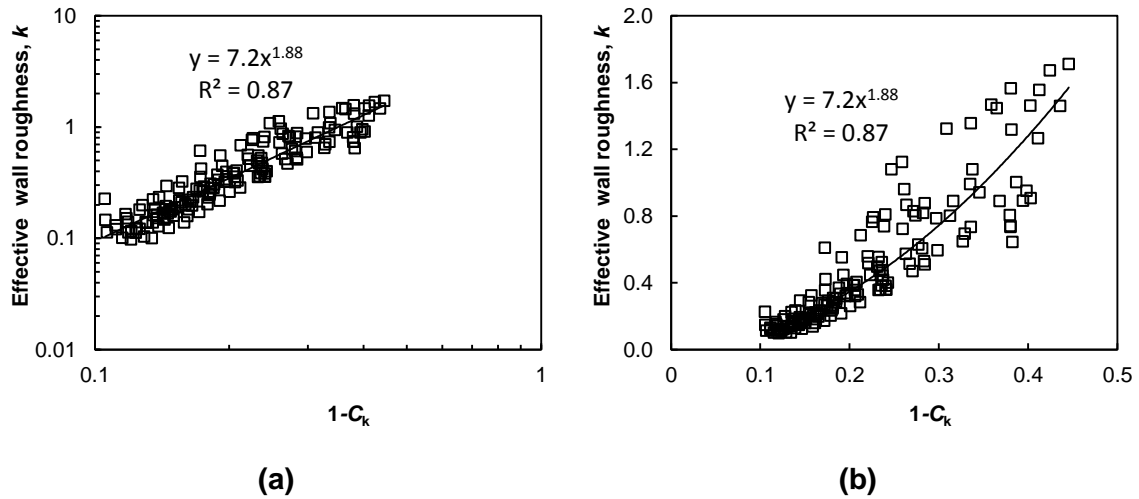


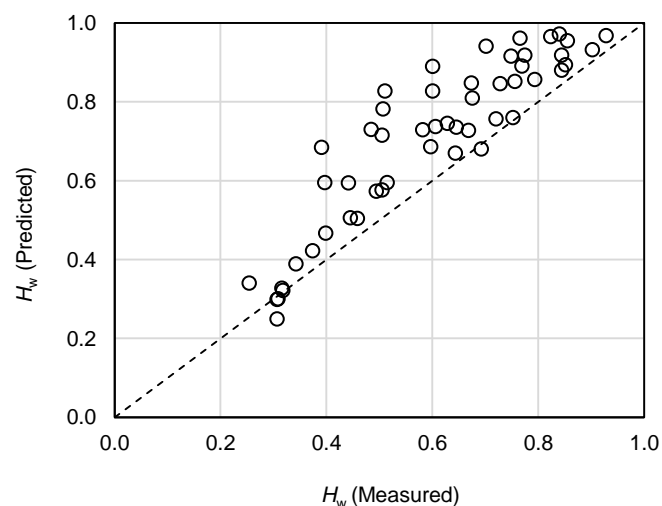
Figure 5-17 Estimated effective wall roughness versus $1-C_k$. (a) logarithmic scale; (b) linear scale.

5.4.3 Evaluation of models

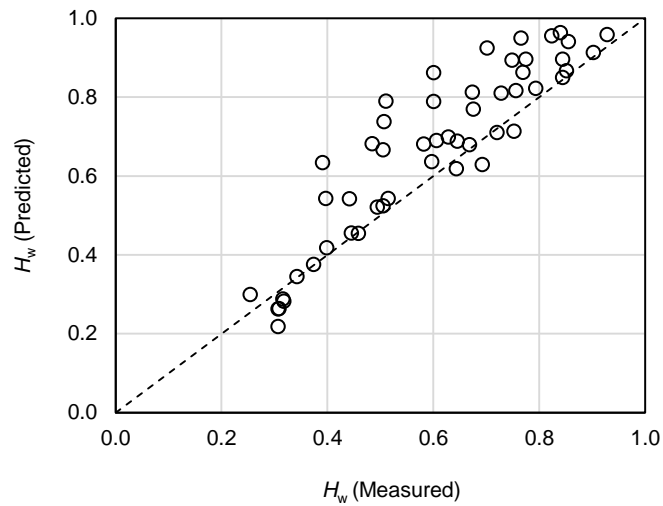
Either the empirical or the mechanistic models contain empirical correlations obtained from experiments. These models need evaluation with experimental data to clarify the application range of different models. Evaluation of the above models for water-lubricated high-viscosity oil-water flow was conducted by comparing predicted and measured water holdups and/or pressure gradients. By the model performance evaluation, light is shed on the applicability of different models.

5.4.3.1 Prediction of the water holdup

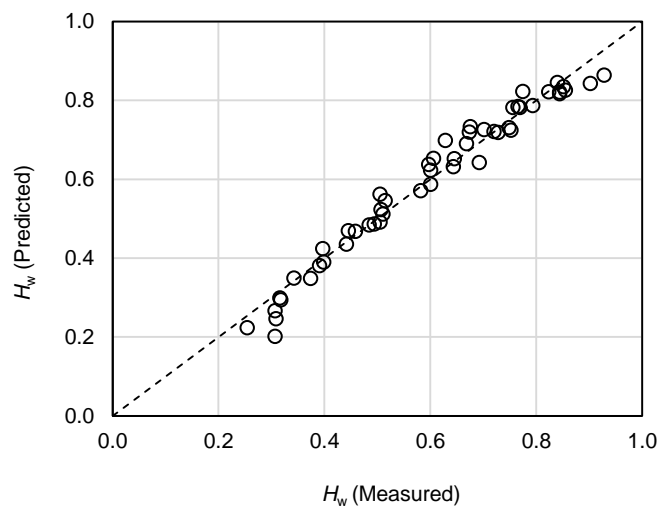
Figures 5-18 (a) to (c) show overall comparisons between measured water holdups and predicted counterparts from the models proposed by Arney et al. (1993), Brauner (1998) and the present study, respectively. It is shown that both the correlation given in Arney et al. (1993) (see Equation 5-14) and the two-fluid model of Brauner (1998) (see Table 5-2) give good predictions for some flow conditions (about 31% and 45% of the compared points have relative errors within $\pm 10\%$ respectively) while over predict the water holdup for many flow conditions at the same time. The correlation proposed in the present study (see Equations 5-41 to 5-43) shows good performance in general (about 88% of the compared points have relative errors within $\pm 10\%$).



(a)



(b)



(c)

Figure 5-18 Overall comparison between measured water holdups (data from the present study, $\mu_c=3\ 300\ \text{cP}$ and $5\ 600\ \text{cP}$) and predicted counterparts. (a) Arney et al. (1993); (b) Brauner (1998); (c) Present study.

As has been discussed in our experimental analysis, the measured water holdup is found to be affected by both the input water volume fraction and superficial oil velocity. In general, the water holdup is lower than the input water volume fraction at low superficial oil velocity, gets close to the input water volume fraction with increase of superficial oil velocity and finally becomes

higher than the input water volume fraction at higher superficial oil velocity. Predicted and measured water holdup (H_w) versus the input water volume fraction (C_w) are shown in Figure 5-19. The dash lines represent where H_w is equal to C_w . It is shown that the models of Arney et al. (1993) and Brauner (1988) always give higher H_w than C_w . This relationship is also reflected in the constitution of these two models. Both the models overestimate the water holdup when the oil flow rate is low, and give good predictions when the oil flow rate is high.

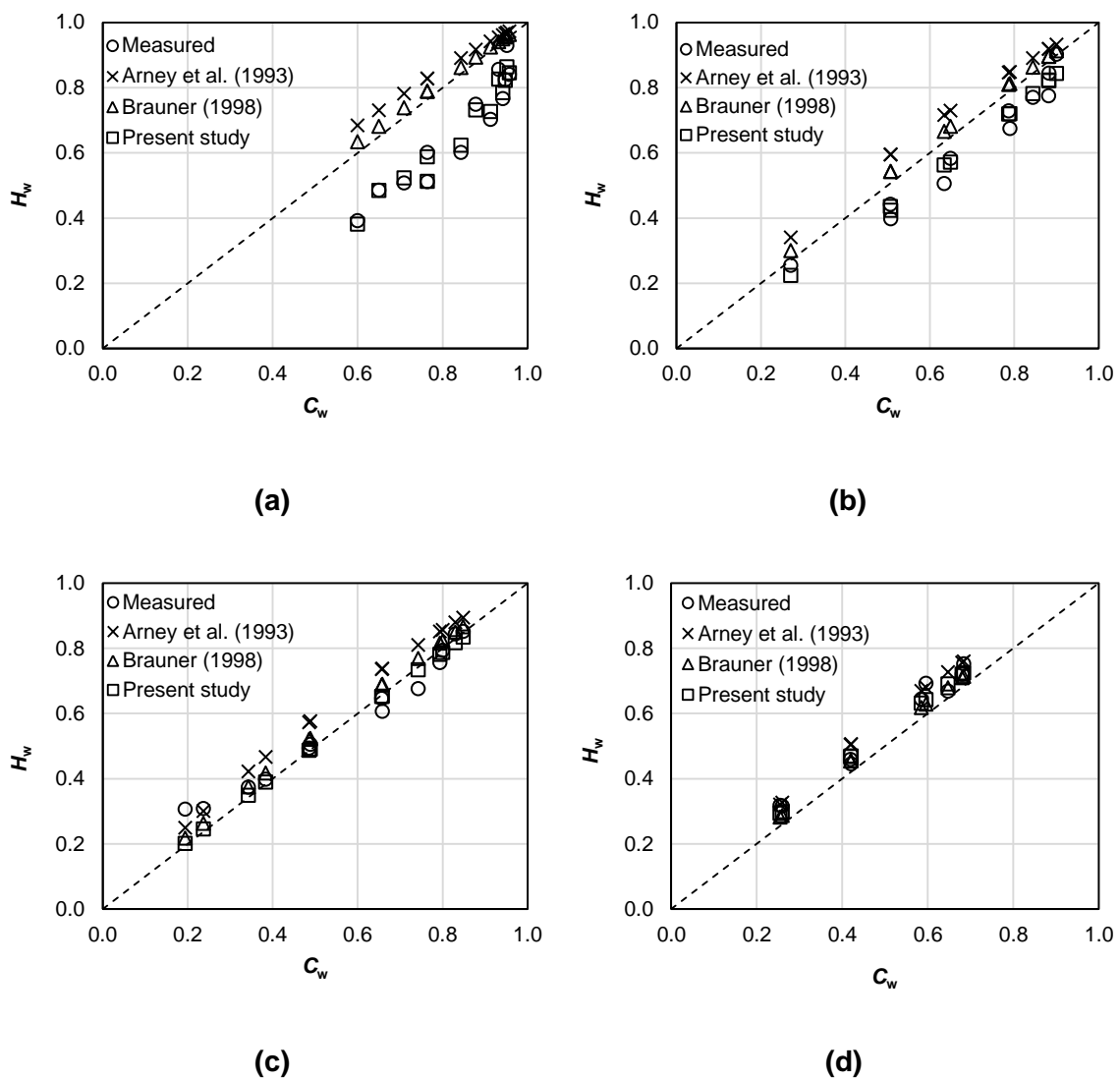


Figure 5-19 Water holdup (H_w) versus input water volume fraction (C_w) at different superficial oil velocities (data from the present study, $\mu_o=3\ 300$ cP and $5\ 600$ cP).

(a) $U_{so}=0.06$ m/s; (b) $U_{so}=0.1$ m/s; (c) $U_{so}=0.2$ m/s; (d) $U_{so}=0.5$ m/s

Most of the experimental data sources from which Arney et al. (1993) proposed their correlation have higher oil densities ranging from 970 to 1010 kg/m³, thus the corresponding core annular flows should be more concentric due to lower buoyancy. The oil used in the present experiments has densities around 905 and 910 kg/m³; the observed flow patterns are eccentric at low oil flow rates and about concentric only at high oil flow rates when the influence of oil inertia outweighs that of buoyancy. This can explain why the correlation of Arney et al. (1993) which seems to fit well with different data sources does not fit most of our experimental data.

The correlation proposed in the present study is based on the fact the correlation of Arney et al. (1993) works well when the oil core is almost concentric and incorporates a coefficient which accounts for the influence of oil concentricity and oil fouling on the water holdup. This modified correlation of Arney et al. (1993) works well in comparison with our experimental data as shown in Figure 5-19. As the calculation of the water holdup with this correlation needs information of the superficial oil velocity and the fluids' densities apart from the input water volume fraction, comparison with the whole data used by Arney et al. (1993) is not achieved due to lack of information (U_{so} is normally not given in the literature). However, it is thought that the new correlation has the capacity to fit the data used by Arney et al. (1993). When the density difference between the fluids is small, the coefficient, C_H , is close to 1, the newly developed correlation (see Equation 5-40) can be simplified to

$$H_w = C_w[1 + 0.31(1 - C_w)] \quad (5-49)$$

Equation 5-49 is similar to the correlation developed by Arney et al. (1993) (see Equation 5-14). The performance of the proposed model is evaluated with partial data from the experiments of Charles et al. (1961) (see Figure 5-20). The oil used by Charles et al. (1961) has density as equal as that of water, thus $C_H=1$ and Equation 5-49 is applied. The core annular flow observed in the experiments of Charles et al. (1961) is virtually concentric. The water holdup was measured by the above authors with the fluid sampling method using two

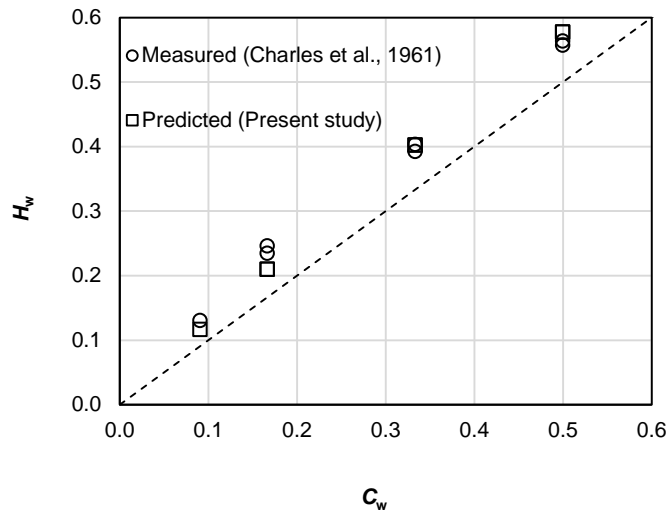
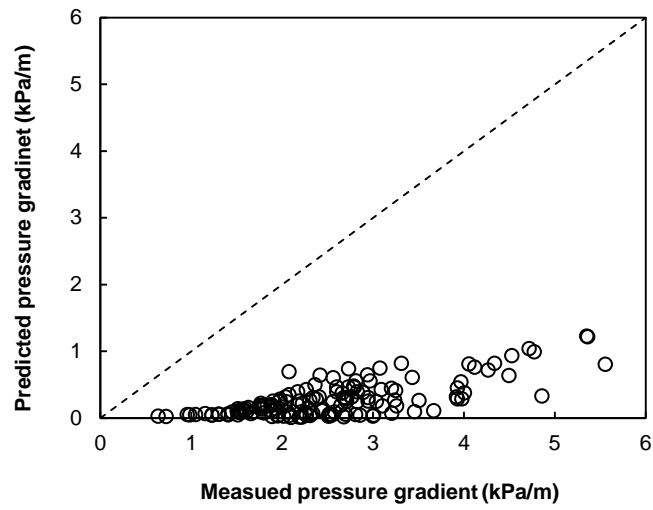


Figure 5-20 Water holdup (H_w) versus input water volume fraction (C_w) (data from Charles et al. (1961), $\rho_o = \rho_w$, $\mu_o = 16.8$ cP).

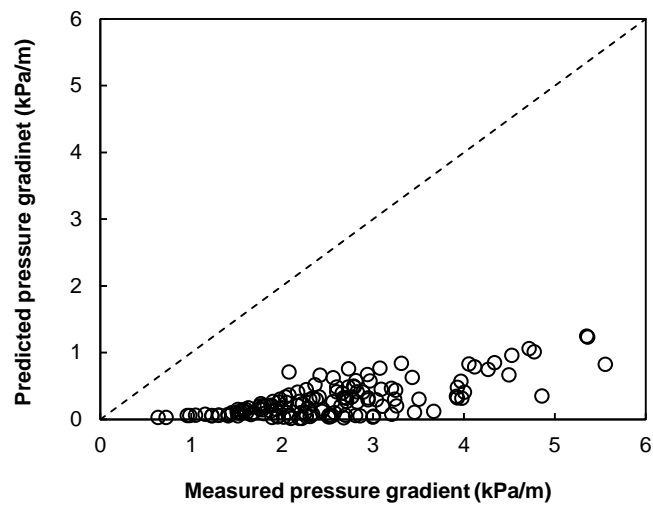
quick-action valves. A good agreement is shown between predicted water holdups from the proposed correlation and measured water holdups from Charles et al. (1961).

5.4.3.2 Prediction of the pressure gradient

The models of Arney et al. (1993) and Brauner (1998) for predicting the pressure gradient of core annular flow are evaluated with the present data. Comparisons between measured and predicted pressure gradients are shown in Figure 5-21 (a) and (b) for the model of Arney et al. (1993) and Brauner (1998), respectively. It is shown that both the models under predict the pressure gradient significantly. In fact, predicted pressure gradients from the two models are close to the pressure gradients of single water flow at the corresponding mixture flow rates. The ratio of the pressure gradient of core annular flow to the pressure gradient of single water flow at same mixture flow rate (i.e., RTW as defined in Section 4.6, Chapter 4,) versus input water volume fraction is depicted in Figure 5-22. It demonstrates that the predicted RTW via the two models ranges from 0.8 to 1.2 (see Figure 5-22 (a)), while the RTW from measurement ranges from 2 to 220 (see Figure 5-22 (b)).

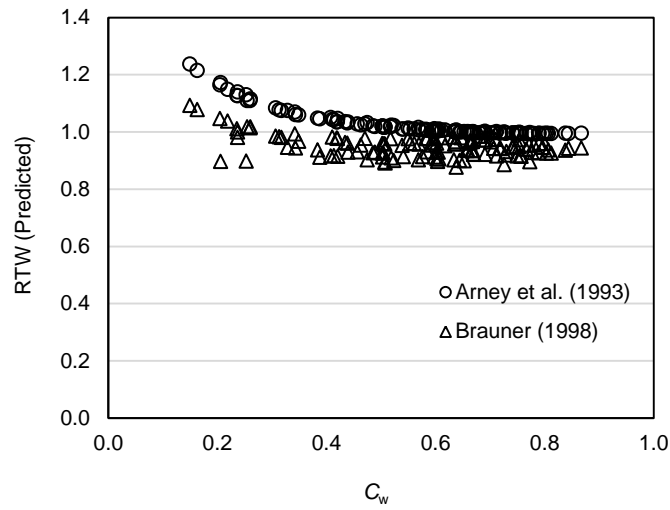


(a)

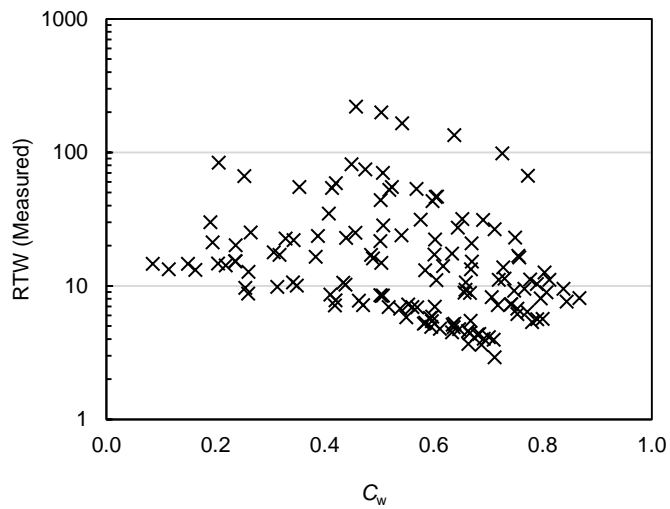


(b)

Figure 5-21 Overall comparison between measured pressure gradients (data from the present study, μ_0 ranges from 3 300 cP to 16 000 cP) and predicted counterparts. (a) Arney et al. (1993); (b) Brauner (1998).



(a)



(b)

Figure 5-22 Ratio of two-phase flow pressure gradient to single water flow pressure gradient (RTW) versus input water volume fraction (data from the present study, μ_o ranges from 3 300 cP to 16 000 cP) (a) RTW calculated from predicted pressure gradients; (b) RTW calculated from measured pressure gradients.

For the model of Arney et al. (1993), the friction factor of the two-phase flow is calculated with the traditional equation for single phase flow with a modified Reynolds number (see Equation 5-11). As $\eta^4(m - 1)$ is small in Equation 5-11,

the modified Reynolds number is close to $\frac{\rho_m U_m D}{\mu_w}$, hence the predicted pressure gradient from this model is close to that of single water flow at the mixture flow rate. For the two-fluid model of core annular flow proposed by Brauner (1998), the model calculates the pressure gradient of core annular flow with two sets of momentum equations of each phase; closure laws are incorporated to get solutions. Oil fouling and oil eccentricity are not accounted for in either the basic constitution of this model or the closure laws incorporated. For high-viscosity core annular flow, the influence of oil fouling cannot be neglected as has been demonstrated in our experimental results. Therefore, the model of Brauner (1998) tends to underestimate the pressure gradient when the influence of oil fouling and/or oil core eccentricity on the pressure gradient is significant.

The models of Arney et al. (1993) and Brauner (1998) have been evaluated previously by the group of Poesio (see Grassi et al., 1998 and Strazza et al., 2011). Different from the large deviation shown in Figure 5-21, a fair agreement was demonstrated when predicted pressure gradients from both models were compared with experimental data from the above authors' experiments (pipe I.D.=21 mm, oil viscosity around 800 cP, a co-axial injection device used to aid the formation of core annular flow). It is noted that oil fouling on the pipe inner wall for core annular flow was not observed by the above authors. Also, it is probable that there are more data points of nearly concentric core annular flow in the above authors' experiments due to a smaller pipe diameter and higher oil flow rates. The oil flow rates covered by the above authors' experiments is higher in general compared to ours; core annular flow is reported to be obtained for U_{so} ranging from 0.2 to 0.7 m/s while for 0.1 to 0.57 m/s in our experiments. In fact, the measured pressure gradients from the above authors' experiments were reported to be close to that of single water flow at the mixture velocity. As has been demonstrated, the models give predictions close to the pressure gradients of single water flow at the mixture flow rates.

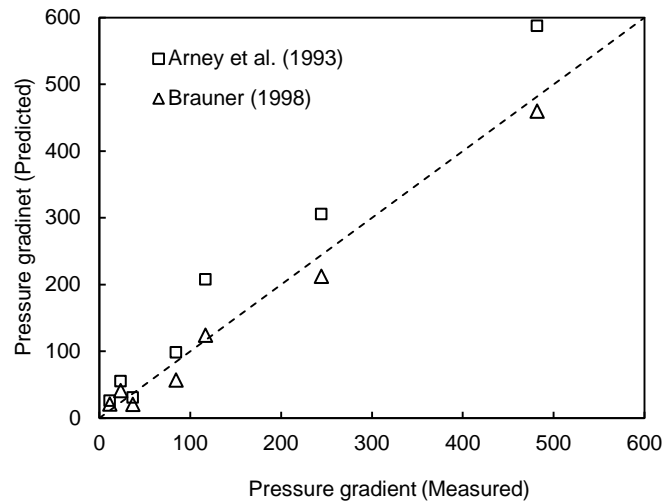


Figure 5-23 Comparison between measured pressure gradients (data from Charles et al., 1961; $\rho_o = \rho_w$, $\mu_o = 16.8$ cP) and predicted counterparts.

The models of Arney et al. (1993) and Brauner (1998) are further evaluated with partial experimental data reported in Charles et al. (1961) as shown in Figure 5-23. Core annular flow in the experimental of Charles et al. (1961) was virtually concentric due to equal densities of oil and water phases. Also, oil fouling on the pipe inner wall was not reported. As shown, both models give reasonable predictions and the two-fluid model of Brauner (1998) shows better performance. Therefore, the models of Arney et al. (1993), and Brauner (1998) can give reasonable predictions when the oil core is virtually concentric and no significant oil fouling on the pipe wall. The large discrepancy shown when compared to the present experimental data is essentially due to the fact that the present experimental data is outside the range of flow conditions where the above models are suitable. It demonstrates the significant influences of oil phase eccentricity and oil fouling on the pipe wall on the water holdup and pressure gradient which should be considered in industrial applications.

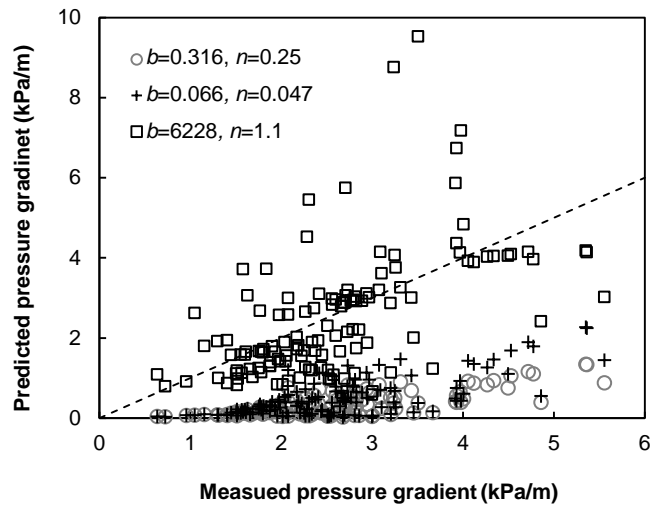


Figure 5-24 Comparison of predicted pressure gradients using various sets of b and n for the model of Bannwart (2001) with the present experimental data. The the bisector is aslo shown (the dash line).

Figure 5-24 shows a comparison of predicted pressure gradient for the model of Bannwart (2001) with the present experimental data. The total flow friction factor constitutes of two coefficients, b and n , which are to be determined from experimental data in the model of Bannwart (2001) (see Equation 5-21). Predictions from the model with the Blasius set of b and n ($b=0.316, n=0.25$), b and n ($b=0.066, n=0.047$) obtained by the above author from experiments ($\mu_o=2700$ cP, $\rho_o=989$ kg/m³, pipe I.D.=26.7 mm; oil fouling observed), and b and n tuned to fit the present experimental data are compared with the experimental data in Figure 5-24. The dash line represents where the predicted pressure gradient is equal to the measured counterpart. It is shown that the predicted pressure gradients from the model with the set of b and n obtained by Bannwart (2001) are generally slightly higher than that predicted with the traditional Blasius coefficients but still much lower than the measured ones. Similar to the present experiments, oil fouling on the pipe wall was reported in Bannwart (2001). As the oil in the experiments of Bannwart (2001) has a higher density of 989 kg/m³, it is suspected that the core annular flow in the above author's experiments was more concentric hence less contact with the pipe wall than that in our experiments. Also, it was reported that the pipe was cleaned with

water before each run in the above author's experiments, while the pipe was not cleaned with water before each run in the present experiments. It is very likely that the degree of oil fouling in the above author's experiments is less significant than that of the present experiments, which can explain why the model with coefficients obtained in Bannwart (2001) underestimates the pressure gradient for the present experimental data though oil fouling is accounted for by the coefficients. The set of coefficients obtained to fit the present data has a much higher b which reflects an overall significant influence of oil fouling on the pressure gradient. The final expression of the pressure gradient in Bannwart (2001) is approximately proportional to U_m^{2-n} . The magnitude of n reflects the increase rate of the pressure gradient with increase of the mixture velocity. The obtained coefficient of n to fit the present experimental data is higher than 1, indicating the pressure gradient increase rate becomes slower with increase of the mixture velocity, which can be explained by the reduced oil fouling influence on the pressure gradient with increase of the mixture velocity. The model with tuned coefficients can give reasonable predictions for most of the data points (about 85% of the compared points have relative errors within $\pm 70\%$). However, as the coefficients of b and n need to be determined empirically from experiments, the applicability of this model is limited.

Comparisons between measured and predicted pressure gradients from the model of McKibben et al. (2000b) and McKibben et al. (2013) are shown in Figure 5-25 and Figure 5-26, respectively. The experiments of McKibben et al. (2000a, 2000b, and 2013) were conducted in steel pipeline flow loops of nominal internal pipe diameters of 50, 100 and 260 mm; viscous lube oil, heavy crude oil and bitumen were used (viscosity ranging from 620 to 91 600 cP). It is shown that when compared with the present experimental data, the correlation proposed in McKibben et al. (2000b) gives reasonable predictions; about 93% of the compared points have relative errors within $\pm 70\%$ for a total data points of 159. The empirical model of McKibben et al. (2000b) has a simple form of modified Fanning friction factor which is proportional to Re_w^{-1} (see Equation 5-24), which can be linked to that the Darcy friction factor (four times of the

Fanning friction factor) in the model of Bannwart (2001) is proportional to $Re_m^{-1.1}$ to fit our experimental data (see Figure 5-24).

The new correlation proposed in McKibben et al. (2013) has a more complex expression of Fanning friction factor which is dependent on the mixture Froude number, superficial water and oil friction factors, and the input water volume fraction (see Equation 5-27). Influences of water lubrication, oil fouling on the pipe inner wall and oil phase eccentricity (this influence is not mentioned but can be reflected in the Froude number; the Froude number is used to account for the difficulty in establishing stable water-lubricated flow by the above authors) are more clearly represented compared to the earlier simpler correlation proposed by the above authors. However, the performance of this correlation is not as good as the earlier one when compared with the present experimental data. The correlation of McKibben et al. (2013) has less underestimations while more overestimations; about 89% of the compared points have relative errors between -40% and +100%, and some predicted pressure gradients are 5 times as high as the measured values.

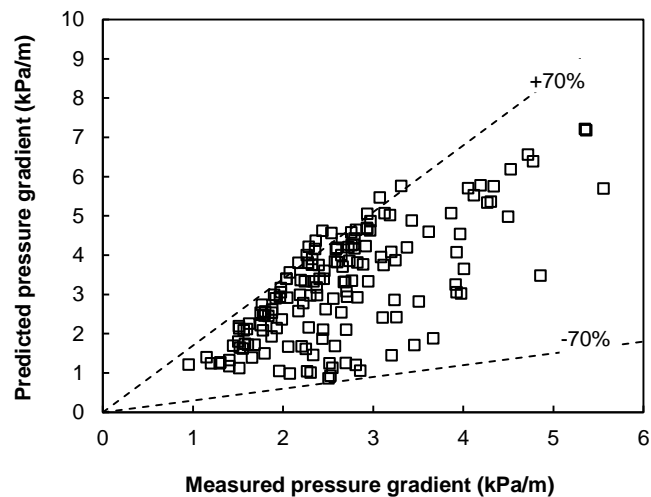


Figure 5-25 Comparison between measured and predicted pressure gradients from the model of McKibben et al. (2000b).

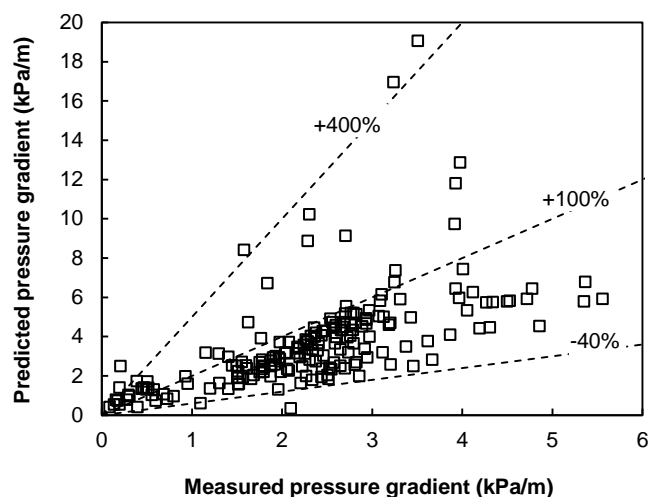


Figure 5-26 Comparison between measured and predicted pressure gradients from the model of McKibben et al. (2013).

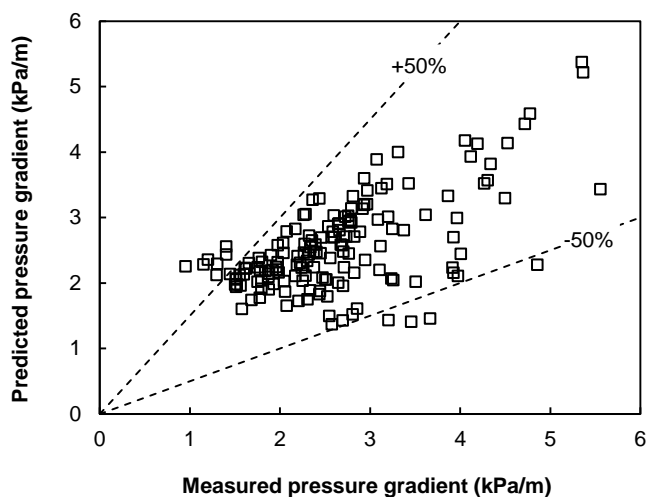


Figure 5-27 Comparison between measured and predicted pressure gradient from the model proposed in the present study.

A comparison between measured and predicted pressure gradient from the model proposed in the present study is shown in Figure 5-27. The performance of this model has slight improvement to that of the model of McKibben et al. (2000b) (about 92% of the compared points have relative errors within $\pm 50\%$ for a total data points of 159). The accuracy of the model can be further improved by separate correlations of the effective wall roughness for different oils by sacrificing the feasibility of the model for wider application. Compared to the

empirical model of McKibben et al. (2000b), the model proposed in the present study does not show advantage in the aspects of simplicity and accuracy. Similar to the model of McKibben et al. (2013), the merit of this model lies in its constitution from which the influences of oil fouling and oil eccentricity are accounted for instead of a modified friction factor accounting for the overall influences. It shows one possible direction to account for the influences of oil fouling and oil phase eccentricity. The correlations proposed in the present study require information of phases' densities, superficial oil velocity, and input water volume fraction for the calculation of the pressure gradient. Due to lack of detailed experimental information in the literature, the proposed correlations were not evaluated with independent experimental data. These correlations should be re-evaluated as more data become available.

It is noted that the accuracy of different models in predicting the pressure gradient of water-lubricated high-viscosity oil-water flow is not high in general; the highest accuracy achieved for the present data base is within $\pm 50\%$. Oil fouling on the pipe wall and oil core eccentricity affect the pressure gradient of the water-lubricated high-viscosity oil-water flow. It is difficult to accurately account for the influences of oil fouling and oil core eccentricity on the pressure gradient which are associated with different parameters such as superficial oil velocity, density difference, input water volume fraction, oil viscosity and the wettability of the pipe by the oil (pipe materials and oil properties). The influences of oil fouling and oil phase eccentricity are not considered in the models of Arney (1903) and Brauner (1998). The overall influences of the oil fouling and oil phase eccentricity are accounted for in models of Bannwart (2001), McKibben et al. (2000b). Influences attributed from major parameters such as oil phase eccentricity and oil fouling are accounted for in the models of McKibben et al. (2013) and the present study. The wettability influence should be considered in the future work to improve the prediction accuracy.

5.5 Summary

An investigation on flow mechanisms and modelling of high-viscosity oil-water flow was conducted with respect to the flow patterns of liquid-liquid flow, the inversion occurrence in high-viscosity oil-water flow, and prediction of water holdup and pressure gradient of water-lubricated high-viscosity oil-water flow.

The ratio of the gravitational force to viscous force ($G/V = \frac{\Delta\rho g D^2}{\mu U}$) was proposed and validated to characterise liquid-liquid two-phase flows featuring different basic flow regimes. Liquid-liquid flows with basic flow patterns of ST and D are gravitational force dominant and characterised with high G/V . Liquid-liquid flows with basic flow patterns of CAF and I are viscous force dominant and characterised with low G/V . Liquid-liquid flows with basic flow patterns of ST, D, CAF and I are gravitational force and viscous force comparable and characterised with medium G/V . Similar to laminar-to-turbulent transition in single phase flow, the transitions of two-phase liquid-liquid flows can be roughly described with the gravitation to viscous force ratio. The transition from viscous force dominant flow to gravitational force and viscous force comparable flow is around a gravitation to viscous force ratio of 1. The transition from gravitational force and viscous force comparable flow to gravitational force dominant flow is around a gravitation to viscous force ratio of 40. Core annular flow is the dominant flow regime in viscous force dominant liquid-liquid flow.

The occurrence of inversion in high-viscosity oil-water flow (or viscous force dominant flow) is associated with the Froude number and the input water volume fraction. The input water volume fraction required to form stable core annular flow decreases with increase in the Froude number until to a critical Froude number above which the inversion occurs as long as the water content is above a minimum of around 10%. An empirical criterion for the formation of stable CAF was proposed.

Models of core annular flow or water-lubricated high-viscosity oil-water flow are reviewed. A correlation for the wall friction factor of water-lubricated high-viscosity oil-water flow with oil fouling on the pipe wall was developed. The

correlation accounts for the influence of oil eccentricity and/or oil fouling with an effective relative wall roughness which is mainly dependent on the Froude number and input water volume fraction. A correlation for the water holdup was also obtained. Evaluation of different models of core annular flow or water-lubricated high-viscosity oil-water flow was conducted. The feasibilities of different models are concluded as follows.

For the prediction of the water holdup, the models of Arney et al. (1993), and Brauner (1998) can give reasonable predictions when the oil core is virtually concentric. However, as the eccentricity degree of the oil core becomes higher the models tend to over predict the water holdup. The modified correlation of Arney et al. (1993) proposed in the present study works well for different flow conditions. It is validated with both the present experimental data and partial data available from Charles et al. (1961).

For the prediction of the pressure gradient, it is shown that the models of Arney et al. (1993) and Brauner (1998) can give reasonable predictions for concentric core annular flow without oil fouling on the pipe wall, but they greatly underestimate the pressure gradient of core annular flow when the oil core is eccentric and/or oil fouling exists on the pipe wall. The model of Bannwart (2001) accounts for the oil fouling influence on the pressure gradient with two parameters to be determined from experiments. The empirical model of McKibben et al. (2000b) is found to be able to give reasonable predictions with relative errors within $\pm 70\%$ for most of the data points. Another empirical model given in McKibben et al. (2013) shows relative errors between -40% and $+100\%$ for the majority of the present data, but as high as $+400\%$ for a few data points. The model developed in the present study has improved performance with relative errors within $\pm 50\%$ for most of the data points. This model needs further validation when more data become available. The accuracy of different empirical or mechanistic models in predicting the pressure gradient of water-lubricated high-viscosity oil-water flow is not high in general. This is associated with the difficulty in accurately accounting for the influences of oil fouling and oil core eccentricity on the pressure gradient which are associated with different

parameters such as superficial oil velocity, density difference, input water volume fraction, oil viscosity and the wettability of the pipe by the oil (pipe materials and oil properties). Care should be taken when applying a model for the prediction of the pressure gradient of water-lubricated high-viscosity oil-water flow; at least, a model which accounts for the influences of oil fouling and oil core eccentricity should be selected to avoid significant underestimations. Further work to improve the models are needed in the future.

6 CFD SIMULATION SETUP AND PROGRAMME

6.1 Introduction

Three-dimensional CFD modelling is time consuming and computational expensive than one-dimensional modelling. However it can provide more information of the flow. It is also an effective alternative to experimental investigation. The simulation setup can be changed more flexibly than the experimental setup. The advancement of computer technology has prompted the use of this approach in recent years.

A number of simulations on liquid-liquid flow have been conducted by making use of the commercial CFD code ANSYS FLUENT. Stratified oil-water flow in a horizontal pipe was modelled by Al-Yaari and Abu-Sharkh (2011) with the VOF approach. Simulation of dispersed oil-water flow in a horizontal tube was conducted by Walvelar et al. (2009) with the Eulerian-Eulerian model. With respect to core annular flow, simulations have been performed with the VOF model for flow through different flow line configurations, see downward flow (Ghosh et al., 2010), U bend flow (Ghosh et al., 2011), and flow through sudden contraction and expansion (Kaushik et al., 2012). Core annular flow through a U bend was also simulated by Jiang et al. (2014) using the Eulerian-Eulerian approach. For the above studies on core annular flow, geometries with co-axial inlets were adopted for relatively small diameter pipes ($d=0.012\text{m}$).

As a study in parallel with the experimental study (Chapter 3 and 4) and mechanism analysis and empirical modelling on high-viscosity oil-water two-phase flow (Chapter 5), 3-D CFD simulation of oil-water two-phase flow using the CFD code FLUENT has been performed with the purpose of obtaining insight into the flow behaviours. The simulation setup and programme are presented in this chapter. The mathematical models adopted in this study are introduced in Section 6.2. Physical models for the numerical study are described in Section 6.3. The simulation setup and runs are presented in Section 6.4. Finally, some preliminary simulation results are presented in Section 6.5.

6.2 Mathematical models

6.2.1 VOF model

The volume of fluid (VOF) model implemented in the CFD code FLUENT was adopted to capture phase distributions. In the VOF model, a single set of conservation equations is shared by the phases. Considering an isothermal system with no mass transfer and no phase change, the conservation equations are:

Mass equation:

$$\frac{\partial(\rho)}{\partial t} + \nabla \cdot (\rho \mathbf{u}) = 0 \quad (6-1)$$

Momentum equation:

$$\frac{\partial(\rho \mathbf{u})}{\partial t} + \nabla \cdot (\rho \mathbf{u} \cdot \mathbf{u}) = -\nabla p + \nabla \cdot [\mu(\nabla \mathbf{u} + \nabla \mathbf{u}^T)] + \rho \mathbf{g} + \mathbf{F} \quad (6-2)$$

The interface between the water phase (primary) and the oil phase (secondary) is tracked by solving the conservation equation for the volume fraction of secondary phase (oil), α_o

$$\frac{\partial(\rho_o \alpha_o)}{\partial t} + \nabla \cdot (\rho_o \alpha_o \mathbf{u}) = 0 \quad (6-3)$$

The volume fraction equation is not solved for the primary phase (water). The volume fraction of the primary phase is determined by the constraint

$$\alpha_w + \alpha_o = 1 \quad (6-4)$$

The phase volume fraction has a value of 0 or 1 when a control volume is entirely filled with oil or water, and a value between 0 and 1 if an interface is present in the control volume.

Material properties in the transport equations are determined by the presence of the component phases in each control volume. For oil-water two-phase flow, the density and viscosity in each cell are:

$$\rho = \alpha_o \rho_o + \alpha_w \rho_w \quad (6-5)$$

$$\mu = \alpha_o \mu_o + \alpha_w \mu_w \quad (6-6)$$

The term \mathbf{F} in the momentum equation stands for the contribution of surface tension. The continuum surface force (CSF) model proposed by Brackbill et al. (1992) was used. It is dependent on the surface tension coefficient, σ , and the curvature of the interface, κ

$$\mathbf{F} = \sigma \kappa \frac{\rho \nabla \alpha_o}{\frac{1}{2}(\rho_w + \rho_o)} \quad (6-7)$$

The curvature, κ , is defined in terms of the divergence of the unit normal, $\hat{\mathbf{n}}$

$$\kappa = \nabla \cdot \hat{\mathbf{n}} \quad (6-8)$$

$$\hat{\mathbf{n}} = \frac{\mathbf{n}}{|\mathbf{n}|} \quad (6-9)$$

where \mathbf{n} is the surface normal, defined as the gradient of the volume fraction of the oil phase, α_o

$$\mathbf{n} = \nabla \alpha_o \quad (6-10)$$

The effect of wall adhesion at fluids interfaces in contact with rigid boundaries is modelled within the framework of the CSF model proposed by Brackbill et al. (1992). The unit surface normal at the live cell next to the wall is replaced by the following equation, which is the so-called dynamic boundary condition, resulting in adjustment of the curvature of the surface near the wall:

$$\hat{\mathbf{n}} = \hat{\mathbf{n}}_w \cos \theta_w + \hat{\mathbf{t}}_w \sin \theta_w \quad (6-11)$$

where $\hat{\mathbf{n}}_w$ and $\hat{\mathbf{t}}_w$ are the unit vectors normal and tangential to the wall, respectively. The contact angle, θ_w , is the angle between the wall and the tangent to the interface at the wall.

6.2.2 SST k - ω turbulence model

The choice of turbulence model is crucial for turbulent two-phase flow modelling. The family of k - ε models is very popular for industrial applications due to its good convergence rate and relatively low memory requirement. The large number of examples in the literature also contributes to its popularity. Another family of two-equation eddy viscosity models is k - ω models. The shear stress transport (SST) k - ω scheme utilizes the original k - ω model of Wilcox in the inner region of the boundary layer and switches to the standard k - ε model in the outer region of the boundary layer and in free shear flows. It has been reported that a treatment of turbulence damping at the interface is necessary to predict the correct pressure losses and phase holdups (Vallée et al., 2008; Lo and Tomasello, 2010). As turbulence damping at the interface can be included in the SST k - ω turbulence model in FLUENT, the SST k - ω model was used in the present study.

The governing equations of the SST k - ω model are:

Turbulent kinetic energy:

$$\frac{\partial(\rho k)}{\partial t} + \nabla \cdot (\rho k \mathbf{u}) = \nabla \cdot \left(\left(\mu + \frac{\mu_t}{\sigma_k} \right) \nabla \cdot k \right) + G_k - Y_k \quad (6-12)$$

Specific dissipation rate:

$$\frac{\partial(\rho \omega)}{\partial t} + \nabla \cdot (\rho \omega \mathbf{u}) = \nabla \cdot \left(\left(\mu + \frac{\mu_t}{\sigma_\omega} \right) \nabla \cdot \omega \right) + G_\omega - Y_\omega + D_\omega \quad (6-13)$$

where G_k , G_ω represent the generation of k and ω , respectively; Y_k , Y_ω represent the dissipation of k and ω , respectively; D_ω represents the cross-diffusion term; μ_t represents the turbulent viscosity, $\mu_t = \alpha^* \frac{\rho k}{\omega}$, α^* represents a coefficient relevant with Reynolds number. More information on the formulation for these quantities can be found in Wilcox (1988), Menter (1994) or Fluent theory guide (2012).

When the turbulence damping option is activated in FLUENT, an additional source term is added to the ω -equation for reduction of the destruction term, Y_ω . This additional source term is expressed as

$$S_\omega = A_i \Delta n \beta \rho_i \omega_\omega^2 \quad (6-14)$$

$$\omega_\omega = B \frac{6\mu_i}{\beta \rho_i \Delta n^2} \quad (6-15)$$

$$A_i = 2\alpha_i |\nabla \alpha_i| \quad (6-16)$$

where A_i represents an interface area density that activates the correction term in the vicinity of the interface only ($A_i=0$ outside the interface region); α_i is the volume fraction of phase i ; Δn is the grid size in the interface region; β is a closure coefficient, $\beta=0.075$; B is a damping factor which can be specified, the default value is 10.

The popular k - ϵ models were also tested in a preliminary study to investigate the influence of turbulence models. The formulations of different k - ϵ models can be found in Fluent theory guide (2012).

6.3 Physical models

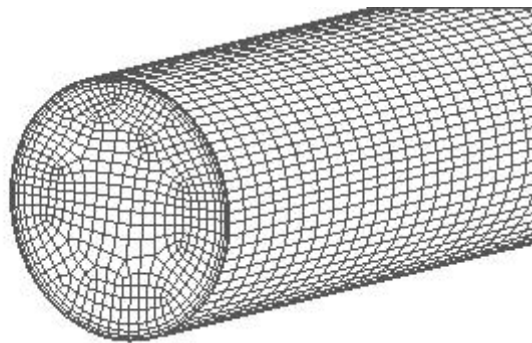
The primary facility for the numerical study is a 1 inch horizontal pipe with T-shaped junction inlets (see Figure 6-1 (a)). The simulation domain, denoting as Geometry A, resembles our experimental test section. The pipe diameter, d , is 0.026 m, with a length of 4 m (154 d) downstream the junction. The length of each branch of the junction is 0.2 m. A hexahedral mesh was generated. Figure 6-1 (b) shows a partial view of the mesh at the oil inlet. The mesh is progressively finer near the pipe wall. A mesh independence study was conducted to ensure the integrity of the solution from the mesh resolution. The final mesh used consists of about 1.2 million cells.

A scale up of the geometry A, denoting as Geometry B, is used to investigate the scale-up ability of the models as well as flow characteristics in a larger

diameter pipe. The pipe diameter of the geometry B is 0.076 m (~3 inch); the length downstream the junction is 15m. The mesh of the geometry B consists of about 1.9 million cells.



(a)



(b)

**Figure 6-1 (a) Schematic of horizontal pipe with Tee junction inlets (Geometry A);
(b) Mesh of the water inlet part.**

6.4 Simulation setup

6.4.1 Boundary conditions

The outlet pressure is applied at the outlet; a gauge pressure of zero, i.e., the atmospheric pressure, is specified at the outlet. No-slip boundary condition is imposed at the wall. The wall contact angle in the wall adhesion modelling (see Equation 6-11) is specified as a boundary condition. A contact angle, 175° , estimated from experimental videos is used in the present study; different contact angles have been tested as discussed in the following section 6.6.5. Velocity inlet boundary is set up at the inlets as introduced as follows.

For the purpose of saving computation time, instead of using a uniform velocity and a longer pipe length to achieve fully developed single phase flow before the junction, the developed velocity profiles of single phase oil and water are coded and loaded into the solver to make sure the fluids are fully developed before the junction. Under experimental conditions, both oil and water flows are fully developed before the mixing junction. Due to the relatively high viscosity of the oil, the single oil flow introduced is always laminar. The single water flow is either laminar or turbulent depending on the Reynolds number. The velocity profiles for single phase laminar flow and turbulent flow are:

Laminar flow:

$$f(r) = 2U \left(1 - \frac{r^2}{R^2} \right) \quad (6-17)$$

Turbulent flow:

$$f(r) = \frac{(m+1)(2m+1)}{2m^2} U \left(1 - \frac{r}{R} \right)^{1/m} \quad (6-18)$$

where U represents the average velocity, i.e., the superficial phase velocity in our context, r represent the radial position in the circular section, R represents the radius of the pipe. For the velocity profile of turbulent flow, m is an empirical

coefficient determined from the range of Reynolds number (see Schlichting, 1979).

Apart from the velocity, the turbulence intensity and hydraulic diameter are specified when the turbulence model is used. According to the Fluent user's guide (2012), the turbulence intensity at the core of a fully-developed duct flow can be estimated through

$$I = 0.16Re^{-1/8} \quad (6-19)$$

6.4.2 Solution setup

The solution setup is based on recommended settings from the Fluent user's guide (2012), settings commonly used for similar problems in the literature and preliminary simulation results. The problem is solved as a transient flow. The explicit VOF scheme is used. Whether the flow is solved as laminar flow or turbulent flow depends on the flow conditions. The water flow rates determine whether the turbulence model is activated or not since the oil phase is laminar due to its high viscosity. For core annular flow, the Reynolds number of the annular water film can be calculated as

$$Re_w = \frac{\rho_w U_w D_{we}}{\mu_w} \quad (6-20)$$

$$D_{we} = \frac{4A_w}{\pi D} = H_w D \quad (6-21)$$

$$U_w = \frac{U_{sw}}{H_w} \quad (6-22)$$

where D_{we} represents the hydraulic diameter, U_w the film average velocity, A_w the cross-sectional area occupied by water ($A_w = AH_w$), H_w the water holdup, U_{sw} the superficial water velocity. Substituting Equations (6-21) and (6-22) into Equation (6-20) yields

$$Re_w = Re_{sw} = \frac{\rho_w U_{sw} D}{\mu_w} \quad (6-23)$$

In the present simulations, the flow is solved as laminar when $Re_{sw} < 2\ 300$.

The simulation domain is initialised with the water inlet flow conditions. The pressure-based segregated algorithm is used to solve the transport equations. The PRESTO! (pressure staggering option) scheme is used for the pressure interpolation. The SIMPLE (Semi-implicit method for pressure linked equations) scheme is used for the pressure-velocity coupling. First-order upwind spatial discretization scheme for momentum equation is applied first and switched to second-order upwind scheme after convergence can be easily achieved after some time of run. The Geo-Reconstruct scheme is used to determine the interface shape. A smaller time step in the magnitude of 10^{-5} s is used first to obtain convergence and later increased to the magnitude of $10^{-4}/10^{-3}$ s at which the global Courant number is around 0.6~0.8. Convergence is judged based on transport equation residuals; absolute criteria are set with 10^{-4} for continuity and momentum equations, and 10^{-6} for turbulence equations. Average static pressures and water volume fractions at various cross sections are monitored. Each simulation case is run until the monitored values have reached a stable solution for enough sampling time.

6.5 Simulation runs

The geometry A was used for the majority of our simulation runs as that geometry resembles our experimental test section. The mathematical models and solution setup parameters introduced in the proceeding sections are selected for most of the runs. Most of the simulation runs were conducted following flow conditions of two experimental data sources - Charles et al. (1961) and the present experimental study – for the sake of model validation. Some simulation runs having flow conditions not available in the experimental data were performed to compare with the mechanism analysis and empirical models introduced in the proceeding chapter.

Some solution setup parameters, namely the initialization method, volume fraction interpolation scheme at the interface, turbulence scheme, and wall contact angle were investigated first for best choices of the solution setup

parameters. Upon selected solution setup parameters, more simulation runs were conducted. The total simulation runs conducted are summarised in Table 6-1. In Table 6-1, the flow conditions and fluid properties are inputs of simulations; estimates of the water film height of CAF are listed to give readers a rough perception of the flow.

In general, with 32 processors of 2 nodes (each node has two eight-core 2.6GHz Xeon CPUs and 64GB RAM) used for each case, the computing time is around 2 to 5 days for a simulation time of around 25s for low-viscosity oil-water flow cases, and 10 to 30 days for high-viscosity oil-water flow cases.

Table 6-1 Summary of simulation runs.

Notation of simulation run ^{a)}	Flow conditions and fluid properties ^{b)}							Experimental data source	Flow pattern (Exp.) ^{d)}
	U_{sw} (m/s)	U_{so} (m/s)	μ_o (cP)	ρ_o (kg/m ³)	Re_{so}	Re_{sw}	Estimate of water film height of CAF ^{c)} (mm)		
L-1	0.03	0.015	16.8	998	23.2	778	-	Charles et al. (1961)	OBL
L-2	0.03	0.06	16.8	998	92.7	778	-	Charles et al. (1961)	OPL
L-3	0.03	0.15	16.8	998	231.7	778	1.1	Charles et al. (1961)	CAF
L-3-2 (Change wall contact angles)									
L-4	0.244	0.048	16.8	998	74.1	6 331	-	Charles et al. (1961)	OBL
L-5	0.244	0.244	16.8	998	376.9	6 331	-	Charles et al. (1961)	OPL
L-5-2									
L-5-3									
L-5-4 (Change mesh sizes)									
L-6	0.244	0.487	16.8	998	752.2	6 331	2.4	Charles et al. (1961)	CAF
L-7	0.55	0.055	16.8	998	84.9	14 271	-	Charles et al. (1961)	Do/w
L-8	0.55	0.274	16.8	998	423.2	14 271	-	Charles et al. (1961)	OPL
L-9	0.55	0.55	16.8	998	849.5	14 271	3.8	Charles et al. (1961)	CAF
L-9-2									
L-9-3									
L-9-4 (Change turbulence schemes)									
L-10	0.55	1.1	16.8	998	1 699	14 271	-	Charles et al. (1961)	Dw/o

Table 6-1 Continued.

Notation of simulation run ^{a)}	Flow conditions and fluid properties ^{b)}							Experimental data source	Flow pattern (Exp.) ^{d)}
	U_{sw} (m/s)	U_{so} (m/s)	μ_o (cP)	ρ_o (kg/m ³)	Re_{so}	Re_{sw}	Estimate of water film height of CAF ^{c)} (mm)		
H-1	0.23	0.06	5 000	910	0.3	5 968	-	The present study	OPL
H-2	0.05	0.10	5 000	910	0.5	1 297	-	The present study	Inv
H-3	0.10	0.11	5 000	910	0.5	2 595	3.6	The present study	CAF
H-3-2 (Change volume fraction interpolation schemes)									
H-4	0.18	0.12	5 000	910	0.6	4 671	4.8	The present study	CAF
H-5	0.41	0.12	5 000	910	0.6	10 639	6.8	The present study	CAF
H-6	0.61	0.12	5 000	910	0.6	15 828	7.7	The present study	CAF
H-7	0.81	0.12	5 000	910	0.6	21 018	-	The present study	OLP
H-7-2 (Change initialization methods)									
H-8	0.02	0.40	5 000	910	1.9	519	-	-	-
H-9	0.20	0.40	5 000	910	1.9	5 190	2.4	The present study	CAF
H-9-2									
H-9-3									
H-9-4 (Change wall contact angles)									
H-10	0.20	0.40	5 000	960	2.0	5 190	-	-	-
H-11	0.20	0.40	5 000	1 100	2.3	5 190	-	-	-

Table 6-1 Continued.

Notation of simulation run ^{a)}	Flow conditions and fluid properties ^{b)}							Experimental data source	Flow pattern (Exp.) ^{d)}
	U_{sw} (m/s)	U_{so} (m/s)	μ_o (cP)	ρ_o (kg/m ³)	Re _{so}	Re _{sw}	Estimate of water film height of CAF ^{c)} (mm)		
H-12	0.20	0.40	1 000	910	9.5	5 190	-	-	-
H-13	0.20	0.40	500	910	18.9	5 190	-	-	-
H-14	0.20	0.40	100	910	94.6	5 190	-	-	-
H-15	0.40	0.40	5 000	910	1.9	10 379	3.8	The present study	CAF
H-16	0.60	0.40	5 000	910	1.9	15 569	4.7	The present study	CAF
H-17	0.80	0.40	5 000	910	1.9	20 758	5.5	The present study	CAF
H-18	0.04	0.80	5 000	910	3.8	1 038	-	-	-
H-19	0.20	0.80	5 000	910	3.8	5 190	-	-	-
H-20	0.20	0.40	5 000	910	1.9	5 190	-	-	-
(Geometry B)									
H-21	0.50	2.00	5 000	910	9.5	37 924	-	-	-
(Geometry B)									

^{a)} L represents relatively low oil viscosity; it is used for the notation of simulations following Charles et al. (1961). H represents high oil viscosity; it is used for the notation of simulations following the present study. Geometry A (I.D.=26 mm) is used for the simulations by default when it is not noted and Geometry B (I.D.=76 mm) is used when it is noted.

^{b)} Other properties not included in the table: $\rho_w=998$ kg/m³, and $\mu_w=1$ cP; the interfacial tension is 0.045 N/m for low viscosity oil runs, and 0.02 N/m for high viscosity oil runs.

^{c)} The estimated film height of core annular flow is calculated under the assumptions that the in situ water holdup is equal to the input water volume fraction and the oil core has a circular shape.

^{d)} OBL for oil bubbles in water, OPL for oil plugs in water, CAF for core annular flow, Do/w for dispersed oil drops in water, Dw/o for dispersed water drops in oil, Inv for inversion, OLP for dispersed oil lumps in water.

6.6 Preliminary simulation results

6.6.1 Influence of mesh sizes

A mesh independence study was conducted to choose a mesh having less number of mesh cells without significantly sacrifice the accuracy of the solution. Simulations using four designed meshes (see Table 6-2) were performed for Case L-5.

The predicted flow patterns are shown in Figure 6-2. The experimental flow pattern is oil plugs in water under this flow condition. As illustrated, Mesh A predicts core annular flow; this disagreement with experimental flow pattern is thought to come from the relatively longer cell length along the flow direction. Mesh B, C and D all successfully predict the flow as oil plugs in water. Furthermore, the predicted pressure gradients from Mesh B, C and D are compared with the experimental value (see Figure 6-3). Mesh C has significant improvement in calculated pressure gradient than Mesh B with a cell increase of around 0.7 million. Mesh D has slight improvement in calculated pressure gradient prediction than Mesh C with a cell increase of around 2.1 million. Therefore, Mesh C was finally used for the present study.

Table 6-2 Meshes used for mesh independence study.

Mesh	Total cells	Cells of the horizontal inlet cross-section	Thickness of the first layer adjacent to the pipe wall (mm)	Length of cells along Flow direction (mm)	y^+ (downstream the junction)
A	242 860	551	0.2	10	0~5
B	540 160	320	0.4	2.5	0~8
C	1 197 440	676	0.2	2.5	0~5
D	3 340 500	1,539	0.05	2	0~3

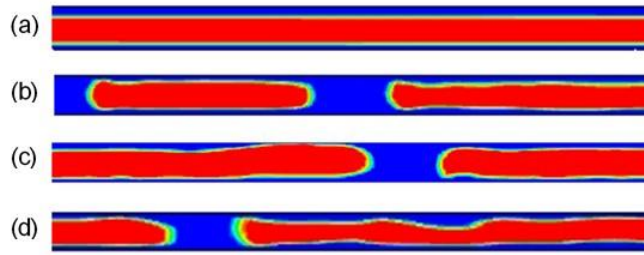


Figure 6-2 Snapshots of flow patterns calculated using different meshes (the red represents oil and the blue represents water). (a) Mesh A; (b) Mesh B; (c) Mesh C; (d) Mesh D.

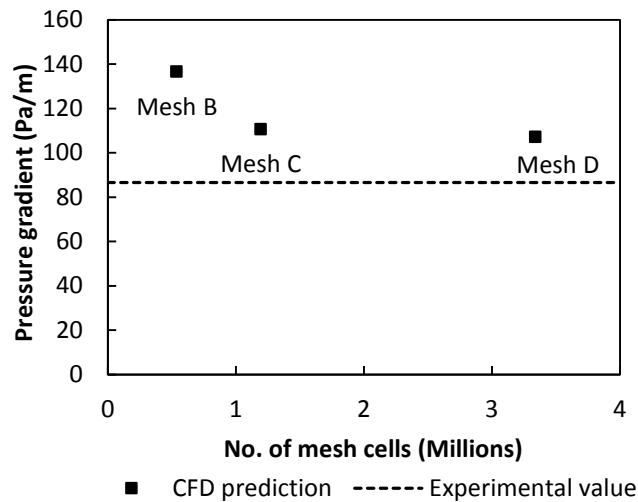


Figure 6-3 Pressure gradients calculated using different meshes.

6.6.2 Influence of initialization methods

Two simulation runs, H-7 and H-7-2, were conducted to investigate the influence of the initialization method of the flow field. The flow field was initialized with the water inlet boundary conditions for the run H-7, while with the oil inlet boundary conditions for the run H-7-2. The area-weighted average pressures and water volume fractions of various cross-sections along the pipe were monitored during the simulation. The monitored pressure and water holdup at 1m and 1.5m downstream the mixing junction (denoting the position of the junction as $z=0$) for the run H-7 and H-7-2 are shown in Figure 6-4 and 6-5 respectively. For the flow system initialized with water, the average pressures

of the two cross-sections are relatively low and fluctuate around certain values when the statistically steady solutions are reached. The average water volume fractions of the two cross-sections are one at the beginning of the run and begin to fluctuate when oil lumps flow through the cross-sections. The flow system initialized with oil has very high pressure at the beginning of the run. The pressure gradually decreases with simulation time until the statistically steady solutions are reached. The average water volume fractions of the two cross-sections are zero at the beginning of the run and gradually increase with simulation time until the flow becomes fully developed. The pressure gradients and water holdups obtained from the run H-7 and H-7-2 are quite close when the statistically steady solutions are reached. A much longer simulation time is needed for the calculation domain initialized with oil to obtain stable solutions.

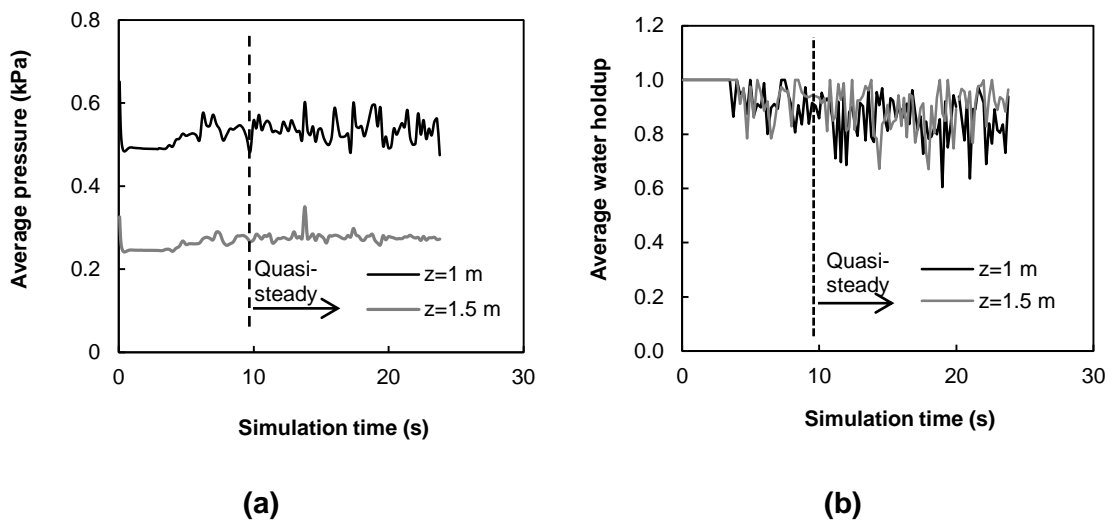


Figure 6-4 Monitored pressure and water holdup of cross-sections with simulation time (Run H-7, water initialization). (a) Face area-weighted average pressure; (b) Face area-weighted average water volume fraction.

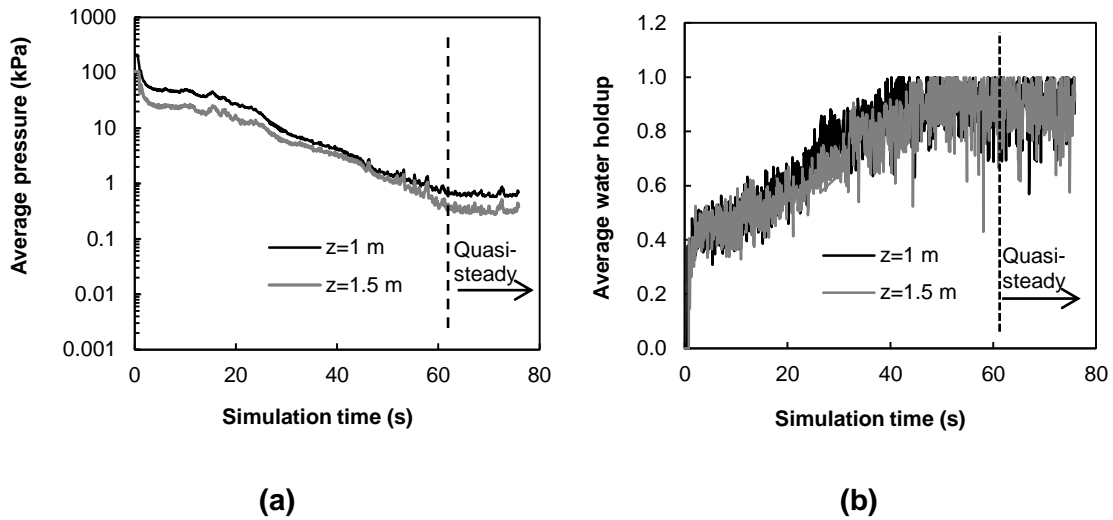


Figure 6-5 Monitored pressure and water holdup of cross-sections with simulation time (Run H-7-2, oil initialization). (a) Face area-weighted average pressure; (b) Face area-weighted average water volume fraction.

Figure 6-6 shows a comparison of histograms of normalised pressure drop ($(P_1 - P_2)_{TP} / (P_1 - P_2)_{SO}$) in 11 seconds from measurement and simulation (Run H-7). The normalised pressure drops in 11 seconds are binned in the range between 0 and 0.1 with an interval of 0.005. Similarity is shown with regard to the narrow spread of histogram. The peak of the normalised pressure drop from experiments is between 0.065 and 0.07, while from CFD simulation is between 0.015 and 0.02. This indicates that the average pressure drop calculated from the CFD models is lower than the experimental counterpart. This underestimation can be explained by the fact that the oil fouling on the pipe wall is not captured in calculated flow regime for the case under consideration. More discussion on the pressure gradient prediction is presented in the following Chapter 7.

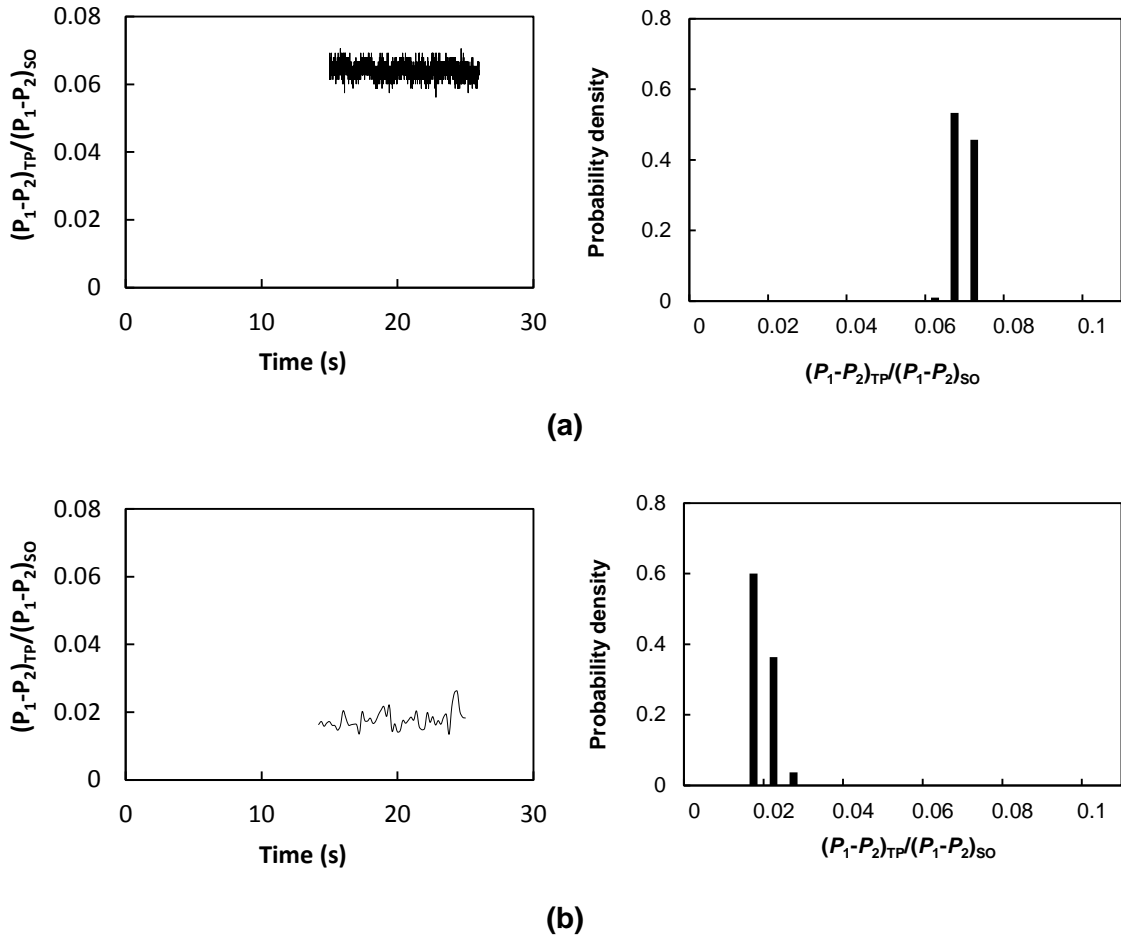


Figure 6-6 Comparison of histograms of normalised pressure drop from measurement (a) and simulation (b).

Figure 6-7 (a) and (b) illustrate the development of calculated phase configuration for flow domains initialized with water and oil respectively. It is shown that the simulations using water initialization and oil initialization converge to similar phase configurations. This is consistent with experiments. In the experiments, whether oil or water was first injected into the test line, no obvious difference in the ultimate flow regime was observed. The liquids injecting sequences affect the flow development progression but don't affect the flow behaviours as long as the flow is developed. The water initialization method is used in the rest simulation runs for the sake of saving computational time.

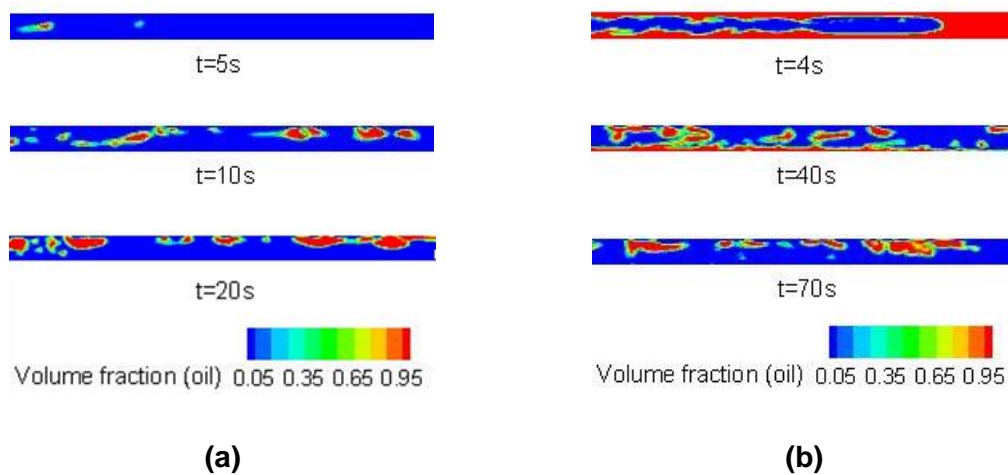


Figure 6-7 Development of phase configuration with simulation time. (a) Water initialization (Run H-7); (b) Oil initialization (Run H-7-2).

6.6.3 Influence of volume fraction interpolation schemes at phase interface

ANSYS Fluent is a finite volume based solver. It only stores the data of the cell centres. However, face values are required for the convection terms and must be interpolated from the cell centre values. The volume fraction interpolation scheme near phase interface affects the calculated interface shape. The Geo-Reconstruct scheme is normally recommended for its high accuracy. It assumes that the interface between two fluids has a linear slope within each cell, and uses this linear shape for calculation of the advection of fluid through the cell faces. The CICSAM (Compressive Interface Capturing Scheme for Arbitrary Meshes) scheme is a high resolution differencing scheme. According to Fluent theory guide (2012), the CICSAM scheme is particularly suitable for flows with high ratios of viscosities between the phases.

Two simulation runs, H-3 and H-3-2, were conducted to investigate which volume fraction interpolation scheme gives more accurate prediction of the phase interface for flows with high viscosity ratios. Predicted flow patterns from runs applying the Geo-Reconstruct scheme and CICSAM scheme, together with the corresponding experimental flow pattern are illustrated in Figure 6-8. It is shown that the core annular flow is predicted from both simulation runs, which is

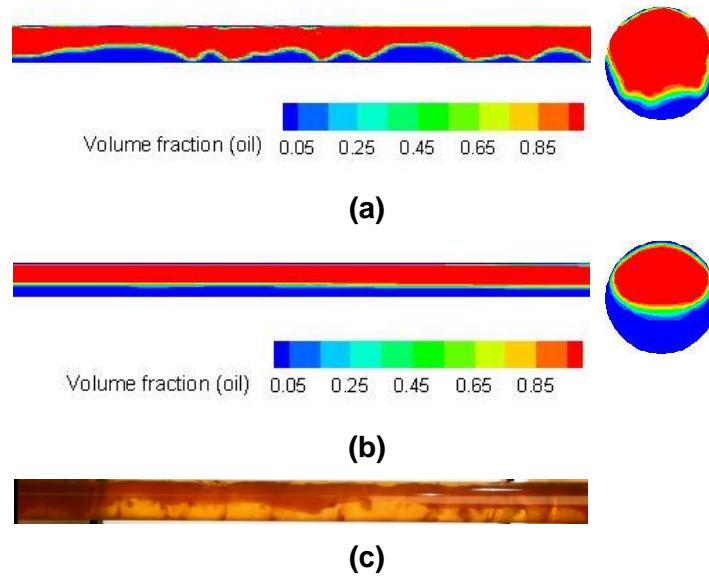


Figure 6-8 Predicted flow patterns from simulations using different volume fraction interpolation schemes at the interface and the corresponding experimental flow pattern. (a) Geo-Reconstruct scheme (Run H-3); (b) CICSAM scheme (Run H-3-2); (c) snapshot from recorded experimental flow.

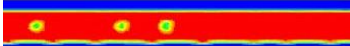


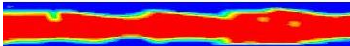

in agreement with the experimental flow pattern. However, the calculated interfaces between the oil core and the annular water are quite different. The calculated interface using the Geo-Reconstruct scheme is more similar to that of the experimental flow; the surface is wavy along the flow direction. The calculated interface using the CICSAM scheme is quite smooth without perceptible waviness along the flow direction. Therefore, the Geo-Reconstruct scheme is used for other simulation cases for its accuracy.

6.6.4 Influence of turbulence schemes

The Reynolds-averaged Navier-Stokes (RANS) models offer an economic approach for computing complex turbulent industrial flows. Typical examples of such models are the $k-\varepsilon$ or the $k-\omega$ models having two additional transport equations. The standard $k-\varepsilon$, RNG $k-\varepsilon$ and SST $k-\omega$ with and without turbulence damping treatment at the phase interface were tested to investigate which turbulent scheme is most suitable for the oil-water two-phase flow simulation. The enhanced wall treatment was applied for the two $k-\varepsilon$ models. In all simulations, the near wall grids have a $y^+ < 5$.

Predictions of flow patterns and pressure gradients from simulation runs using different turbulence models as well as the corresponding experimental counterparts are displayed in Table 6-3. It is demonstrated that the tested turbulence schemes all successfully predict core annular flow. The SST $k-\omega$ model with the turbulence damping treatment activated gives the best prediction in the pressure gradient for the case under consideration. It is noted that the drawing of the experimental flow pattern is taken from Charles et al. (1961). It is not mentioned in Charles et al. (1961) whether an optical matching box was used or not in the above authors' experimental hence it is not clear that whether the drawing of the experimental flow regime has some degree of distortion. Since we are comparing the flow regimes qualitatively, distortion, if there is any, in experimental flow regime drawings is not considered.

Table 6-3 Predicted flow patterns and pressure gradients with different turbulence schemes and comparison with experiments.

	Flow pattern ^{a)}	dp/dx (Pa/m)	Relative error for dp/dx
Run L-9-2, standard $k-\epsilon$		582	+21%
Run L-9-3, RNG $k-\epsilon$		575	+19%
Run L-9-4, SST $k-\omega$ (without turbulence damping treatment)		561	+16%
Run L-9, SST $k-\omega$ (with turbulence damping treatment)		427	-11%
Experiment		482	

^{a)} The red represents water and the blue represents oil in simulation results; drawing of experimental flow pattern is taken from Charles et al. (1961), the black represents water, and white with dots inside represents oil.

Cross-sectional turbulence characteristics obtained from different turbulence schemes are shown in Figure 6-9. Turbulence properties calculated with the standard $k-\varepsilon$ and RNG $k-\varepsilon$ schemes are comparable. The magnitudes of turbulence properties calculated with the SST $k-\omega$ scheme without turbulence damping treatment are slightly smaller than those predicted with the $k-\varepsilon$ schemes, but still they are of same order.

The cross-sectional distributions calculated with the SST $k-\omega$ scheme with the turbulence damping activated (Run-9) differ from those obtained with the other three schemes, especially in the region near the interface of the oil and water. The turbulence intensity distribution matches the phase distribution, and similarly for the turbulent viscosity and effective viscosity. The magnitudes of turbulence characteristics of the oil core are nearly one order lower than those obtained with the other three schemes. The lower turbulence intensity across the oil core can be attributed to the additional source term added to the ω -equation. Compared to Run L-9-4, the calculated ω from Run-9 is higher, leading to a lower turbulence viscosity ($\mu_t \approx \frac{\rho k}{\omega}$). The turbulence intensity and viscosity from the standard $k-\varepsilon$ and RNG $k-\varepsilon$ models are thought to be over predicted due to lack of special treatment of turbulence at the interface, which leads to the overestimated pressure gradients in Table 6-3.

Lo and Tomasello (2010) also reported that the $k-\varepsilon$ models over predict the pressure gradient in simulations of gas-liquid stratified flow and emphasised the necessity to include the turbulence damping treatment at the phase interface. For high-viscosity oil-water two-phase flow, the turbulence damping effect of the highly viscous oil on the low viscous water would be more effective. Therefore, the SST $k-\omega$ model with turbulence damping treatment at the phase interface activated is used in the present study.

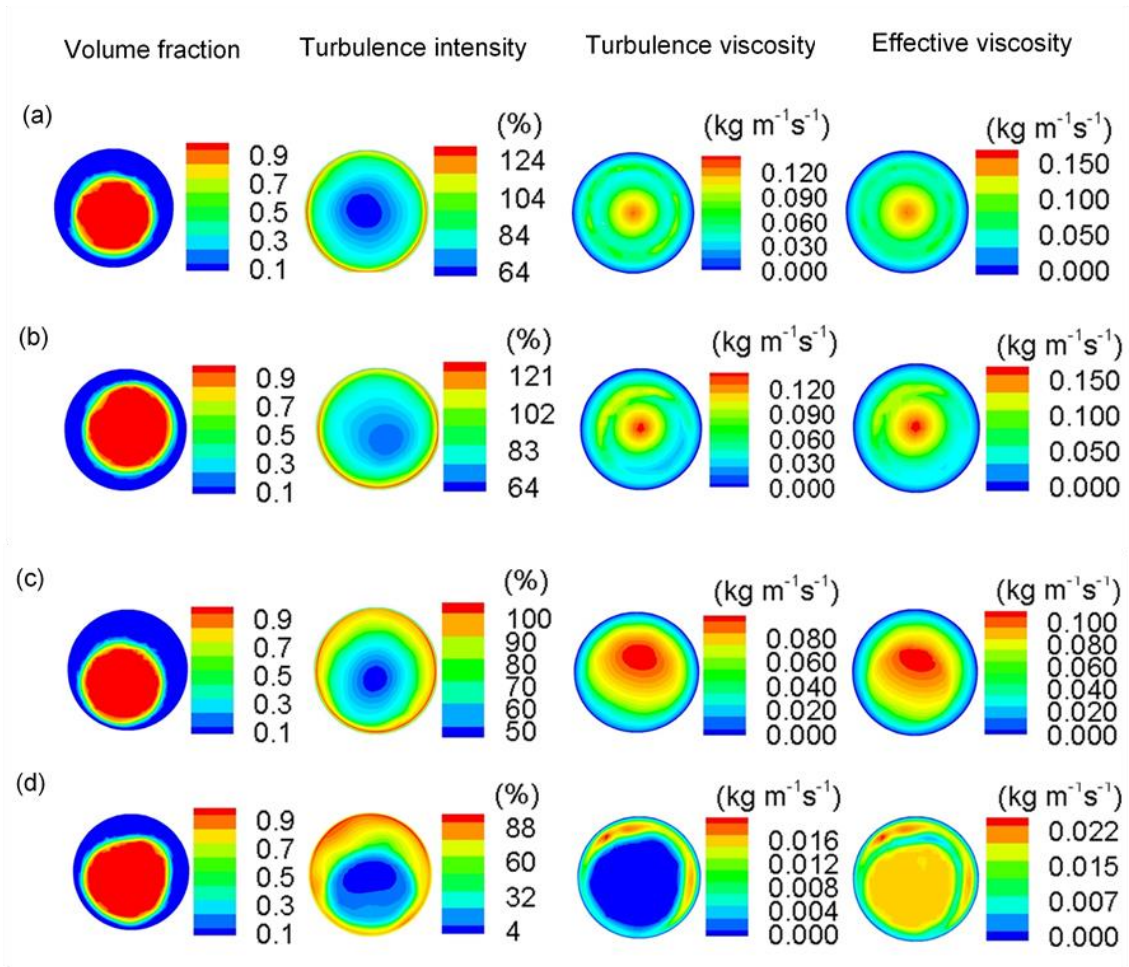


Figure 6-9 Cross-sectional turbulence characteristics from runs using different turbulence schemes. (a) standard $k-\epsilon$ (Run L-9-2); (b) RNG $k-\epsilon$ (Run L-9-3); (c) SST $k-\omega$ without turbulence damping (Run L-9-4); (d) SST $k-\omega$ with turbulence damping (Run L-9).

6.6.5 Influence of wall contact angles

Force balance or equilibrium at the solid-liquid boundary is given by Young's equation for contact angles greater than zero (see Figure 6-10):

$$\sigma_{LG} \cos \theta_Y = \sigma_{SG} - \sigma_{SL} \quad (6-24)$$

where θ_Y is Yang's contact angle, σ_{SL} , σ_{SG} , σ_{LG} are the interfacial tensions of solid-liquid, solid-gas and liquid-gas, respectively. This equation also applies if

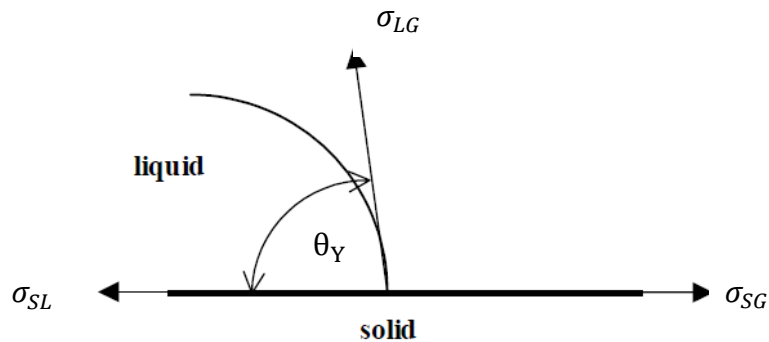


Figure 6-10 Wall contact angles.

the 'gas' phase is another liquid, immiscible with the droplet of the first 'liquid' phase.

When the force balance is in equilibrium, three thermodynamic parameters σ_{SL} , σ_{SG} , σ_{LG} determine a unique static contact angle θ_Y . When the force balance is out of equilibrium, the contact line will move towards its equilibrium position. The contact line motion induces an apparent dynamic (time-dependent) contact angle (Van Mourik et al., 2005). For liquid moving quickly over a surface, the contact angle can be altered from its value at rest. ANSYS Fluent allows one to input either a static value for the wall contact angle, or to use User Defined Functions to compute the dynamic contact angle which needs further modelling.

Modelling of the dynamic contact angle is an area of active research (see Jiang et al., 1979; Bracke et al., 1989; Seebergh and Berg, 1992; Nichita et al., 2010; Sui et al., 2014). Existing models are empirically based and most of the experiments only cover small capillary numbers ($Ca < 0.03$), so the models based on those experiments are not generally valid (Van Mourik et al., 2005). The wall contact angle has the most influence on the flow kinetics for flow with low capillary number (Van Mourik et al., 2005). For high-viscosity oil-water flow, the capillary number ($Ca = \frac{\mu U}{\sigma}$) is high due to high viscous force.

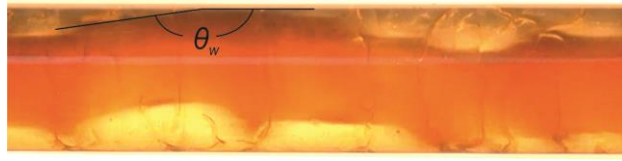


Figure 6-11 Illustration of the wall contact angle (θ_w).

Static contact angles are used in the simulations on high-viscosity oil core annular flow performed by Ghosh et al. (2010 and 2011) and Kaushik et al. (2012) and reasonable results are obtained. It is worth remarking here that prescribing a constant contact angle does not mean that liquid at the boundary will not move. The liquid will move towards its equilibrium position induced by a pressure correction each time step.

Modelling of the dynamic contact angle is beyond the scope of the present study which aims to test the available CFD models in the commercial code Fluent and study oil-water flow characteristics. A static wall contact angle was prescribed in the present simulation study. The angle when the oil core is in contact with the pipe wall is estimated as obtuse from experimental videos (see Figure 6-11). The angle changes with time and the oil core is not always in contact with the wall. Therefore, an obtuse angle close to 180° is thought to be appropriate for high-viscosity oil cases under consideration. As no oil fouling on the pipe was observed in the experiments of Charles et al., (1961), indicating rare oil contact with the wall, an angle close to 180° is thought to be appropriate for low-viscosity oil cases too.

Simulation runs were conducted to investigate the influence of wall contact angles. For low-viscosity oil-water flow, change of wall contact angle might affect the calculated flow significantly as the flow has low capillary number hence the surface tension influence is important. Case L-3 and L-3-2 were specified with angles of 175° and 60° , respectively. Figure 6-12 shows the calculated flow patterns from Cases L-3 and L-3-2 and the corresponding experimental flow pattern. Dramatic difference between the calculated flow patterns is demonstrated in Figure 6-9. With a wall contact angle of 175° which indicates that the wall is rarely wetted by the oil phase, core annular flow is the

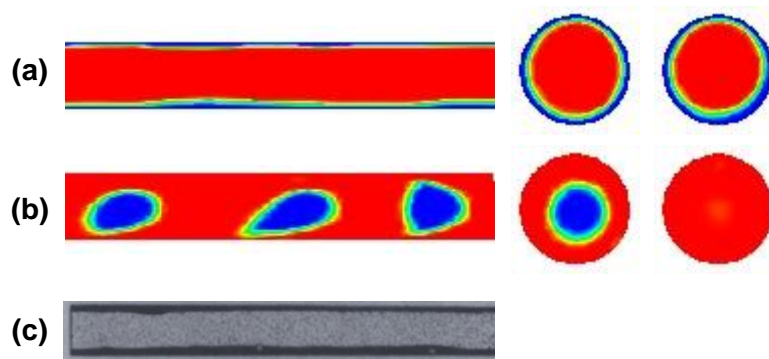


Figure 6-12 Calculated flow patterns (the red represents oil and the blue represents water) with different wall contact angles and the corresponding experimental flow pattern (oil core inside annular water) for a low-viscosity oil-water case. (a) 175°; (b) 60°; (c) a flow pattern drawing based on experiments (Charles et al., 1961).

calculated flow regime; this flow regime agrees with the flow regime observed in the experiments of Charles et al. (1961). When the wall contact angle is reduced to 60° which suggests that the wall tends to be wetted by the oil phase, the calculated phase configuration becomes dispersed water bubbles in oil, which is dramatically inconsistent with the experiments.

The influence of wall contact angle for high-viscosity oil-water flow is shown in Figure 6-13. The calculated flow patterns from cases H-9, H-9-2, H-9-3, and H-9-4 with angles of 175°, 120°, 60° and 5° are shown in Figures 6-13 (a) to (d), respectively. The corresponding experimental flow pattern is displayed in Figure 6-13 (e) for comparison. For the high-viscosity oil-water case, the difference between the calculated flow patterns from cases using different wall contact angles is not as dramatic as that in the low-viscosity oil-water case shown in Figure 6-12. The water lubrication characteristic is reflected in all the cases. With decrease in the wall contact angle, the oil fouling on the pipe wall becomes more significant. Flow patterns predicted from the cases with contact angles of 175° and 120° are more similar to the experimental flow pattern. It is difficult to say which contact angle is better between the 175° and 120° for the case under consideration. In reality, the dynamic contact angle may vary between them. For a particular case, there might be a static angle which can best represent the

average influence of the dynamic contact angle. However, it is computationally expensive to run different cases with different angles to find that representative static contact angle (that is when experiments are available to make the judgement) for each simulation case. Further, the best representative static contact angle is likely to be different for cases with different flow conditions.

As have been discussed above, an obtuse angle close to 180° is thought to be appropriate for the cases in the present study. A contact angle of 175° is used in all the simulation cases. A fair agreement is shown between simulation results and experiments for most of the simulation cases as presented in the following Chapter. When applying a constant wall contact angle in the continuum surface force model incorporated in Fluent, caution should be taken in the numerical results. Errors resulted from the physically deficient representation of the wall adhesion effect are possible; this can be reflected in parameters such as the oil fouling film height and pressure gradient.

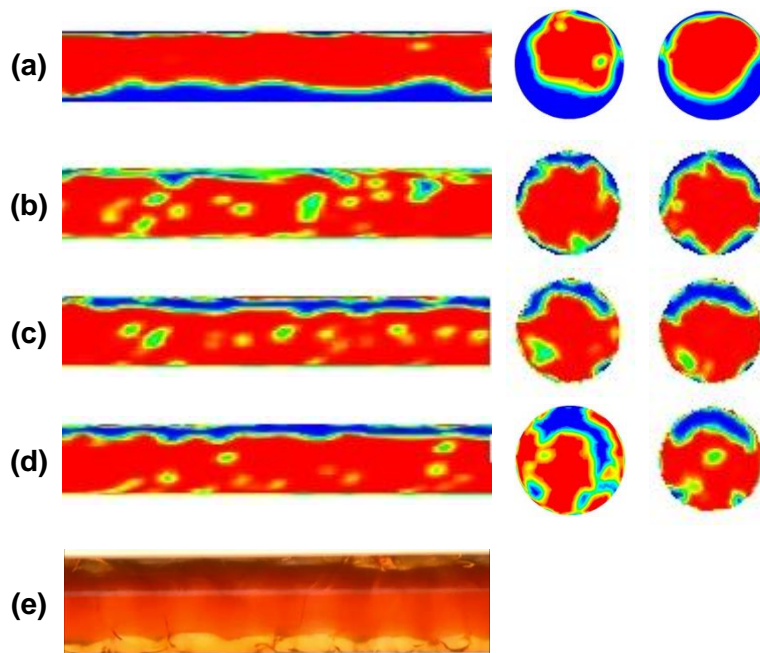


Figure 6-13 Calculated flow patterns (the red represents oil and the blue represents water) with different wall contact angles and the corresponding experimental flow pattern (oil core inside annular water) for a high-viscosity oil-water case. (a) 175° ; (b) 120° ; (c) 60° ; (d) 5° ; (e) snapshot form recorded experimental flow.

6.7 Summary

The mathematical models adopted in this numerical study, the VOF multiphase model in conjunction with SST $k-\omega$ model for turbulent flow, are described in this chapter. The simulation setup is introduced and the simulation cases are outlined. Check of simulation setup is conducted with preliminary simulation results. Influences of mesh sizes, initialization methods, volume fraction interpolation schemes, turbulence schemes and contact angles are summarised as follows.

Numerical errors can be resulted from meshes. The mesh used for the present study was selected upon a mesh independence study. Simulations with both the water initialization method and the oil initialization method ultimately lead to similar results which is in consistent with experiments. The water initialization method was selected to save computational time. The Geo-Reconstruct scheme for the volume fraction interpolation was selected as more accurate prediction of the phase interface was obtained with it. The SST $k-\omega$ turbulence scheme with turbulence damping treatment at the phase interface outperforms the SST $k-\omega$ turbulence scheme without turbulence damping treatment and $k-\epsilon$ turbulence schemes. The wall adhesion modelling is not well established yet in the VOF model. A static contact angle estimated from experiments was used in the present study. The wall contact angle significantly affects the phase configurations of oil-water flow with low capillary number. For high-viscosity oil-water flow with high capillary number, the wall contact angle affect the phase configuration with regard to the oil fouling film capture. Errors resulted from the physically deficient representation of the wall adhesion effect are possible in simulation results.

Discussion of major simulation results is presented in the following Chapter 7.

7 SIMULATION RESULTS

7.1 Introduction

Analysis of CFD simulation results was conducted. Similarly to the discussion on experimental results (Chapter 4) and mechanism analysis and empirical modelling (Chapter 5), the discussion on simulation results also covers the aspects of flow patterns, the formation of water-lubricated flow, water holdup and pressure gradient of water-lubricated flow. Comparison with experimental results (two data sources, namely Charles et al. (1961) and the present study) was conducted to validate the CFD models. Flow mechanisms discussed in Chapter 5 were further validated with the CFD simulation results. Apart from the above aspects, cross-sectional flow characteristics which are not captured in both experimental measurement and empirical/mechanistic modelling are presented to gain some insight into the flow behaviours.

7.2 Flow patterns

7.2.1 Comparison with experimental flow patterns

Simulation runs (L-1 to L-10) following the flow conditions of the experimental study of Charles et al. (1961) were performed. The above experimental study is characterised with low-viscosity oil (16.8 cP) and equal-density oil and water. Different from the present experimental study in which core annular flow is a dominant flow pattern, five flow patterns are reported among which not a single one is obviously dominant (see Figure 7-1).

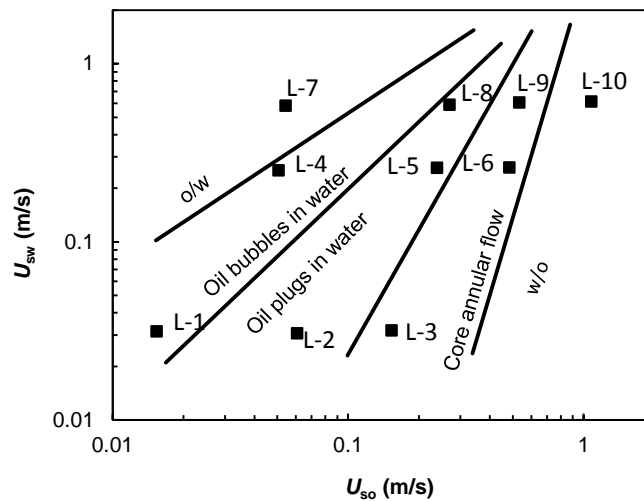



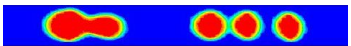




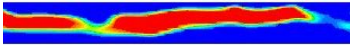


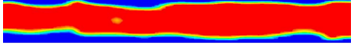

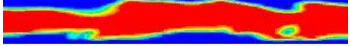

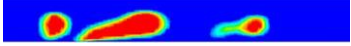
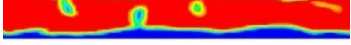


Figure 7-1 Adapted flow pattern map after Charles et al. (1961). Simulation runs performed are marked out.

A comparison of predicted flow patterns with experimental counterparts from Charles et al. (1961) is displayed in Table 7-1. The flow patterns predicted from the CFD model are in good agreement with experimental flow patterns for core annular flow, oil plugs/bubbles in water. However, a disagreement is shown between predicted and experimental phase configurations concerning dispersed flow (droplets of one phase in another). This can be explained by the fact that the VOF model is not appropriate if the interface length is small compared to a computational grid. The interface between phases is tracked by calculation of the phase volume fraction in each computational cell (see the VOF model in Section 6.2). The computational grid scale along the flow direction is around 2.5 mm in this study. The sizes of visible small drops in experiments should also be around the magnitude of millimetre. To capture such small dispersed drops with the VOF model in a 4m-length pipe, a much finer grid is essential, which implies much more expensive computation. The Mixture model, Euler-Euler, or Euler-Lagrange schemes are normally used for simulation of dispersed flow in a pipe.

Table 7-1 Comparison of predicted flow patterns with experimental counterparts from Charles et al. (1961).

Flow pattern	Run	Experimental flow pattern ^{a)}	Predicted flow pattern ^{b)}
Oil bubbles in water	L-1		
	L-4		
Oil plugs in water	L-2		
	L-5		
	L-8	-	
Core annular flow	L-3		
	L-6	-	
	L-9		
Oil drops in water	L-7		
Water drops in oil	L-10	-	

^{a)} Illustrations of experimental flow patterns are drawings from Charles et al. (1961); the black represents water and the white with dots inside represents oil.

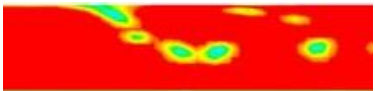

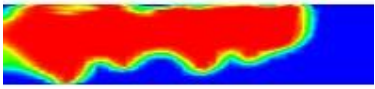

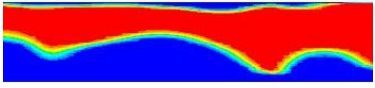

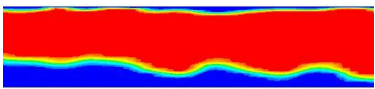
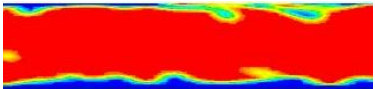


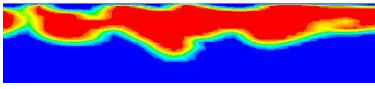

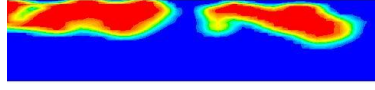
^{b)} Contours of oil volume fraction from CFD simulations; the red represents oil and the blue represents water.

For high-viscosity oil-water flow, core annular flow is the dominant flow regime. Apart from the core annular flow, oil plugs and dispersed oil lumps in water, instead of dispersed oil drops in water, can be formed. As the interface length scale of the dispersed oil lumps is still comparable to the pipe diameter, the VOF model is capable to capture the phase interfaces with reasonable mesh resolution.

A comparison of typical flow patterns from CFD simulations and the corresponding experimental counterparts from the present experimental study is displayed in Table 7-2. In general, the predicted flow patterns under various

flow conditions agree with experimental observations. When water content is low (Run H-8), oil is the continuous dominant phase and discontinuous water steams/bubbles are observed to be entrained inside the oil phase or adjacent to the pipe wall. With increase of water content, oil plugs in water, core annular flow or dispersed oil lumps in water are predicted, which is consistent with the experiments. Unlike the equal-density oil-water flow, the oil phase inside the annular water flows in the upper part of the pipe except for cases when the oil

Table 7-2 Comparison of typical flow patterns from simulations and the corresponding experimental counterparts from the present experimental study.

Flow pattern	Run	Experimental flow pattern ^{a)}	Predicted flow pattern ^{b)}
Oil-continuous	H-8	-	
Oil plugs in water	H-1		
Core annular flow	H-4		
	H-9		
	H-19	-	
	H-21	-	
Oil lumps in water	H-6		
	H-7		

^{a)} Snapshots of recorded experimental videos.

^{b)} Contours of oil volume fraction; the red represents oil and the blue represents water.

flow rate is high. It was observed in the experiments that the oil phase is more concentric when the oil flow rate is high; this is reflected from calculated flow patterns. The run H-19 uses a higher U_{so} with all the other parameters similar to those used in the run H-9, and the predicted oil core from Run H-19 is more concentric than that from Run H-9.

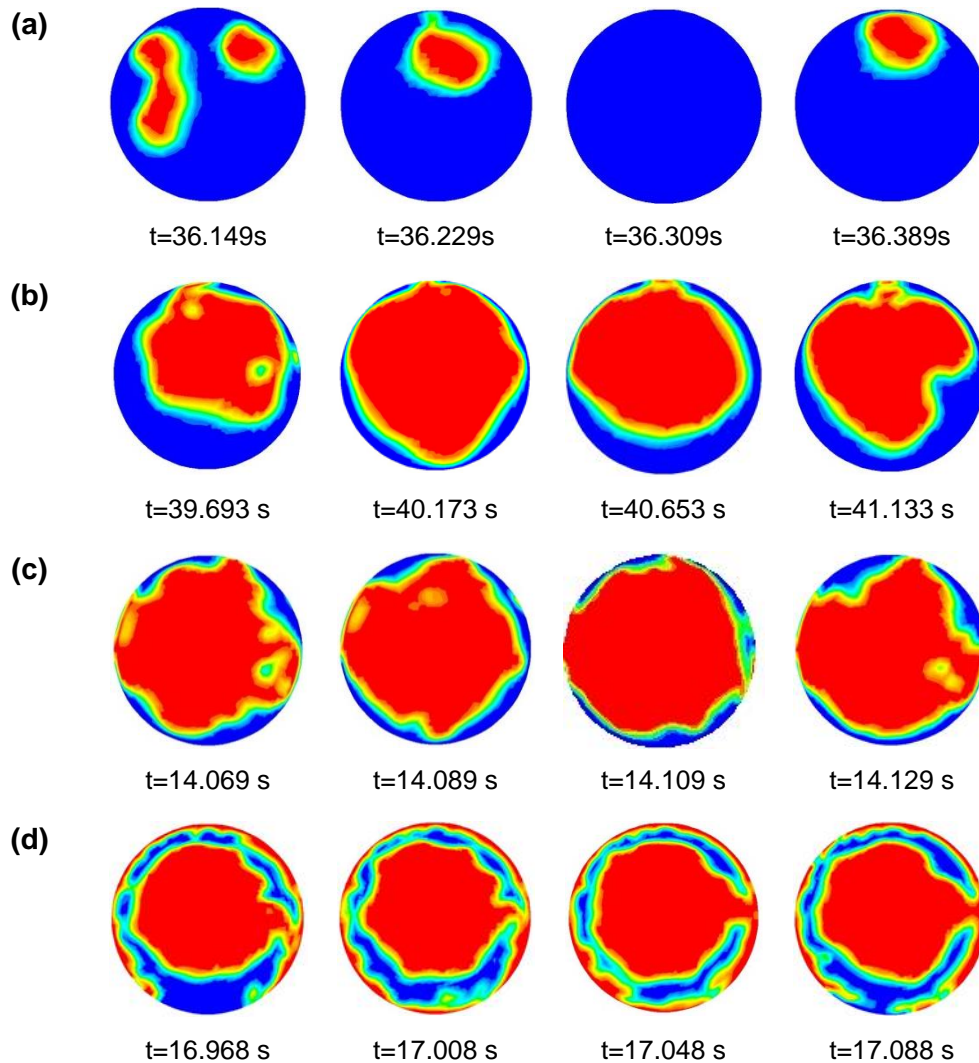


Figure 7-2 Calculated phase configurations at various cross-sections (the red represents oil and the blue represents water). (a) Run H-7; (b) Run H-9; (c) Run H-19; (d) Run H-21.

Oil fouling on the pipe wall is a distinctive phenomenon in high-viscosity oil-water flow. It can be observed in Table 7-2 that oil fouling is captured for a limited number of runs. To have a clear view of oil fouling films on the pipe wall, calculated phase configurations at a cross-section ($z=3.5$ m for the 1 inch pipe and $z=14$ m for the 3 inch pipe) with simulation time for the run H-7, H-9, H-19, and H-21 are displayed in Figure 7-2. The run H-7 simulates dispersed oil lumps in water flow (see Figure 7-2 (a)). The oil fouling on the pipe wall is seldom captured in this case while thin oil fouling film on the pipe wall can be observed in the experiments. The run H-9 and H-19 simulate core annular flow in a 26 mm I.D. pipe. Limited contact between the oil core and pipe wall and oil fouling spots can be observed in the calculated phase configurations (see Figure 7-2 (b) and (c)). The run H-21 simulates oil-water flow in a 76 mm I.D. pipe. The oil fouling film is clearly captured in this case (see Figure 7-2 (d)).

As has been discussed in Section 6.6.5 in Chapter 6, the wall adhesion effect is affected by the specified static wall contact angle. Besides, the mesh resolution near the pipe wall can also affect the accuracy. In the present study, a static wall contact angle was specified in all the simulation cases. The oil fouling captured on the pipe wall of the 76 mm I.D. pipe is heavier than that of the 26 mm I.D. pipe, this suggests that the oil fouling is heavier in a larger diameter pipe. However, the quantitative results must be treated with caution. The heights of the first two cell layers adjacent to the pipe wall are respectively 0.2 mm and 0.3 mm for the mesh of the 26 mm I.D. pipe, and 1 mm and 1.25 mm for the mesh of the 76 mm I.D. pipe. The oil fouling film captured in the 76 mm I.D. pipe covers 1 to 2 cells, i.e., the oil fouling film height varies from 1 mm to 2.25 mm. The few oil fouling spots captured in the 26 mm I.D. pipe covers 1 cell, i.e., 0.2mm. These quantitative parameters have no validation from experiments.

7.2.2 Influence of parameters on flow pattern

(1) *Ratio of gravitational force to viscous force (G/V)*

The gravitation to viscous force ratio ($G/V = \frac{\Delta\rho g D^2}{\mu U}$) has been proposed to characterise liquid-liquid flows in Chapter 5 (see Section 5.2). Liquid-liquid flows

with basic flow patterns of stratified flow and dispersed flow are gravitational force dominant which are characterised with high G/V . Liquid-liquid flows with basic flow patterns of intermittent flow and CAF are viscous force dominant which are characterised with low G/V . Liquid-liquid flows with basic flow patterns of stratified flow, dispersed flow, intermittent flow and CAF are gravitational force and viscous force comparable; they are characterised with medium G/V .

The high-viscosity oil-water flow in the present experimental study is viscous force dominant with G/V lower than 1 (refer to Figure 5-8). Core annular flow and intermittent flow (oil plugs or lumps in water) were observed in experiments. Stratified flow was rarely observed. It is believed that for the present experimental flow pipeline, stratified flow would develop if the viscosity of the oil is smaller hence the flow system having a higher G/V . Also, stratified flow would develop if the oil used in the present experimental study flows in a larger diameter pipe, i.e., forming a new flow system having a higher G/V . Simulation runs were performed to validate the above statement.

Figure 7-3 shows the change of phase configuration with change of oil viscosity. An obvious annular water layer can be seen in Figure 7-3 (a) when the viscosity of the oil is 5 000 cP and the corresponding gravitation to viscous force ratio is 0.16. The top water layer becomes very thin and discontinuous for the case in which the oil viscosity is 1 000 cP and the corresponding gravitation to viscous force ratio is 0.96. It is very possible that a phase configuration like this is defined as stratified flow. Flow condition similar to this case can be found in the experimental study of Sotgia et al. (2008). The flow regime at this flow condition is wavy-stratified flow in the flow map produced by the above authors (refer to Figure 4-8). With further decrease of oil viscosity hence increase of the gravitation to viscous force ratio, the predicted flow regime is wavy-stratified or stratified flow as shown in Figure 7-3 (c) and (d). Comparing Figure 7-3 (c) and (d), it is shown that the interface of the stratified flow has a smaller curvature for the case having a higher gravitation to viscous force ratio.

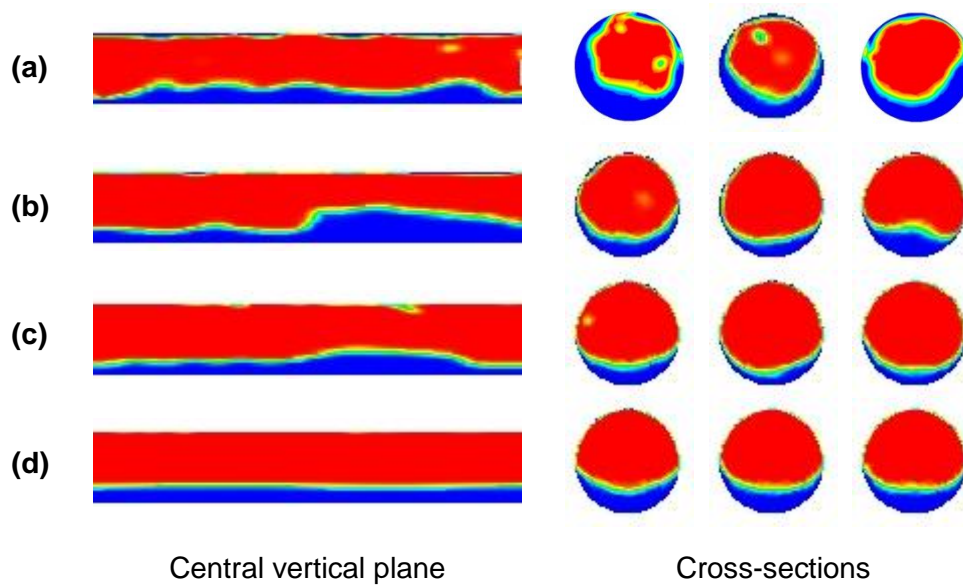


Figure 7-3 Change of phase configuration with change of oil viscosity at $U_{so}=0.4$ m/s, and $U_{sw}=0.2$ m/s (the red represents oil and the blue represents water). (a) 5 000 cP ($G/V=0.16$; Run H-9); (b) 1 000 cP ($G/V=0.96$; Run H-12); (c) 500 cP ($G/V=1.92$; Run H-13); (d) 100 cP ($G/V=9.68$; Run H-14).

The change of phase configuration with change of pipe diameter is displayed in Figure 7-4. For the flow condition of $U_{so}=0.4$ m/s, and $U_{sw}=0.2$ m/s, CAF develops in a 26 mm I.D. pipe, while wavy stratified flow develops in a 76 mm I.D. pipe. The corresponding gravitation to viscous force ratio for the smaller diameter pipe is 0.16, indicating viscous force dominant; the gravitation to viscous force ratio is 1.68 for the larger diameter pipe, indicating viscous force and gravitational force comparable flow. For viscous force and gravitational force comparable flow, stratified flow is one of the possible flow patterns. Referring to Figure 5-8 in Chapter 5, it is shown that stratified flow is most likely to develop for $G/V=1.68$ and C_w around 0.33. It can also be observed in Figure 7-4 (b) that there are entrained discontinuous water streams inside and at the top of the oil layer. This flow regime is thought to be a transitional flow pattern from stratified flow to core annular flow; core annular flow develops when the discontinuous water streams becomes continuous.

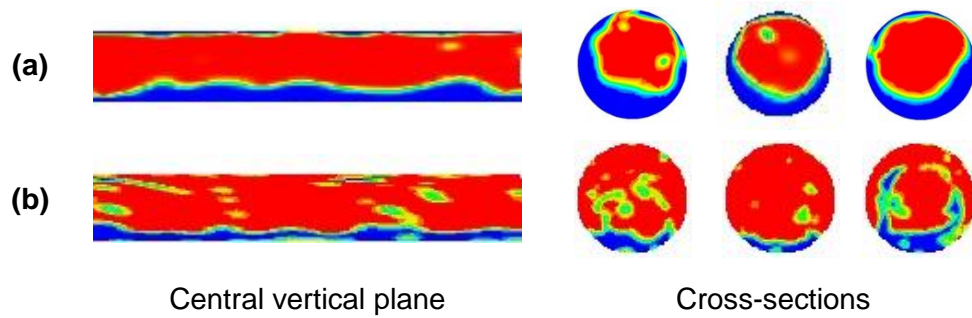


Figure 7-4 Change of phase configuration with change of pipe diameter at $U_{so}=0.4$ m/s, and $U_{sw}=0.2$ m/s (the red represents oil and the blue represents water). (a) 26 mm ($G/V=0.16$; Run H-9); (b) 76 mm ($G/V=1.68$; Run H-20).

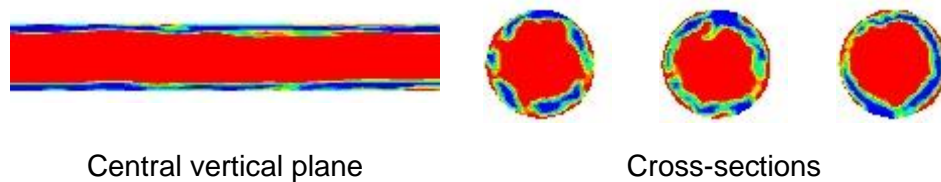


Figure 7-5 Phase configuration in a 76 mm I.D. horizontal pipe at $U_{so}=2.0$ m/s, and $U_{sw}=0.5$ m/s ($G/V=0.4$, Run H-21; the red represents oil and the blue represents water).

It is anticipated that the core annular flow would develop in the 76 mm I.D. pipe when the gravitation to viscous force ratio is lower than 1, hence viscous force becomes dominant. Figure 7-5 shows the phase configuration of oil-water flow in the 76 mm I.D. pipe at $U_{so}=2.0$ m/s, and $U_{sw}=0.5$ m/s under which $G/V = 0.4$. Core annular flow develops for this case as expected. For oil-water flow in a larger diameter pipe, higher oil flow rate is required to form stable core annular flow.

(2) Froude number (ratio of inertial force to gravitational force)

The degree of oil concentricity is described using an expression associated with the Froude number ($Fr = \frac{U_{so}}{\sqrt{gD\frac{\Delta\rho}{\rho_w}}}$) in Chapter 5. The Froude number is the ratio of the inertial force to the buoyancy force. The oil phase inside the water is inclined to be more concentric when the inertial force is dominant and more eccentric when the buoyancy force is dominant.

The influence of oil flow rate has been demonstrated in our experimental investigation. It was observed that the oil core was more concentric for higher oil superficial velocities. This trend is also found in our simulation results as shown in Figure 7-6.

Figure 7-7 shows calculated phase configurations with different oil densities. It is shown that the oil phase inside the water is more concentric when the density of the oil phase is close to that of water. Also, the oil core would flow in the lower part of the pipe if the oil density is much higher than the water density.

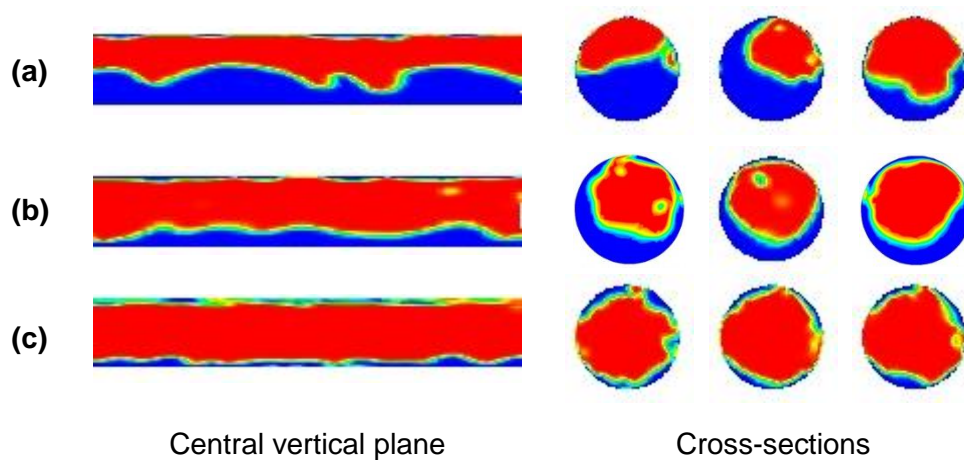


Figure 7-6 Change of phase configuration with change of superficial oil velocities. (the red represents oil and the blue represents water). (a) $U_{so}=0.12$ m/s ($Fr=0.8$; Run H-4); (b) $U_{so}=0.4$ m/s ($Fr=2.67$; Run H-9). (c) $U_{so}=0.8$ m/s ($Fr=5.34$; Run H-19).

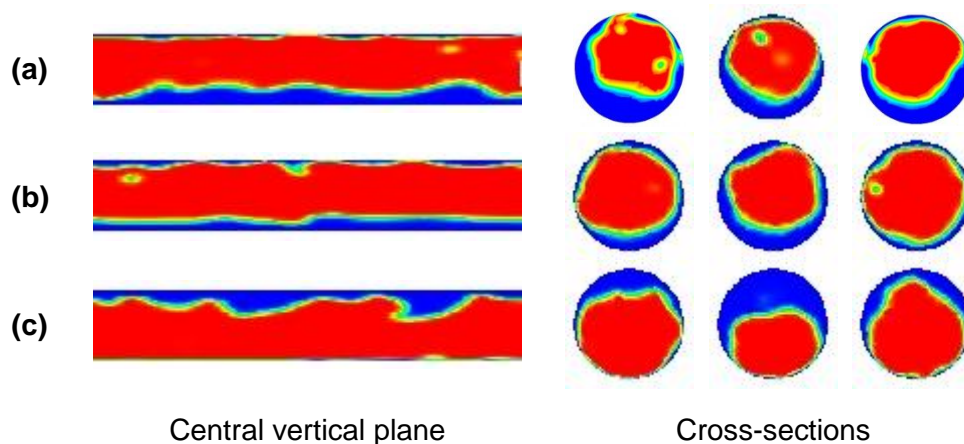


Figure 7-7 Change of phase configuration with change of oil densities. (the red represents oil and the blue represents water). (a) 910kg/m^3 ($Fr=2.67$; Run H-9); (b) 960kg/m^3 ($Fr=4.06$; Run H-10); (c) 1100kg/m^3 ($Fr=2.48$; Run H-11).

7.2.3 Formation of water-lubricated flow

An empirical criterion for the formation of stable water-lubricated flow is proposed in Chapter 5 (refer to Section 5.3). As the CFD model is validated to be able to predict reasonable flow regimes for high-viscosity oil-water flow, a numerical experimental study was conducted to assess the criterion. A comparison of predicted flow regimes with the proposed criterion for the formation of stable water-lubricated flow is shown in Figure 7-8. According to the criterion, stable water-lubricated high-viscosity oil-water flow develops above the inversion line; below the inversion line, a buffer inversion zone exists close to the inversion line and oil-continuous flow develops below the buffer inversion zone. Simulation runs are marked in the map together with the predicted flow regimes; only the simulation runs with flow conditions different from the experimental flow conditions are labelled. It is shown the criterion empirically obtained from the experimental study predicts well for the new flow conditions. The new flow conditions include low water flow rates (Run H-8), high oil flow rates (Run H-18 and H-19), different oil densities (Run H-10 and H-11),

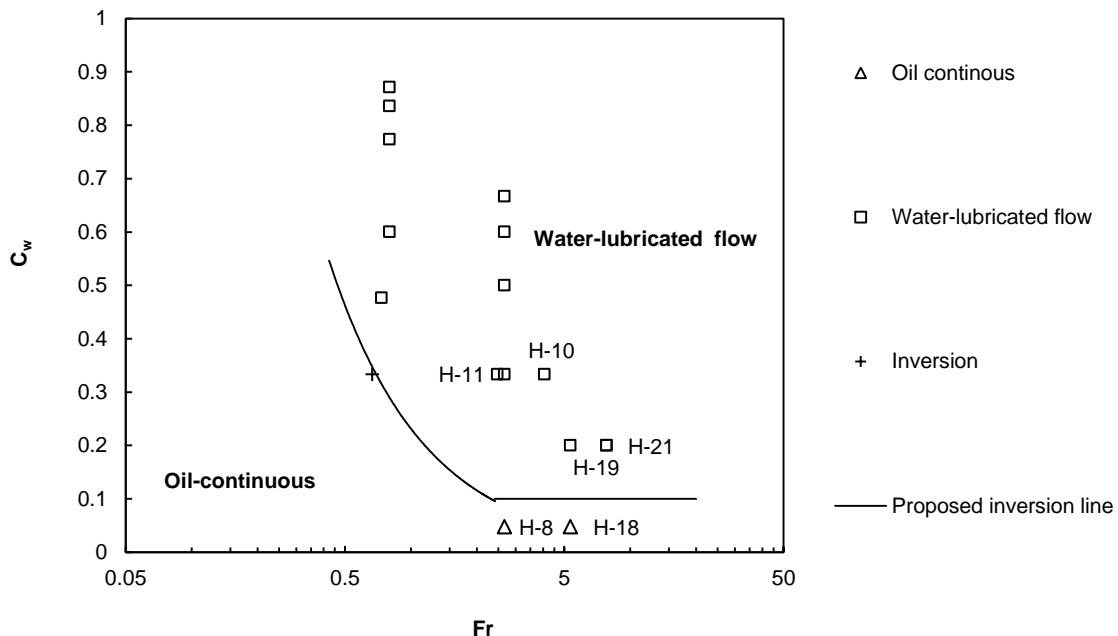


Figure 7-8 Comparison of predicted flow regimes with the proposed inversion criterion for the formation of stable water-lubricated flow.

and a larger pipe diameter (Run H-21). It is noted that a few simulation runs, namely Run H-12, H-13, H-14 and H-20, are not included in the map as the corresponding gravitation to viscous force ratios are higher than 0.15 indicating viscous force and gradational force comparable flow, while the transition criterion is limited for viscous dominant flow.

7.3 Water holdup of water-lubricated flow

A comparison of predicted water holdups (H_w) from simulations of low-viscosity equal-density oil-water flow with experimental counterparts from Charles et al. (1961) is shown in Figure 7-9. Dispersed flow cases are not included given the deficiency of qualitative predictions (see Section 7.2.1). The quantitative agreement between predictions and experiments appears to be good.

Figure 7-10 shows the measured and predicted water holdups (H_w) with change of input water volume fraction (C_w). The predicted H_w from CFD simulation is higher than C_w , which is consistent with experimental measurements. As discussed in the proceeding chapters, H_w is higher than C_w when the oil phase is virtually concentric. For the simulations with the experimental conditions of Charles et al. (1961), the oil phase is virtually concentric inside the continuous water as the oil phase density is equal to the water phase density.

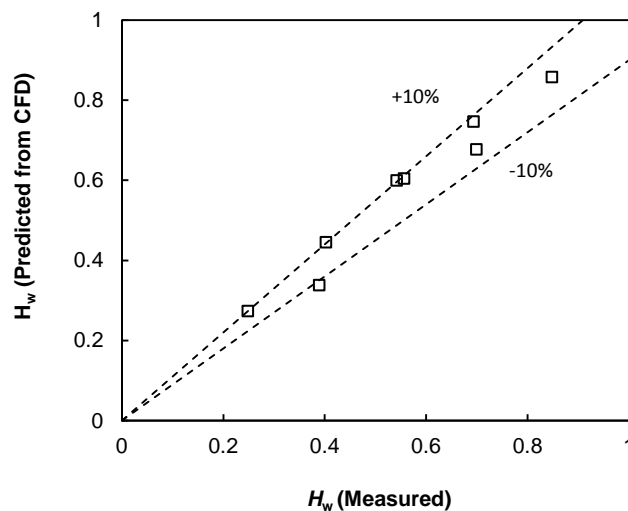


Figure 7-9 Comparison of predicted water holdups with experimental counterparts from Charles et al. (1961).

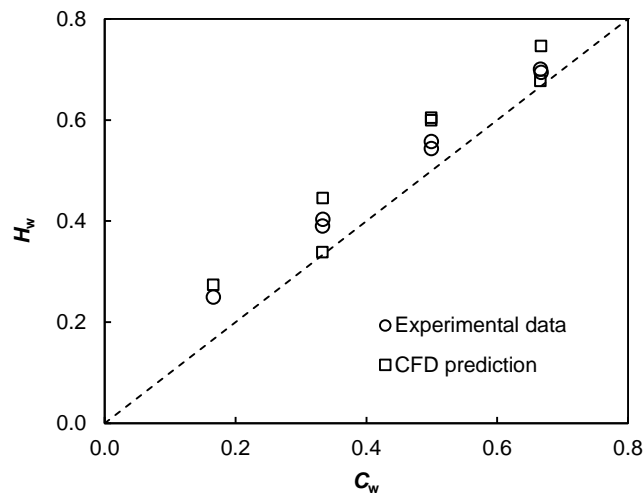


Figure 7-10 Water holdup versus input water volume fraction from measurements (Charles et al, 1961) and CFD model.

Table 7-3 lists measured and predicted water holdups for water-lubricated high-viscosity oil-water flow cases. For simulation cases having the corresponding experimental measurements, the discrepancy in water holdups between CFD simulations and experiments is around 13%. From experimental measurements and observations, it is found that that H_w is lower than C_w at low oil flow rates when the oil phase is more eccentric; H_w gets close to C_w at medium oil flow rates, and becomes higher than C_w when the oil phase is virtually concentric. It can be observed in Table 7-3 that for the lower U_{s0} around 0.1 m/s, the calculated H_w from CFD simulations is lower than C_w . For higher U_{s0} of 0.8 m/s and 2.0 m/s, the predicted water holdups are higher than the input water volume fractions. The qualitative relationship among H_w , C_w and U_{s0} in general agrees well with measurements.

Table 7-3 Measured and predicted water holdups for water-lubricated high-viscosity oil-water flow.

Simulation run	U_{sw} (m/s)	U_{so} (m/s)	C_w	H_w (Measured)	H_w (CFD)	H_w (Correlation ^{a)})	Relative error (CFD)
H-3	0.10	0.11	0.476	0.393	0.359	0.418	-9%
H-4	0.18	0.12	0.600	0.502	0.433	0.545	-14%
H-5	0.41	0.12	0.774	0.670	0.757	0.716	13%
H-6	0.61	0.12	0.836	0.766	0.812	0.781	6%
H-7	0.81	0.12	0.871	0.772	0.864	0.820	12%
H-9	0.20	0.40	0.333	0.339	0.331	0.370	-2%
H-15	0.40	0.40	0.500	0.511	0.47	0.539	-8%
H-16	0.60	0.40	0.600	0.594	0.582	0.636	-2%
H-17	0.80	0.40	0.667	0.625	0.61	0.698	-2%
H-19	0.20	0.80	0.200	-	0.241	0.239	-
H-21	0.50	2.00	0.200	-	0.266	0.245	-

^{a)} The modified correlation of Arney et al. (1903) proposed in the present study (see Equations (5-41) to (5-43) in Chapter 5).

7.4 Pressure gradient of water-lubricated flow

A comparison of predicted pressure gradients from simulations of low-viscosity equal-density oil-water flow with experimental data from Charles et al. (1961) is shown in Table 7-4. Dispersed flow cases are not included due to the deficiency of qualitative predictions (see Section 7.2.1). It is shown that the quantitative prediction from the CFD model is reasonable; the relative error varies within a margin of 30% for the cases performed.

Table 7-4 Comparison of predicted pressure gradients with experimental counterparts from Charles et al. (1961).

Simulation run	U_{sw} (m/s)	U_{so} (m/s)	Flow pattern ^{a)} (CFD)	Dp/dz (Measured) (Pa/m)	Dp/dz (CFD) (Pa/m)	Relative error
L-1	0.03	0.015	OBL	10.2	9.95	-2.5%
L-2	0.03	0.06	OPL	15.3	18.8	22.9%
L-3	0.03	0.15	CAF	34 ~41	26.3	-29.9% ^{b)}
L-4	0.244	0.048	OBL	37.4	46.3	23.9%
L-5	0.244	0.244	OPL	86.6	110.5	27.6%
L-6	0.244	0.487	CAF	244.5	198.1	-19.0%
L-8	0.55	0.274	OPL	295.5	286.5	-3.0%
L-9	0.55	0.55	CAF	482.2	427.0	-11.4%

^{a)} OBL for oil bubbles in water, OPL for oil plugs in water, CAF for core annular flow.

^{b)} The average experimental pressure gradient, 37.5 Pa/m, is used for the calculation of the relative error.

Table 7-5 lists predicted pressure gradients from simulations of high-viscosity oil-water flow and experimental data from the present study. As presented in Section 3.5.4 in Chapter 3, the repeatability of the pressure gradient measurement is reasonable. For the simulations, a good repeatability can be achieved as long as the simulation setup is the same. Influences of major simulation setup parameters have been presented in Section 6.6 in Chapter 6. In Table 7-5, though the CFD model gives good predictions for some cases, the highest relative error is as high as 70%. The higher error for high-viscosity oil-water flow cases than the low-viscosity equal-density flow cases is thought to be associated with underestimate or overestimate of oil fouling on the pipe wall. For the run H-6 and H-7 of which the pressure gradient is under predicted, little oil contact with the pipe wall can be observed in the calculated phase configurations, while thin oil fouling film can still be observed in experiments. For the run H-3 of which the pressure gradient is over predicted, the oil contact with the pipe wall is over predicted comparing to the experiment situation. As has been discussed in the proceeding sections (see Section 6.6.5 in Chapter 6 and 7.2.1 in this chapter), the capture of the oil fouling on the pipe is affected by

Table 7-5 Comparison of predicted pressure gradients with experimental counterparts from the present study.

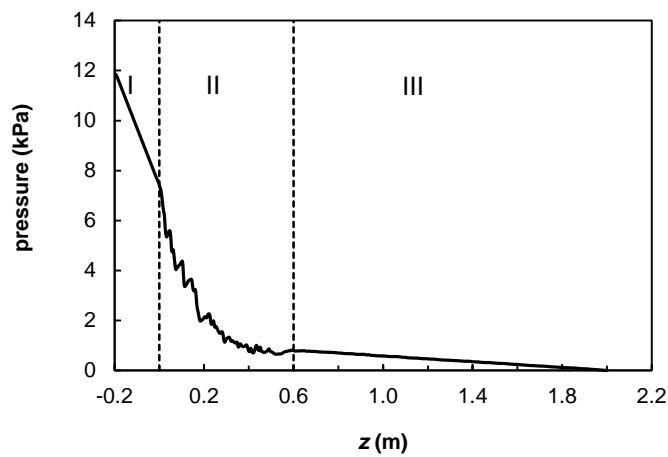
Simulation run	U_{sw} (m/s)	U_{so} (m/s)	Flow pattern ^{a)} (CFD)	Dp/dz (Measured) (kPa/m)	Dp/dz (CFD) (kPa/m)	Relative error
H-1	0.23	0.06	OPL	0.964	0.845	-12%
H-2	0.05	0.10	Inversion	1.25	1.17	-6%
H-3	0.10	0.11	CAF	1.24	2.06	66%
H-4	0.18	0.12	CAF	1.31	2.15	64%
H-5	0.41	0.12	CAF	1.75	1.08	-38%
H-6	0.61	0.12	OLP	1.97	0.61	-69%
H-7	0.81	0.12	OLP	2.33	0.86	-63%
H-8	0.02	0.40	OC	-	62.73	-
H-9	0.20	0.40	CAF	3.11	3.26	5%
H-15	0.40	0.40	CAF	2.68	2.54	-5%
H-16	0.60	0.40	CAF	2.6	2.67	3%
H-17	0.80	0.40	CAF-OLP	2.94	4.6	56%
H-18	0.04	0.80	OC	-	130.36	-
H-19	0.20	0.80	CAF	-	12.06	-
H-20	0.20	0.40	ST	-	5.58	-
H-21	0.50	2.00	CAF	-	8.2	-

^{a)} OPL for oil plugs in water, CAF for core annular flow, OLP for dispersed oil lumps in water, OC for oil-continuous flow, CAF-OPL for transitional flow between CAF and OLP, and ST for stratified flow.

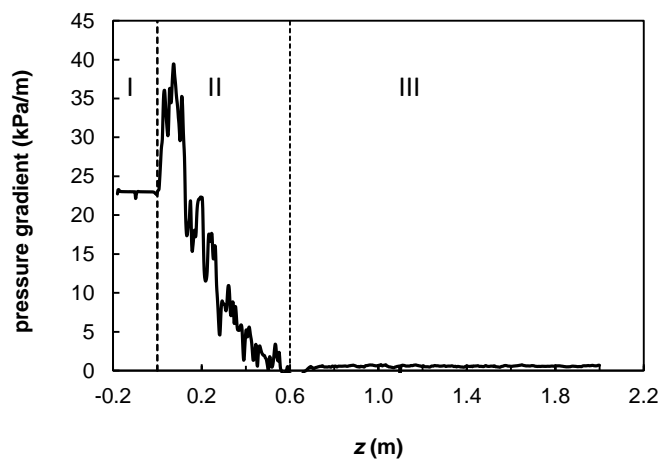
the wall contact angle modelling as well as the mesh resolution. Efforts to improve the modelling of the wall contact angle are worthwhile in future studies.

Though the calculated pressure gradient from the CFD model is not very accurate due to deficiency in the oil fouling capture, the water lubrication effect of water-lubricated high-viscosity oil-water flow in reducing the pressure gradient of single oil flow is demonstrated. Figure 7-11 (a) shows pressure along the horizontal pipe for the simulation case H-7. The slope of the line reflects the pressure gradient, which is displayed in Figure 7-11 (b). Zone I represents the horizontal pipe section before the intersection; single oil flows in

that section before $z=0$ where it meets water. The pressure gradient is constant along the pipe in zone I. Zone II represents the flow developing region after oil meets water at the intersection. The pressure gradient first has a sudden increase at the intersection as transient change occurs here, and then decreases gradually along the pipe until to a lower value in zone III. In zone III, the oil-water flow is developed; the pressure gradient varies around a constant value along the pipe. Comparing the pressure gradient of zone I and zone III, it shows that with addition of water, the pressure gradient is significantly reduced.

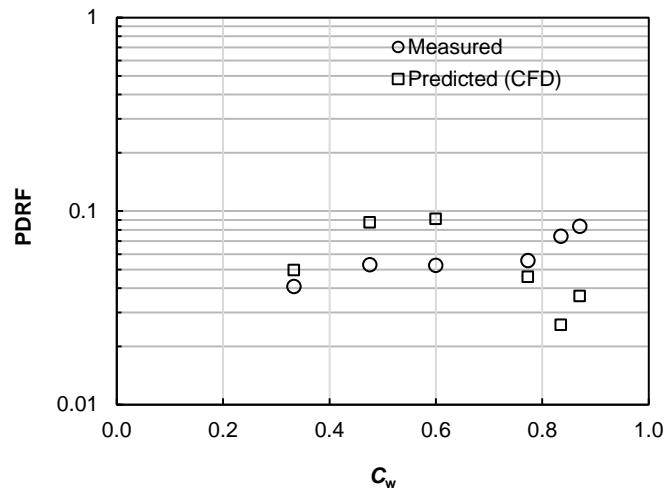


(a)

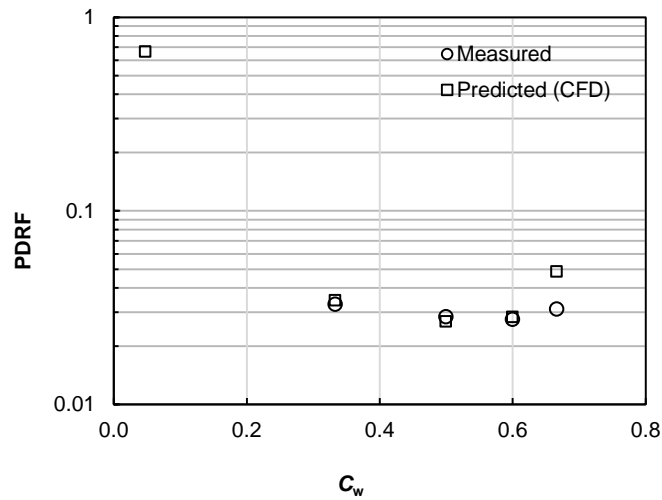


(b)

Figure 7-11 Pressure (a) and pressure gradient (b) along the horizontal pipe.



(a)



(b)

Figure 7-12 Pressure drop reduction factor (PDRF) from simulations and measurements versus input water volume fraction (C_w) at different superficial oil velocities. (a) $U_{so}=0.1$ m/s; (b) $U_{so}=0.4$ m/s.

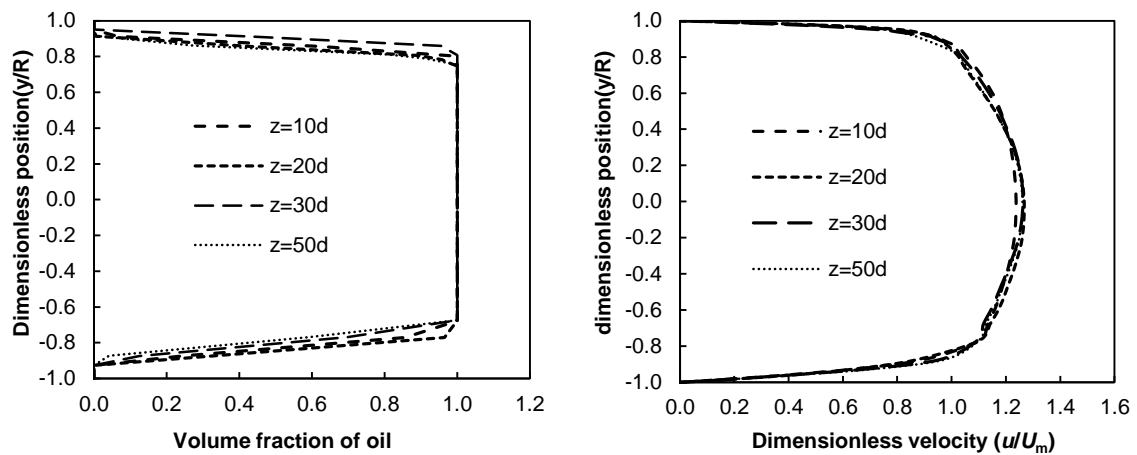
A comparison between PDRF (Pressure Drop Reduction Factor, ratio of the pressure gradient of oil-water flow to single oil flow at the same oil flow rate, see Section 4.6.1 in Chapter 4) obtained from CFD simulations and measurements is shown in Figure 7-12. In Figure 7-12 (a), all the cases are water-lubricated oil-water flow. Reasonable agreement is shown between measured and

predicted PDRF. In Figure 7-12 (b), there is one simulation case having a low C_w around 0.05 for which oil-continuous flow is predicted. The PDRF from CFD simulation for the oil-continuous flow is close to 1, indicating minor effect of water lubrication. A good agreement between measured and predicted PDRF for water-lubricated high-viscosity oil-water flow is shown in Figure 7-12 (b).

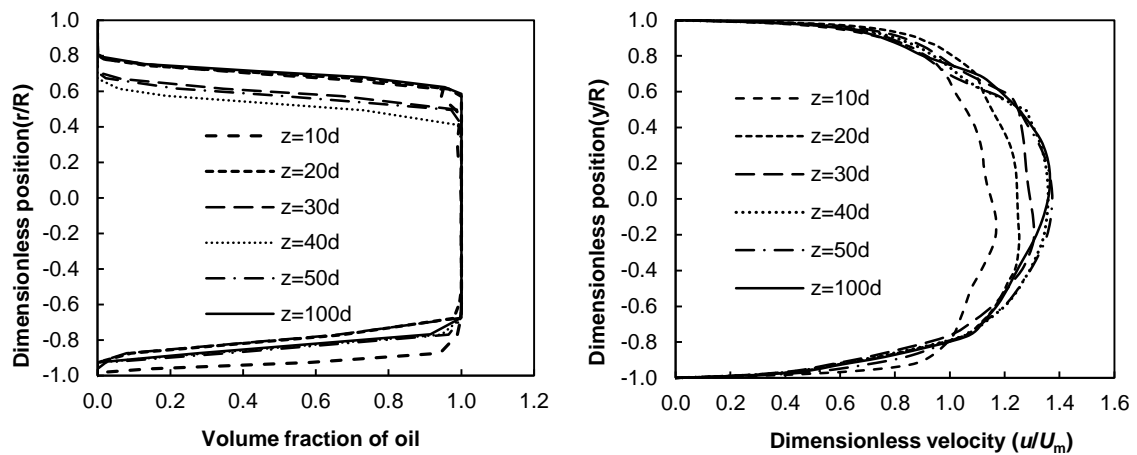
7.5 Cross-sectional flow characteristics of CAF

Phase distributions and dimensionless velocity profiles at different positions downstream the junction for low-viscosity equal-density core annular flow (CAF) are drawn in Figure 7-13. The laminar case in Figure 7-13 (a) shows a nearly perfect CAF with established velocity profile at a distance of $20d$ downstream the mixing point. For turbulent cases shown in Figure 7-13 (b) and (c), the volume fraction of the oil phase varies along the flow direction, reflecting the fluctuation of the phase interface along the flow direction. Different from single phase flow, the dimensionless velocity profile along the pipe varies even the flow gets developed due to the fluctuation of the phase interface. The two-phase flow is regarded as fully developed where the u_{max}/U_m becomes constant.

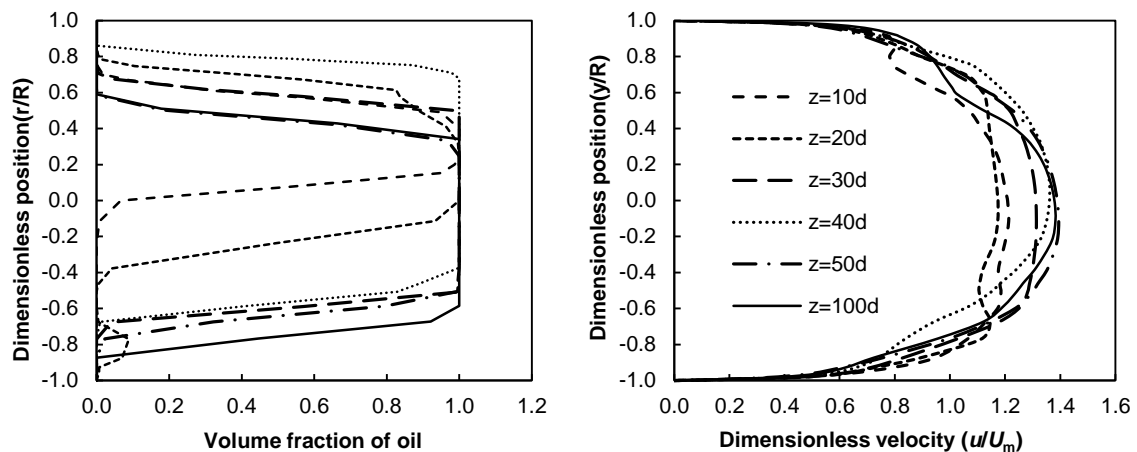
The velocity profile of developed CAF is of our interest. The velocity profile of developed flow in Figure 7-13 is different from that of the single phase flow. For the laminar CAF case shown in Figure 7-13 (a), the velocity profile is radically different from the parabolic velocity distribution of single phase flow. The velocity gradient of the water ring near the pipe wall becomes greater while the velocity distribution of the oil core in the middle of the tube is much flatter. For single phase laminar flow $u_{max}/U_m = 2$ while it is shown that $u_{max}/U_m = 1.26$ for the laminar core annular flow case under consideration. For turbulent cases shown in Figure 7-13 (b) and (c), the velocity distribution of annular flow is similar to that of turbulent single phase flow in general. There is no obvious sharp change in the velocity gradient at the interface. For single phase turbulent flow, u_{max}/U_m asymptotically reaches the value 1.22 to 1.25 with increasing Reynolds number (Prandtl and Tietjens, 1934); the simulation shows u_{max}/U_m varies from 1.36 to 1.38 for superficial water phase Reynolds number (Re_{sw}) from 6 331 to 14 271.



(a) Run L-3, $Re_{sw}=778$



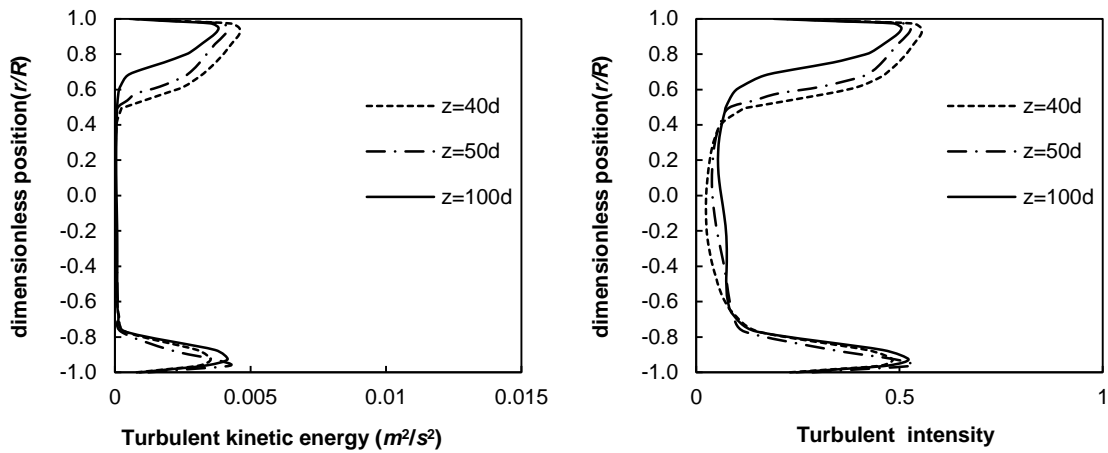
(b) Run L-6, $Re_{sw}=6331$



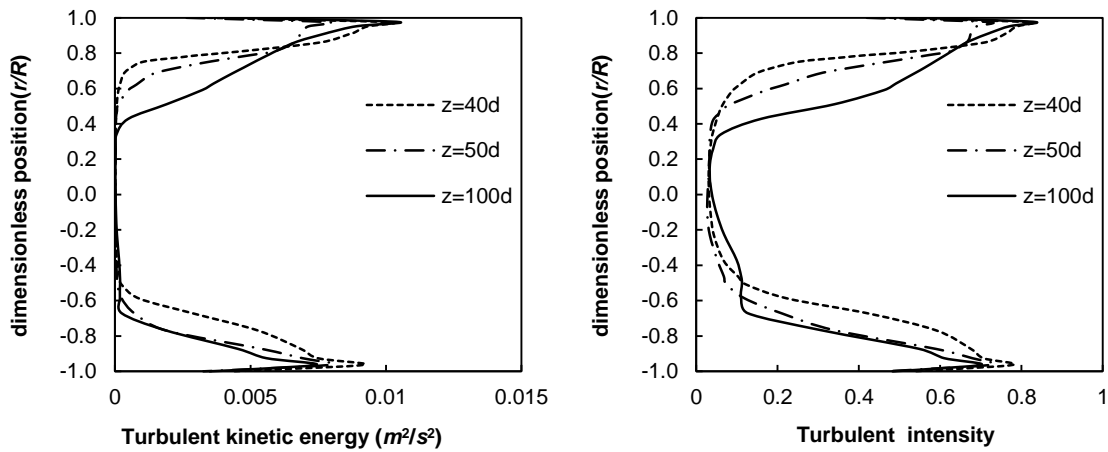
(c) Run L-9, $Re_{sw}=14271$

Figure 7-13 Dimensionless phase distribution and velocity profiles of low-viscosity equal-density CAF at different distances downstream the junction; left hand side for phase distribution and right hand side for velocity distribution.

Figure 7-14 shows turbulent kinetic energy and turbulent intensity along the vertical line on the symmetry plane of various cross-sections of developed CAF for the low-viscosity oil, equal-density cases. Turbulent kinetic energy, k , is the mean kinetic energy per unit mass associated with eddies in turbulent flow, $k = \frac{1}{2}(\overline{u'^2} + \overline{v'^2} + \overline{w'^2})$. The turbulent intensity, I , is defined as the ratio of the root-mean-square of the velocity fluctuations to the mean flow velocity, $I = \frac{\sqrt{\frac{1}{3}(\overline{u'^2} + \overline{v'^2} + \overline{w'^2})}}{U_{avg}} = \frac{(\frac{2}{3}k)^{1/2}}{U_{avg}}$. The turbulent kinetic energy indicates the turbulence strength and the turbulent intensity indicates the relative turbulence strength. The distributions of turbulent kinetic energy and intensity are reasonable in Figure 7-14. It is indicated that the turbulence strength is low in the central part of pipe where the oil core flows. The oil viscosity for these cases is 16.8 cP; with this viscosity, the oil alone would flow in the pipe as laminar flow. Also, turbulence strength is low at the pipe wall and the interface of oil and water (refer to Figure 7-13 (b) and (c) for the position of phase interface) due to turbulence damping effect from the pipe wall and the oil phase. The highest turbulent kinetic energy and intensity locate in annular water layer close to the pipe wall. Comparing Figure 7-14 (a) and (b), it shows that the turbulence strength in the annular water layer is increased with increase of the water flow rate.



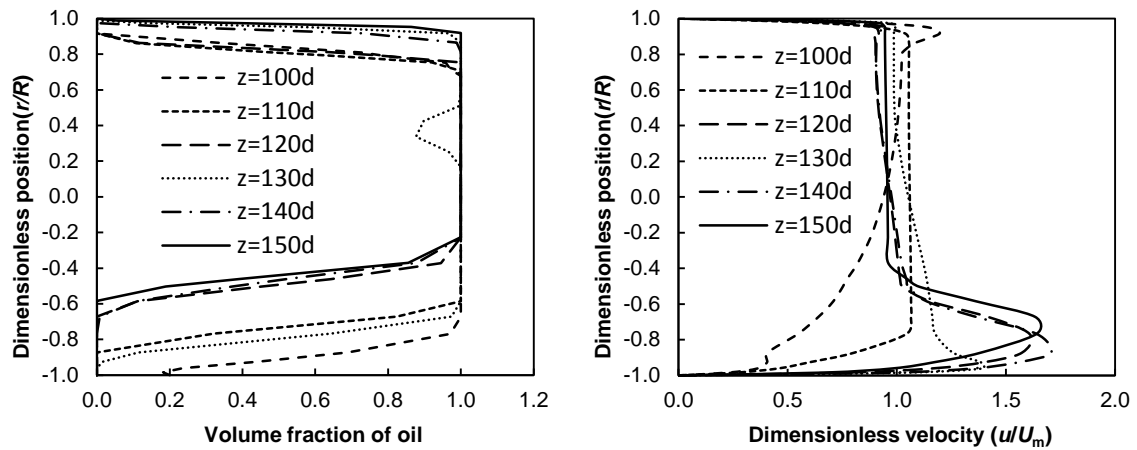
(a) Run L-6, $Re_{sw}=6\ 331$



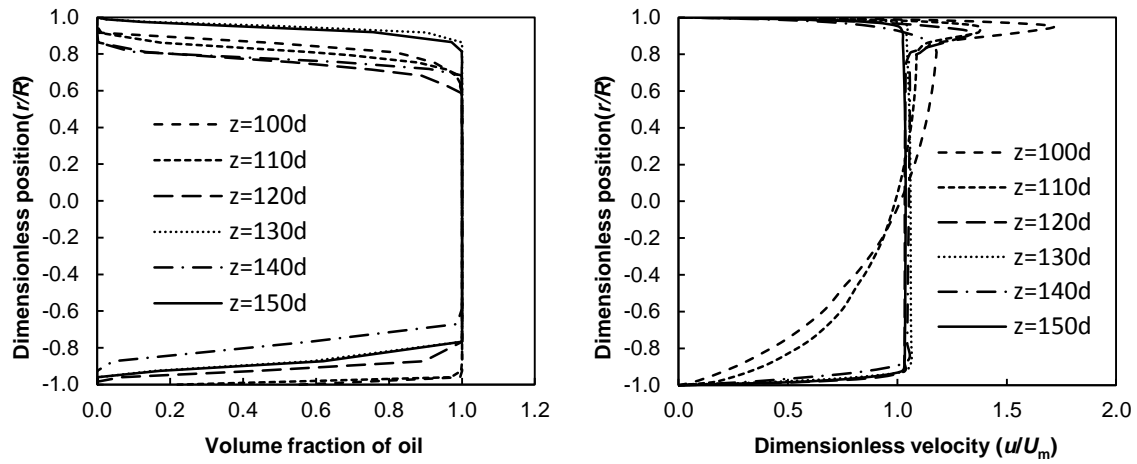
(b) Run L-9, $Re_{sw}=14\ 271$

Figure 7-14 Turbulent kinetic energy and intensity of developed low-viscosity equal-density CAF.

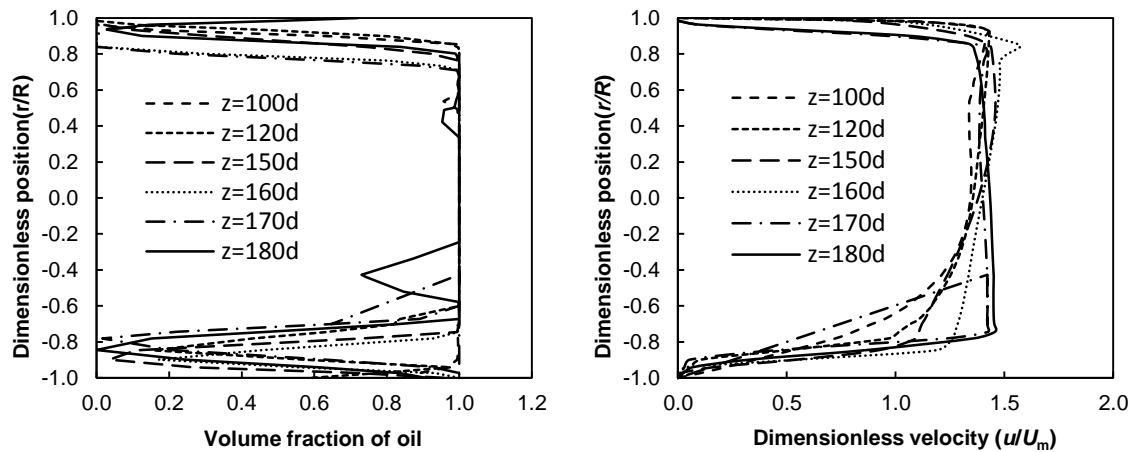
Phase distributions and dimensionless velocity profiles at different positions downstream the junction for high-viscosity oil CAF are shown in Figure 7-15. Three typical cases, eccentric CAF (Run H-9), virtually concentric CAF due to higher oil density (Run H-10), and virtually concentric CAF due to higher oil inertia (Run H-21), are depicted in Figure 7-15 (a), (b) and (c).



(a) Run H-9, I.D. =26 mm, $Re_{sw}=5\ 190$, $\rho_o=910\text{ kg/m}^3$



(b) Run H-10, I.D. =26 mm, $Re_{sw}=5\ 190$, $\rho_o=960\text{ kg/m}^3$



(c) Run H-21, I.D. =76 mm, $Re_{sw}=37\ 924$, $\rho_o=910\text{ kg/m}^3$

Figure 7-15 Dimensionless phase distribution and velocity profiles of high-viscosity oil CAF at different distances downstream the junction; left hand side for phase distribution and right hand side for velocity distribution.

Comparing to Figure 7-13, a pronounced difference in the velocity profiles is that the velocity of the oil core is nearly flat for high-viscosity oil CAF. The oil viscosity for these cases is 5 000 cP, which is around 5 000 times of the water viscosity. It appears that when the oil viscosity is much higher than the water viscosity, the oil core flows inside the water as a rigid body. The above assumption has been used as an assumption in some analytical studies (see Ooms et al,1984; Ooms et al., 2012). This assumption is validated by the CFD simulation results. It is worth emphasizing that the assumption of the rigid oil core in CAF is valid only when the oil viscosity is significantly higher than the annular water viscosity, e.g., three orders higher of the water viscosity as cases shown in Figure 7-15. The oil core cannot be treated as a rigid body when the oil viscosity is just one order higher than the water viscosity (see Figure 7-13).

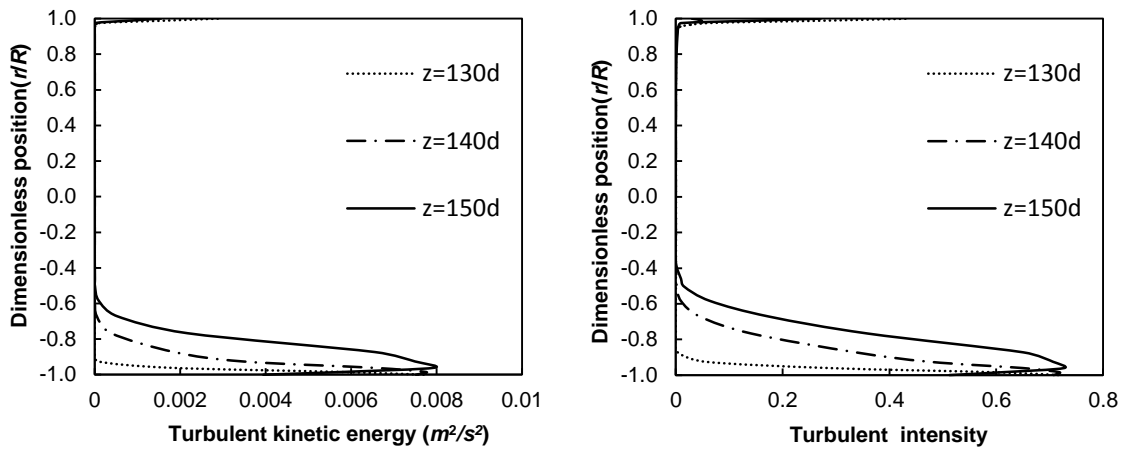
Comparing Figure 7-15 (a) to Figure 7-15 (b) and (c), it is shown the velocity distribution of eccentric CAF is different to that of concentric CAF. For developed concentric CAF as shown in Figure 7-15 (b) and (c), the velocity profile is almost symmetric. The oil core flows as a solid body with a velocity higher than the average velocity of the annular water layer. In the annular water layer, the velocity decreases quickly towards the pipe wall. For the developed eccentric CAF as shown in Figure 7-15 (a), the top water layer is very thin and the bottom water layer has a relatively higher height. The velocity distribution for eccentric CAF is far off symmetric. Above the oil core, the velocity decreases quickly towards the pipe wall in the thin top water layer. Below the oil core, the velocity first increases then decreases towards the pipe wall. The oil-water slip ratios (i.e., the phase average velocity ratios, U_o/U_w) are higher than 1 for the concentric CAF shown in Figure 7-15 (b) and (c), while is slightly lower than 1 for the eccentric CAF shown in Figure 7-15 (a). This agrees with the experimental finding presented in Section 4.5 in Chapter 4.

It is noted that the average oil core velocity of developed CAF in Figure 7-15 (a) and (b) is close to the mixture velocity, while it is as high as around 1.4 times of the mixture velocity in Figure 7-15 (c). This might be related to the absolute height of the water layer, hence the degree of the water lubrication effect. The

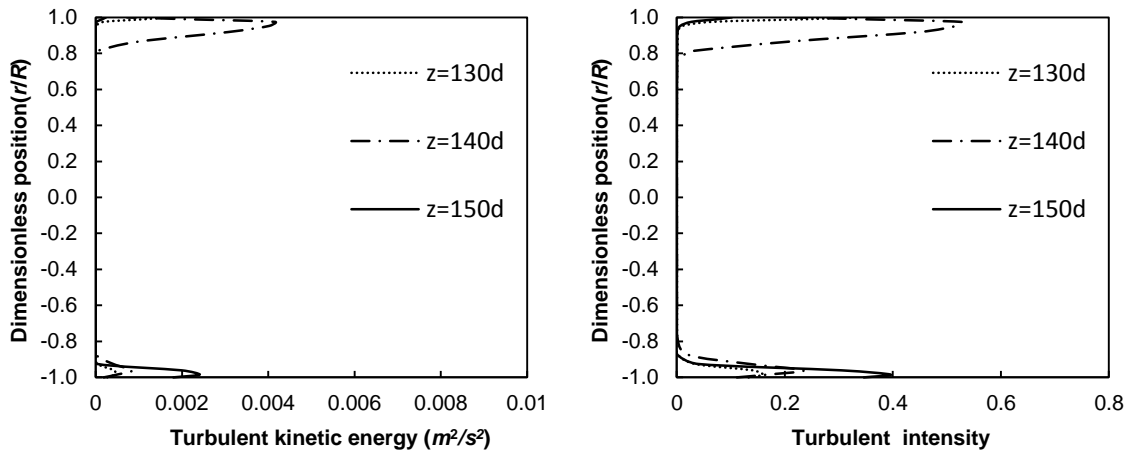
cases in Figure 7-15 (a) and (b) are CAF in a 26 mm I.D. pipe, while the case in Figure 7-15 (c) is CAF in a 76 mm I.D. pipe. Though the relative water layer heights for the two concentric CAF illustrated in Figure 7-15 (b) and (c) are similar (around 10%-20% of the pipe diameter), the absolute height of the water layer is higher for the case shown in Figure 7-15 (c).

It is also noted that the oil volume fraction distribution of the developed CAF in Figure 7-15 (c) is slightly different from those shown in Figure 7-15 (a) and (b), reflecting the captured oil fouling film on the pipe wall. As has been discussed in Section 7.2.1, oil fouling film is more clearly captured in the simulation case H-21 of which the pipe diameter is 76 mm.

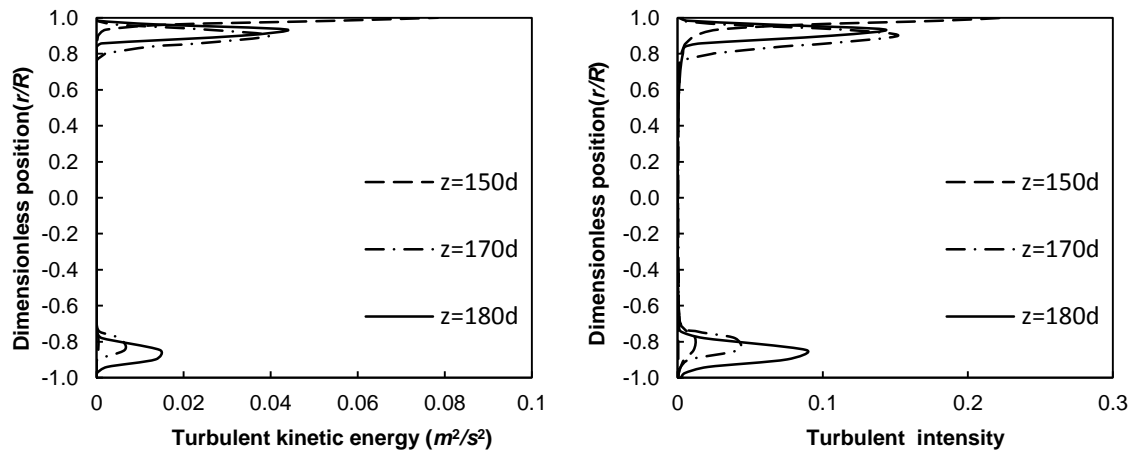
Figure 7-16 shows turbulent kinetic energy and turbulent intensity of developed high-viscosity oil CAF along the vertical line on the symmetry plane of various cross-sections. The distributions of the turbulent kinetic energy and turbulent intensity match the phase distribution having higher values in the annular water layer, and very low values in the high-viscosity oil core. For the eccentric CAF case in which the oil flows in the upper part of the pipe, the turbulent intensity in the bottom water layer is higher than that in the upper thinner water layer (see Figure 7-16 (a)). Comparing Figure 7-16 to Figure 7-14, it is noted that the turbulent kinetic energy in the oil core of high-viscosity oil CAF is much lower than that of low-viscosity oil CAF; the turbulent kinetic energy of the oil core is between 10^{-8} and $10^{-10} \text{ m}^2/\text{s}^2$ in Figure 7-16, while of the order of $10^{-5} \text{ m}^2/\text{s}^2$ in Figure 7-14. This is reasonable as the higher the oil viscosity is, the less turbulent the flow will be.



(a) Run H-9, I.D. =26 mm, $Re_{sw}=5\ 190$, $\rho_o=910\ \text{kg/m}^3$



(b) Run H-10, I.D. =26 mm, $Re_{sw}=5\ 190$, $\rho_o=960\ \text{kg/m}^3$



(c) Run H-21, I.D. =76 mm, $Re_{sw}=37\ 924$, $\rho_o=910\ \text{kg/m}^3$

Figure 7-16 Turbulent kinetic energy and intensity of developed high-viscosity oil CAF.

7.6 Summary

CFD simulation results are discussed in aspects of flow patterns, water holdups, pressure gradients and cross-sectional flow characteristics.

Comparison with experimental results (two data sources, namely Charles et al. (1961) and the present study) was conducted to validate the CFD model. It shows that VOF multiphase model in conjunction with the SST $k-\omega$ scheme with turbulence damping activated for turbulent flow is viable to predict the phase configurations of liquid-liquid pipeline flow with interface length scale comparable to the pipe diameter, such as core annular flow, oil plugs/bubbles in water. For low-viscosity equal-density oil-water flow, a good agreement is demonstrated between predicted and experimental flow patterns. For high-viscosity oil-water flow, apart from the oil fouling film on the pipe wall, the phase configurations calculated from the CFD model agree well with the experimental flow patterns and the anticipated flow patterns from mechanism analysis and the criterion of the inversion occurrence. The oil fouling film on the pipe wall is not well captured for the majority of the simulation cases. This is thought mainly due to the inherent deficient physical representation of the wall adhesion effect in the continuum surface force model incorporated in Fluent.

The quantitative predictions in the water holdup and pressure gradient are reasonable. Particularly, the qualitative trend between water holdup and input water volume fraction for water-lubricated oil-water flow having different degree of eccentricity is reflected in the CFD simulation results. The pressure gradient from the CFD model shows higher relative errors for cases of high-viscosity oil-water flow; this is linked to the capture of the oil fouling film on the pipe wall. The water-lubricated high-viscosity oil-water flow in reducing the pressure gradient of single oil flow is reflected.

Pronounced difference between the velocity profiles of developed CAF for low-viscosity oil equal-density cases and high-viscosity oil cases is shown. For turbulent annular water cases, the velocity distribution of CAF for low-viscosity oil equal-density cases is similar to that of turbulent single phase flow in general;

the velocity distribution of CAF for high-viscosity oil cases is characterised with nearly constant velocity across the oil core. It is demonstrated that the oil core flows inside the water as a solid body when the oil viscosity is significantly higher than the water viscosity. The turbulent intensity distribution matches the phase distribution, having high turbulent intensity in the annular water layer, and low turbulent intensity in the oil core.

8 CONCLUSIONS AND RECOMMENDATIONS

8.1 Conclusions

The major objective of the present study is to investigate horizontal high-viscosity oil-water flow to have an improved understanding of the flow behaviours. To that end, the experimental investigation, mechanism analysis and empirical modelling, and CFD simulation were carried out. Conclusions drawn from investigations in the above three aspects are summarised separately as follows.

(1) Experiments

Experiments on high-viscosity oil-water flow in a horizontal 1 inch pipe were conducted. Apart from the flow patterns and pressure drop of the two phase flow, the water holdup was measured using a sampling method. The experimental data on horizontal high-viscosity oil-water flow, especially the water holdup data which is very limited in literature, contributes to the database of two phase liquid-liquid flow. The experimental data from the present study and collated data from previous experimental studies in the same group constitute a large data base. Analysis on the experimental results and related literature data was conducted. Information and knowledge obtained from the experimental results is:

- The major flow patterns observed in high-viscosity oil-water flow through a 1 inch horizontal pipe are oil-continuous flow, inversion, core annular flow (CAF), oil plugs, and dispersed oil lumps. The CAF is the dominant flow regime covering a wide range of oil and water flow rates.
- The inversion from oil-continuous to water-lubricated flow is not completed abruptly but within a certain range of input water volume fraction. The inversion region can be distinguished with a sharp drop in the pressure gradient soon after the initiation of the inversion. The inversion occurs at a lower input water volume fraction with increase of the superficial oil velocity. The oil viscosity shows minor effect on the

occurrence of inversion for the viscosities investigated (3 300 to 16 000 cP).

- The water holdup (H_w) of water-lubricated flow is not only related to the input water volume fraction (C_w), but also with the oil flow rate which is closely related to the oil phase concentricity and fouling on the wall. Generally speaking, H_w is lower than C_w at low oil flow rates when the oil phase is far off concentric. H_w gets close to C_w at medium oil flow rates, and becomes higher than C_w at high oil flow rates when the oil phase is virtually concentric. Correspondingly, the oil-water slip ratio of core annular flow is higher than 1 for virtually concentric CAF, and lower than 1 when the oil core is far off concentric.
- For the present experimental study, the pressure gradient of water-lubricated flow was reduced to between 2% and 20% of the pressure gradient of single oil flow. This shows the great energy-saving benefit of water-lubricated heavy oil transport. The pressure gradient of water-lubricated heavy oil flow can be one to two orders of magnitude higher than that of single water flow. This increased frictional loss is closely associated with oil fouling on the pipe wall.

(2) Mechanism analysis and empirical modelling

A survey on flow regimes of liquid-liquid flows in horizontal pipes was conducted with a question in mind that under what conditions the liquid-liquid flows exhibit same basic flow regimes or under what conditions the flow regime maps of different liquid-liquid flows are comparable. The ratio of the gravitational force to viscous force was proposed and validated to characterise liquid-liquid flows featured with different basic flow regimes.

An empirical criterion for the completion of the inversion from oil-continuous to water-continuous (or formation of stable CAF) was proposed based on the present experimental study and previous work of McKibben et al. (2000a). Evaluation of the existing models of water-lubricated high-viscosity oil-water flow was conducted. Attempts were also made to develop empirical correlations

to predict water holdups and pressure gradients of water-lubricated flow. The proposed correlations incorporate dimensionless parameters which can reflect physics to some extent. These empirical correlations should be re-evaluated as more data become available.

Information and knowledge obtained from the mechanism analysis and empirical modelling of liquid-liquid flow is:

- The ratio of gravitational force to viscous force ($G/V = \frac{\Delta\rho g D^2}{\mu U}$), shows feasibility to characterise liquid-liquid flows featured with different basic flow structures. Liquid-liquid flows with basic flow patterns of ST and D are gravitational force dominant flow (S_G) and characterised with high G/V . Liquid-liquid flows with basic flow patterns of I and CAF are viscous force dominant (S_V) and characterised with low G/V . Liquid-liquid flows with basic flow patterns of ST, D, I and CAF are gravitational force and viscous force comparable (S_{GV}) and characterised with medium G/V . Similar to laminar-to-turbulent transition in single phase flow, the transitions of two-phase liquid-liquid flows can be roughly described with the gravitation to viscous force ratio. The transition from S_V to S_{GV} is around a gravitation to viscous force ratio of 1; the transition from S_{GV} to S_G is around a gravitation to viscous force ratio of 40. Core annular flow is the dominant flow regime in viscous force dominant liquid-liquid flow of which G/V is lower than 1. Figure 5-9 in Section 5.2.2 Chapter 5 demonstrates the above statement and is reproduced as follows.

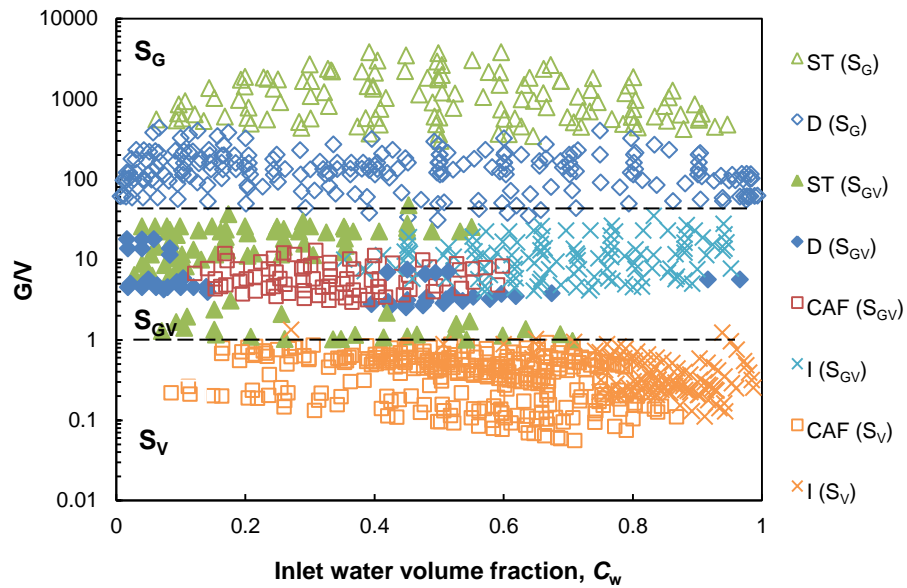


Figure 5-9 Basic flow patterns formed with gravitation to viscous force ratio (G/V) and C_w in two-phase oil-water flow, S_G , S_V , and S_{GV} .

- For viscous force dominant flow ($G/V = \frac{\Delta\rho g D^2}{\mu U} < 1$), the input water volume fraction required to form stable core annular flow decreases with increase in Froude number (Fr) until to a critical Froude number above which the inversion occurs as long as the water content is above a minimum of around 10%. The empirical criterion proposed (Equations (5-8) to (5-10) in Section 5.3 Chapter 5; they are reproduced as follows) can give a guide for determination of the inversion when Fr is between 0.4 and 30; caution should be taken if Fr is out of the range investigated in the present study. Figure 5-9 and Equations (5-8) to (5-10) together provide a guide for industrial operations of core annular flow.

$$Fr > Fr_c,$$

$$C_w \geq 0.1 \quad (5-8)$$

$$0.4 < Fr < Fr_c,$$

$$C_w \geq 0.23Fr^{-1} \quad (5-9)$$

$$Fr = \frac{U_{so}}{\sqrt{gD \frac{(\rho_w - \rho_o)}{\rho_w}}} \quad (5-10)$$

where the Fr_c is around 2.5.

- For the prediction of water holdup, the correlations/models of Arney et al. (1993) and Brauner (1998) can give reasonable predictions when the oil phase is virtually concentric. However, as the degree of eccentricity of the oil phase becomes higher, the correlations/models of Arney et al. (1993), Brauner (1998) tend to over predict the water holdup. The modified correlation of Arney et al. (1993) proposed in the present study works well for water-lubricated oil-water flow with either concentric or eccentric oil phase; it is validated with both the present experimental data and partial data available from Charles et al. (1961).
- For the prediction of pressure gradient, the correlations/models of Arney et al. (1993) and Brauner (1998) can give reasonable predictions for core annular flow when there is no oil fouling on the pipe wall, but greatly underestimate the pressure gradient of core annular flow when oil fouling exists on the pipe inner wall. The empirical model of McKibben et al. (2000b) is found to be able to give reasonable predictions with relative errors within $\pm 70\%$ for most of the present experimental data. A new empirical model given in McKibben et al. (2013) has relative errors between -40% and $+100\%$ for the majority of flow conditions, while has relative errors as high as $+400\%$ for a few data points. An attempt has been made to develop a model to account for the the influences of oil phase eccentricity and oil fouling on the pipe wall through a dimensionless effective relative wall roughness which was correlated with the Froude number and input water volume fraction. The model proposed was not evaluated with dependent data as there are limited experimental studies on high-viscosity oil-water flow with oil fouling on the pipe wall in the open literature. Furthermore, for the limited studies available, not enough information is given to evaluate the model

proposed. The model should be re-evaluated as more data becomes available. These could lead to modifications to improve them. The accuracy of different models in predicting the pressure gradient of water-lubricated high-viscosity oil-water flow is not high in general due to complex influences of different parameters on the degree of oil fouling on the pipe wall. Care should be taken when applying a model for the prediction of pressure gradient of water-lubricated high-viscosity oil-water flow. For industrial applications, at least, a model which accounts for the oil fouling influence should be selected to avoid significant underestimations.

(3) CFD modelling of liquid-liquid flow

3-D CFD modelling of liquid-liquid flow in horizontal pipes was performed. The majority of simulation runs were conducted following flow conditions of the present experimental study and Charles et al. (1961) for model validation. Some simulation runs having flow conditions not available in experimental data, e.g., change in pipe diameter, oil density, oil viscosity, and flow rates, were performed to compare with findings from mechanism analysis and empirical modelling. Information and knowledge obtained from the 3-D CFD modelling of liquid-liquid flow is:

- The VOF multiphase model in conjunction with the SST $k-\omega$ scheme with turbulence damping activated for turbulent flow is viable to predict the phase configurations of liquid-liquid pipeline flow with interface length scale comparable to the pipe diameter, such as core annular flow, oil plugs/bubbles in water. The VOF approach is not an ideal choice for modelling dispersed drops of one phase in another as the interface length scale tends to become smaller than the computational grid size. The oil fouling film on the pipe wall for water-lubricated high-viscosity oil-water flow is clearly captured only for limited cases. This is related to the inherent deficient physical representation of the wall adhesion effect in the continuum surface force model incorporated in Fluent.

- The phase configurations calculated from the CFD model agree well with the anticipated phase configurations from mechanism analysis and the criterion for the formation of stable water-lubricated flow.
- The qualitative trend between water holdup, input water volume fraction and oil flow rate as found in experiments is reflected in the CFD simulation results.
- The pressure gradient calculated from the CFD model shows relative errors as high as $\pm 70\%$ for cases of high-viscosity oil-water flow; this is linked with inaccurate capture of the oil fouling on the pipe wall. The water lubrication effect of water-lubricated high-viscosity oil-water flow in reducing the pressure gradient of single oil flow is demonstrated.
- For turbulent annular water core annular flow, the velocity distribution of CAF for low-viscosity oil equal-density cases is similar with that of turbulent single phase flow in general. The velocity distribution of CAF for high-viscosity oil cases is characterised with nearly constant velocity across the oil core, indicating that the oil core flows inside the water as a solid body when the oil viscosity is significantly higher than the water viscosity. The turbulent intensity distribution matches the phase distribution having high turbulent intensity in the annular water layer, and low turbulent intensity in the oil core.

8.2 Recommendations

As stated in the conclusions, the accuracy of different models in predicting the pressure gradient of water-lubricated high-viscosity oil-water flow is not high in general due to complex influences of different parameters on the degree of oil fouling on the pipe wall. Further work to improve the accuracy of models could be done by investigating the characteristics of oil fouling film on the pipe wall experimentally and computationally. Specifically, suggestions on the area of high-viscosity oil-water flow include the following:

- Development of measurement techniques for the measurement of the height and velocity of the oil fouling film on the pipe wall. Possible

measurement techniques could be microwave techniques and ultrasound techniques.

- Experimentally investigate the influence of wall wettability on oil fouling.
- CFD simulation of core annular flow with focus on the oil fouling film. Simulations applying dynamic contact angles may provide improved capture of the oil fouling film.
- The empirical correlations should be re-evaluated as more data become available.
- Development of the two-fluid mechanistic model.

The two-fluid model proposed in Brauner (1998) does not consider the oil fouling film separately. One possible approach to improve the model is to treat the oil fouling film as a separate layer with its own transport equations. Consequently, extra closures, e.g., the relation between film velocity and height, are required to obtain solutions.

- When the pipeline is unexpectedly shut down for a period of time, the annular- water-continuous flow regime cannot be maintained. The oil and water would become stratified. Preliminary experiments on the restart of core annular flow have been conducted (see Appendix F). Further experimental and mechanistic investigations on the restart of core annular flow would be useful to facilitate its application.
- Future experimental studies on high-viscosity oil-water flow in vertical pipe, or more complicated pipeline configurations, e.g., inclined pipe through a bend to a vertical pipe, can be considered.

REFERENCES

- Al-Awadi, H. (2011). Multiphase characteristics of high viscosity oil. (PhD thesis), Cranfield University, UK.
- Al-Yaari, M. A., Abu-Sharkh, B. F. (2011). CFD prediction of stratified oil-water flow in a horizontal pipe. *Asian Trans. Eng.*, 1(5), 68-75.
- Alagbe, S. O. (2013). Experimental and numerical investigation of high viscosity oil-based multiphase flows. (PhD thesis), Cranfield University, UK.
- Alboundwarej, H., Felix, J., Taylor, S., Badry, R., Bremner, C., Brough, B., Skeates, C., Baker, A., Palmer, D., Pattison, K., Beshry, M., Krawchuk, P., Brown, G., Calvo, R., Triana, J. A. C., Hathcock, R., Koerner, K., Hughes, T., Kundu, D., West, C., (2006). Highlighting heavy oil. *Oilfield review*, 18(2), 34-53.
- Alikhan, A. A., Ali, S. M. F. (1983). Current status of nonthermal heavy oil recovery. Paper presented at the SPE Rocky Mountain Regional Meeting, Salt Lake City, Utah, 22-25 May, 1983.
- Anderson, J. D., Wendt, J. (1995). *Computational fluid dynamics*. New York: McGraw-Hill.
- Angeli, P., Hewitt, G. (2000). Flow structure in horizontal oil–water flow. *International journal of multiphase flow*, 26(7), 1117-1140.
- ANSYS® Fluent, *Fluent Theory Guide* (2012). USA: ANSYS Inc.
- ANSYS® Fluent, *Fluent user's guide* (2012). USA: ANSYS Inc.
- Argillier, J. F., Barre, L., Brucy, F., Dournaux, J. L., Henaut, I., Bouchard, R. (2001). Influence of Asphaltenes Content and Dilution on Heavy Oil Rheology. *Porlamar, Venezuela*, 12-14 March, 2001.
- Arney, M. S., Bai, R., Guevara, E., Joseph, D., Liu, K. (1993). Friction factor and holdup studies for lubricated pipelining—I. Experiments and correlations. *International journal of multiphase flow*, 19(6), 1061-1076.
- Arney, M. S., Ribeiro, G. S., Guevara, E., Bai, R., Joseph, D. D. (1996). Cement-lined pipes for water lubricated transport of heavy oil. *International journal of multiphase flow*, 22(2), 207-221.
- Ashrafizadeh, S. N., Kamran, M. (2010). Emulsification of heavy crude oil in water for pipeline transportation. *Journal of Petroleum Science and Engineering*, 71(3–4), 205-211.
- Bai, R., Chen, K., Joseph, D. (1992). Lubricated pipelining: stability of core-annular flow. Part 5. Experiments and comparison with theory. *J. Fluid Mech.*, 240(97), 132.

- Bannwart, A. C. (1998). Wavespeed and volumetric fraction in core annular flow. *International journal of multiphase flow*, 24(6), 961-974.
- Bannwart, A. C. (2001). Modeling aspects of oil–water core–annular flows. *Journal of Petroleum Science and Engineering*, 32(2), 127-143.
- Bannwart, A. C., Barbosa, A., Ribeiro, G. S. (2007). A model for interpretation of a re-start experiment of viscous oil-water annular flow. Paper presented at the Proceedings of the 18th conference on Proceedings of the 18th IASTED International Conference: modelling and simulation, Montreal, Canada, 30 May-1 June, 2007.
- Bannwart, A. C., Rodriguez, O. M., Biazussi, J. L., Martins, F. N., Selli, M. F., de Carvalho, C. H. (2012). Water-assisted Flow of Heavy Oil in a Vertical Pipe: Pilot-scale Experiments. *International Journal of Chemical Reactor Engineering*, 10(1).
- Bannwart, A. C., Rodriguez, O. M., de Carvalho, C. H., Wang, I. S., Vara, R. M. (2004). Flow patterns in heavy crude oil-water flow. *Journal of energy resources technology*, 126(3), 184-189.
- Barnea, D., Luninski, Y., Taitel, Y. (1983). Flow pattern in horizontal and vertical two phase flow in small diameter pipes. *The Canadian Journal of Chemical Engineering*, 61(5), 617-620.
- Beretta, A., Ferrari, P., Galbiati, L., Andreini, P. (1997). Horizontal oil-water flow in small diameter tubes. Flow patterns. *International communications in heat and mass transfer*, 24(2), 223-229.
- Brackbill, J., Kothe, D. B., Zemach, C. (1992). A continuum method for modeling surface tension. *Journal of computational physics*, 100(2), 335-354.
- Bracke, M., De Voeght, F., Joos, P. (1989). The Kinetics of Wetting: The Dynamic Contact Angle. *Prog. Colloid Polym. Sci*, 79, 142-149.
- Brauner, N. (1998). Liquid-liquid two-phase flow. *Heat Exchanger Design Updates: The Update Journal of the Heat Exchanger Design Handbook*, 5(1).
- Brauner, N., Moalem Maron, D., Rovinsky, J. (1998). A two-fluid model for stratified flows with curved interfaces. *International journal of multiphase flow*, 24(6), 975-1004.
- Brauner, N. (2002). *Liquid-Liquid Two-Phase Flow Systems*. In V. Bertola (Ed.), *Modeling and Control of Two-Phase Flow Phenomena*. CISM Center, Udine, Italy.
- Brennen, C. E. (2005). *Fundamentals of multiphase flow*. New York: Cambridge University Press.

- Broussard, D. E., Scott, P. R., Kruka, V. R. (1976). Conservation of water for core flow, US Patent 3,977,469.
- Charles, M. E., Govier, G. t., Hodgson, G. (1961). The horizontal pipeline flow of equal density oil-water mixtures. *The Canadian Journal of Chemical Engineering*, 39(1), 27-36.
- Chilton, E. G., Handley, L. R. (1958). Method and apparatus for lubricating pipe lines, US Patent 2,821,205.
- Clark, A. F., Shapiro, A. (1950). Method of pumping viscous petroleum, US Patent No. 2,533,878.
- Clark, B., Graves, W. G., Lopez-de-Cardenas, J. E., Gurfinkel, M. E., Peats, A. W. (2007). Heavy oil, extra-heavy oil, and bitumen, report of National Petroleum Council, USA (Accessed on 5th May, 2013).
- Colebrook, C. F. (1939). Turbulent Flow in Pipes, with particular reference to the Transition Region between the Smooth and Rough Pipe Laws. *Journal of the ICE*, 11(4), 133-156.
- Crowe, C. T. (2005). *Multiphase flow handbook*. Florida: CRC press.
- Daas, M., Kang, C., Jepson, W. (2000). Quantitative analysis of drag reduction in horizontal slug flow. Paper presented at the SPE Annual Technical Conference and Exhibition, Texas, USA, 1-4 October, 2000.
- da Silva, R. C. R., Mohamed, R. S., Bannwart, A. C. (2006). Wettability alteration of internal surfaces of pipelines for use in the transportation of heavy oil via core-flow. *Journal of Petroleum Science and Engineering*, 51(1), 17-25.
- Dusseault, M. (2001). Comparing Venezuelan and Canadian heavy oil and tar sands. Paper presented at the Canadian International Petroleum Conference, Alberta, Canada, 12-14 June, 2001.
- Escojido, D. M., Urribarri, O., Gonzalez, J. (1991). Part 1: Transportation of Heavy Crude Oil and Natural Bitumen. Paper presented at the 13th World Petroleum Congress, Buenos Aires, Argentina, 20-25 October, 1991.
- Farrar, B., Bruun, H. (1996). A computer based hot-film technique used for flow measurements in a vertical kerosene-water pipe flow. *International journal of multiphase flow*, 22(4), 733-751.
- Ferziger, J. H., Peric, M. (2012). *Computational methods for fluid dynamics*: Springer Science & Business Media.
- Ghosh, S., Das, G., Das, P. K. (2010). Simulation of core annular downflow through CFD—A comprehensive study. *Chemical Engineering and Processing: Process Intensification*, 49(11), 1222-1228.

- Ghosh, S., Das, G., Das, P. K. (2011). Simulation of core annular in return bends—A comprehensive CFD study. *Chemical Engineering Research and Design*, 89(11), 2244-2253.
- Ghosh, S., Mandal, T., Das, G., Das, P. (2009). Review of oil water core annular flow. *Renewable and Sustainable Energy Reviews*, 13(8), 1957-1965.
- Grassi, B., Strazza, D., Poesio, P. (2008). Experimental validation of theoretical models in two-phase high-viscosity ratio liquid-liquid flows in horizontal and slightly inclined pipes. *International journal of multiphase flow*, 34(10), 950-965.
- Guevara, E., Ninez, G., Gonzalez, J. (1997). Highly Viscous Oil Transportation Methods in the Venezuelan Oil Industry. Paper presented at the 15th World Petroleum Congress, Beijing, China, 12-17 October, 1997.
- Gupta, P., Doraiah, A., Ray, S. (2007). In situ combustion delivers results. *World oil.com*. Available at: <http://www.worldoil.com/November-2007-In-situ-combustion-delivers-results.html> (Accessed 7th May, 2013).
- Henaut, I., Argillier, J., Pierre, C., Moan, M. (2003). Thermal flow properties of heavy oils. Paper presented at the Offshore Technology Conference, Houston, USA, 5-8 May, 2003.
- Ioannou, K., Nydal, O. J., Angeli, P. (2005). Phase inversion in dispersed liquid-liquid flows. *Experimental thermal and fluid science*, 29(3), 331-339.
- Isaac, J. D., Speed, J. B. (1904). Method of piping fluids, US Patent No. 759,374.
- James, M., Wing, R. (2009). High temperature electric submersible pumps effective in oil sands production. *Pumps & Systems*.
- Jiang, F., Wang, Y., Ou, J., Chen, C. (2014). Numerical Simulation of Oil-Water Core Annular Flow in a U-Bend Based on the Eulerian Model. *Chemical Engineering & Technology*, 37(4), 659-666.
- Jiang, T.-S., Soo-Gun, O., Slattery, J. C. (1979). Correlation for dynamic contact angle. *Journal of Colloid and Interface Science*, 69(1), 74-77.
- Joseph, D. D., Bai, R., Chen, K., Renardy, Y. Y. (1997). Core-annular flows. *Annual Review of Fluid Mechanics*, 29(1), 65-90.
- Joseph, D. D., Bai, R., Mata, C., Sury, K., Grant, C. (1999). Self-lubricated transport of bitumen froth. *Journal of Fluid Mechanics*, 386(1), 127-148.
- Joseph, D. D., Renardy, Y. Y. (1993). *Fundamentals of two-fluid dynamics. Pt. II: Lubricated transport, drops and miscible liquids (Vol. 4)*. New York: Springer-Verlag.

- Kaushik, V., Ghosh, S., Das, G., Das, P. K. (2012). CFD simulation of core annular flow through sudden contraction and expansion. *Journal of Petroleum Science and Engineering*, 86, 153-164.
- Kumara, W., Elseth, G., Halvorsen, B., Melaaen, M. (2010). Comparison of Particle Image Velocimetry and Laser Doppler Anemometry measurement methods applied to the oil–water flow in horizontal pipe. *Flow Measurement and Instrumentation*, 21(2), 105-117.
- Kumara, W., Halvorsen, B., Melaaen, M. (2010). Particle image velocimetry for characterizing the flow structure of oil–water flow in horizontal and slightly inclined pipes. *Chemical Engineering Science*, 65(15), 4332-4349.
- Liu, Y., Zhang, H., Wang, S., Wang, J. (2008). Prediction of pressure gradient and holdup in small Eötvös number liquid-liquid segregated flow. *Chinese Journal of Chemical Engineering*, 16(2), 184-191.
- Lo, S., Tomasello, A. (2010). Recent progress in CFD modelling of multiphase flow in horizontal and near-horizontal pipes. Paper presented at the 7th North American Conference on Multiphase Technology, Banff, Canada, 2-4 June 2010.
- Lovick, J., Angeli, P. (2004). Experimental studies on the dual continuous flow pattern in oil–water flows. *International journal of multiphase flow*, 30(2), 139-157.
- Lyman, T., Piper, E., Riddell, A. (1984). Heavy Oil Mining Technical and Economic Analysis. Paper presented at the SPE California Regional Meeting, California, USA, 11-13 April, 1984.
- Martínez-Palou, R., de Lourdes Mosqueira, M., Zapata-Rendón, B., Mar-Juárez, E., Bernal-Huicochea, C., de la Cruz Clavel-López, J., Aburto, J. (2011). Transportation of heavy and extra-heavy crude oil by pipeline: A review. *Journal of Petroleum Science and Engineering*, 75(3), 274-282.
- McKibben, M. J., Gillies, R. G., Shook, C. A. (2000a). A laboratory investigation of horizontal well heavy oil-water flows. *The Canadian Journal of Chemical Engineering*, 78(4), 743-751.
- McKibben, M. J., Gillies, R. G., Shook, C. A. (2000b). Predicting pressure gradients in heavy oil-water pipelines. *The Canadian Journal of Chemical Engineering*, 78(4), 752-756.
- McKibben, M. J., Sanders, R. S., Gillies, R. G. (2013). A New Method for Predicting Friction Losses and Solids Deposition during the Water-Assisted Pipeline Transport of Heavy Oils and Co-Produced Sand. Paper presented at the SPE Heavy Oil Conference-Canada, Alberta, Canada, 11-13 June, 2013.

- Menter, F. R. (1994). Two-equation eddy-viscosity turbulence models for engineering applications. *AIAA journal*, 32(8), 1598-1605.
- Nädler, M., Mewes, D. (1997). Flow induced emulsification in the flow of two immiscible liquids in horizontal pipes. *International journal of multiphase flow*, 23(1), 55-68.
- Nichita, B. A., Zun, I., Thome, J. R. (2010). A VOF method coupled with a dynamic contact angle model for simulation of two-phase flows with partial wetting. Paper presented at the 7th International Conference on Multiphase Flow, ICMF 2010, Tampa, FL, 30 May-4 June, 2010.
- Núñez, G. A., Rivas, H., Joseph, D. (1998). Drive to produce heavy crude prompts variety of transportation methods. *Oil and Gas Journal*, 96(43), 59-68.
- Oliemans, R., Ooms, G., Wu, H., Duijvestijn, A. (1987). Core-annular oil/water flow: the turbulent-lubricating-film model and measurements in a 5 cm pipe loop. *International journal of multiphase flow*, 13(1), 23-31.
- Oliemans, R. V. A., Ooms, G. (1986). Core-annular flow of oil and water. *Multiphase Science and Technology*, 2(1-4), 427-476.
- Ooms, G., Segal, A., Van Der Wees, A., Meerhoff, R., & Oliemans, R. (1984). A theoretical model for core-annular flow of a very viscous oil core and a water annulus through a horizontal pipe. *International journal of multiphase flow*, 10(1), 41-60.
- Pedersen, K. S., Rønningsen, H. P. (2003). Influence of wax inhibitors on wax appearance temperature, pour point, and viscosity of waxy crude oils. *Energy & fuels*, 17(2), 321-328.
- Peysson, Y., Bensakhria, A., Antonini, G., Argillier, J. (2007). Pipeline lubrication of heavy oil: experimental investigation of flow and restart problems. *SPE Production & Operations*, 22(01), 135-140.
- Piela, K., Delfos, R., Ooms, G., Westerweel, J., Oliemans, R. (2008). On the phase inversion process in an oil–water pipe flow. *International journal of multiphase flow*, 34(7), 665-677.
- Piela, K., Delfos, R., Ooms, G., Westerweel, J., Oliemans, R. (2009). Dispersed oil–water–gas flow through a horizontal pipe. *AIChE Journal*, 55(5), 1090-1102.
- Piela, K., Delfos, R., Ooms, G., Westerweel, J., Oliemans, R., Mudde, R. (2006). Experimental investigation of phase inversion in an oil–water flow through a horizontal pipe loop. *International journal of multiphase flow*, 32(9), 1087-1099.

- PlotDigitizer. (2014). Available at: <http://plotdigitizer.sourceforge.net/> (Accessed on 7th June, 2014).
- Pospisil, G. (2011). Heavy Oil Challenges & Opportunities-North Slope Alaska, report prepared by BP Exploration (Alaska) Inc. (Accessed on 5th May, 2013).
- Ranade, V. V. (2002). Computational Flow Modeling for Chemical Reactor Engineering. Bath: Academic Press.
- Rodriguez, O., Bannwart, A. C., & de Carvalho, C. (2009). Pressure loss in core-annular flow: modeling, experimental investigation and full-scale experiments. *Journal of Petroleum Science and Engineering*, 65(1), 67-75.
- Rodriguez, O. M., Baldani, L. (2012). Prediction of pressure gradient and holdup in wavy stratified liquid-liquid inclined pipe flow. *Journal of Petroleum Science and Engineering*, 96, 140-151.
- Rodriguez, O. M., Castro, M. S. (2014). Interfacial-tension-force model for the wavy-stratified liquid-liquid flow pattern transition. *International journal of multiphase flow*, 58, 114-126.
- Russell, T., Hodgson, G., Govier, G. (1959). Horizontal pipeline flow of mixtures of oil and water. *The Canadian Journal of Chemical Engineering*, 37(1), 9-17.
- Sanders, R. S., Ko, T., Bai, R., Joseph, D. D. (2004). Factors Governing Friction Losses in Self-lubricated Transport of Bitumen Froth: 1. Water Release. *The Canadian Journal of Chemical Engineering*, 82(4), 735-742.
- Schlichting, H. (1979). *Boundary-layer theory* (K. J, Trans. 7th ed.). New York: McGraw-Hill.
- Schramm, G. (1994). *A practical approach to rheology and rheometry*. Karlsruhe: Haake.
- Seebergh, J. E., Berg, J. C. (1992). Dynamic wetting in the low capillary number regime. *Chemical Engineering Science*, 47(17), 4455-4464.
- Sotgia, G., Tartarini, P., Stalio, E. (2008). Experimental analysis of flow regimes and pressure drop reduction in oil-water mixtures. *International journal of multiphase flow*, 34(12), 1161-1174.
- Sridhar, S., Zhang, H.-q., Sarica, C., Pereyra, E. J. (2011). Experiments and Model Assessment on High-Viscosity Oil/Water Inclined Pipe Flows. Paper presented at the SPE Annual Technical Conference and Exhibition.
- Strazza, D., Demori, M., Ferrari, V., Poesio, P. (2011). Capacitance sensor for hold-up measurement in high-viscous-oil/conductive-water core-annular flows. *Flow Measurement and Instrumentation*, 22(5), 360-369.

- Strazza, D., Grassi, B., Demori, M., Ferrari, V., Poesio, P. (2011). Core-annular flow in horizontal and slightly inclined pipes: Existence, pressure drops, and hold-up. *Chemical Engineering Science*, 66(12), 2853-2863.
- Strazza, D., Poesio, P. (2012). Experimental study on the restart of core-annular flow. *Chemical Engineering Research and Design*, 90(11), 1711-1718.
- Sui, Y., Ding, H., Spelt, P. D. (2014). Numerical simulations of flows with moving contact lines. *Annual Review of Fluid Mechanics*, 46, 97-119.
- Taitel, Y., Dukler, A. (1976). A model for predicting flow regime transitions in horizontal and near horizontal gas-liquid flow. *AIChE Journal*, 22(1), 47-55.
- Trallero, J., Sarica, C., Brill, J. (1997). A Study of Oil-Water Flow Patterns in Horizontal Pipes. *SPE Production & Facilities*, 12(03), 165-172.
- Urquhart, R. (1986). Heavy oil transportation-present and future. *Journal of Canadian Petroleum Technology*, 25(02).
- Vallée, C., Höhne, T., Prasser, H.-M., Sühnel, T. (2008). Experimental investigation and CFD simulation of horizontal stratified two-phase flow phenomena. *Nuclear Engineering and Design*, 238(3), 637-646.
- Van Mourik, S., Veldman, A., Dreyer, M. (2005). Simulation of capillary flow with a dynamic contact angle. *Microgravity-Science and Technology*, 17(3), 87-93.
- Veil, J., Quinn, J. (2008). Water issues associated with heavy oil production, report prepared by Argonne National Laboratory (ANL), USA (Accessed on 5th May, 2013).
- Versteeg, H. K., Malalasekera, W. (2007). An introduction to computational fluid dynamics: the finite volume method. Essex: Pearson Education.
- Vielma, M. A., Atmaca, S., Sarica, C., Zhang, H.-Q. (2008). Characterization of oil/water flows in horizontal pipes. *SPE Projects, Facilities & Construction*, 3(4), 1-21.
- Walvekar, R. G., Choong, T. S., Hussain, S., Khalid, M., Chuah, T. (2009). Numerical study of dispersed oil-water turbulent flow in horizontal tube. *Journal of Petroleum Science and Engineering*, 65(3), 123-128.
- Wang, W., Gong, J., Angeli, P. (2011). Investigation on heavy crude-water two phase flow and related flow characteristics. *International journal of multiphase flow*, 37(9), 1156-1164.
- Wegmann, A., Rudolf von Rohr, P. (2006). Two phase liquid-liquid flows in pipes of small diameters. *International journal of multiphase flow*, 32(8), 1017-1028.

- White, F. M. (2003). Fluid mechanics. New York : McGraw-Hill.
- Wilcox, D. C. (1998). Turbulence modeling for CFD. California: DCW industries
- Yang, Z. (2014). A Study of Viscous Oil and Water Pipe Flow. Paper presented at the 9th North American Conference on Multiphase Technology, Banff, Canada, 11-13 June, 2014.
- Yuan, Y., & Lee, T. R. (2013). Contact angle and wetting properties. In Surface science techniques (pp. 3-34). Springer.
- Zagustin, K., Guevara, E., Nunez, G. (1988). Process for restarting core flow with very viscous oils after a long standstill period, U.S. Patent No. 4,745,937.
- Zhang, H.-Q., Vuong, D. H., Sarica, C. (2012). Modeling high-viscosity oil/water concurrent flow in horizontal and vertical pipes. SPE J, 17, 243-250.
- Zigrang, D., Sylvester, N. (1985). A review of explicit friction factor equations. Journal of energy resources technology, 107(2), 280-283.
- Zorgani, E. (2012). An experimental study of sand behaviour in multiphase pipelines. (PhD thesis), Cranfield University, UK.

APPENDICES

Appendix A Tabulated experimental data

The experimental data on high-viscosity oil-water flow in a horizontal 1 inch pipeline are listed in the following tables. Table A-1 lists the data, including pressure gradients, water holdups and flow regimes from the present experiments. Table A-2 to A-4 list the collected data from previous experiments of Al-Awadi (2011), Zorgani (2012), and Solomon (2013) respectively conducted in the same experimental rig in the PSE Lab, Cranfield University. The water holdup was not measured in previous experiments thus not included in Table A-2 to A-4.

Table A-1 Experimental data from the present experiments (Oil CYL 680).

U_{so} (m/s)	U_{sw} (m/s)	$-dp/dz$ (kPa/m)	Water holdup H_w	Observed flow regime
<i>Series 1:</i>				
<i>Oil temperature: 11.5±1°C, oil density: 910±2 kg/m³, oil viscosity: 5 600±600 cP.</i>				
0.034	0	13.833	-	Single oil flow
0.047	0.071	0.640	0.388	Oil plugs in water
0.041	0.132	0.517	0.507	Oil plugs in water
0.042	0.225	0.680	0.597	Oil plugs in water
0.039	0.406	1.219	0.699	Oil plugs in water
0.038	0.610	1.634	0.762	Oil plugs in water
0.044	0.797	1.941	0.820	Dispersed oil lumps in water
0.044	0.990	2.541	0.837	Oil plugs in water
0.101	0	28.143	-	Single oil flow
0.118	0.075	0.637	0.350	CAF
0.093	0.095	0.725	0.393	CAF
0.106	0.184	0.958	0.502	CAF
0.107	0.402	1.516	0.670	CAF
0.110	0.595	1.969	0.766	CAF

Table A-1 Continued.

U_{so} (m/s)	U_{sw} (m/s)	$-dp/dz$ (kPa/m)	Water holdup H_w	Observed flow regime
0.108	0.802	2.277	0.772	Dispersed oil lumps in water
0.105	0.950	2.659	0.899	Dispersed oil lumps in water
0.198	0	50.392	-	Single oil flow
0.215	0.067	1.050	0.305	CAF
0.206	0.128	1.157	0.395	CAF
0.199	0.188	1.556	0.491	CAF
0.202	0.390	1.784	0.603	CAF
0.205	0.592	2.343	0.672	CAF
0.201	0.806	2.730	0.790	CAF
0.204	0.997	3.190	0.841	Dispersed oil lumps in water
0.394	0.122	2.317	0.303	CAF
0.403	0.184	1.841	0.339	CAF
0.391	0.403	2.764	0.511	CAF
0.389	0.589	3.288	0.594	CAF
0.388	0.781	3.489	0.625	CAF
0.527	0.185	2.308	0.313	CAF
0.537	0.390	3.252	0.442	CAF
0.550	0.773	4.123	0.640	CAF
0.540	0.991	4.777	0.665	CAF
0.544	1.175	5.366	0.749	CAF
<i>Series 2:</i>				
<i>Oil temperature: 20.5±1°C, oil density: 905±1 kg/m³, oil viscosity: 3 300±500 cP.</i>				
0.051	0	10.57	-	Single oil flow
0.063	0.041	6.656	0.367	Inversion
0.063	0.117	0.775	0.481	Oil plugs in water
0.057	0.139	1.060	0.504	Oil plugs in water
0.058	0.188	1.090	0.597	Dispersed oil lumps in water
0.056	0.407	1.572	0.745	Dispersed oil lumps in water

Table A-1 Continued.

U_{so} (m/s)	U_{sw} (m/s)	$-dp/dz$ (kPa/m)	Water holdup H_w	Observed flow regime
0.059	0.814	2.172	0.852	Dispersed oil lumps in water
0.060	1.175	3.842	0.925	Dispersed oil lumps in water
0.097	0	15.783	-	Single oil flow
0.101	0.037	0.473	0.251	Oil plugs in water
0.103	0.106	0.839	0.438	Oil plugs in water
0.104	0.193	1.204	0.579	Oil plugs in water
0.112	0.412	1.514	0.725	Dispersed oil lumps in water
0.109	0.813	2.741	0.841	Dispersed oil lumps in water
0.108	1.176	4.310	-	Dispersed oil lumps in water
0.205	0	31.214	-	Single oil flow
0.213	0.051	0.985	0.303	CAF
0.208	0.109	1.407	0.371	CAF
0.210	0.201	1.613	0.502	CAF
0.211	0.403	1.807	0.642	CAF
0.209	0.804	2.919	0.753	Dispersed oil lumps in water
0.209	1.175	4.195	0.848	Dispersed oil lumps in water
0.550	0.188	2.708	0.315	CAF
0.549	0.396	3.092	0.455	CAF
0.552	0.814	4.057	0.689	CAF
0.552	1.176	5.354	0.717	CAF

Table A-2 Collected data from the experiments of Al-Awadi (2011) (Oil CYL 1000).

U_{so} (m/s)	U_{sw} (m/s)	$-dp/dz$ (kPa/m)	Observed flow regime
<i>Series 1:</i>			
<i>Oil temperature: 25±2°C, oil density: 920±2 kg/m³, oil viscosity: 3 800±600 cP.</i>			
0.065	0	13.980	Single oil flow
0.066	0.013	13.930	Oil-continuous
0.070	0.020	14.160	Oil-continuous
0.062	0.021	12.100	Oil-continuous
0.062	0.025	11.210	Oil-continuous
0.055	0.031	9.290	Inversion
0.064	0.040	1.890	Inversion
0.060	0.050	1.890	Inversion
0.063	0.063	1.970	Inversion
0.058	0.110	1.680	Oil plugs in water
0.064	0.200	1.540	Oil plugs in water
0.063	0.303	2.060	Oil plugs in water
0.062	0.402	2.080	Oil plugs in water
0.063	0.500	2.390	Oil plugs in water
0.066	0.601	2.670	Dispersed oil lumps in water
0.064	0.704	2.850	Dispersed oil lumps in water
0.061	0.800	3.080	Dispersed oil lumps in water
0.064	0.906	3.360	Dispersed oil lumps in water
0.060	1.000	3.570	Dispersed oil lumps in water
0.099	0	18.010	Single oil flow
0.098	0.012	16.770	Oil-continuous
0.099	0.020	15.490	Oil-continuous
0.096	0.029	4.790	Inversion
0.095	0.048	1.890	Inversion
0.098	0.080	1.890	CAF

Table A-2 Continued.

U_{so} (m/s)	U_{sw} (m/s)	$-dp/dz$ (kPa/m)	Observed flow regime
0.099	0.102	2.020	CAF
0.099	0.151	1.960	CAF
0.100	0.300	2.210	CAF
0.145	0	25.850	Single oil flow
0.144	0.018	21.720	Oil-continuous
0.143	0.031	2.080	Inversion
0.148	0.050	1.790	Inversion
0.146	0.080	1.950	CAF
0.146	0.103	2.270	CAF
0.148	0.150	2.520	CAF
0.147	0.200	2.340	CAF
0.148	0.300	2.440	CAF
0.194	0	32.81	Single oil flow
0.201	0.013	28.310	Oil-continuous
0.198	0.032	3.660	Inversion
0.199	0.047	1.230	CAF
0.200	0.072	1.230	CAF
0.200	0.098	1.300	CAF
0.200	0.157	1.800	CAF
0.198	0.200	2.060	CAF
0.200	0.302	2.450	CAF
0.201	0.406	2.650	CAF
0.196	0.504	2.830	CAF
0.201	0.596	2.950	CAF
0.566	0	74.09	Single oil flow
0.566	0.012	53.710	Oil-continuous
0.575	0.029	3.200	Inversion

Table A-2 Continued.

U_{so} (m/s)	U_{sw} (m/s)	$-dp/dz$ (kPa/m)	Observed flow regime
0.569	0.053	3.040	CAF
0.572	0.074	2.950	CAF
0.574	0.101	3.510	CAF
0.575	0.148	3.980	CAF
0.571	0.160	3.930	CAF
0.575	0.203	3.920	CAF
0.575	0.299	4.010	CAF
0.575	0.401	3.930	CAF
0.575	0.512	3.970	CAF
0.575	0.703	4.270	CAF
0.575	0.802	4.340	CAF
0.575	0.906	4.530	CAF
0.575	0.997	4.720	CAF
<i>Series 2:</i>			
<i>Oil temperature: 16.5±0.5°C, oil density: 930±1 kg/m³, oil viscosity: 8 300±300 cP.</i>			
0.319	0.014	13.870	-
0.319	0.030	1.350	-
0.320	0.052	1.200	-
0.319	0.071	1.310	-
0.318	0.099	1.580	-
0.318	0.514	4.860	-
<i>Series 3:</i>			
<i>Oil temperature: 10.7±1°C, oil density: 935±2 kg/m³, oil viscosity: 13 200±500 cP.</i>			
0.046		36.47	Single oil flow
0.052	0.017	21.460	Oil-continuous
0.055	0.021	17.070	-
0.059	0.025	12.730	Inversion
0.056	0.030	7.560	Inversion

Table A-2 Continued.

U_{so} (m/s)	U_{sw} (m/s)	$-dp/dz$ (kPa/m)	Observed flow regime
0.059	0.034	4.280	Inversion
0.058	0.049	2.100	CAF
0.058	0.059	2.220	CAF
0.059	0.070	2.190	CAF
0.059	0.104	2.680	CAF
0.057	0.151	3.000	CAF
0.059	0.201	3.010	CAF
0.105	0	52.070	Single oil flow
0.101	0.009	41.590	Oil-continuous
0.105	0.022	21.820	Oil-continuous
0.101	0.052	1.960	Inversion
0.104	0.080	2.340	Inversion
0.104	0.102	2.510	CAF
0.103	0.150	2.860	CAF
0.107	0.301	3.460	CAF
0.135	0	79.660	Single oil flow
0.133	0.015	27.640	Oil-continuous
0.138	0.029	3.240	Inversion
0.137	0.049	2.120	Inversion
0.140	0.081	2.140	Inversion
0.139	0.101	2.310	CAF
0.138	0.149	2.810	CAF
0.139	0.207	3.210	CAF
0.139	0.311	3.670	CAF
<i>Series 4:</i>			
<i>Oil temperature: 8.8±1°C, oil density: 938±2 kg/m³, oil viscosity: 16 000±500 cP</i>			
0.109	0	77.070	Single oil flow
0.108	0.019	26.690	-

Table A-2 Continued.

U_{so} (m/s)	U_{sw} (m/s)	$-dp/dz$ (kPa/m)	Observed flow regime
0.119	0.052	3.300	-
0.116	0.081	2.310	-
0.116	0.105	2.530	-
0.112	0.123	2.080	-
0.116	0.153	2.550	-
0.118	0.182	2.700	-
0.116	0.287	2.580	-

Table A-3 Collected data from the experiments of Zorgani (2012) (Oil CYL 680).

U_{so} (m/s)	U_{sw} (m/s)	$-dp/dz$ (kPa/m)	Observed flow regime
<i>Oil temperature: 11.5±2°C, oil density: 910±2 kg/m³, oil viscosity: 5 600±800 cP.</i>			
0.111	0	34.428	Single oil flow
0.110	0.023	4.452	Inversion
0.102	0.039	1.314	Inversion
0.099	0.047	1.076	CAF
0.098	0.064	1.423	CAF
0.111	0.082	1.528	CAF
0.109	0.100	1.237	CAF

Table A-4 Collected data from the experiments of Alagbe (2013) (Oil CYL 680).

U_{so} (m/s)	U_{sw} (m/s)	$-dp/dz$ (kPa/m)	Observed flow regime
<i>Oil temperature: 15.5±1°C, oil density: 906±1 kg/m³, oil viscosity: 3 700±300 cP.</i>			
0.090	0	16.184	Single oil flow
0.100	0.181	1.408	Oil plugs in water
0.095	0.298	1.524	Oil plugs in water
0.093	0.405	1.568	Oil plugs in water
0.091	0.497516	1.797	Oil plugs in water
0.092	0.602	1.924	Dispersed oil lumps in water
0.097	0.707	2.201	Dispersed oil lumps in water
0.094	0.802	2.397	Dispersed oil lumps in water
0.092	0.900	2.590	Dispersed oil lumps in water
0.094	1.002	2.760	Dispersed oil lumps in water
0.147	0	25.583	Single oil flow
0.152	0.180	1.660	CAF
0.152	0.310	1.877	CAF
0.152	0.413	1.991	CAF
0.155	0.510	2.227	CAF
0.155	0.606	2.377	CAF
0.159	0.703	2.462	Dispersed oil lumps in water
0.153	0.805	2.650	Dispersed oil lumps in water
0.153	0.907	2.795	Dispersed oil lumps in water
0.154	1.012	2.973	Dispersed oil lumps in water
0.351	0.188	1.630	CAF
0.352	0.303	1.770	CAF
0.349	0.408	1.979	CAF
0.347	0.506	2.079	CAF
0.350	0.609	2.269	CAF
0.352	0.694	2.365	CAF

Table A-4 Continued.

U_{so} (m/s)	U_{sw} (m/s)	$-dp/dz$ (kPa/m)	Observed flow regime
0.347	0.816	2.565	CAF
0.362	0.897	2.078	CAF
<i>Oil temperature: 12.5±2°C, oil density: 910±3 kg/m³, oil viscosity: 5 000±600 cP.</i>			
0.058	0	17.185	Single oil flow
0.051	0.048	5.576	Oil plugs in water
0.058	0.138	1.009	Oil plugs in water
0.060	0.225	0.964	Oil plugs in water
0.063	0.329	1.206	Oil plugs in water
0.057	0.410	1.425	Oil plugs in water
0.058	0.541	1.630	Oil plugs in water
0.055	0.652	1.789	Dispersed oil lumps in water
0.056	0.719	1.804	Dispersed oil lumps in water
0.056	0.722	1.808	Dispersed oil lumps in water
0.059	0.826	1.783	Dispersed oil lumps in water
0.057	0.911	2.042	Dispersed oil lumps in water
0.057	1.033	2.207	Dispersed oil lumps in water
0.110	0	23.21	Single oil flow
0.120	0.182	1.309	CAF
0.117	0.314	1.507	CAF
0.118	0.412	1.754	CAF
0.121	0.505	1.883	CAF
0.123	0.609	1.978	Dispersed oil lumps in water
0.118	0.695	2.043	Dispersed oil lumps in water
0.121	0.814	2.326	Dispersed oil lumps in water
0.200	0	45.71	Single oil flow
0.200	0.203	1.450903	CAF
0.200	0.307	1.603	CAF

Table A-4 Continued.

U_{so} (m/s)	U_{sw} (m/s)	$-dp/dz$ (kPa/m)	Observed flow regime
0.202	0.404	1.757	CAF
0.202	0.514	1.904	CAF
0.200	0.613	2.040	CAF
0.200	0.712	2.174	CAF
0.196	0.812	2.289	CAF
0.195	0.910	2.442	Dispersed oil lumps in water
0.198	1.013	2.512	Dispersed oil lumps in water
0.393	0.183	3.108	CAF
0.389	0.303	2.560	CAF
0.392	0.400	2.681	CAF
0.403	0.499	2.893	CAF
0.381	0.506	2.664	CAF
0.404	0.598	2.602	CAF
0.404	0.708	2.813	CAF
0.404	0.806	2.940	CAF
0.403	0.906	3.079	CAF
<i>Oil temperature: 7.5±2°C, oil density: 916±3 kg/m³, oil viscosity: 7 100±600 cP.</i>			
0.054	0	23.763	Single oil flow
0.057	0.172	0.923	Oil plugs in water
0.058	0.297	1.259	Oil plugs in water
0.060	0.413	1.439	Oil plugs in water
0.060	0.499	1.502	Oil plugs in water
0.058	0.598	1.770	Oil plugs in water
0.061	0.696	2.010	Dispersed oil lumps in water
0.060	0.805	2.227	Dispersed oil lumps in water
0.055	0.905	2.396	Dispersed oil lumps in water
0.061	1.016	2.594	Dispersed oil lumps in water

Table A-4 Continued.

U_{so} (m/s)	U_{sw} (m/s)	$-dp/dz$ (kPa/m)	Observed flow regime
0.090	0	38.595	Single oil flow
0.093	0.175	1.516	CAF
0.100	0.311	1.688	CAF
0.098	0.401	1.782	CAF
0.098	0.508	1.880	CAF
0.092	0.605	2.051	CAF
0.100	0.697	2.247	Dispersed oil lumps in water
0.098	0.802	2.325	Dispersed oil lumps in water
0.099	0.895	2.359	Dispersed oil lumps in water
0.098	0.994	2.541	Dispersed oil lumps in water
0.210	0	66.849	Single oil flow
0.210	0.176	2.256	CAF
0.212	0.299	1.934	CAF
0.210	0.406	2.174	CAF
0.210	0.506	2.192	CAF
0.210	0.602	2.410	CAF
0.209	0.707	2.604	CAF
0.214	0.807	2.789	CAF
0.212	0.905	2.940	Dispersed oil lumps in water
0.213	1.002	3.131	Dispersed oil lumps in water
0.401	0.178	3.263	CAF
0.398	0.305	2.713	CAF
0.399	0.403	2.767	CAF
0.400	0.512	2.829	CAF
0.402	0.597	2.797	CAF
0.401	0.707	2.971	CAF
0.404	0.797	2.419	CAF

Appendix B Summary of data collected from the literature

In the analysis of flow patterns of oil-water flow, a large amount of data on flow regimes was collected from the open literature. Figures 5-5 to 5-9 presented in Chapter 5 were drawn with calculated gravitation to viscous force ratios from the collected data. A summary of collected data sets used in flow pattern analysis is listed in Table B-1.

The original data from the literature listed in Table B-1 is in the type of graphs. The data collected is in a form of CSV file. The data was obtained by the mean of data extraction. A program Plot Digitizer (see PlotDigitizer, 2014) was used. It is an open source software that allows a user to import a graph, define the frame of reference, read the coordinates of any point, and export the values to a text file. Additionally, a magnifying tool is provided to facilitate an accurate extraction of points.

Table B-1 Summary of collected data sets used in flow pattern analysis.

Source	Data collected
Trallero et al. (1997)	U_{so} , U_{sw} and flow regimes
Nädler and Mewes (1997)	U_{so} , U_{sw} and flow regimes
Angeli and Hewitt (2000)	U_m , C_w and flow regimes
Lovick and Angeli (2004)	U_m , C_o and flow regimes
Wegmann and Rudolf von Rohr (2006)	U_m , C_w and flow regimes
Grassi et al. (2008)	U_{so} , U_{sw} , and flow regimes
Sotgia et al. (2008)	U_{so} , U_{sw} , and flow regimes
Vielma et al. (2008)	U_{so} , U_{sw} , and flow regimes

The collected data are either superficial phase velocities (U_{so} and U_{sw}) or input phase volume fractions and the mixture velocities (C_w/C_o and U_{mix}), together with corresponding flow patterns. The following equations are used to transform the collected data to gravitation to viscous force ratio (G/V) and C_w for representation of flow maps as shown in Figures 5-5 to 5-9.

$$G/V = \frac{\Delta\rho g D^2}{\mu U} \quad (\text{B-1})$$

$$C_w = \frac{U_{sw}}{U_{so} + U_{sw}} = 1 - C_o \quad (\text{B-2})$$

$$U_{sw} = U_m C_w \quad (\text{B-3})$$

$$U_{so} = U_m (1 - C_w) \quad (\text{B-4})$$

Appendix C Calibration of pressure transducers

The two pressure transducers and the differential pressure transducer were calibrated before experimental runs. The instrument used for the calibration has a handheld pneumatic pressure pump (model: ADT 914, range: -14~375 psi, adjustment resolution: 10 Pa) together with a digital pressure gauge (model: ADT 681, range: 0~20 bar, accuracy: $\pm 0.2\%$ FS). The voltage reading was obtained from a 12-bit NI card (NI 9205). The specifications of the pressure transducers are listed in Table C-1. The voltage change with input pressure for the pressure transducers is listed in Table C-2. It demonstrates that all the pressure transducers function reasonably well. Figures C-1 shows the liner responses between pressure and the voltage signal for different pressure transducers. The slopes and offsets of the pressure transducers obtained from the calibration were put in the Labview programme to obtain accurate pressure readings directly during experiments.

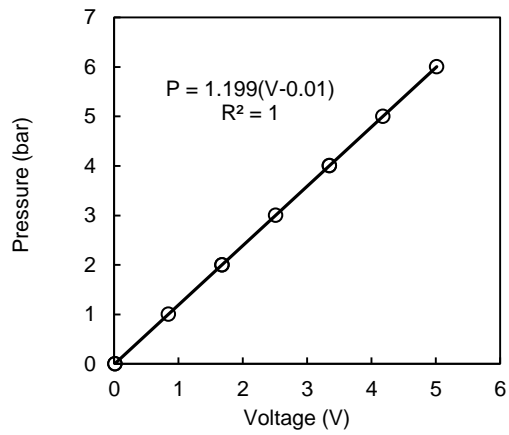
Table C-1 Specification of pressure transducers used in the present experiments.

Label	Range	Model	Serial number
P1	6 bar g ^{a)}	S-11	S/N 1104YQJR
P2	6 bar g ^{a)}	S-11	S/N 1104YQJQ
DP	-200 to 200 mbar d ^{b)}	PMP4170	S/N 3046221

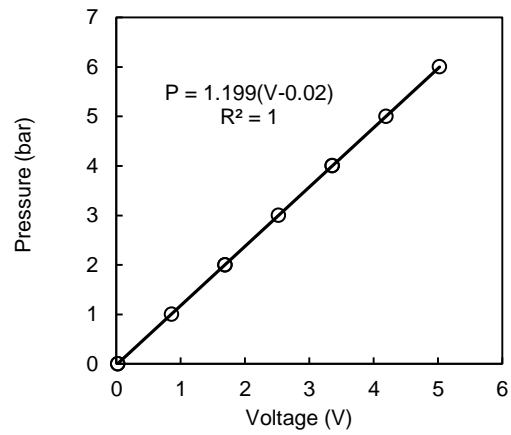
^{a)} g means gauge pressure; ^{b)} d means differential pressure.

Table C-2 Calibration data for pressure transducers.

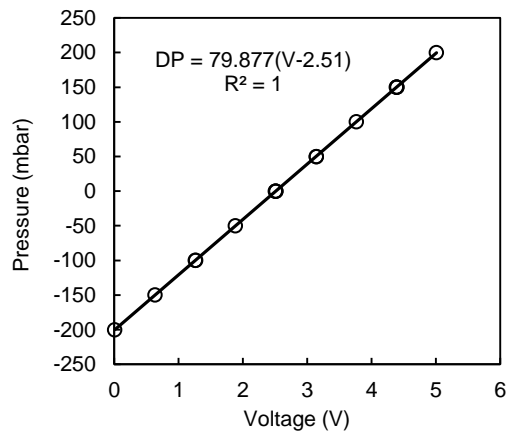
P1		P2		DP	
Pressure(bar)	Voltage(V)	Pressure(bar)	Voltage(V)	Pressure(mbar)	Voltage(V)
0	0.01	0	0.02	0	2.505
1	0.842	1	0.855	-50	1.884
2	1.676	2	1.687	-100	1.263
3	2.51	3	2.522	-150	0.634
4	3.344	4	3.357	-200	0.007
5	4.18	5	4.19	-100	1.262
6	5.016	6	5.025	0	2.508
4	3.345	4	3.357	50	3.143
2	1.677	2	1.688	100	3.763
0	0.01	0	0.02	150	4.387
				200	5.011
				150	4.392
				50	3.14
				0	2.513



(a)



(b)



(c)

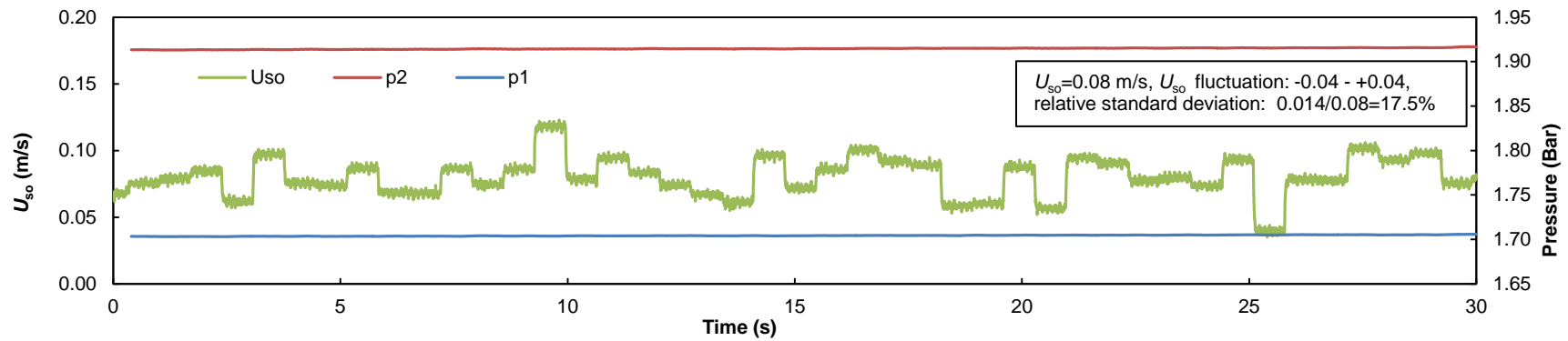
Figure C-1 Calibrated relationship between pressure and voltage for the pressure transducers. (a) Pressure transducer P1; (b) Pressure transducer P2; (c) Differential pressure transducer, DP.

Appendix D Practical considerations on the experimental setup of the oil system

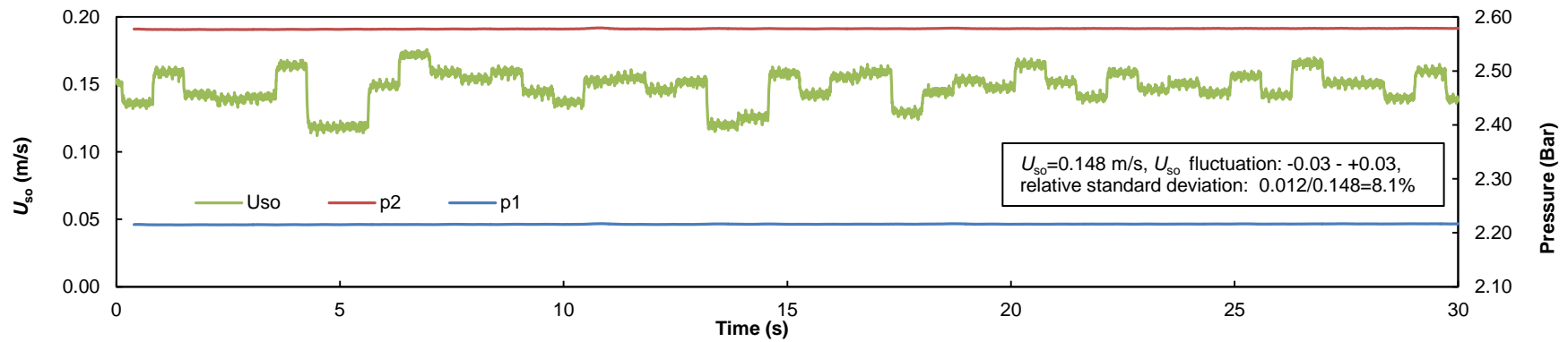
The experimental setup of the oil system in the present study has been introduced in Chapter 3. The performance of the oil pump and some practical considerations on the setup of the oil system is discussed here.

For the present experimental setup (see Section 3.3 in Chapter 3), it is observed that there are slight 'pulsations' in the signals of the oil flow rates. Figure D-1 shows typical raw signals of the superficial oil velocity and the corresponding signals from two gauge pressure transducers for single oil flow. Figure D-2 shows typical signals of the superficial oil velocity, superficial water velocity and the corresponding signals from two gauge pressure transducers for core annular flow. For single oil flow (see Figure D-1), slight pulsations in U_{so} is exhibited while no obvious pulsations in the pressure signals can be observed. The slight pulsations in the oil flow rates near the pump outlet can be damped downstream the horizontal test line thus little fluctuation is reflected in the pressure signals. For oil-water core annular flow (see Figure D-2), slight pulsations in U_{so} is exhibited and fluctuations in the pressure signals can be observed as well. Also, when the pulsations in U_{so} have higher magnitude, there appears some correlation between the peaks of U_{so} and pressure signals. The fluctuation of the interface of core annular flow and the dynamic breaking and reforming of oil fouling film on the wall can result in the fluctuation of the pressure signals. When the magnitude of pulsations in U_{so} is higher, the change in flow rate also affect the pressure signals resulting similar trends between the peaks of U_{so} and pressure signals. This might be explained by that when the flow passage of the oil is reduced in two-phase flow, pulsations in the oil flow rates near the pump outlet cannot be damped as much as for single oil flow.

For the flow conditions investigated in the present study, the relative standard deviations vary between 3%-33% with higher relative deviations for low U_{so} . As the measured pressure drop for single oil flow agrees well with the theoretical

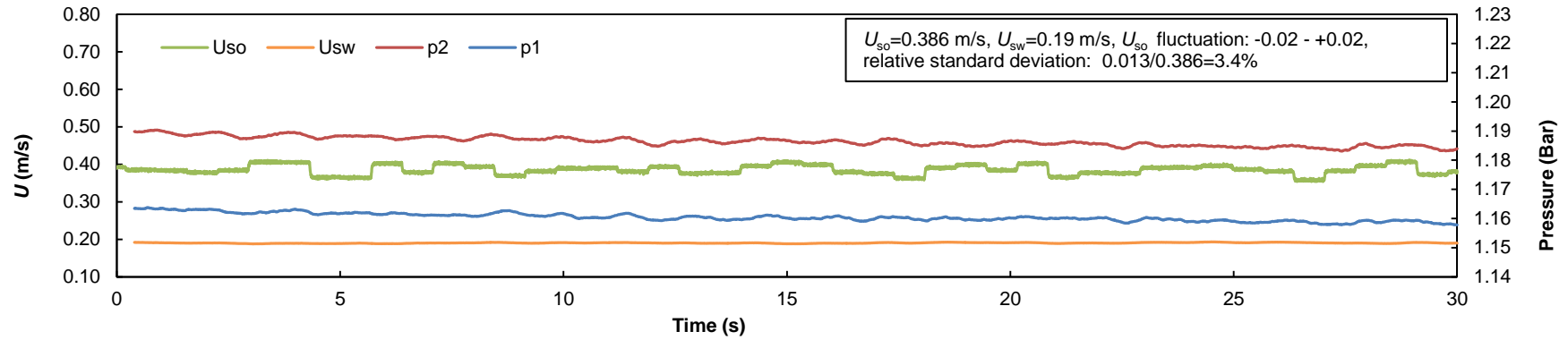


(a)

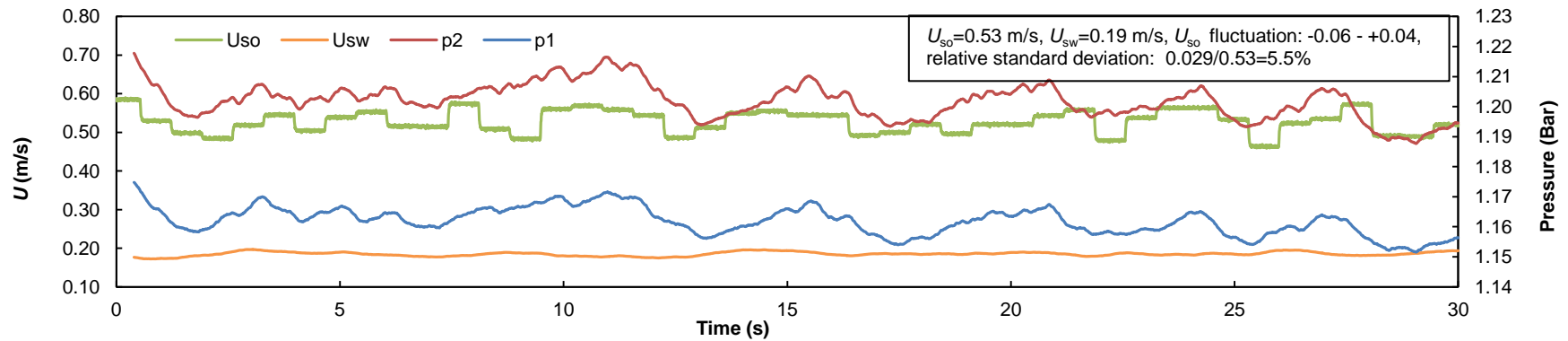


(b)

Figure D-1 Typical signals of the superficial oil velocity and the corresponding signals from two gauge pressure transducers for single oil flow



(a)



(b)

Figure D-2 Typical signals of the superficial oil velocity, superficial water velocity and the corresponding signals from two gauge pressure transducers for oil-water core annular flow.

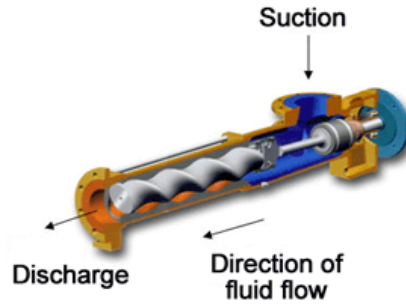


Figure D-3 Schematic of the working principle of progressive cavity pump.

pressure drop calculated with time-average velocity (see Section 3.5.1 in Chapter 3), there is no evidence to doubt the accuracy of the oil flow meter.

Normally, there is little pulsation in the flow rate when the fluid is pumped by a PCP (progressive cavity pump). Figure D-3 shows the working principle of a progressive cavity pump. A PCP transfers fluid by means of the progress, through the pump, of a sequence of small, fixed shape, discrete cavities, as its rotor is turned. The cavities taper down toward their ends and overlap with their neighbours, so that, in general, no flow pulsing is caused by the arrival of cavities at the outlet. In Figure D-1 and D-2, the frequency of pulsations does not correlate with the flow rate hence the speed of the pump, thus the pulsation of the flow rate is less possible due to the normal meaning of 'pump pulsation' linked to pump working principle such as the piston pump.

In the present study, the water is also pumped with a PCP. As shown in Figure D-2, there is little pulsation in the water flow rate. It is suspected that the slight pulsation in the oil flow rate is linked to the high viscosity of the oil. When the fluid becomes very viscous, a high suction is needed to draw the fluid into the pump cavities. The oil flow drawn into the pump might lose its continuity due to insufficient suction to overcome the frictional resistance. The suction force is a relative pressure difference provided by the atmosphere pressure, gravity force, and the vacuum at the suction end. It is suggested to arrange the oil tank to a higher level in any future study with the experimental facility. Also, a larger diameter suction pipe (2 inch in the present study) can help reduce the frictional resistance to the flow hence aid smooth flow into to the pump.

Appendix E Wall wettability and contact angle

Wettability describes the preference of a solid to be in contact with one fluid rather than another. Figure E-1 illustrates three scenarios of which an oil drop is surrounded by water on a solid surface. On a water-wet surface, the oil drop beads up, minimising its contact with the solid (see Figure E-1 (a)). On an oil-wet surface, the oil drop spreads, resulting in a contact angle of about 180° (see Figure E-1 (c)). If the condition is neither strongly water-wetting nor oil-wetting, the balance of forces in the oil/water/solid system will result in a contact angle, θ , between the fluids at the solid surface (see Figure E-1 (b)).

When the force balance is in equilibrium, there exists a unique static contact angle. In practice, however, there exist many metastable states of a droplet on a solid, and the observed contact angles can be within a range. If a small enough amount of liquid is added to a drop, the contact line will still be pinned and the contact angle will increase; similarly, if a small enough amount of liquid is removed from a drop, the contact line will still be pinned and the contact angle will decrease (see Figure E-2). Hence, a drop placed on a surface has a spectrum of contact angles ranging from the so-called advancing (maximal) contact angle, θ_A , to the so-called receding (minimal) contact angle, θ_R . The static contact angle is somewhere between those values. The difference between the advancing angle and the receding angle is called the hysteresis (Yuan and Lee, 2013).

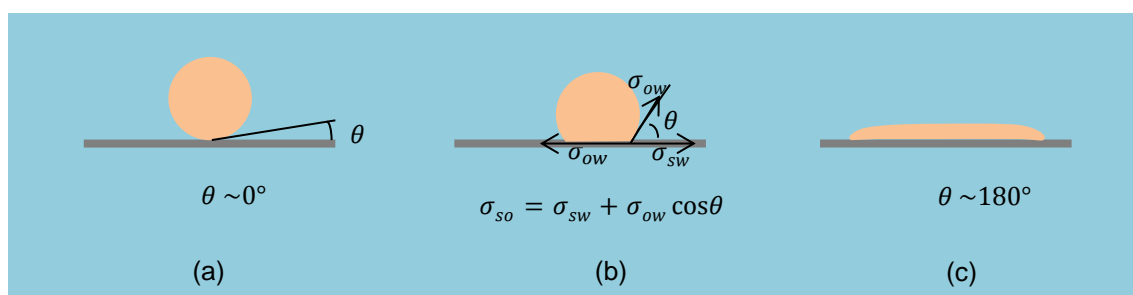


Figure E-1 Oil drops (orange) surrounded by water (blue) on solid surfaces.

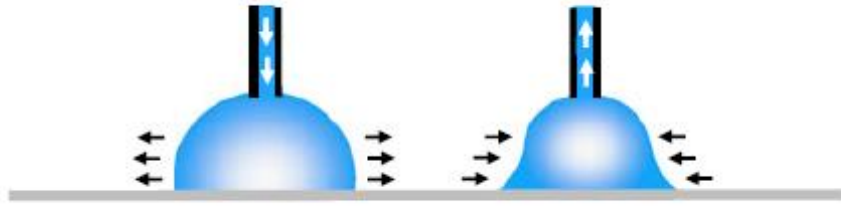


Figure E-2 Diagram of advancing contact angle and receding contact angle.

The commercial instruments for contact angle measurement are generally based on the sessile droplet method or the Wilhelmy plate method. The sessile drop contact angle is measured by a contact angle goniometer using an optical subsystem to capture the profile of a pure liquid on a solid substrate. The angle formed between the liquid/solid interface and the liquid/vapour or liquid-liquid interface is the contact angle. The Wilhelmy method employs a sensitive force meter to measure a force that can be translated into a value of the contact angle. In this method, a small plate-shaped sample of the solid in question, attached to the arm of a force meter, is vertically dipped into a pool of the probe liquid, and the force exerted on the sample by the liquid is measured by the force meter.

In the context of water-lubricated flow, the contact angles of oil-in-water droplets should be gauged. The sessile droplet method can be applied to determine the contact angles of oil-in-water droplets on the solid surface. Figure E-3 shows a schematic of experimental cell for the measurement of oil-in-water droplet contact angle with solid surface. The dynamic contact angles can be measured by changing the volume of the oil droplet as illustrated in Figure E-2.

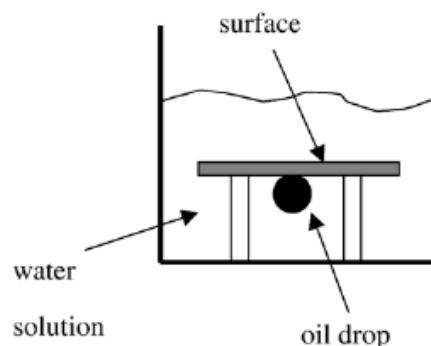


Figure E-3 Schematic of experimental cell for the measurement of oil-in-water droplet contact angle with solid surface (da Silva et al., 2006).

Appendix F Preliminary experiments on restart of core annular flow

F.1 Introduction

In any pipeline transport of water-lubricated high-viscosity oil-water flow, there exists a high possibility of a breakdown which interrupts the transport. The shutdown can occur for a variety of reasons, for example, the mechanical failure of a pump, an electrical power failure, or pipeline blockage due to accumulation of oil fouling. When the flow stops in a pipeline, the water-continuous flow regime cannot be maintained. The two phases evolve to stratified flow after a short standstill time. Difficulty in restarting the flow is one of the major concerns which restrict the implementation of water-lubricated flow technology.

An approach which provides a smooth restart of core annular flow after a long standstill period is patented by Zagustin et al. (1988). This approach initiates the flow by pumping water gradually into the pipeline until a desired steady state condition is reached. Arney et al. (1996) performed experiments on restart of core annular flow in steel pipe and cement-lined pipe by pumping water and showed that the cement-lined pipe can resist oil fouling and has short restart time. Bannwart et al. (2007) proposed a semi-empirical model to estimate the transient pressure with restart time during the restart of core annular flow. Peysson et al. (2007) performed an experimental study on restart of core annular flow after a short standstill time (within 60 seconds) by pumping both water and oil at the same time and measured the pressure drop. Strazza et al. (2012) conducted an experimental study on restart of core annular flow using only water for cleaning the pipe.

Some preliminary experiments on shutdown and restart of core annular flow were conducted. The experimental setup for these tests is the same as that in our experiments on high-viscosity oil-water transport as introduced in Chapter 3. Experimental procedures and results are presented in the following sections.

F.2 Experimental procedures

The experimental procedure is introduced below:

- 1) Develop stable water-assisted flow; start collecting data from instrumentations for the following processes to monitor the transient flow characteristics during shutdown and restart.
- 2) Switch off both oil and water pumps, then close the downstream valve on the very end of the horizontal multiphase flow test line and the valve upstream the Tee junction on the horizontal single oil flow line. The flow is stopped in the horizontal multiphase flow test line. Wait for a planned standstill before move to the next step.
- 3) Open the downstream valve on the very end of the horizontal multiphase flow test line. Then switch on the water pump to restart the flow using only water.

F.3 Experimental results

Pressure gradients obtained from two point pressure transducers and a differential pressure transducer during shutdown and restart with only water at two different flow rates are shown in Figure F-1. It can be seen that the pressure gradient obtained from the two point pressure transducers and the differential pressure transducer agrees with each other in general, except that the differential pressure transducer did not capture two pressure surges due to its limit in time response. Before shutdown, CAF was established at $U_{so}=0.4\text{m/s}$, $U_{sw}=0.2\text{m/s}$ for oil viscosity around

5 000 cP. The pressure gradient fluctuated around 2~3 kPa/m for the stable CAF. When both oil and water pumps stopped working, the pressure gradient started dropping quickly due to drop of flow rate. As the valves downstream were closed immediately after switching off the pumps to trap fluids, a negative pressure peak with a high magnitude, i.e., the so called pressure surge or fluid hammer, is seen in Figure F-1. The pressure gradient fluctuated around zero soon after the valves were closed. After a duration of standstill time, another pressure surge in Figure F-1 indicates when the valves downstream were made open before restarting the water pump. As the pump started working, the water flow rate increased to the desired flow rate gradually. At the same time, the pressure gradient started increasing to a peak

before dropping down quickly once the flow was re-established. This peak is the so called maximum pressure gradient during a restart process. The pressure gradient during restart process only is presented in Figure F-2.

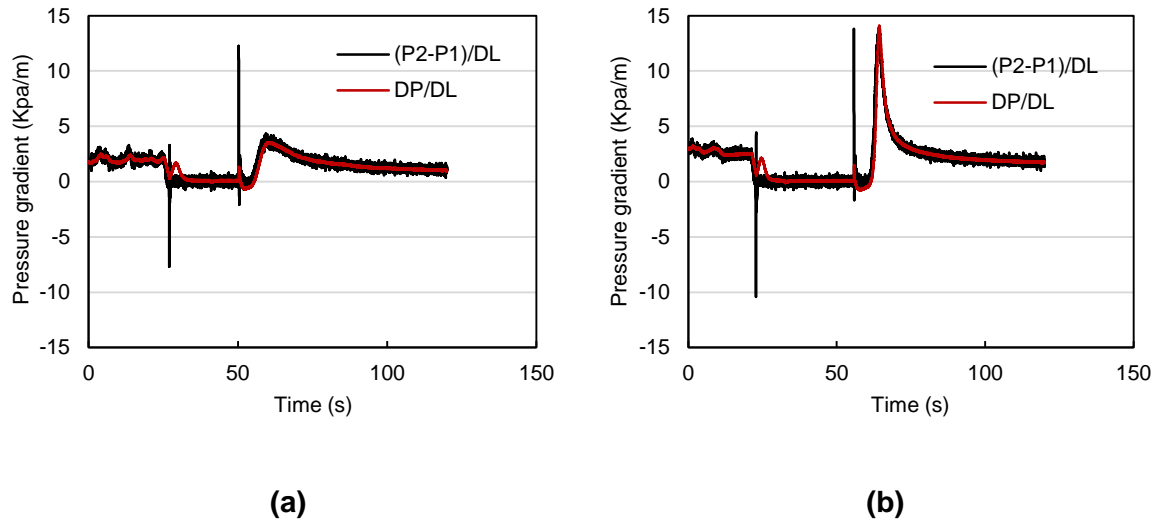


Figure F-1 Pressure gradient obtained from two point pressure transducers (P1 and P2) and a differential pressure transducer (DP) during shutdown and restart; before shutdown $U_{so}=0.4$ m/s, $U_{so}=0.2$ m/s, stable CAF is established. (a) Restart with $U_{sw}=0.2$ m/s; (b) Restart with $U_{sw}=0.6$ m/s

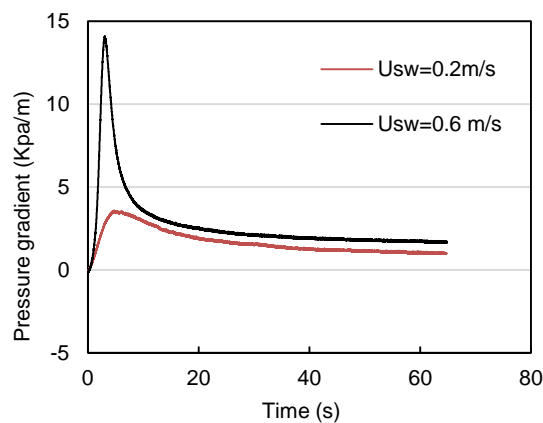


Figure F-2 Pressure gradient obtained from the differential pressure transducer during restart at different restart water flow rates U_{sw} . Before shutdown $U_{so}=0.4$ m/s, $U_{so}=0.2$ m/s, stable CAF was established.

It is demonstrated in Figure F-2 that a higher maximum restart pressure is required for a higher restart water flow rate. The benefit of a higher water flow rate is that it flushes away the oil fouling film faster. One restart procedure which can provide a smooth restart has been patented by Zagustin et al. (1988) in which the water flow rate is gradually increased until the oil is detached from the pipe wall.

For the water-lubricated transport of heavy oil flow, the restart pressure must be taken into account in the design of the pipeline. Solutions to reduce the restart pressure need to be sought and examined. The reduction of the restart pressure can be achieved through 1) increase of the wettability of the pipe wall by the water phase, e.g., film coating of the pipe inner wall, additions of chemicals into the water phase ; 2) oil viscosity reduction during the restart process, e.g., using hot water during restart, applying electrical heating method along the pipeline; and 3) proper restart procedure to minimise to restart pressure, e.g., gradually increase the water flow rate during restart as proposed by Zagustin et al. (1988). A combination of the above approaches can be useful.

Appendix G Heavy oil production and transportation techniques

A brief summary on heavy oil production and transportation techniques has been given in the literature review (see Chapter 2). Introduction of different production and transportation techniques are presented here.

G.1 Production techniques

G.1.1 Surface mining

Surfacing mining (open-pit mining) is the only commercial production method if the resource lies within 50 to 75 m of the surface (Clark et al., 2007). Most surface mining occurs in Canada where the surface access and volume of the shallow oil sand deposits make this approach economic.

The process of surface mining resembles that in coal and metal mining - overburden and heavy oil would be systematically removed from a deepening pit; overburden and waste ore would be stockpiled and reclaimed (Lyman et al., 1984). Once extracted from the surface mine, oil sands would be transported to processing plants where heavy oil is separated through warm water washing or solvent extraction.

G.1.2 Cold Production

(1) Primary Cold Production

Some heavy oils can be produced by primary cold production. Much of the oil in the Orinoco heavy oil belt in Venezuela is currently being recovered by cold production due to its low enough viscosity, as are reservoirs offshore Brazil (Alboudwarej et al., 2006). For some wells, diluents are injected to decrease fluid viscosity, and artificial lift technology, such as electrical submersible pumps (ESPs) and progressing cavity pumps (PCPs), lift the hydrocarbons to the surface.

(2) Cold Heavy Oil Production with Sand (CHOPS)

Cold heavy oil production with sand (CHOPS) is another primary production approach that has applicability in heavy oil reservoirs; it is widely used in unconsolidated sandstones.

CHOPS operates contrarily to those conventional oil recovery processes - instead of blocking sand ingress with screen or gravel packs, it boosts sand to enter the well by aggressive perforation and swabbing strategies (Dusseault, 2001). As sand move from the formation into the well, it leaves behind channels referred to as 'wormholes' (see Figure G-1), which increases permeability near the wellbore and allows more oil to reach wellbore. Heavy oil production has increased 10- to 20-fold after cconverting wells from traditional production to CHOPS (Veil and Quinn, 2008).

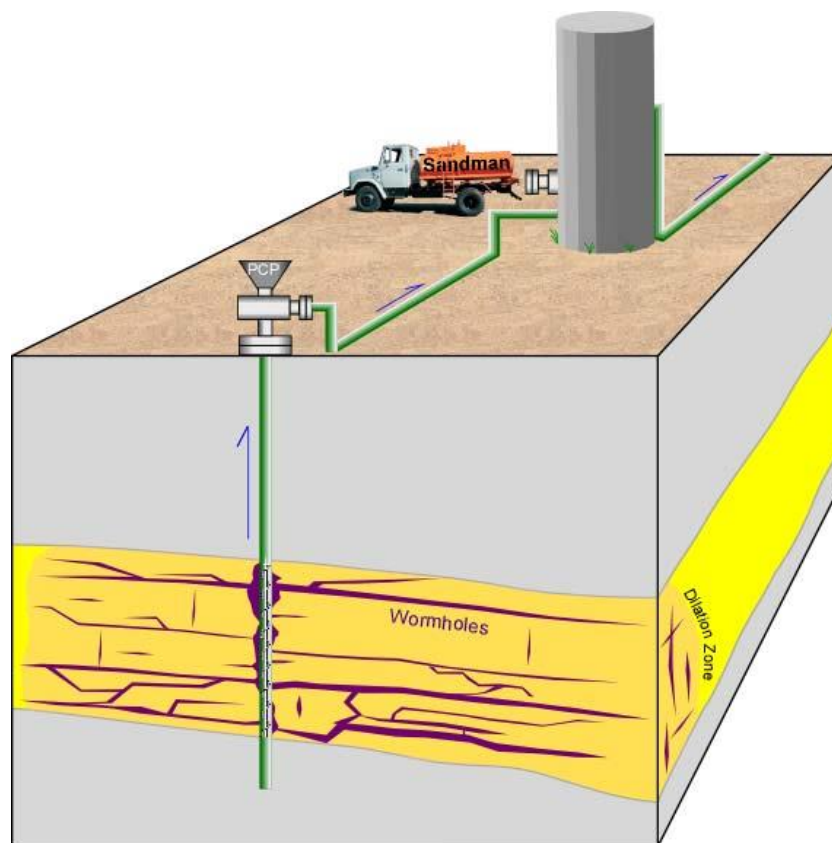


Figure G-1 A schematic of a CHOPS well (Pospisil, 2011).

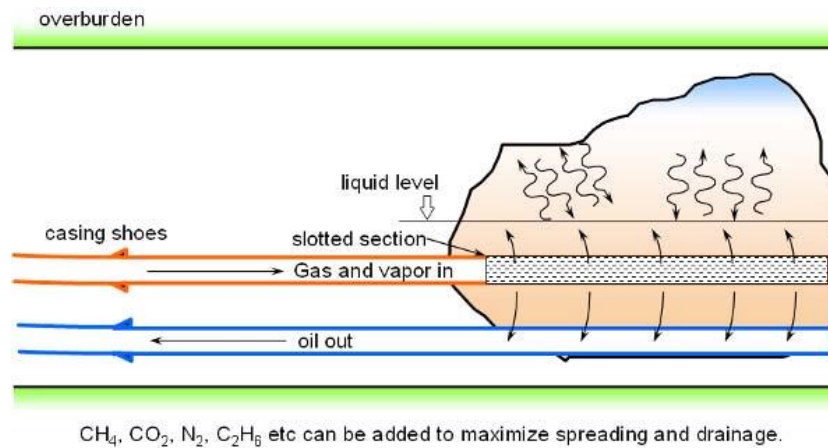


Figure G-2 A schematic of the VAPEX process (Dusseault 2008a, cited in Veil and Quinn, 2008)

(3) Water Flooding

Water flooding is a cold enhanced oil recovery (EOR) method which has been used for decades to enhance recovery of conventional oil and to extend the life of producing reservoirs; it can be employed in heavy oil deposits too. Water flood is usually aided with polymer addition to improve sweep efficiency (Alikhan and Farouq Ali, 1983).

(4) Vapour-Assisted Petroleum Extraction (VAPEX)

Vapour-Assisted Petroleum Extraction (VAPEX) is a relatively new technology being tested. The VAPEX process typically involves miscible solvent injection through a horizontal well that is aligned with a horizontal production well located about three to five meters below it, as shown in Figure G-2.

G.1.3 Thermal Production

(1) Steam Flooding

Steam flooding is the basic form of thermal treatment technology. As shown in Figure G-3, steam is pumped through vertical injection wells into a heavy oil formation, as the steam loses heat to the formation, it condenses into hot water, which, coupled with the continuous supply of steam behind it, provides the drive to move the oil to production wells.

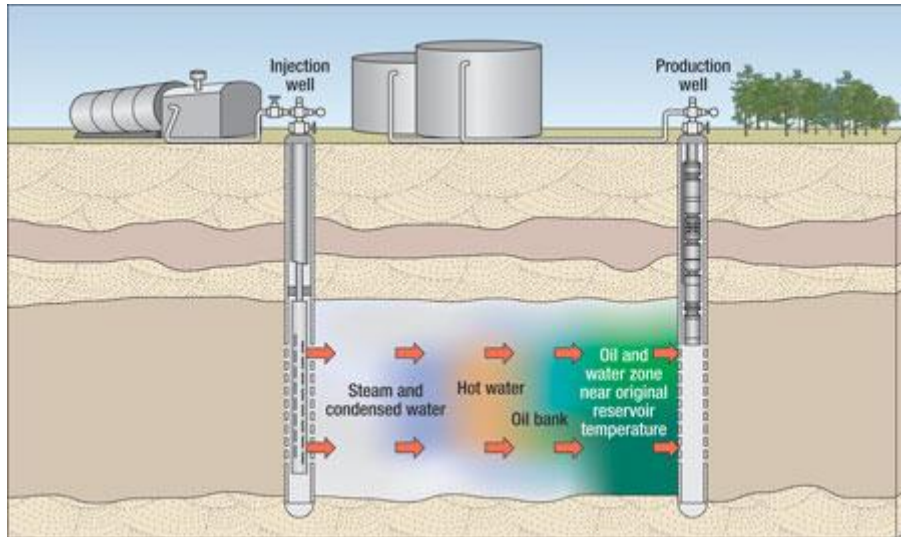


Figure G-3 A schematic of steam flooding for heavy oil recovery (James and Wing, 2010).

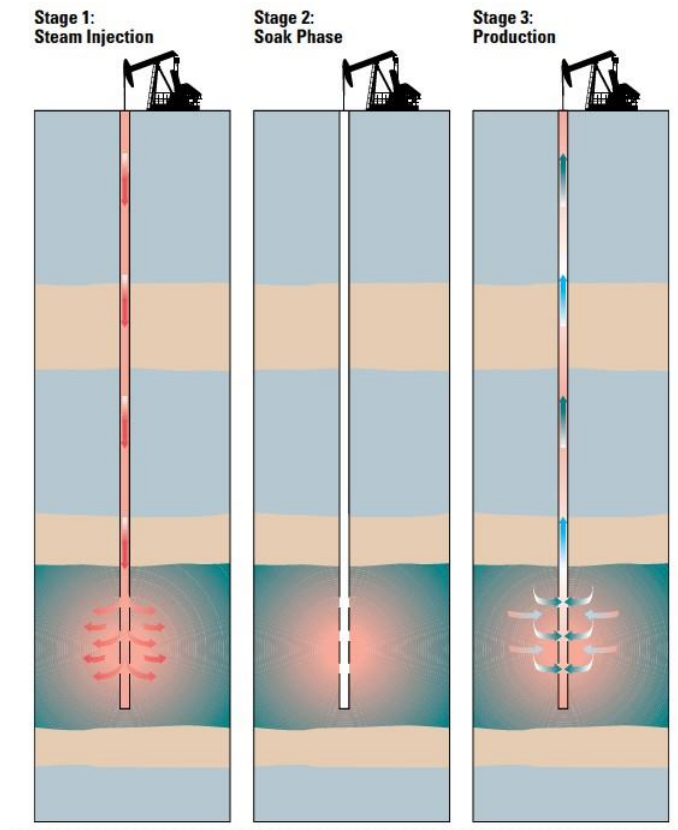


Figure G-4 A schematic of cyclic steam stimulation for heavy oil recovery (Alboudwarej et al., 2006).

(2) Cyclic Steam Stimulation (CSS)

Cyclic steam stimulation, also known as steam soak, or huff and puff, is a single well thermal production method applied in stages as shown in Figure G-4 . First, a predetermined amount of steam is injected into a well that has been drilled or converted for injection purpose. The well is then shut in to allow the steam to heat or 'soak' the heavy oil around the well. Finally, after a sufficient time, the injection wells are back in production until the heat is dissipated with the produced oils.

(3) Steam-Assisted Gravity Drainage (SAGD)

Steam-Assisted Gravity Drainage (SAGD) is used in many fields in western Canada due to its ability to produce heavy oil from formations too shallow for conventional steam injection methods.

In SAGD, a pair of parallel horizontal wells is drilled with one well about 5 to 7 m above the other (see Figure G-5). Steam injected into the upper well heats the heavy oil, reducing its viscosity. Gravity causes the mobilized oil to flow down toward the lower well.

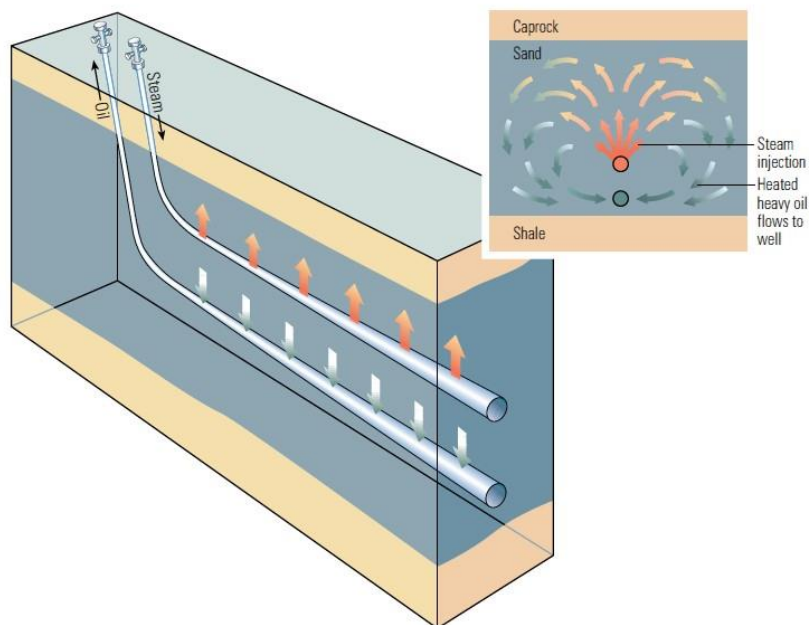


Figure G-5 A schematic of steam-assisted gravity drainage for heavy oil recovery (Alboudwarej et al., 2006).

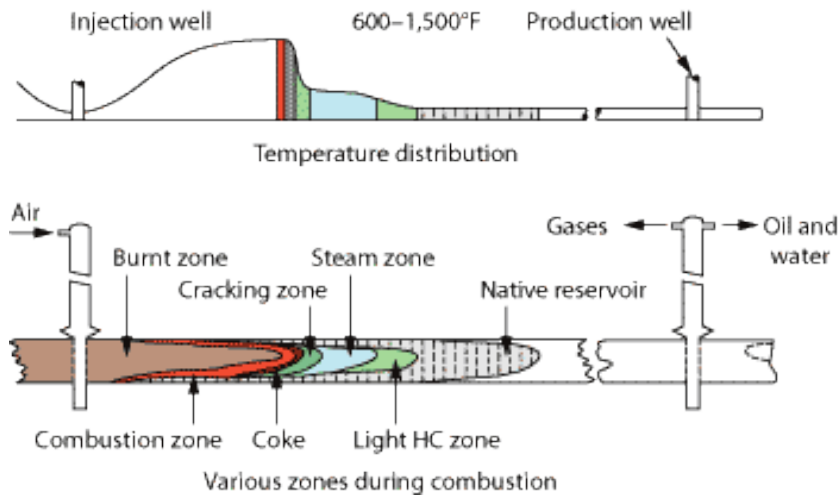


Figure G-6 A schematic of in situ combustion for heavy oil recovery (Gupta et al., 2007).

(4) In situ Combustion

In situ combustion, also known as fire flooding, is a method for mobilizing highly viscous oil.

Toe-to-heel air injection (THAI) is one version of this technology, as shown in Figure G-6. It combines a vertical air injection well with a horizontal production well. First, steam is injected into the vertical well to heat the horizontal well and condition the reservoir around the vertical well. After adequate time, compressed air is injected into the vertical well and combustion is initiated. The combustion front moves from the 'toe end' of the horizontal well to the 'heel end', sweeps the oil to the collection well, ultimately capturing up to 80% of the original oil in place.

G.2 Transportation techniques

G.2.1 Heating

Heating is a widely used method in to transport heavy crude oil. Raising the temperature of heavy oil could substantially reduce its viscosity. Heating oil method could be divided into gas/fuel-fired heating and electrical heating.

Direct gas/fuel-fired heating is the traditional way of heating oil for its transport. It contains direct-fired heaters (gas/fuel-fired) at pumping stations along the pipeline to raise the temperature of heavy oil. As the heated oil flows forward long the pipe, the

heated fluid constantly loses heat to the colder ambient, its temperature gradually decreases in most circumstances (sometimes, the temperature goes up when the produced heat due to friction between the oil and the pipe is more than heat loss), so the oil needs reheating in the next pumping and/or heating station. To reduce energy loss during the transportation, pipe insulation is of great importance. Insulation options include applying insulation coating around the pipe and burying the pipe underground. The design of oil pipelines using the traditional heating method involves many considerations: temperature to be heated to for the optimum viscosity; heat losses; number of pumping and heating stations; start-up and shut-down operations etc. (Escojido et al., 1991). An example for this kind of pipeline system is one in California, which transports heavy oil with 14° to 16° API gravity by heating the oil, maintaining the oil temperature between about 49 °C to 54 °C (Urquhart, 1986).

The electrical heating was proposed originally for subsea pipelines, but could be applied for onshore pipelines as well. For short-length subsea pipelines (less than a mile), the produced fluids would be transported as quickly as possible through well-insulated pipelines to minimize temperature decrease along its way. Insulation-only becomes not enough when longer lengths of pipelines are needed to transport the oil, while supplying pumping or heating along the pipelines is difficult for remote subsea wells and pipelines. Heating the crude electrically was proposed. Two configurations for electrical heating are available: a single heated electrically insulated pipeline (SHIP) where electrical current flows along the pipe; and a pipe-in-pipe subsea pipeline where the oil flows through the inner electrically insulated pipe which is surrounded concentrically by an electrically conductive outer pipe (Martínez-Palou et al., 2011).

G.2.2 Dilution

Dilution is another widely used method for reducing the viscosity of heavy oils. Heavy oil viscosity reduction is obtained through blending heavy oil with light hydrocarbons. Henaut et al. (2003) concluded that the high viscosity of heavy oil mainly comes from the overlapping of its asphaltenes; adding diluents into heavy oil reduces concentration as well as the overlapping of asphaltenes, leading to the

viscosity reduction (see Figure G-7). Dilution to reduce heavy oil viscosity is effective since a fraction of 20~30% of diluent is often enough to get a low enough viscosity (see Figure G-8).

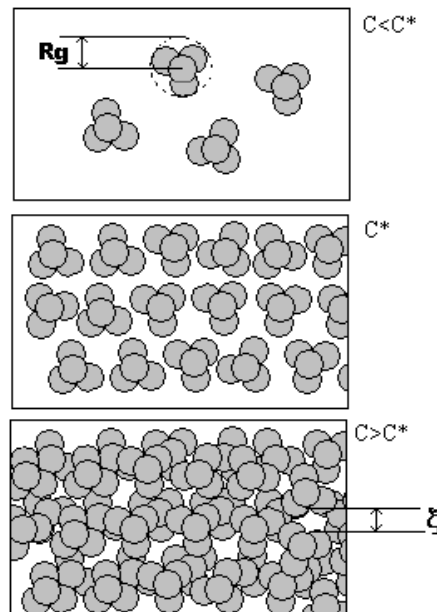


Figure G-7 A schematic representation of asphaltenes association - the bottom diagram represents status of heavy oil, while the top two represent status of diluted heavy oil (Henaut et al., 2003).

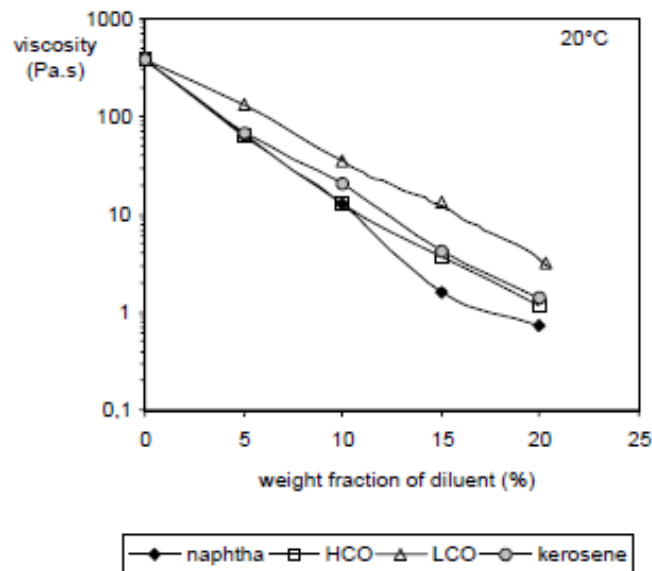


Figure G-8 Influence of dilution on the the viscosity of the Venezuelan crude at 20 °C (Argillier et al., 2001).

Dilution for heavy oil transport is most widely used where lighter crude oil is available. Diluents could either be recycled or not. If the diluent is to be recycled, additional substantial investments are needed to separate the diluent, build and operate a separate diluent return pipeline. If not to be recycled, the heavy oil would be sold with diluent together as some kind of 'upgraded' oil. For the both ways, light crude oil of higher quality as well higher market price than heavy oil is used, so economical evaluation is needed to assess the financial viability of this method in the first place.

G.2.3 Addition of Chemical Additives

(1) Pour Point Depressants (PPD)

Adding pour point depressants (PPD) into crude oil is another way to transport heavy waxy crude oils, especially for pipelines from off-shore to ground facilities. PPD, alternatively known as wax crystal modifiers or wax inhibitors, are chemical additives that modify the crystal morphology and the way the crystals interact, thereby reducing the tendency of crystals to interlock and form three-dimensional networks (Pedersen and Rønningsen, 2003). It helps to reduce the crude oil's pour point, viscosity and yield stress appreciably.

(2) Drag Reducing Additives (DRA)

Drag reducing additives (DAR) are well known to reduce pressure drop substantially in turbulent flow when a small amount of DRA is injected in the pipeline. Different from pour point depressants reducing the pour point as well as the viscosity of oil products, it reduces friction between the fluid and the pipe by altering the flow behaviour, suppressing the growth of turbulent eddies (Martínez-Palou et al., 2011). In commercial operations, drag reducing additives must be shear-stable during its flowing in the pipeline, and be effective at very low concentrations. In addition, the treated crude must not cause any downstream refining problems. Long-chained polymers with a very high molecular weight are by far the most efficient drag reducers.

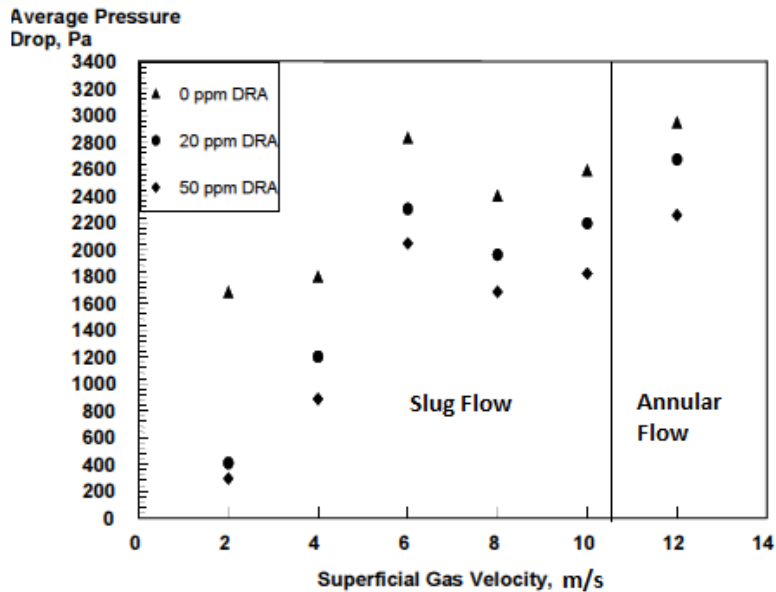


Figure G-9 Pressure drop reduction for slug flow and annular flow with the presence of DRA, adapted from Daas et al. (2000).

DRA cannot work if the flow in the pipe is laminar as it works by reducing the energy loss by turbulence. Pure heavy and extra heavy crude oils would flow in laminar due to the high viscosity if no other methods are applied. For heated heavy oil, diluted heavy oil, or multiphase heavy oil flow, DRA could reduce the friction effectively (see Figure G-9). The effectiveness of DRA depends on many parameters such as fluids' viscosity and velocity, oil composition, pipe diameter and roughness, water cut, DRA types and concentration, shear degradation of DRA.

G.2.4 Water-assisted

(1) O/W emulsion

Pipelining heavy crude oils as oil-in-water (O/W) emulsions is a relatively new technique. In this method, the heavy oil is dispersed in a water continuous phase by the use of surfactants and detergents, forming an O/W emulsion, and thus achieving a reduction in the apparent viscosity. Figure G-10 depicts some possible emulsion patterns in petroleum production and transport. To transport crude oils as O/W emulsions, steps to be performed include selecting an appropriate surfactant and producing the O/W emulsions, pipelining the produced emulsions to the desired destination, and separating oil and water phases (Ashrafizadeh and Kamran, 2010).

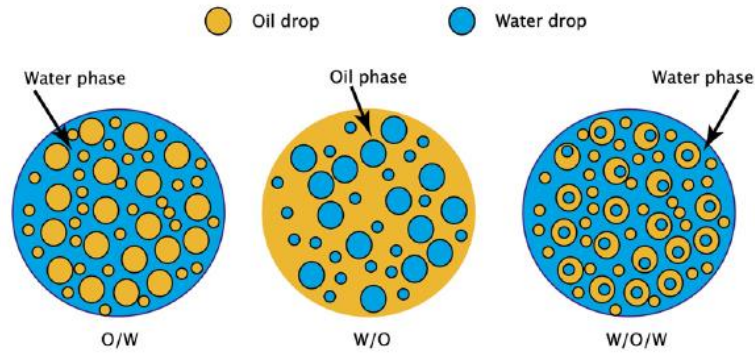


Figure G-10 Illustrations of possible emulsion patterns in petroleum production and transport (Martínez-Palou et al., 2011).

The principle difficulty with the use of this technology is the selection of effective surfactants for specific oils, as well as the high cost of the surfactants; surfactants must be capable of stabilizing the emulsion during transportation, while must not be too stabilizing to separate the water from the oil once the mixture reaches the processing plant. Many parameters affect the stability of the emulsions, e.g., oil-water ratio, surfactant type, size of the dispersed droplets, temperature, PH of water. Figure G-11 shows the oil-water ratio effect on apparent viscosity. As shown, the higher the water fraction is, the lower the apparent viscosity is. However, in heavy oil transportation, it is desirable to pipeline as much oil as possible and as little water as possible for economic consideration.

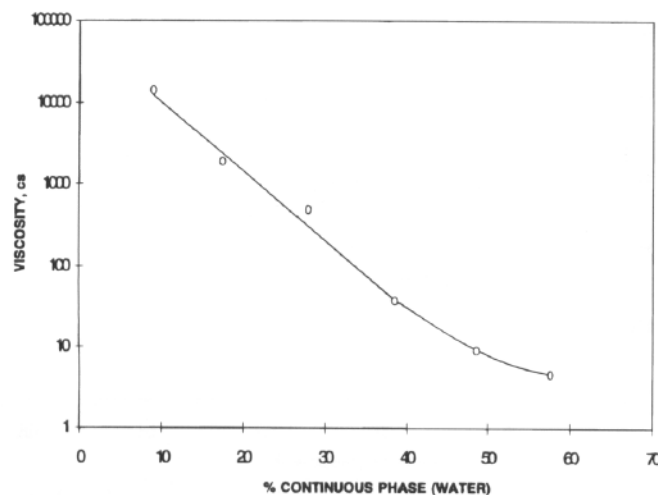


Figure G-11 Oil-water ratio effect on apparent viscosity (Guevara et al., 1997).

(2) Water-lubricated flow

Developing water-lubricated flow is another solution to transport heavy oils. In this method, water is introduced into the flow to act as a lubricating layer surrounding the viscous oil, reducing considerably the resistance to flow. The viscous oil flows inside the continuous-annular water can be in forms of continuous oil core, or discontinuous oil plugs or lumps. Core annular flow (CAF) in which the oil flows as a continuous core is the most attractive flow pattern for heavy oil transportation. CAF can have the lowest pressure drop for same flow conditions, which implies the least horsepower requirement.

The high viscous oil tends to adhere to pipe inner wall upon contact of oil core with the pipe wall. The lubricated flow can still be robust even when the inner wall of a pipe is coated with oil fouling film (Joseph et al, 1997). Sometimes, however, the fouling builds up, leading to rapidly increase in the pressure drop. Another major problem associated with this transportation method is difficulty in restarting the flow in case of unscheduled shutdown.